UNIVERSIDAD DE COSTA RICA

SISTEMA DE ESTUDIOS DE POSGRADO

DESCRIPCIÓN DE CAMBIOS FISIOLÓGICOS RELACIONADOS CON VÍAS AUTOFÁGICAS EN CÉLULAS ENDOTELIALES DURANTE SU INTERACCIÓN CON DIVERSOS ESTÍMULOS PRODUCIDOS POR *PLASMODIUM BERGHEI*

Tesis sometida a la consideración de la Comisión del Posgrado en
Microbiología, Parasitología, Química Clínica e Inmunología para
optar al grado y título de Maestría Académica en Microbiología

JERSON JAFETH CASTRO ARAYA

Ciudad Universitaria Rodrigo Facio, Costa Rica

2026

Dedicatory

To Yacky, who was like a sister to me.

Thank you for inspiring in me the value of education and the belief that we can always go further. Your tireless passion for learning and growth will always remain with me.

Acknowledgements

I would first like to express my deepest gratitude to my support system, my pillars and my reason for being: my fiancé Michael, and my parents, Erick and Marta. Your love, encouragement, and unwavering support have been the foundation that made this journey possible. Everything I have achieved is also a reflection of you, and this accomplishment belongs to you as much as it does to me.

I am also sincerely grateful to the staff of the Protozoology Section, the Tropical Disease Research Center (CIET), and the Materials Science and Engineering Research Center (CICIMA) for their logistical support throughout the different stages of this project.

I would like to extend my appreciation to my friends and colleagues at the Faculty of Microbiology who contributed to this work in different ways. I am especially thankful to Dr. Jorge Arias for generating the cell lines used in this study, to Dr. Isaac Quirós for developing the image analysis pipelines, to Dr. Juan Manuel Valverde for his guidance in proteomic data analysis, and to Dr. Lissette Retana for introducing me to the fascinating world of extracellular vesicles.

I am equally grateful to those who, through conversations in the hallways or over a cup of coffee, offered encouragement and motivation along the way. Those small moments of support played a meaningful role in helping me reach this milestone.

Finally, I am deeply grateful to everyone who, in one way or another, was part of this journey and contributed to making this work possible. This thesis is the result of many shared efforts, conversations, and acts of generosity along the way.

Esta tesis fue aceptada por la Comisión del Posgrado en Microbiología, Parasitología, Química Clínica e Inmunología de la Universidad de Costa Rica, como requisito parcial para optar al grado y título de Maestría Académica en Microbiología

Ph.D. Rodrigo Mora Rodríguez
Representante del Decano del Sistema de Estudios de Posgrado

Mónica Prado
Ph.D. Mónica Prado Porras
Directora de Tesis

Ph.D. Alicia Rojas Araya
Asesora

Ph.D. Julián Fernández Ulate
Asesor

MS.c. Lucía Figueroa Protti
Representante del Director del Programa de Posgrado en Microbiología, Parasitología, Química Clínica e Inmunología

Jerson Jafeth Castro Araya
Sustentante

Table of contents

Abstract

This study established and validated an integrated *in vitro* system to investigate *Plasmodium berghei* blood stage biology, with three main objectives: to define optimal culture conditions for blood-stage parasites, to characterize extracellular vesicles (EVs) produced under these conditions, and to evaluate the impact of parasite-derived stimuli on endothelial autophagy.

Short-term culture conditions for *P. berghei* were successfully optimized using a serum-free, nutrient-rich medium, incubation at 35 °C, and a controlled microaerophilic atmosphere. Under these conditions, parasites maintained viability, normal morphology, and asexual development for approximately four days while preserving infectivity *in vivo*. Limitations to prolonged culture were mainly associated with the requirement for fresh reticulocytes and the rapid loss of merozoite reinvasion capacity *in vitro*.

A comprehensive biophysical and proteomic characterization of *P. berghei*-derived EVs was performed for the first time. The isolated vesicle population was heterogeneous, with an average size of approximately 100 nm and physicochemical properties consistent with small EVs. Proteomic analysis identified parasite- and host-derived proteins enriched in the EV fraction, with cargo dominated by soluble cytosolic proteins involved in central metabolic pathways, protein synthesis, and turnover. The detection of virulence-associated and moonlighting proteins supports a role for EVs in extending parasite-host interactions beyond infected red blood cells (iRBCs). The detection of an ESCRT-related VPS homolog provides initial mechanistic support for conserved vesicle formation pathways in *Plasmodium*.

Genetically modified tEnd.1 endothelial cell lines expressing fluorescent LC3 reporters were generated and validated to monitor autophagic activity. Using these models, exposure to parasite-derived stimuli, including iRBCs, EVs, and parasite-conditioned supernatants, consistently resulted in impaired autophagic flux. This impairment was characterized by autophagosome accumulation accompanied by reduced autolysosome formation and displayed stimulus-dependent temporal dynamics.

Mechanistically, these effects are consistent with a convergence of adhesion-dependent stress, inflammatory signaling, and lysosomal dysfunction, ultimately disrupting autophagosome-lysosome fusion and degradative capacity.

In conclusion, this work provides an integrated framework linking parasite culture optimization, EV characterization, and endothelial autophagic responses. It advances the understanding of EV biology in rodent malaria models and establishes vesicle-mediated modulation of endothelial homeostasis as a novel axis of host-pathogen interaction, offering a foundation for future studies on malaria pathogenesis.

Resumen

Este estudio estableció y validó un sistema integrado *in vitro* para investigar la biología de la fase sanguínea de *Plasmodium berghei*, con tres objetivos principales: definir las condiciones óptimas de cultivo para los parásitos, caracterizar las vesículas extracelulares (EVs) producidas bajo estas condiciones y evaluar el impacto de estímulos derivados del parásito sobre la autofagia endotelial.

Las condiciones de cultivo a corto plazo para *P. berghei* fueron optimizadas exitosamente mediante el uso de un medio libre de suero y rico en nutrientes, incubación a 35 °C y una atmósfera microaerofílica controlada. Bajo estas condiciones, los parásitos mantuvieron su viabilidad, morfología normal y desarrollo asexual durante aproximadamente cuatro días, preservando además su infectividad *in vivo*. Las principales limitaciones para el cultivo prolongado estuvieron asociadas con el requerimiento de reticulocitos y la rápida pérdida de la capacidad de reinvasión de los merozoítos *in vitro*.

Por primera vez, se realizó una caracterización biofísica y proteómica integral de EVs derivadas de *P. berghei*. La población vesicular aislada fue heterogénea, con un tamaño promedio de aproximadamente 100 nm y propiedades fisicoquímicas comparables con EVs pequeñas. El análisis proteómico identificó proteínas de origen parasitario y del hospedero, con una carga dominada por proteínas citosólicas solubles involucradas en rutas metabólicas centrales, síntesis y recambio proteico. La detección de proteínas asociadas a virulencia y proteínas *moonlighting* respalda un papel de las EVs en la extensión de las interacciones parásito-hospedero más allá de los eritrocitos infectados (iRBCs). Asimismo, la detección de una proteína relacionada con el homólogo de VPS del sistema ESCRT proporciona un soporte mecanístico inicial para la producción de EVs en *Plasmodium*.

Se generaron y validaron líneas endoteliales tEnd.1 genéticamente modificadas que expresan reporteros fluorescentes de LC3 para el monitoreo de la actividad autofágica. Utilizando estos modelos, la exposición a estímulos derivados de *P. berghei*, incluidos iRBCs, EVs y sobrenadantes condicionados del parásito, resultó consistentemente en una alteración del flujo autofágico. Esta alteración se caracterizó por la acumulación de autofagosomas acompañada de una reducción en la formación de autolisosomas y presentó dinámicas temporales dependientes del tipo de estímulo.

Desde el punto de vista mecanístico, estos efectos son coherentes con la convergencia de estrés dependiente de adhesión, señalización inflamatoria y disfunción lisosomal, lo que finalmente conduce a la alteración de la fusión autofagosoma-lisosoma y de la capacidad degradativa.

En conjunto, este trabajo proporciona un marco integrado que vincula la optimización del cultivo parasitario, la caracterización de EVs y las respuestas autofágicas endoteliales. Además, amplía la comprensión de la biología de las EVs en modelos de malaria murina y establece la modulación vesicular de la homeostasis endotelial como un nuevo eje de interacción hospedero-patógeno, ofreciendo una base para futuras investigaciones sobre la patogénesis de la malaria.

List of figures

List of tables

List of abbreviations

%	percent
°C	degrees Celsius
3-MA	3-methyladenine
AA	normal hemoglobin
ADP	adenosine diphosphate
AFM	atomic force microscopy
AGC	automatic gain control
AMA	apical membrane antigen
AMBRA	autophagy and Beclin 1 regulator
AMP	adenosine monophosphate
AMPK	AMP-activated protein kinase
ANOVA	analysis of variance
AR	autophagic receptors
ARF	ADP-ribosylation factor
AS	sickle cell trait
ATG	autophagy-related gene/protein
ATP	adenosine triphosphate
BAF	bafilomycin A1
BBB	blood-brain barrier
BC	before Christ
BCA	bicinchoninic acid
BCL2	B-cell lymphoma 2
BECN1	Beclin 1 gene
BEI	Biodefense and Emerging Infections
CD	cluster of differentiation
CelTOS	cell-traversal protein for ookinetes and sporozoites
CHMP	charged multivesicular body protein

CICUA	Comité Institucional para el Cuidado y Uso de Animales
cm^2	square centimeter
CMA	chaperone-mediated autophagy
CO_2	carbon dioxide
COVET	cytosolic vacuole escape and trafficking
CQ	chloroquine
CSP	circumsporozoite protein
DLS	dynamic light scattering
DMEM-F12	Dulbecco's Modified Eagle Medium/Nutrient Mixture F-12
DNA	desoxyribonucleic acid
dpc	days post-culture
EBA	erythrocyte binding antigen
EBSS	Earle’s Balanced Salt Solution
EC	endothelial cell
EF	elongation factor
ELISA	enzyme-linked immunosorbent assays
ER	endoplasmic reticulum
ESCRT	endosomal sorting complexes required for transport
EV	extracellular vesicle
FCS	fetal calf serum
FIP200	focal adhesion kinase family interacting protein of 200 kDa
FWHM	full width at half maximum
g	grams; g-force
GABARAP	gamma aminobutyric acid type A receptor associated protein
GAPDH	glyceraldehyde-3-phosphate dehydrogenase
GATE-16	Golgi-associated ATPase enhancer of 16 kDa
GEST	gamete egress and sporozoite traversing protein
GFP	green fluorescent protein

GO	gene ontology
GRAMD1A	GRAM domain-containing protein 1A
GTP	guanosine triphosphate
h	hours
HEPES	N-(2-Hydroxyethyl)piperazine-N'-(2-ethanesulfonic acid)
HOPS	homotypic fusion and protein sorting complex
HSP	heat shock protein
HSPG	heparan-sulfate proteoglycan
HZ	hemozoin
ICR	Institute of Cancer Research
IFN-γ	interferon gamma.
IL-	interleukin
ILV	intraluminal vesicle
iNOS	inducible nitric oxide synthase
iRBC	infected red blood cell
ISEV	International Society for Extracellular Vesicles
JNK	c-Jun N-terminal kinase
KAT2B	lysine-acetyltransferase 2B
kcps	kilocounts per second
kDa	kilodalton
kg	kilogram
kV	kilovolt
L	liter
LAMP	lysosome-associated membrane protein
LANDO	LC3-associated endocytosis
LAP	LC3-associated phagocytosis
LC3	microtubule-associated-protein-one-light-chain-three
LCMS/MS	liquid chromatography - tandem mass spectrometry

LDH	lactate dehydrogenase
LDL	low density lipoproteins
LEBi	Laboratorio de Ensayos Biológicos
LYNUS	lysosomal nutrient sensor
m/z	mass-to-charge ratio
MACS	magnetic-activated cell sorting
MAPK	mitogen-activated protein kinase
MCP-1	monocyte chemoattractant protein 1
mg	milligram
MHC-I	major histocompatibility complex class I
min	minutes
miRNAs	micro ribonucleic acids
MISEV	Minimal Information for Studies of Extracellular Vesicles
mL	milliliter
mmol	millimole
M. musculus	*Mus musculus*
MOI	multiplicity of infection
mol	mole
MR4	Malaria Research and Reference Reagent Resource Center
MS	mass spectrometry
ms	millisecond
MSP	merozoite surface protein
mT	middle T
mTORC	mechanistic target of rapamycin complex
mV	millivolt
MVB	multivesicular body
n	nano; number of specimen/experiments
$N\ m^{-1}$	newton per meter

N_2	nitrogen
$NaHCO_3$	sodium bicarbonate
NBR1	neighbor of BRCA1 gene 1
NDP52	nuclear dot protein 52 kDa
NF-κB	nuclear factor kappa-light-chain-enhancer of activated B cells
NLRP3	NOD-like receptor family pyrin domain containing 3
nm	nanometer
NO	nitric oxide
NOS	nitric oxide synthase
NRBF2	nuclear receptor binding factor 2
NTA	nanoparticle tracking analysis
NVEP	non-vesicular extracellular particle
O_2	oxygen
P	probability value (p-value)
P. berghei	*Plasmodium berghei*
P.b-EVs	*P. berghei*-derived EVs
P.b-SN	*P. berghei*-derived EV-reduced supernatant
P. chabaudi	*Plasmodium chabaudi*
P. falciparum	*Plasmodium falciparum*
P. knowlesi	*Plasmodium knowlesi*
P. malariae	*Plasmodium malariae*
P. ovale	*Plasmodium ovale*
P. vivax	*Plasmodium vivax*
P. yoelii	*Plasmodium yoelii*
p36	36-kDa *Plasmodium* protein
p52	52-kDa *Plasmodium* protein
p62	sequestosome 1 (SQSTM1)
PAAR	*Plasmodium*-associated autophagy-related

PAMP	pathogen-associated molecular pattern
PASE	PI3P-associated sporozoite elimination
PBS	phosphate buffer saline
PCR	polymerase chain reaction
PDI	polydispersity index
PE	phosphatidylethanolamine
PECAM-1	platelet endothelial cell adhesion molecule-1
PEG	polyethylene glycol
PFA	paraformaldehyde
PfEMP1	*Plasmodium falciparum* erythrocyte membrane protein 1
pH	potential of hydrogen
PI	phosphatidylinositol
PI3KC3	class III PI3-kinase complex
PI3P	phosphatidylinositol-3-phosphate
PLP-1	perforin-like protein 1
PP2A	protein phosphatase 2A
PV	parasitophorous vacuole
PVM	parasitophorous vacuole membrane
Rab	Ras-associated binding protein
RAB33A	Ras-related protein Rab-33A
RAP	rhoptry-associated proteins
RAPA	rapamycin
RBC	red blood cell
RDT	rapid diagnostic test
RESA	ring-infected erythrocyte surface antigen
RhoA	Ras homolog family member A
RNA	ribonucleic acid
RNS	reactive nitrogen species

RON	rhoptry neck protein
ROS	reactive oxygen species
RP	ribosomal protein
rpm	revolutions per minute
RPMI	Roswell Park Memorial Institute
rRNA	ribosomal ribonucleic acid
s	seconds
SASP	senescence-associated secretory phenotype
SDS-PAGE	sodium dodecyl sulfate - polyacrylamide gel electrophoresis
SN	supernatant
SNARE	soluble NSF attachment protein receptor
SPECT	sporozoite microneme protein essential for cell traversal
SS	sickle cell disease
SSU	small ribosomal subunit
STV	starvation-induced autophagy
STX	syntaxin
TEM	transmission electron microscopy
tEnd.1	murine thymic endothelioma 1 cell line
tf	tandem fluorescent
TFEB	transcription factor EB
TLR	toll-like receptor
TNF	tumor necrosis factor
TRAP	thrombospondin-related anonymous protein
TRPS	Tunable Resistive Pulse Sensing
TSG101	tumor susceptibility gene 101
U	unit
UBL	ubiquitin-like
ULK1	unc-51-like kinase 1

uPA	urokinase-type plasminogen activator
V	volt
Vamp	vesicle-associated membrane protein
VPS	vacuolar protein sorting
WHO	World Health Organization
WIPI	WD repeat domain phosphoinositide-interacting protein
μg	microgram
μL	microliter
μm	micrometer
μmol	micromole

1. Introduction

1. Chapter 1: Malaria

Malaria or paludism is a vector-borne disease caused by protozoa of the genus *Plasmodium,* transmitted to humans by infected female mosquitoes (1). It remains as one of the leading causes of mortality worldwide, with an estimated 263 million people affected and 597,000 deaths in 2023 globally according to the latest World Health Organization Malaria Report (2). Despite more than a century of global effort and research aimed at improving prevention, diagnosis, and treatment for malaria, this infection continues to be a significant health burden around the world (3).

1.1.Background

Malaria is an ancient disease, with references dating back to 2700 BC describing periodic fevers, poor health, and enlarged spleens in people living near marshes (1). Throughout history, it affected individuals from all social classes, including notable figures such as Christopher Columbus, George Washington, and Alexander the Great. Early explanations attributed malaria to supernatural forces, until Hippocrates proposed in the 4th century BC that it resulted from inhaling swamp vapors, an idea that persisted for more than two millennia and gave rise to the term "malaria," derived from *mal'aria* or *malus aer* (1, 3).

With the rise of germ theory, researchers intensified the search for malaria's cause. Although some attributed the disease to bacteria like *Bacillus malariae*, understanding shifted in 1880 when Charles Laveran identified a protozoan parasite in the blood of malaria patients, the first protozoan known to invade human blood cells. Despite initial skepticism, his discovery was accepted in 1884, and he was later awarded the 1907 Nobel Prize in Medicine for this breakthrough (1).

Following Laveran's discovery, interest grew in identifying blood parasites in different hosts, aided by improved staining techniques such as Romanowsky's. By 1890, the protozoan nature of malaria was well established, and the species responsible for benign tertian, malignant tertian, and quartan malaria, now known as *Plasmodium vivax*, *P. falciparum*, and *P. malariae*, had been defined. Subsequent milestones included the discovery of mosquito vectors for avian malaria by Ronald Ross in 1897 and for human malaria by Italian researchers between 1898 and 1900 (1).

1.2.Epidemiology

The spread of malaria has often been determined by changes to the environment caused by human activity, including population movements and agricultural practices such as deforestation and irrigation (4). The different malaria species that infect humans present a differential geographical distribution. Being *P. vivax* and *P. malariae* the most common ones in America and Europe, *P. falciparum* in Africa and *P. knowlesi* is mostly restricted to South-East Asia (3, 5).

One factor that explains this phenomenon is the selective pressure exerted by the parasite on humans. It is known for a fact that the evolution of malaria parasites has shaped the human genome, by selecting genetic mutations that protect against the disease. This theory was called the malaria hypothesis proposed by Haldane in 1948 (6). These mutations include thalassemia, glucose-6-phosphate dehydrogenase deficiency, ovalocytosis, RBC Duffy negativity, sickle cell disease, and other hemoglobinopathies. These traits are particularly prevalent in regions where malaria is endemic, and they offer insights into the coevolution of humans and malaria parasites (7).

In 2023, there were 263 million cases and 597,000 deaths reported in 83 countries. About 94% of cases and deaths, mostly involving children under the age of five, were reported from Africa. The WHO is currently promoting the malaria eliminating countries for 2025 (E-2025) initiative in 25 countries, including Costa Rica. These countries were selected based on criteria such as having a government-endorsed elimination plan, meeting a defined threshold of malaria case reductions in recent years, meeting pre-defined program requirements, and expert opinions (2).

1.2.1. Costa Rica

Since 2015, Costa Rica has been working to eradicate malaria by the year 2025. However, the incidence of autochthonous cases has increased in recent years (Figure 1.1). Fortunately, since 2010, there have been no recorded malaria-related fatalities in the nation (2). Notably, there has been a change in the proportion of malaria-causing species.

P. vivax was the cause of every single case until 2017. In 2018, reports of autochthonous cases caused by *P. falciparum* started to come in, and by 2021, *P. falciparum* accounted for 90% of all cases reported.

Until November 2025, only 59 malaria cases have been reported and 6 active sources of malaria transmission in the country. These outbreaks are concentrated in the northern region, and the Caribbean region (8). It is important to follow up on the preventive measures adopted by government authorities to achieve the goal of eradicating malaria from the country in the coming years.

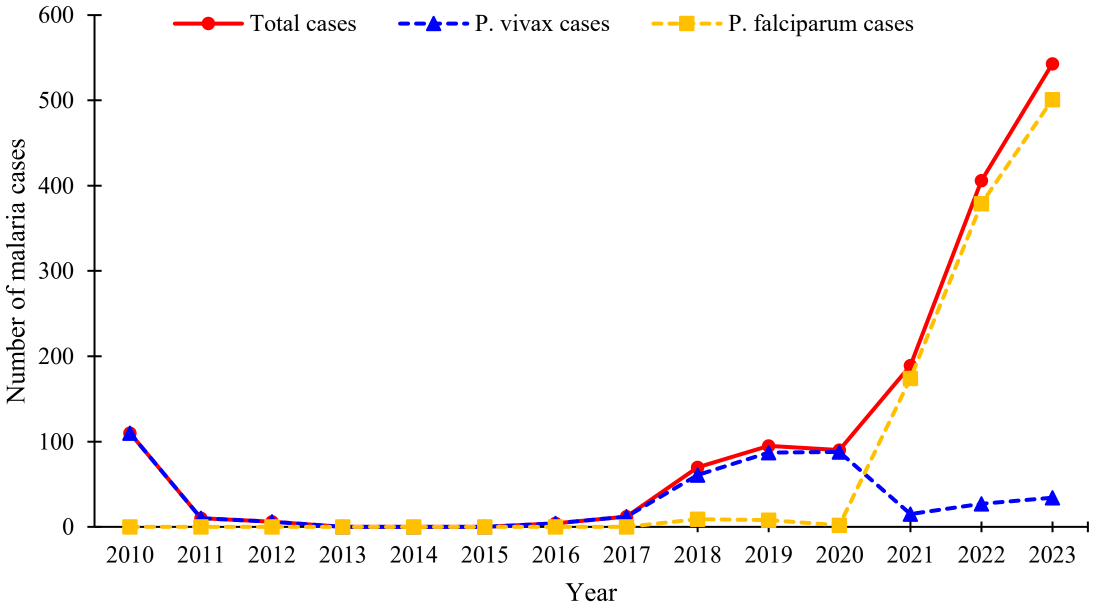

Figure 1.1. Number of indigenous cases per year and *Plasmodium* species in Costa Rica (2010-2023). Figure generated using data obtained from (2).

1.3.Agent

Plasmodium is a genus of intracellular protozoa within the phylum Apicomplexa, characterized by an apical complex and an intraerythrocytic life cycle. Phylogenetic studies of the SSU rRNA gene indicate that the *Plasmodium* lineage diverged from other apicomplexans hundreds of millions of years ago, likely originating from a free-living, chloroplast-containing protozoan (9). This ancestral organism already carried out sexual reproduction and later evolved schizogony, the asexual replication process seen in modern *Plasmodium* species (6, 7).

Over millions of years, early *Plasmodium* forms adapted to infect ancient blood-feeding Dipterans (mosquito ancestors) and subsequently evolved a two-host life cycle involving vertebrates. Today, nearly 200 *Plasmodium* species have been described, infecting mammals, reptiles, and birds, with five known to infect humans: *P. falciparum, P. vivax, P. malariae, P. ovale*, and *P. knowlesi*. Additional species infect non-human primates and are closely related to human parasites, though human infections with these are rare (3, 10).

1.3.1. Life cycle

Malaria parasites have a complex life cycle involving an *Anopheles* mosquito vector and a vertebrate host (Figure 1.2). Infection begins when an infected female mosquito inoculates sporozoites into the skin during a blood meal (11). Lacking tropism for blood vessels, sporozoites move randomly through the dermis using gliding motility until they encounter a vessel and enter the bloodstream. Many fail during this process, being destroyed in the skin or diverted to lymph nodes, where they can trigger early immune responses (12, 13).

Within 1 to 3 hours, successful sporozoites reach the liver sinusoids, where interactions between the sporozoite circumsporozoite surface protein (CSP) and highly sulfated heparin sulfate proteoglycans (HSPGs) signal their arrival at the liver (13). This interaction triggers a shift from a migratory to an invasive phenotype, leading to secretion of microneme and rhoptry proteins that mediate hepatocyte invasion. Proteins such as TRAP, p36, p52, RONs, and AMA1 facilitate attachment, moving junction formation, and the development of the parasitophorous vacuole (PV) in which the parasite will grow (14, 15).

Sporozoites traverse several cells before establishing productive infection, aided by traversal proteins such as SPECT, PLP-1, CelTOS, and GEST (11, 14, 16). Once inside a suitable hepatocyte, species like *P. vivax* and *P. ovale* may form dormant hypnozoites, whereas others initiate schizogony, an intense phase of asexual replication. Over several days, the parasite remodels the PV membrane (PVM) to maximize nutrient uptake, especially lipids, allowing the production of tens of thousands of merozoites (14).

As replication proceeds, the parasite expands within the hepatocyte, forming cytomeres that divide into thousands of merozoites through synchronized nuclear and organelle fission (15, 17). At the final liver stage, merozoites exit by first breaking down the PVM and then budding off inside host-derived vesicles called merosomes. These merosomes enter the bloodstream undetected by the immune system and release merozoites in the lung capillaries, where they initiate red blood cell infection and begin the symptomatic blood stage of malaria (14, 18).

After the free merozoites enter the bloodstream, they invade erythrocytes in a rapid and complex process that involves pre-invasion, active invasion, and echinocytosis (11). Pre-invasion is the initial reversible interaction between merozoites and erythrocytes through the merozoite surface protein 1 (MSP1). This first contact reorientates the parasite and triggers the release and remodeling of proteins that mediate the formation of an irreversible and strong attachment to the RBC (19).

Then, the actomyosin motor is subsequently used to drive merozoite invasion through the RBC membrane. Once inside, it undergoes a process of fusion with the RBC membrane at the posterior end, which seals the parasite within the PV. This is followed by echinocytosis, a process that causes the erythrocyte to shrink and form spiky protrusions, possibly due to calcium influx (11, 20).

Inside, the merozoite changes into a ring-stage parasite, and then into a trophozoite. These two stages are equivalent to the G1 phase of cell cycle, where the parasites feed from hemoglobin and grow (21). Then it multiplies asexually by schizogony to produce 8 to 64 new merozoites (depending on the species). This whole process can take up to 24 (*P. knowlesi, P. berghei*), 48 (*P. falciparum, P. ovale, P. vivax*), or 72 hours (*P. malariae*) until the RBC bursts and the parasites restart their intraerythrocytic proliferation cycle (10, 21).

Some merozoites subsequently differentiate into the gametocyte, the following developmental stage for sexual reproduction by a process called gametocytogenesis. The commitment to develop into gametocytes appears since the previous intraerythrocytic cycle. This process is highly regulated by the transcription factor AP2-G (11, 21). However, the stimuli and time required for gametocyte production is poorly understood and varies through the species. Gametocyte production is increased by high parasitaemias, exposure to antimalarial drugs and presence of extracellular vesicles (11).

In the vector, female *Anopheles* mosquitoes acquire malaria parasites when they ingest RBCs containing gametocytes during a blood meal (22). In the mosquito midgut, gametocytes exit the erythrocytes and undergo gametogenesis, a process triggered by environmental changes such as a temperature drop, the presence of xanthurenic acid, and an increase in extracellular pH (23). Male microgametes rapidly form through three rounds of mitosis followed by exflagellation, and within the first hour after feeding, they fertilize female macrogametes to produce diploid and subsequently tetraploid zygotes (24, 25). After 18–24 hours, these zygotes undergo meiosis and transform into motile ookinetes, which traverse the midgut epithelium and lodge beneath the basal lamina to develop into oocysts, a major bottleneck where parasite numbers can drop dramatically (23, 26).

Within the oocyst, the parasite undergoes sporogony, an extensive replication process lasting 10–14 days that generates thousands of sporozoites (22). After 1 to 3 weeks, the mature oocyst ruptures, releasing sporozoites into the mosquito haemocoel, from where they migrate to and invade the salivary glands. Once established there, the sporozoites are ready to be transmitted to a vertebrate host during the mosquito's next blood meal, thus completing the vector phase of the malaria life cycle (23, 26).

1.3.2. Rodent malaria models

The understanding of the biology and pathological features of malaria has been greatly impacted using animal models. Among these, the use of rodent models stands out, despite their differences from human species in terms of stage specific morphologies, duration of life cycle and host cell preferences (Table 1.1). Nonetheless, they offer benefits such as their ease of handling in rodents, experimental tractability of all life cycle stages under lab conditions as well as the availability of a wide array of genetic manipulation systems (27, 28).

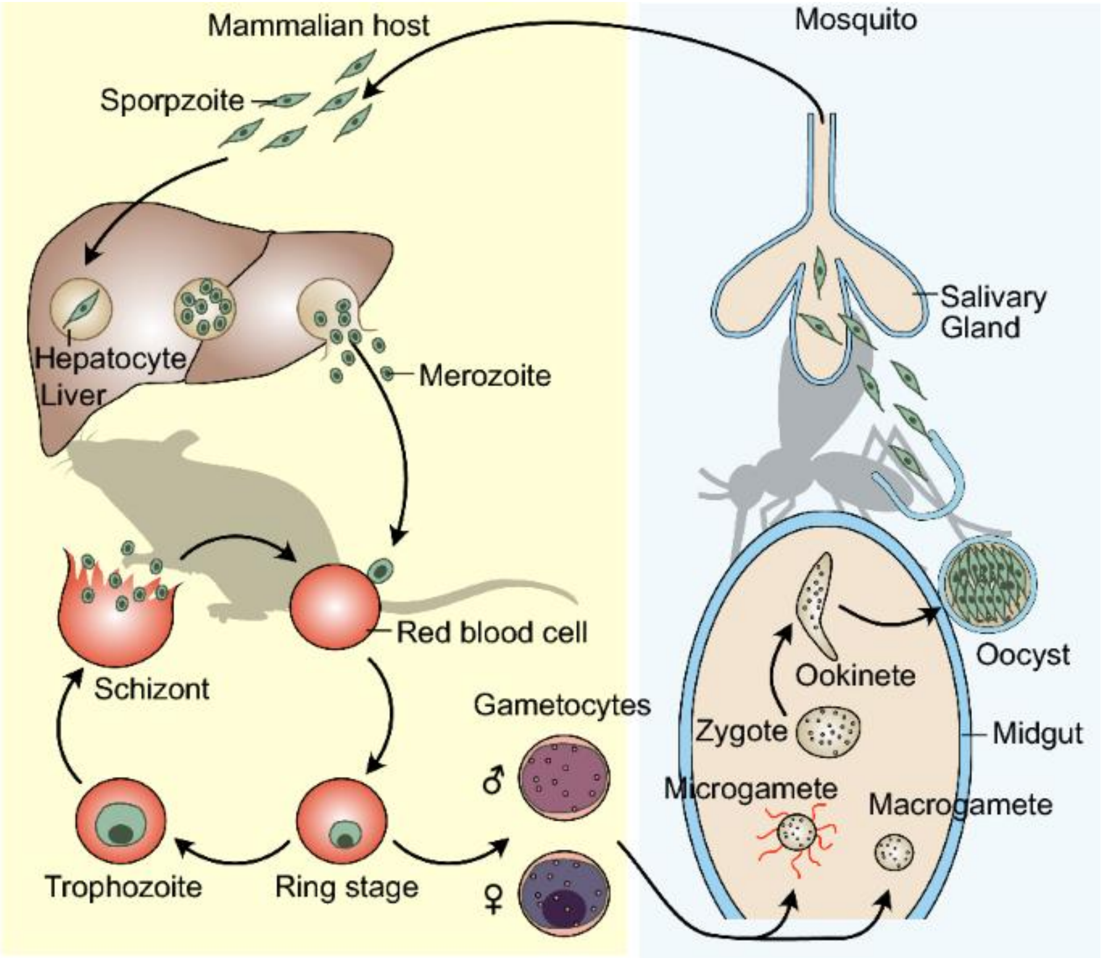

Figure 1.2. *Plasmodium berghei* life cycle. The life cycle of *Plasmodium* involves a vertebrate host (a rodent for *P. berghei*) and an *Anopheles* mosquito vector. Sporozoites are transmitted to the vertebrate host during a mosquito blood meal and travel to the liver, where they invade hepatocytes and develop within a PV. Throughout the liver stage, parasites differentiate and multiply, eventually releasing merozoites into the bloodstream. During the blood stage, merozoites invade RBCs, progressing through ring, trophozoite, and schizont stages, which produce additional merozoites that perpetuate the erythrocytic cycle. A subset of parasites differentiates into gametocytes, which are taken up by an *Anopheles* mosquito during feeding. In the mosquito midgut, gametocytes mature into gametes, undergo fertilization to form a zygote, and develop into ookinetes that traverse the midgut epithelium and form oocysts. Within oocysts, thousands of sporozoites are produced and migrate to the salivary glands, where they become infective to a new host, completing the life cycle. From (29).

Table 1.1. Comparison of some human and rodent *Plasmodium* species in relation to key life cycle features, host tropisms and disease pathogenesis.

Features	**Human *Plasmodium***		**Rodent *Plasmodium***		
	P. falciparum	***P. vivax***	***P. berghei***	***P. yoelii***	***P. chabaudi***
Commonly used strains	3D7, NF54, HB, Dd2, 7G8, FCB	Sal-1	NK65, ANKA, K173	17X, YM	AS
Liver stage duration (h)	~ 144 - 168	~ 192	~ 50	~ 50	~ 52 - 53
Blood stage duration (h)	24 - 48	48	22 - 24	18	24
RBC tropism	Mature and young RBCs	Reticulocytes	Reticulocytes	Reticulocytes	Mature RBCs
Tissue sequestration	Spleen, brain, liver, lungs, bone marrow	Spleen, liver, lungs, bone marrow	Spleen, liver, lungs	Organs not characterized	Liver
Natural host	Human	*Aotus lemurinus*	*Grammomys surdaster*	*Grammomys surdaster*	*Grammomys surdaster*

Adapted from (27).

Rodent models avoid the ethical limitations of studying malaria in humans or non-human primates and allow the analysis of complex host–parasite interactions not possible *in vitro*. They have been instrumental in advancing knowledge of pre-hepatic and hepatic stages, enabling the development of pre-erythrocytic vaccines, clarifying immune responses during the blood stage, elucidating antimalarial drug mechanisms, and establishing experimental models for severe malaria (27, 28).

However, despite their value and practicality, important differences exist between murine and human malaria, including variability in disease presentations across mouse–parasite combinations, differences in infection outcomes, and distinct immune response patterns. Thus, rodent models provide a useful but imperfect approximation of human malaria pathophysiology (30, 31).

1.3.2.1.*Plasmodium berghei*

Plasmodium berghei was first described in 1948 by Vincke and Lips, infecting Congo tree rats (*Grammomys surdaster*) and transmitted by *Anopheles dureni*. It was subsequently shown that *P. berghei* was also capable of infecting other rodent species, including *Mus musculus* (32). Recently, it was discovered that this parasite species shares a highly conserved chromosomal gene synteny with *P. falciparum* (27).

Vincke and Lips described this new species as follows: ring stage is usually uninucleate with a large vacuole, while trophozoites are non-vacuolate, slightly amoeboid, and have black pigment granules. Schizonts contain 6 to 20 merozoites with a small nucleus. Furthermore, infected erythrocytes suffer hypertrophy but without granulation, and polyparasitism is very common. Finally, the gametocytes measure 7-8 µm in diameter and retain their vacuole. The macrogametocyte contains dispersed pigment granules and a small peripheral nucleus, while the microgametocyte has a vacuole and a nucleus that is larger but less dense than that of the macrogametocyte (33).

The clinical course of the disease in rodents is characterized by lethargy, piloerection, decreased locomotion, anemia, hepatosplenomegaly, hematuria, pulmonary edema, and death within 7 days (34). The study of severe malaria syndromes, such as severe anemia, placental malaria, experimental cerebral malaria, acute kidney injury and respiratory distress, have been modeled in rodents using different parasite/mouse strain combinations (28).

1.4.Clinical presentation

Malaria exhibits a complex pathophysiology and presents with a broad clinical spectrum, ranging from severe and complicated forms to mild, uncomplicated, or asymptomatic infections. Uncomplicated symptomatic malaria is the most frequent presentation, with an incubation period of 9 to 30 days. Early symptoms are nonspecific and may include malaise, anorexia, dizziness, headache, myalgias, nausea, diarrhea, and fever. A hallmark of malaria is the paroxysmal fever pattern, characterized by cycles of cold, hot, and sweating stages (35).

The periodicity of these episodes depends on the infecting species and correlates with the synchronous rupture of schizonts and release of merozoites. Fever may occur every 24, 36, or 48 hours in *P. falciparum* infections, every 48 hours in *P. vivax* and *P. ovale*, and every 72 hours in *P. malariae*. Although uncommon, severe complications such as splenic rupture or hyperparasitemia may arise, particularly in asplenic individuals (35).

Severe malaria represents a life-threatening manifestation, most observed in non-immune individuals infected with *P. falciparum*. This form of the disease is associated with dysfunction of major organ systems, including the central nervous, pulmonary, renal, and hematopoietic systems. Cerebral malaria is the most lethal complication when untreated and is defined by a coma persisting for more than 30 minutes following a seizure, although any degree of altered consciousness warrants management as severe malaria (36). During severe disease, multiple metabolic abnormalities arise, including lactic acidosis and hypoglycemia, which reflect impaired tissue perfusion and disrupted hepatic gluconeogenesis. Pulmonary and renal failure may occur, particularly in pregnant patients, and severe anemia can exacerbate existing complications through extensive hemolysis and inadequate bone marrow compensation (35, 36).

In contrast, asymptomatic malaria remains poorly characterized due to the absence of standardized diagnostic criteria. It is generally defined by the presence of parasitemia on peripheral thick blood smears in individuals with no fever and without malaria-related symptoms. This presentation is most often observed in populations with partial immunity and plays a key role in sustaining transmission within endemic regions (37).

1.4.1. Physiopathology

Malaria pathology is primarily driven by the asexual blood stages of the parasite, which are responsible for the clinical manifestations and complications that define severe disease. Although liver stages were considered clinically silent, evidence now shows that they can induce transient tissue damage mediated by type I interferon responses. However, it is during the blood stages that parasite replication becomes highly visible to the immune system, provoking strong host responses that shape the course of infection (38).

One major contributor to pathology is the intense inflammatory reaction to parasite components and host cell damage. Proinflammatory cytokines such as IL-6, IL-8, IL-12, IL-18, IFN-γ, and TNF are crucial for parasite control, yet their excessive production correlates with worsening symptoms, including fever, anemia, liver dysfunction, and endothelial leak. This dysregulated inflammation not only amplifies tissue injury but also contributes to metabolic disturbances that accompany severe malaria (39, 40).

A second hallmark of severe disease is microvascular obstruction, which is tightly linked to endothelial activation. *Plasmodium falciparum* iRBCs present surface proteins like PfEMP1 that form adhesive knobs, enabling them to bind to endothelial receptors. This cytoadherence promotes endothelial activation and dysfunction, reduces blood flow, and causes localized tissue hypoxia, particularly in vulnerable organs such as the brain, lungs, and placenta. These endothelial responses are central to life-threatening complications, including cerebral malaria and respiratory distress (11, 41).

Because endothelial cells sit at the interface of parasite-host interactions, they represent a critical therapeutic target. iRBC-induced activation alters endothelial barrier integrity, coagulation, and inflammatory signaling, amplifying systemic damage even when parasites are being cleared. Importantly, antiparasitic drugs alone cannot always prevent mortality in severe cases, underscoring that restoring endothelial homeostasis is essential. Stabilizing endothelial function may prevent fatal outcomes such as severe acidosis, hypoxia, and organ failure, making the endothelium a promising focus for adjunctive therapies in malaria (41, 42).

1.5. Diagnosis

Malaria's clinical course and treatment success depend heavily on prompt and accurate diagnosis, especially in vulnerable populations such as young children and pregnant women, who account for more than 90% of malaria-related deaths (43). Light microscopy of stained thin and thick peripheral blood smears was the first method used to diagnose malaria and remains the gold standard (44, 45). The development of Romanowsky-type stains in 1891, which laid the foundation for stains such as Leishman, Giemsa, and Wright, marked one of the most significant technical advances in parasitology by enabling rapid, inexpensive diagnosis and species identification (45).

Despite its widespread use and utility in monitoring treatment response, microscopy has important limitations: it is time-consuming, requires highly trained personnel, and has a detection threshold of approximately 50–100 parasites/μL (45). To address these shortcomings, more sensitive diagnostic technologies have been developed, which broadly fall into immunological and molecular categories. Immunological methods detect parasite proteins in blood or serum and include rapid diagnostic tests (RDTs) and enzyme-linked immunosorbent assays (ELISA) (44, 46).

Molecular diagnostic methods, by contrast, detect parasite genetic material in blood or in less invasive samples such as urine or saliva. Common targets include the 18S rRNA gene and mitochondrial DNA, detected using techniques such as polymerase chain reaction (PCR). These methods offer exceptional sensitivity (1 parasite/μL) and high specificity, enabling accurate species identification and parasitemia estimation. However, their widespread implementation is hindered by high costs and the need for specialized equipment (47). Therefore, it remains difficult to develop a diagnostic method that is highly sensitive, inexpensive, and easily applicable in a variety of socioeconomic contexts.

1.6.Treatment

Most antimalarial drugs available target the blood stage of the parasite's life cycle, which is responsible for causing clinical symptoms. These compounds exhibit high stage selectivity and are further classified into three main classes: quinoline derivatives, antifolates, and artemisinin derivatives. Their main targets include hemoglobin breakdown, folate synthesis, and redox balance, respectively. All these effects lead to the parasite’s oxidative damage, diminished biomolecule synthesis, and finally death (48).

Unfortunately, there is reported resistance to all the antimalarial drugs used nowadays. Drug resistance may result from amplification of the gene encoding the target enzyme or transporter that expels the drug from the parasite. Furthermore, mechanisms that reduce the drug's toxicity can also facilitate resistance (49). Hence, there is a priority to look out for new targets and develop new strategies to treat this disease.

1.7.Prevention

The basis of malaria prevention came along with the discovery of the role of mosquitoes in transmitting malaria (1). Insecticide-treated nets are considered the most effective strategy reported to prevent malaria, compared to indoor residual spraying and prophylactic drugs (50). This demonstrates the possibility of controlling the disease by reducing contact with infected mosquitoes, leading to various methods being developed such as avoidance, screening, mosquito-proofing dwellings, using oils and larvivorous fish or draining habitats over time (1).

Another prevention strategy that has been a tremendous challenge is the development of effective vaccines. This is mainly due to its complex life cycle and various immune escape mechanisms that make human immunity against parasites unique. Malaria vaccines are categorized according to the parasite's targeted developmental stage: pre-erythrocytic vaccines (anti-infection), erythrocytic vaccines, and transmission-blocking vaccines (51).

Up until now, the WHO has only approved one vaccine (RTS,S/AS01) for broad use in 2021. However, in October 2023, they suggested the use of a second vaccination (R21/Matrix-M^{TM}). Both are pre-erythrocytic vaccines based on CSP-containing virus-like particles (51, 52). These are the results of over 60 years of effort, and they offer us new hope for the prevention and treatment of this disease.

2. Chapter 2: Extracellular vesicles

Extracellular vesicles (EVs) refer to a diverse group of non-replicating lipid-bound vesicles secreted by cells into the extracellular space. Initially, EVs were described as a way for living cells to get rid of unwanted material. Nowadays, EVs are understood as extracellular vehicles containing bioactive molecules like proteins, lipids, metabolites, and nucleic acids, with a wide range of functions that grow every year (53, 54). The increasing fascination and practical uses of these subcellular secretion structures prompted the establishment of the International Society of Extracellular Vesicles (ISEV) in 2012 (55).

The first evidence of EVs is attributed to Chargaff and West (1946) as they describe clotting properties in small blood corpuscles derived from platelets, which they referred to as platelet dust (56, 57). However, Aaronson et al. (1971) are credited with coining the terms "intracellular" and "extracellular" vesicles. They provided the initial ultrastructural evidence, using electron microscopy, of a flagellated alga (*Ochromonas danica*) producing membrane structures both inside and outside the cell (55, 58). The understanding of EVs is rapidly increasing, yet this can lead to challenges like insufficient reproducibility, non-standardized methodologies, and lack of appropriate terminology (55).

2.1.Types

An issue in the field of EV research is the lack of well-defined categories for different types of EVs. Currently, there are multiple classification standards and subtypes that make universal understanding difficult. For instance, certain authors used the physical attributes of the EVs, such as size (small, medium, or large) and density (low, middle, or high), to classify them. Some authors prefer to use biochemical composition that relies on molecular markers (57), and others choose to base the classification on descriptions of environmental conditions or cell type, for example: oncosomes (from cancer cells), stressed EVs (from stressed cells), or autophagic EVs (from autophagic cells) (59).

Fortunately, most investigators reached consensus on what they called a classical classification, which is based on their biogenesis, release pathway, and composition. Through these features, two main classes of EVs were established: exosomes, and ectosomes (Figure 1.3) (60). While there are no universally recognized markers for each kind, their protein profiles exhibit small variations from one another because of the biogenesis pathway. Nevertheless, it is crucial to acknowledge that several components have a substantial degree of overlap, which might provide challenges when attempting to analyze them (54, 61).

2.1.1. Exosomes

Exosomes, are nano-sized vesicles with a size range of 30 to 150 nm. Their formation is dependent on the endocytic process. Following the internalization of cargo by a cell through endocytosis, the early endosome can commit to endosomal maturation into a late endosome. The exosomes are formed from inward budding of late endosomal structures. The formation of intraluminal vesicles (ILVs) results in the encapsulation of cargo, leading to the formation of multivesicular bodies (MVBs). These MVBs can either be sent to the lysosome for degradation or fused with the cell’s plasma membrane to release its content, including the exosomes (62, 63).

Because the most common pathway for exosome biogenesis depends on ESCRT proteins, these are usually used to identify them. Additional proteins such as Alix, TSG101, HSP70, HSP90β, LAMP1 flotillin, and caveolins along with tetraspanin family members including CD63, CD9, and CD81, are also employed as markers. However, these markers can also be found in other types of EVs. The cargo composition exhibits significant variability. Cargo sorting involves protein monoubiquitination, RNA-binding proteins in microRNAs, lipid rafts, and their interaction with exosomal membrane proteins (62, 63). In general, proteins involved in the endosomal pathways coming from the endoplasmic reticulum and Golgi apparatus are also commonly found in exosomes (54).

2.1.2. Ectosomes

Ectosomes, on the other hand, are formed through direct outward blebbing and pinching of the plasma membrane. This results in a wide range of sizes, ranging from 200 to 5000 nm in diameter (64). The mechanism of biogenesis is not well comprehended, however, it is hypothesized to entail cytoskeleton constituents, motor proteins, ESCRT machinery, small GTPases such as ARF1/6 and RhoA, and sphingomyelinase (65). The rate of ectosome production and reception depends on the cell's physiology and microenvironmental conditions since both processes are energy-dependent and requires active remodeling of plasma membrane composition (66).

There is a wide range of ectosome subtypes generated through distinct cellular processes, including apoptotic bodies, microvesicles, migrasomes, oncosomes, and exophers, among others. These vesicle populations differ in size, biogenesis, and functional roles, reflecting the diverse mechanisms by which cells release extracellular material (60).

In terms of cargo diversity, ectosomes are known to contain a wide variety of molecules, which is again indicative of the multiple intracellular trafficking routes that transport this cargo to the cell surface. Proteins are sorted by certain GTPases, such as ARF6, while it is believed that nucleic acids are co-transported with certain proteins (64, 66). Normally, their content is enriched with cytosolic and plasma membrane associated proteins like cytoskeletal proteins, integrins, Annexin V, major histocompatibility complex class I (MHC-I), CD40, heat shock proteins, glycosylated and phosphorylated proteins (54).

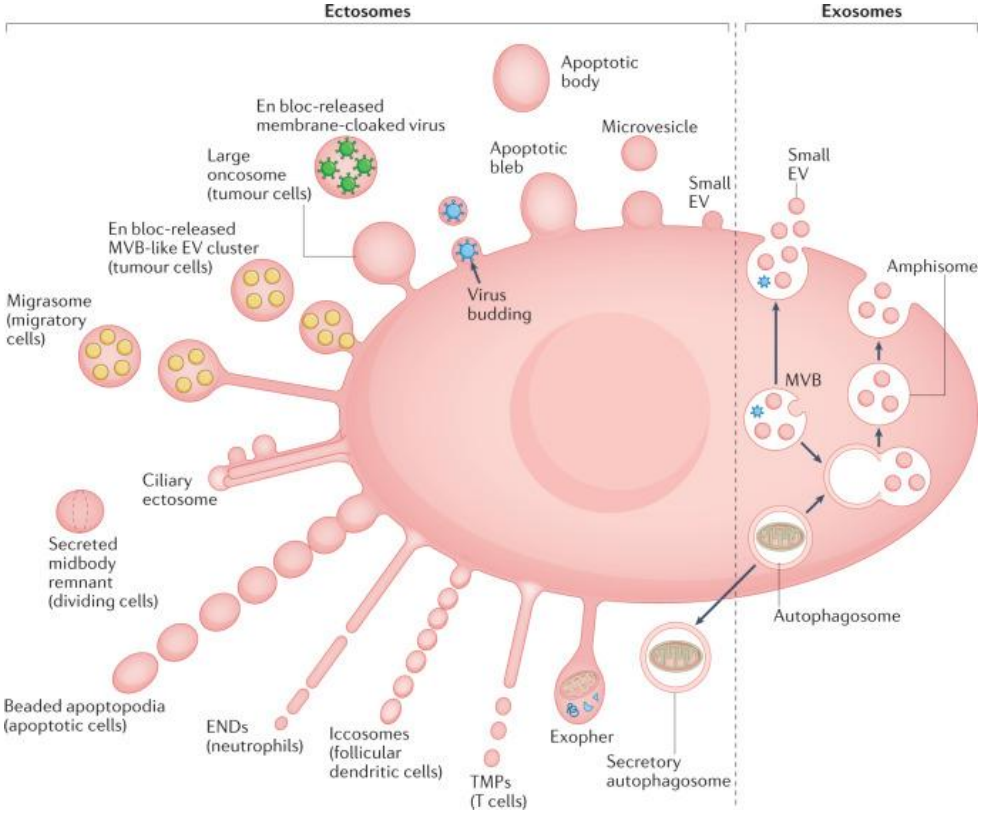

Figure 1.3. Classification of extracellular vesicles based on biogenesis and release pathway. Exosomes originate within the endosomal system. Early endosomes mature into late endosomes, where inward budding of the limiting membrane produces intraluminal vesicles inside MVBs. MVBs can either fuse with lysosomes for cargo degradation or fuse with the plasma membrane to release intraluminal vesicles as exosomes into the extracellular space. Ectosomes are produced directly at the plasma membrane through outward budding and fission. Their formation involves cytoskeletal rearrangements, changes in membrane lipid asymmetry and local accumulation of signaling molecules like small GTPases. Additional ectosome subtypes generated through plasma membrane derived processes include apoptotic bodies, migrasomes, oncosomes, and exophers. From (60).

2.2.Separation and concentration

The study and characterization of EVs begins with their separation from extracellular media and concentration to further analysis. EVs can be detected in several matrices, including culture supernatant and bodily fluids such as plasma, urine, tears, bile, breast milk, amniotic fluid, cerebral spinal fluid, and gastric acid. Therefore, the initial stage involves selecting a suitable separation method, considering the matrix complexity, the recovery efficiency, EV concentration and properties, achievable purity, sample volume, and costs (54, 67). The ISEV board members release a list of suggested minimal information for studies of extracellular vesicles (MISEV) every four years. This list includes guidelines for EV separation, characterization, and functional studies. The term EV isolation is not recommended since absolute purification is still an unrealistic goal (68).

There are five primary separation-based approaches for extracting and concentrating EV from a complex sample. Each of these have their own advantages and disadvantages in terms of cost, efficiency, and purity. The first and most widely used protocols that account for approximately 80% of all EV separation reports are the ultracentrifugation-based methods. Ultracentrifugation is an inexpensive and straightforward technique; however, it demonstrates limited efficiency in terms of both yield and purity (67, 69). Differential centrifugation was the first method used for EV separation and remains as the gold standard for this purpose. Other variations include density gradient centrifugation, rate-zonal centrifugation and isopycnic centrifugation (54).

The second method is sized exclusion-based separation, which includes ultrafiltration and size-exclusion chromatography. These methods are very effective and keep the biophysical and functional properties of concentrated EV. The third method is based on precipitation using polymers like polyethylene glycol (PEG), lectins, or organic solvents. Despite their simplicity and affordability, these exhibit a low level of purity because of the co-precipitation of non-EV material, which can have a negative impact on the biological activity of EVs. Then there is the immunoaffinity capture-based separation using antibodies against specific markers on the EV surface through immunoassays or magnetic beads coated with antibodies. Besides offering high efficiency and specificity, most EV markers remain unidentified (54, 67, 69).

Finally, there are separations based on microfluidic technologies that can separate EVs based on their physical and biochemical properties simultaneously. These microfluidic technologies offer advantages such as high throughput, low sample volume requirements, and the ability to separate EVs in a label-free manner (70). Moreover, recent advancements in EV separation techniques have focused on combining multiple methods to improve purity and yield, further enhancing the potential of EV research and applications.

2.3.Characterization

EV characterization involves employing different and complementary methods to evaluate the efficiency of the separation steps and correlate the presence of biomarkers or functions with the extracted EVs. These analyses include both quantitative and qualitative measurements (68). Since absolute quantification is difficult, biomolecule concentrations, such as proteins, lipids, or RNA, are frequently employed as indirect measures to estimate the amount of EVs present. Direct estimation is possible using techniques based on light scattering like nanoparticle tracking analysis (NTA) and dynamic light scattering (DLS) (67, 71). The inherent heterogeneity of EV composition has made it difficult to reach a consensus regarding the most reliable measure of material quantity for studying their biological roles (68).

The physical characterization of EVs comprises the determination of their size, shape, surface roughness, and elastic properties. To achieve this objective, it is usual to utilize one or more techniques such as NTA, DLS, transmission electron microscopy (TEM), and atomic force microscopy (AFM). Biochemical characterization involves determining their composition in terms of proteins, lipids, metabolites, or nucleic acids. To reveal their identity, immunoassays and instrumental omics analysis are used for this purpose (54, 67, 71). As a quality control, it is recommended to at least evidence the presence of one transmembrane protein, one cytosolic protein, and one common contaminant protein commonly co-isolated with the EVs, like apolipoproteins or albumin (68). Some technologies, like flow cytometry, allow physical and biochemical analyses simultaneously (71).

2.4.Biological roles

Originally, EVs were perceived as a means of cellular disposal. However, it has subsequently been discovered that EVs play a role in various pathological and physiological processes. Due to their overlapping functions, distinguishing between the specific roles of each EV type can be challenging (54). However, studying their cargo and targeting mechanisms can provide valuable insights into their distinct roles in cellular processes. In general, different types of EVs have been implicated in cell homeostasis, tissue repair and regeneration, immune responses, blood coagulation, reproduction, cancer development, neurodegenerative diseases, and infectious diseases (72–74).

Therefore, these multifunctional roles have aroused interest in using EVs as early biomarkers for several diseases and as therapeutic targets. The latter strategy involves either increasing or decreasing the release and uptake of EVs or using their ability to target only particular cells and tissues, bypassing potential barriers, and improving treatment efficacy. Additionally, their natural biocompatibility and low immunogenicity make them a safer alternative to traditional drug delivery systems, reducing the risk of adverse reactions and side effects. These features make them highly promising candidates for targeted drug administration (72, 75).

2.4.1. Infectious diseases

As EVs are used in cell-to-cell communication, they are emerging as important mediators in physiological and pathological interactions between microorganisms and their hosts. In general, they have been involved in pathogenicity, virulence, predation, stress responses, biofilm formation, host metabolism and immune response modulation, developmental signaling, environmental modification and development of antimicrobial resistance. Furthermore, the hosts' EVs can actively combat pathogens by directly targeting pathogen cells or by contributing to the control of immune responses (74, 76).

2.4.1.1.Parasitic infections

Parasites, ranging from single-celled protozoa to multicellular helminths, must establish numerous interactions with their hosts to exploit them while maintaining a state of silence. Parasitic EVs have been utilized as means of communication to promote coordination between parasites, and for communication with the host to either enhance adhesion and virulence or decrease the immune response (77). Therefore, parasitic EVs have been proposed as more specific and stable biomarkers for diagnosis and as the basis for next generation vaccines against parasites. Understanding the biogenesis, content, and functions of parasitic EVs may help to create innovative treatment approaches to combat these disorders (78).

EVs from protozoan parasites like *Plasmodium* spp., *Leishmania* spp., *Trypanosoma* spp., *Toxoplasma gondii*, *Giardia intestinalis*, *Trichomonas vaginalis*, *Entamoeba histolytica*, and *Naegleria fowleri* have been found to participate in several different processes during infection. For instance, they can trigger a proinflammatory or immunosupressive response, induce host gene silencing, parasite attachment, invasion, migration, stage conversion, and drug resistance (77, 79, 80). Likewise, different helminth species like *Echinococcus granulosus*, *Brugia malayi*, *Trichinella spiralis*, *Fasciola hepatica*, and *Schistosoma japonicum* have been documented to secrete EVs into the host's body to manipulate the host's immune response and evade elimination (81).

2.4.1.1.1. Malaria

The functions of *Plasmodium*'s EVs during malaria infection have drawn significant attention, particularly during the blood stages. During this phase, the EVs are released by infected RBCs into the bloodstream and can circulate throughout the body to exert their effects. The main roles of these EVs are potent activation of macrophages via Toll-like receptors (TLR) increasing a proinflammatory response correlated with the clinical manifestations such as fever and cerebral dysfunction and DNA transfer between infected RBCs that induces gametocytogenesis and drug resistance (79, 80).

Additionally, *Plasmodium*’s EVs can stimulate the production of host’s EVs from endothelial cells, leucocytes, and platelets that can also participate in the systemic damage observed during severe malaria (82). Currently, it remains unclear whether there is a variation in the composition of EV content based on the developmental stage of the parasite. Recently, two subpopulations of *Plasmodium falciparum* EVs were identified based on their size, content, composition, and membrane fusion properties (83). Nevertheless, there is still a considerable amount of research needed to fully understand the features and effects of these secreted products on the progression of the disease.

2.4.2. Non-infectious diseases

Moreover, EVs are a key feature of several non-infectious diseases' progression. The role of increased levels of circulating EVs in individuals with inflammatory disorders remains unclear, as it is unsure whether they act as a causative factor or as a result of chronic inflammation. Nevertheless, various research studies have established a connection between inflammation caused by EVs and cardiovascular conditions, including atherosclerosis, acute myocardial infarction, and stroke (73). Also, EVs have been involved in neurodegenerative diseases as propagators of pathogenic proteins or RNAs that can perpetuate neuroinflammation and brain dysfunction (84).

Finally, EVs have received special attention in cancer research. Many studies have shown multitasking features of EVs in different types of cancers. The dynamic transfer of biomolecules between cancer cells and both healthy cells and other cancer cells has the capacity to control various tumoral processes such as migration, cell death, autophagy, proliferation, metastasis, immune evasion, creating protumor microinches. Therefore, artificial EVs have been suggested as an innovative treatment to transport interfering chemicals and medications directly into cancer cells (85, 86).

3. Chapter 3: Autophagy

Autophagy (from the Greek words *auto*, meaning 'self', and *phagein*, meaning 'to eat') is a highly conserved eukaryotic pathway that degrades damaged cellular components, such as organelles and aggregates of misfolded protein, through lysosomes (87). Despite this term was first used in the 1960s by Christian de Duve at the time he discovered lysosomes, it did not receive much attention until nearly 30 years later, with the discovery of autophagy-related proteins (ATGs) in *Saccharomyces cerevisiae* (88, 89).

The current state of knowledge on the role of autophagic mechanisms in many physiological and pathological processes is rapidly growing. It is now understood that autophagy is a physiological response to several types of stress, and that dysregulation of this process can lead to a wide range of disorders such as cancer, infectious diseases, chronic diseases, neurodegenerative processes, and aging-related conditions (89, 90).

3.1.Types of autophagy

Autophagy types have evolved over time, with two parameters defining their classification: mechanism and selectivity. Mechanism refers to the process of initiating and executing autophagy, such as macroautophagy, microautophagy, or chaperone-mediated autophagy (CMA). Selectivity refers to whether there is a specific cargo to be degraded within the autophagosome (91, 92). By considering mechanisms and selectivity, researchers can understand autophagy types and their roles in cellular homeostasis and disease.

Consequently, since CMA is a selective mechanism, only macro- and microautophagy can be either selective or nonselective. Nonselective or bulk autophagy is utilized by starving cells to generate energy substrates. Selective autophagy, on the other hand, targets damaged or unnecessary macromolecules, organelles, and invasive microorganisms (93). Additionally, there is a labeling step in selective autophagy, usually by ubiquitinylation, that is recognized by receptors on the autophagosome or lysosome membranes. From then on, these processes' names have become more diverse based on their cargo. For example: mitophagy (mitochondria), ribophagy (ribosomes), xenophagy (microorganisms), lipophagy (lipids), glycophagy (glycogen), and aggrephagy (protein aggregates), to name a few (91).

3.1.1. Macroautophagy

Macroautophagy, also referred as just autophagy, involves the encapsulation of cellular components within a membrane structure called the autophagosome, which is formed at a considerable distance from the degradation site. An exceptional characteristic of this mechanism is that, in contrast to vesicle-trafficking processes, autophagosomes are generated anew rather than by membrane budding. Autophagosomes can originate from various membrane sources, including the endoplasmic reticulum, mitochondria, Golgi complex, and plasma membrane (94).

After its formation, the phagophore structure starts to enlarge, capturing cytoplasmic material in a selective or nonselective way. Subsequently, it envelops the cargo to create a spherical autophagosome, which ultimately merges and transfers its contents into the lysosome, known as the autolysosome. The autophagosome can alternatively merge with a late endosome, resulting in the formation of an amphisome and finally form the autolysosome (92, 93).

In addition, macroautophagy can be categorized depending on its molecular mechanism into conventional or canonical autophagy and alternative or non-canonical autophagy. Both forms of macroautophagy have comparable morphological and functional characteristics. Typically, the canonical macroautophagic process involves a series of stages, including initiation, nucleation, elongation, closure, fusion, and degradation (Figure 1.4). These stages rely on both hierarchical ATG and non-ATG proteins that assemble as complexes (Table 1.2). Nevertheless, in non-canonical autophagy, certain stages and molecular machinery may not be required (95, 96).

3.1.1.1.Canonical macroautophagy

Canonical autophagy initiation depends on the activation of the ULK1-complex, which is mostly translocated from lipid-rich regions in the endoplasmic reticulum (ER) membrane known as omegasomes. During a fed state, mTORC1 is attached to the ULK1-complex and inactivates it by phosphorylation. Contrary to this, during starvation, mTORC1 dissociates from the complex, allowing its dephosphorylation. Furthermore, AMPK enhances the activation of autophagy in response to a decrease in energy levels caused by a rise in AMP concentration (92, 97).

In the nucleation stage, there is an increase and gathering of proteins necessary for phagophore expansion. The class III PI3-kinase complex (PI3KC3) I is responsible for the production of phosphatidylinositol-3-phosphate (PI3P) from phosphatidylinositol (PI). This synthesis is crucial for the recruitment and accurate positioning of WIPI proteins, ATG proteins and autophagic receptors (AR) like p62 (87). The upregulation of this complex is primarily mediated by the ULK1-complex. Additionally, NRBF2 also enhances the kinase activity of the complex. On the other hand, the complex is downregulated by BCL2, which binds to BECN1 and inhibits the complex (97, 98).

Subsequently, the phagophore membrane must undergo enlargement through expansion and lipidation as it engulfs the cargo. Since the expanding phagophore lacks transmembrane proteins, membrane expansion depends on the delivery of lipids and ubiquitin-like (UBL) proteins. The primary processes involved in lipid delivery encompass the recycling of ATG9-positive vesicles, the direct extrusion form organelles like ER and mitochondria, and protein-mediated lipid transport facilitated by proteins such as ATG2, WIPI4 and GRAMD1A (99). Furthermore, UBL proteins have a role in the processing and lipidation of Atg8-related proteins, which facilitates the curving of the phagophore membrane (92, 99).

Atg8-related proteins are animal orthologs to yeast Atg8 involved in intracellular trafficking. In animals, there are three subfamilies of Atg8-related proteins: LC3, GABARAP and GATE-16. Of these, LC3 processing plays a major role in autophagy (100). Initially, the cytosolic form of LC3 undergoes proteolysis by ATG4, resulting in the formation of LC3-I. Then, this LC3-I is recognized and transferred by E1- and E2-like enzymes (ATG7 and ATG3 respectively) to an E3-like complex. The E3-like complex forms a conjugate between LC3-I and phosphatidylethanolamine (PE), resulting in the formation of LC3-II, which can bind to the phagophore. LC3-II is crucial for phagophore elongation and closure into a round shaped and mature autophagosome and can undergo recycling through deconjugation mediated by ATG4 (92, 99).

The processing of LC3 is highly regulated. Thus, the local accumulation of ULK1-complex at expanding phagophores will inhibit the activity of ATG4 proteins. Furthermore, the activity of the E3-like complex can be suppressed by the Golgi protein RAB33A and by acetylation mediated by the acetyltransferase KAT2B (92). WIPI proteins have an active role in elongation. Due to their participation in the retrieval of vesicles that contain ATG9, the recruitment of the E3 complex, and the attachment of the phagophore to the ER (101, 102).

The molecular mechanisms of phagophore closure into a mature autophagosome have been elusive. However, recent advances have implicated the participation of ESCRT machinery and Atg8-related proteins in this process. Once the LC3-II positive phagophore membrane has reached enough size, ESCRT-I components are recruited, and subsequently, the filament-forming ESCRT-III proteins. The filament facilitates the recruitment of the AAA-ATPase VPS4, which is responsible for resolving the fission process and disassembling the ESCRT complex. While the ESCRT complex plays a significant role in the process of phagophore closure, it may not be essential. Further investigation is needed to understand the involvement of additional proteins, such as dynamin and the COVET complex, in phagophore closure and scission (103, 104).

Therefore, fully closed and loaded autophagosomes are moved across the microtubular network within the cell towards a late endosome and/or a lysosome to form an amphisome or an autolysosome respectively (92) Similar to other vesicular trafficking processes, the fusing of autophagosomes depends on the presence of SNARE complexes, which facilitate the proximity of the membranes. Additionally, small GTPases are involved in recruiting motor proteins and tethering factors such as the HOPS complex. In addition, there are other components like phosphoinositides, lysosomal pH, and ion composition that may be involved in the fusion process (105, 106).

In the final step, lysosomal lipases disrupt the autophagosome's inner membrane to release its content, which more than 60 different hydrolases then digest. These enzymes have an acidic optimal pH and work together to degrade from simple macromolecules to complete microorganisms. Finally, several lysosomal transporters carry the produced catabolites back to the cytosol in a poorly understood process (107). Nutrient generation from cargo degradation is an important down regulator for autophagy. The lysosomal nutrient sensor (LYNUS) transduces the signal of lysosomal nutrient levels by inactivating transcription factor EB (TFEB). TFEB is a master transcriptional regulator of autophagy by promoting expression of several ATG and no-ATG proteins and lysosome biogenesis (108).

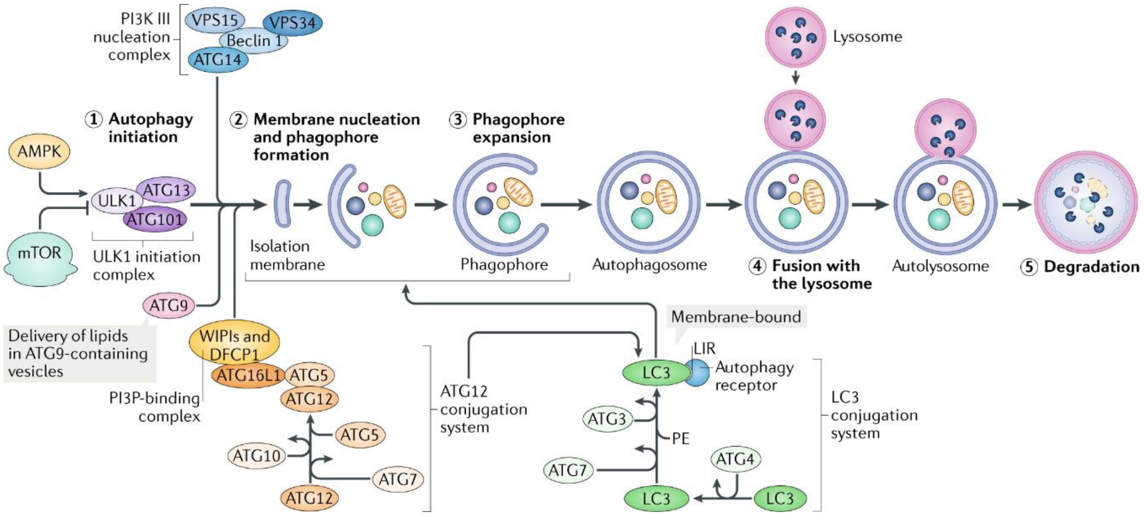

Figure 1.4. Canonical macroautophagy pathway. The central metabolic sensors mTORC1 (autophagy inhibitor) and AMPK (autophagy activator) are key controllers of this process. When autophagy begins, portions of the cytoplasm are enclosed by a growing double membrane (omegasome). This starts with the emergence of a cup-shaped phagophore, which expands and ultimately closes to form a double-membrane autophagosome. These autophagosomes then fuse with acidic lysosomes to generate autolysosomes, where the enclosed material is degraded. Autophagy proceeds through several coordinated stages: (1) initiation, (2) membrane nucleation and phagophore formation, (3) phagophore expansion, (4) fusion with lysosomes, and (5) degradation. Each step is controlled by numerous autophagy-related proteins (ATGs), which assemble into mayor complexes. From (109).

Table 1.2. The primary complexes implicated in the different stages of canonical macroautophagy and their regulators.

Stage	Complex	Proteins involved	Regulators
Initiation	ULK1-complex	ULK1/2, ATG13, FIP200, ATG101	mTORC1 ↓ AMPK ↑
Nucleation	Class III PI3-kinase complex I	VPS34, VPS15, BECN1, ATG14L, AMBRA1	BCL2 ↓ ULK1-complex ↑ NRBF2 ↑
Elongation	Ubiquitin-like proteins	E1-like: ATG7	
		E2-like: ATG3	
		E3-like: ATG5, ATG12, ATG16L	RAB33A ↓ KAT2B ↓
	LC3 conjugation system	ATG4, Ubiquitin-like proteins	ULK1-complex ↓
Closure	ESCRT complex	I: VPS37A, VPS28, TSG101	
		III: CHMP2A, CHMP4B	
Fusion	SNARE complex	STX17, Vamp7, Vamp8	
	GTPases	Rab2, Rab7, Arl8	
	HOPS complex	VPS33, VPS39, VPS16, VPS11, VPS18, VPS41	

↓: inhibits autophagy; ↑: activates autophagy

3.1.1.2.Non-canonical macroautophagy

Non-canonical autophagy refers to mechanisms in which a double-membrane-bound vacuole forms in the cytoplasm and later merges with the lysosomal compartment to break down its contents. Typically, these types of autophagy exhibit three primary features: the creation of the double-membraned autophagosome does not depend on the sequential involvement of all ATG proteins, the double membrane can originate from various sources rather than one, and certain ATG proteins can be recruited to an existing membrane that differs from the phagophore (95, 110).

Multiple distinct routes have been documented for non-canonical autophagy. Some of the extensively researched examples include ULK1-independent autophagy, BECN1/PIK3C3-independent autophagy and autophagy independent of the ATG conjugation systems (95, 110). The investigation of non-canonical autophagy's role in physiological and pathological processes is currently underway due to its demonstrated significance in several chronic, neurodegenerative, neoplastic, and infectious illnesses (96).

3.1.2. Microautophagy

Microautophagy allows for the direct engulfment of cytoplasmic components by the lysosome or late endosome without taking them from an autophagosome. This occurs through evagination or protrusion of the lysosomal or endosomal membrane, and it is differentiated into an autophagic tube. The autophagic tube then fuses with the lysosome or endosome, leading to degradation of the cargo within. There are different classifications for this process according to morphological criteria and the capture mechanism (111, 112).

As mentioned, microautophagy can also be either selective or non-selective. Non-selective microautophagy engulfs soluble intracellular substrates through tubular invaginations and activity of the vacuolar ATPase and proton gradient (113). However, selective microautophagy sequesters specific organelles with arm-like protrusions based on specific interactions. Some of the substrates degraded by microautophagy include lipid droplets (microlipophagy), proteins (microproteophagy), endosomes (endosomal microautophagy), mitocondria (micromitophagy), peroxisomes (micropexophagy) and others (111, 112).

3.1.3. Chaperone-mediated autophagy (CMA)

CMA is a type of selective autophagy that is mechanistically unrelated to macro- and microautophagy and only occurs in mammalian cells (93). Cargo delivery by CMA does not require the formation of intermediate vesicle compartments, membrane fusion, or membrane deformity of any kind, as seen in macro- and microautophagy. Instead, substrates are moved directly across the lysosome membrane by a translocation protein complex (114).

Contrary to macro- and microautophagy, CMA is exclusively selective. All CMA substrates contain a pentapeptide motif KFERQ, which is present in 40% of cytosolic proteins. During CMA, the complex consisting of cytosolic heat shock 70 kDa protein 8 (HSPA8/HSP70) and other cochaperones recognize KFERQ-like motifs. Subsequently, the lysosome-associated membrane protein 2A (LAMP2A) receptor, attaches to the complex and transports the cargo across the membrane by unfolding it during the process. Inside the lysosome, lysosomal HSPA8 pulls and refolds the cargo (114, 115).

3.2. Role of autophagy in endothelial homeostasis

Autophagy's involvement in maintaining the balance of endothelial cells and its potential connection to vascular disorders are under investigation. In general, autophagy has been involved in nitric oxide (NO) production, vascular network growth via vasculogenesis or angiogenesis, quiescence regulation, vascular permeability, and vascular secretion. Hence, a fundamental amount of autophagy is necessary to preserve endothelial function. However, excessive or deficient levels of autophagy have demonstrated heightened vulnerability to pathological conditions and elevated cellular death (116, 117).

For instance, inhibition of autophagy can upregulate the inflammatory senescence-associated secretory phenotype (SASP). SASP is defined by the production of inflammatory cytokines and their effects on nearby cells, contributing to the development and advancement of vascular disease in chronic diseases (118). Furthermore, there is a strong correlation between autophagy and atherosclerosis. Patients with metabolic syndrome exhibit reduced endothelial autophagy due to elevated levels of glucose and fatty acids. Additionally, endothelial autophagy promotes the removal of lipid deposits in the vessel wall. Hence, autophagy may elucidate the underlying mechanism of atherosclerosis and vascular dysfunction (119, 120).

Moreover, autophagy is known to intervene during ischemic diseases. During ischemia the vascular network must reestablish to support tissue regeneration and as previously mentioned, autophagy is crucial in this process. Nevertheless, an excess of autophagy can result in the development of abnormal blood vessel growth in cancer or retinopathies, as well as the degradation of the endothelial barrier integrity (121, 122). Therefore, targeting defective autophagy to restore endothelial function in vascular diseases offers a promising method for treating both infectious and non-infectious illnesses (117).

3.3. Role of host's autophagy in parasitic infections

Autophagy has a strong association with parasite infections due to its significant involvement in disease progression and its interaction with the innate immune system. Depending on the context, autophagy plays a dual role in disease inhibition and progression. Intracellular protozoa parasites exhibit complex life cycles and are exposed to different types of cells and hosts. Some of them, like *Plasmodium* spp., *Leishmania* spp., *Toxoplasma gondii*, and *Trypanosoma* spp., have worked their ways to manipulate the host's autophagy machinery either to enhance their growth by nutrient uptake or to avoid parasite clearance from the cell (123, 124).

There are two main non-canonical pathways to deal with intracellular pathogens: xenophagy and LC3-associated phagocytosis (LAP). Xenophagy is the process by which the autophagy machinery directly identifies and responds to a foreign invader, leading to the creation of an autophagosome surrounding the pathogen. In contrast, LAP involves the recruitment of LC3 and other autophagy proteins into pre-existing particles within a phagosome or endosome. The activation of either of the two systems seems to depend on the sub-cellular location of the pathogen and the condition of the vacuole membrane that isolates it (123, 125).

Interestingly, pathogens have developed strategies to avoid these systems and exploit them for their own benefit. Parasites often employ three mechanisms to disrupt the autophagy process in their host: inhibition of host ATG proteins to prevent autophagy induction, interference with the downstream autophagy breakdown pathway, and manipulation of host autophagy to facilitate their growth and reproduction. By these means, pathogens manipulate their surroundings to acquire resources, reuse autophagic membranes or vacuoles to stay hidden, and recreate optimal conditions for their survival and reproduction (123, 124).

3.3.1. Autophagy and malaria

Plasmodium parasites can modulate their host's autophagy pathways to survive and proliferate. There is strong evidence of mechanisms slightly different from xenophagy and LAP during hepatic stages used by the parasite to avoid elimination and support development (123, 126). *Plasmodium* sporozoites are targeted for elimination in the liver by non-canonical pathways that are independent of the ULK1-complex and the nutritional status of the cell. However, the canonical pathway, although inefficient at eliminating parasites, has also been implicated in providing nutrients and boosting parasites' growth (125).

The collection of these autophagy-related mechanisms that function as intracellular immune responses against liver stages have been classified into three categories: the *Plasmodium*-associated autophagy-related (PAAR) response, the LAP-like response, and the PI3P-associated sporozoite elimination (PASE) (Figure 1.5) (127, 128).

During the early liver stage, defective sporozoites that fail to complete transmigration or properly remodel the PVM are eliminated through the PASE response. The host cell rapidly recruits the PI3KC3 complex to the compromised vacuole, generating PI3P and triggering the transient recruitment of autophagy- and lysosome-associated markers. This leads to vacuole acidification and swift parasite degradation. Importantly, PASE acts as an early quality-control mechanism that restricts liver infection by clearing nonviable parasites before they initiate replication. (128).

In contrast, during later liver stages, viable sporozoites that have successfully invaded and remodeled their PVM are targeted by the PAAR response. Here, the host cell decorates the PVM with lipidated LC3 through the Atg5-dependent machinery and subsequently recruits ubiquitin-binding effectors such as p62, NDP52, and NBR1(127, 128). This mechanism has been evidenced in mouse parasites like *P. berghei* and *P. yoelii*, and it is estimated to eliminate up to 50% of invasive sporozoites (125). However, the parasites can surpass the PAAR response through a non-canonical interaction between LC3 and PVM protein upregulated in infective sporozoites 3 (UIS3). This interaction blocks the recruitment of the effector proteins and lysosomal fusion (123, 129).

Conversely, the LAP-like response has been observed in *P. vivax* infection, and, like LAP, it entails the recruitment of LC3, followed by proteins implicated in PI3P production. In contrast to the PAAR response, the LAP-like response is reliant on the presence of IFN-γ, as the detection of parasites fails to occur spontaneously (130). Additionally, this method exhibits lower efficacy in removing invading sporozoites, clearing only 30% of them. This phenomenon may be attributed to the evasion methods employed by *P. vivax* to maintain undetectable dormancy stages (125).

Since mature RBCs lack organelles and autophagy machinery, they are not directly involved in this process. However, autophagy is crucial during hematopoiesis and reticulocyte remodeling (131). In fact, there is evidence of reticulocyte-invading species like *P. vivax* and *P. yoelii* that can accelerate the maturation of reticulocytes by autophagy inducing mechanisms (132).

Nonetheless, during the blood stage, *Plasmodium* can trigger autophagic pathways in different tissues. Recent studies evaluated the effect of *P. berghei*'s extracellular vesicles on cerebral malaria. The findings demonstrated that astrocytes effectively grab these vesicles and trigger autophagy by LAP, leading to a proinflammatory reaction (133, 134). Furthermore, it is speculated that *Plasmodium*-induced autophagy in the placenta may play a crucial role in the outcome of pregnancy during placental malaria (135).

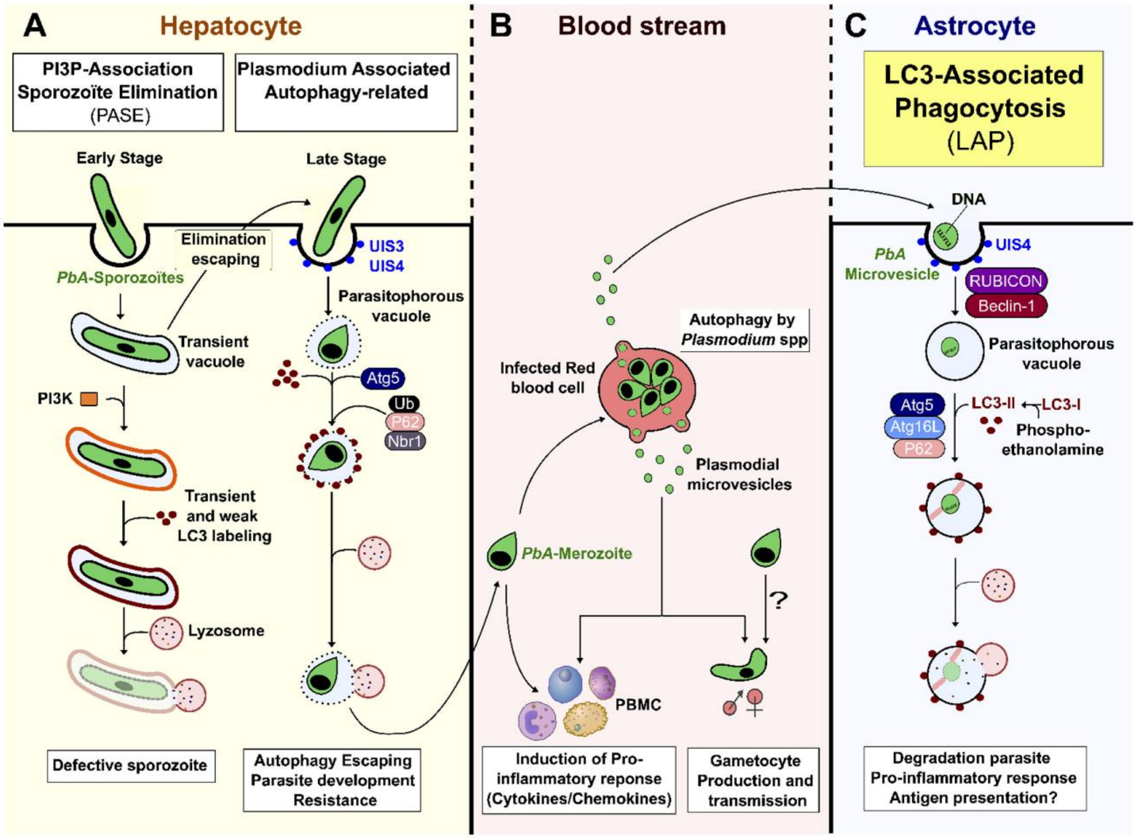

Figure 1.5. Role of host autophagy in *Plasmodium* infection and pathogenesis. (A) During early liver stages, *Plasmodium* sporozoites enter hepatocytes and form a PV. If the parasite cannot remodel this compartment, PI3K is recruited and triggers early parasite clearance through PASE, a process only briefly involving LC3. At later liver stages, LC3 is loaded onto the PV through Atg5, activating the PAAR response, which can label parasites for degradation but often does not result in their complete elimination. (B) In RBCs, the parasite uses an autophagy-related mechanism to generate EVs that transfer genetic material and promote gametocyte formation, while also inducing inflammation. (C) Parasite-derived EVs can reach astrocytes, where LC3-mediated LAP targets them for lysosomal destruction and drives a pro-inflammatory response linked to experimental cerebral malaria. From (133).

2. Justification

Malaria is a parasitic disease with high morbidity and mortality around the world. This disease mainly affects children under the age of 5 and pregnant women from tropical areas. The incidence and mortality rates linked to malaria are higher in regions with unfavorable socioeconomic conditions. Despite progress in clinical understanding of the impact of this disease, the investigation into the relationship between human sickness and its pathogenic mechanisms is still restricted.

For this reason, the use of animal models has played a significant role in comprehending diseases and the biology of the microorganisms that cause them. In malaria research, experiments conducted on rodents, birds, and non-human primates have provided valuable insights into host-parasite interactions that were previously difficult to study in humans due to ethical concerns (27).

Of the existing animal models, rodents have been the most widely used for both biological and methodological reasons due to their small size and easy breeding. These models have been crucial for the study of liver stages, syndromes arising from the blood stages of infection, and malaria transmission to and from the mammal host. Several *in vivo* observations have resemblances to human pathology (136).

The investigation of the impact of *Plasmodium*-induced stimuli on endothelial cells is crucial since endothelium serves as the initial point of contact in a malaria infection. This interaction disrupts the normal functioning and homeostasis of the endothelium, leading to physiopathological processes such as inflammation or ischemia, that further aggravate the disease (41, 117).

On one hand, autophagy is a crucial physiological process that plays a vital role in maintaining the endothelial homeostasis and function. However, this process can be readily disturbed by infectious or chronic diseases. On the other hand, *Plasmodium* parasites are known to interfere with and evade autophagic pathways during liver stages, although there is limited understanding of their impact on the blood stages. Thus, this work should provide evidence of the impact of stimuli produced by *P. berghei* during blood stages on the autophagic pathways of murine endothelial cells. Additionally, it seeks to provide valuable insights into the significance of these pathways in the development of malaria (137).

The current proposal aims to analyze the process of autophagy in endothelial cells after exposure to various stimuli derived from different fractions of a *P. berghei* culture. The above is to develop a more comprehensive knowledge of the host-parasite interactions that form the basis of malaria infection.

3. Hypothesis

The hypothesis of the present study is that *Plasmodium berghei* induces changes in the expression of characteristic autophagy markers in endothelial cells through interaction with stimuli produced by the parasite.

4. Objectives

4.1. General Objective

- To characterize the autophagy process induced in endothelial cells by contact with various *Plasmodium berghei* stimuli isolated from infected cultures to determine the activation of this process in the pathogenesis of malaria.

4.2. Specific Objectives

- To standardize the culture conditions of *Plasmodium berghei* in order to obtain viable parasites for further analysis.
- To determine the activation of autophagy pathways *in vitro* through various stimuli from *P. berghei* culture on tEnd.1 endothelial cells by the expression of classical autophagy markers.
- To analyze the protein profiles derived from *P. berghei* culture supernatants, and extracellular vesicles to determine differences in the expressed components.

5. Materials and methods

5.1. Culture of *Plasmodium berghei* parasites

5.1.1. *Plasmodium berghei* parasites

Transgenic *Plasmodium berghei*-ANKA strains derived from the strain originally described by Vincke and Lips in 1948 (33) were used to infect mice and to establish *in vitro* cultures. Transgenic strains were previously generated to express red fluorescent protein (mCherry-*P. berghei* ANKA) (138, 139).

mCherry was expressed in *P. berghei* under the constitutive eef1aa-promoter and were localized cytosolically. These strains were provided by the BEI Resources Malaria Research and Reference Reagent Resource Center (MR4).

5.1.1.1. Blood stabilates

Blood stabilates from transgenic *P. berghei*-ANKA were previously prepared with fresh heparin-anticoagulated blood from infected mice with parasitemia of 3% to 15% in freezing solution and were kept at -80 °C until further use.

5.1.2. Mice

6- to 8-week-old ICR (CD-1®) female mice were used as the animal model. ICR mice are an outbred strain widely used in biomedical research due to their robust genetic variability, making them suitable for toxicological, pharmacological, and behavioral studies.

The mice were housed under standard laboratory conditions, including a 12-hour light/dark cycle, room temperature (18-26 °C), and humidity (80%). Animals had *ad libitum* access to a standard laboratory diet and water. All procedures were approved by the local Comité Institucional para el Cuidado y Uso de Animales (CICUA) del Laboratorio de Ensayos Biológicos (LEBi).

5.1.2.1. Mice infection from blood stabilates

Stabilates (section 5.1.1.1) were thawed and injected intraperitoneally into 6- to 8-week-old ICR (CD-1®) female mice. Parasitemia was evaluated five days after injection utilizing Giemsa-stained thin smears.

5.1.2.2. Induction of reticulocytosis in healthy mice

Due to the reticulocyte tropism of *P. berghei*, reticulocytosis was induced in healthy mice by administering phenylhydrazine intraperitoneally (100 mg/kg) 72 hours prior to blood collection. This blood was used both to dilute the parasitemia of the initial culture and to supplement the cultures with reticulocytes on subsequent days.

5.1.2.3. Determination of parasitemia via blood smears

Parasitemia of infected mice was assessed by taking a blood sample from the tail vein by venipuncture. The blood sample was smeared onto a microscopic slide and air-dried at room temperature. Afterwards, the slide was fixed using methanol for 3 minutes, followed by 10% Giemsa stain (1:10 dilution in Giemsa buffer) for 8 minutes. The slide was rinsed with tap water and air-dried at room temperature. The slide was examined under a light microscope and the number of infected and total red blood cells (RBC) were counted in five fields at 1000× magnification. Parasitemia was then calculated as infected RBC/total RBC × 100 and given as a percentage.

To monitor parasitemia in cultures, the percentage of parasitemia relative to the initial parasitemia on day 0 was used as the metric. This normalization was applied to minimize variations due to differences in the initial parasitemia across cultures.

5.1.2.4. Blood collection from infected and healthy mice

Mice with parasitemias between 5% and 10% were used for the establishment of parasite culture and the isolation of infected red blood cells (iRBCs) in stimulation assays. Healthy mice of matched age and weight were also used to obtain non-infected red blood cells.

Total blood was collected aseptically by cardiac puncture after CO_2 euthanasia into lithium heparin-containing tubes. The blood was centrifuged at 1500 g for 5 minutes to manually remove the plasma and buffy coat. The RBCs were subsequently washed using a sterile saline solution and centrifuged at 1500 g for 5 minutes. This washing step was repeated three times.

Washed RBCs were immediately used for culture setup or for further separation using Percoll gradient (section 5.2.1) in stimulation assays.

5.1.3. Establishment of *P. berghei* culture conditions

To establish the ideal cultivation conditions for *P. berghei*, different reported protocols were followed, considering both physical and chemical variables. In general, the procedure followed by (140) was modified as described. The culture was set up with RBC suspended in a Roswell Park Memorial Institute (RPMI) 1640 based medium supplemented as described below. The culture was adjusted to a hematocrit of 5% and an initial parasitemia of 5% using non-infected RBC from healthy mice. The culture final volume was 5 mL and was sustained in 25 cm^2 flasks, agitated vertically at 100 rpm with an Orbi-Shaker™.

Every 24 hours, the culture was transferred into a Falcon tube of 15 mL and centrifuged at 1500 g for 5 minutes for supernatant removal. The supernatant was kept at 4 °C for subsequent experiments, and fresh media was added. Vigorous pipetting of RBC during this process is highly recommended to promote the rupture of mature schizonts.

Thin smears were prepared from the pelleted RBC every day, stained with 10% Giemsa’s stain, and analyzed microscopically to document the parasitemia (as detailed in section 5.1.2.2) and check for adequate parasite morphology. As the proportion of merozoites escalated, new RBC were introduced to maintain a hematocrit level of 5%.

In each experiment, negative control was established using only RBC from healthy phenylhydrazine treated mice suspended in media at a hematocrit of 5%.

5.1.3.1. Effect of media composition

To assess the influence of medium composition on the *in vitro* growth and development of *P. berghei*, three distinct complete media formulas documented in the literature were used. All procedures employed RPMI 1640 as the base medium and reported adequate growth of *Plasmodium* parasites for at least 5 days. A comparison of the variations in media composition is found in Table 1.1.

All media's final pH was sustained between 7.2 and 7.4. The pH was adjusted using HCl (10 mol/L) or NaOH (10 mol/L). All preparations were filtered through a 0.22 µm membrane and stored at 4°C.

For these experiments, previous selected incubation conditions were used, including a temperature of 35 °C and a gas mixture atmosphere (90 % N_2, 5 % O_2 and 5 % CO_2, as described in section 5.1.3.2.2).

5.1.3.1.1. Modified media composition proposed by Trager and Jensen (1976)

Trager and Jensen are recognized for the first report on the cultivation of blood stages of *Plasmodium* parasites in 1976, specifically *P. falciparum* (141). Their study has since served as the foundation for much of the current knowledge on the cultivation of this parasite. Throughout the years, different authors have suggested modifications to the original protocol to tailor it to their laboratory conditions. Significant modifications include the transition from human or animal serum to using a lipid-rich bovine serum albumin alternative (AlbuMAX^{TM}) and the addition of hypoxanthine as a purine source (142).

Briefly, the original protocol established by Trager and Jensen consists of a suspension of RBC in RPMI medium supplemented with HEPES buffer (25 mmol/L), $NaHCO_3$ (0.2%) and type AB human serum (10%) (141). The final composition used consisted of RPMI 1640 supplemented with glucose (11 mmol/L), HEPES buffer (25 mmol/L), $NaHCO_3$ (12 mmol/L), hypoxanthine (200 μmol/L), AlbuMAX^{TM} II (0.5%) and gentamicin solution (20 μg/mL).

5.1.3.1.2. Media composition proposed by Janse et al., (1984)

Janse et al., proposed a more suitable media composition specifically for the generation of gametocytes in *P. berghei*. They reported long-term *in vitro* cultures using rat RBC (143).

The final composition consisted of RPMI 1640 supplemented with HEPES buffer (25 mmol/L), $NaHCO_3$ (25 mmol/L), fetal calf serum (10%), penicillin solution (100 U/mL) and streptomycin solution (100 μg/mL).

5.1.3.1.3. Media composition proposed by Jambou et al., (2011)

Jambou et al. developed an alternate method for the *in vitro* cultivation of *P. berghei* blood stages. They claimed the resolution of all inconveniences observed in prior formulations, including hemolysis, reinvasion failure, and the low stability of murine RBC (144).

The final composition used consisted of a mixture of RPMI 1640 (75%) and Dulbecco's Modified Eagle Medium/Nutrient Mixture F-12 or DMEM-F12 (25%) supplemented with glucose (17 mmol/L), HEPES buffer (25 mmol/L), $NaHCO_3$ (32 mmol/L), hypoxanthine (200 µmol/L), AlbuMAX^{TM} II (0.5%), gelatin (0.5%), calcium (2 mmol/L), choline (1 mmol/L) and gentamicin solution (20 µg/mL).

Table 5.1. Final composition of the media used for *P. berghei* culture.

Component	**Trager & Jensen, modified media for *P. falciparum***	**Janse et al., media for *P. berghei***	**Jambou et al., media for *P. berghei***
RPMI 1640 (% base medium)	100	100	75
DMEM-F12 (% base medium)	–	–	25
Glucose (mmol/L)	11	–	17
HEPES buffer (mmol/L)	25	25	25
$NaHCO_3$ (mmol/L)	12	25	32
Hypoxanthine (µmol/L)	200	–	200
Calcium (mmol/L)	–	–	2
Choline (mmol/L)	–	–	1
Gelatin (%)	–	–	0.1
AlbuMAX^{TM} II (%)	0.5	–	0.5
Fetal calf serum (%)	–	10	–
Antibiotics (final concentration)	Gentamicin (20 µg/mL)	Penicillin (100 U/mL) and streptomycin (100 µg/mL)	Gentamicin (20 µg/mL)

– : not used in this formulation

5.1.3.2. Effect of incubation conditions

Additionally, the impact of two physicochemical variables, temperature and atmosphere, that vary across publications on the *in vitro* study of the blood phase of *P. berghei* was evaluated.

For these tests, the modified Trager and Jensen media was used, as it is the most widely used for the cultivation of *Plasmodium* parasites.

5.1.3.2.1. Effect of temperature

Three distinct incubation temperatures were examined: 28 °C, 35 °C, and 37 °C, similar as (140). In this case the atmosphere was kept constant using a mixture of gases (90% N_2, 5% CO_2 and 5% O_2).

5.1.3.2.2. Effect of atmosphere

As *Plasmodium* is considered a microaerophilic protozoan, precise regulation of the gaseous environment is crucial for its development (145). Two different atmospheric conditions to reduce the amount of O_2 present were studied: using a candle jar and a gas mixture, both incubated at 35 °C.

For the candle jar atmosphere, the culture bottles were placed with their lids slightly unfastened in a container alongside a lit candle. The container remained sealed until the candle had gone out. The approximate atmospheric composition was 3-5% CO_2, 17% O_2, and the remainder N_2.

For the controlled gas atmosphere, the culture bottles were flushed for 15 seconds with a mixture of 90% N_2, 5% CO_2 and 5% O_2, and the lids were completely sealed.

5.1.4. Assessment of parasite infectivity after *in vitro* culture

To assess whether *Plasmodium berghei* parasites retained their infectivity during the first two days of *in vitro* culture, infected red blood cells (iRBCs) were harvested from cultures maintained under the selected conditions at day 1 and day 2 post-culture initiation. A total of 1×10^5 iRBCs were intraperitoneally injected into groups of three ICR (CD-1®) female mice per time point (n = 3 for day 1 and n = 3 for day 2). Parasitemia was monitored daily for six days by preparing Giemsa-stained thin blood smears from tail blood samples. The onset and progression of infection *in vivo* were used as indicators of preserved parasite infectivity after culture.

5.2. Isolation of *Plasmodium berghei* stimuli

For stimulation and characterization studies, several stimuli were extracted from *P. berghei* cultures exhibiting parasitaemias of more than 3%, specifically on days 1 and 2 post-culture initiation, as these days corresponded to peak parasitemias and optimal parasite morphology. The selected conditions for *P. berghei* culture were Jambou medium and incubation at 35 °C with gas mixture atmosphere.

5.2.1. Infected red blood cells enrichment

Infected and non-infected RBC were isolated from infected and healthy mice's blood, respectively (as described in section 5.1.2.3) using Percoll gradients (146). Solutions of 60%, 50%, 40% and 30% Percoll were prepared using RPMI medium as a diluent. Subsequently, 2 mL of the 60% solution was introduced into a 15 mL Falcon tube. Additionally, 2 mL of the 50% solution was meticulously poured through the tube wall, followed by the addition of 2 mL of the 40% and 30% solution respectively.

The pelleted and previously washed RBC from mice blood were subsequently diluted 1:4 in RPMI media and layered over the Percoll gradient. The tube was eventually centrifuged in a swing-out rotor at 1500 g at room temperature for 15 minutes without brake.

Infected RBCs with mature forms were collected from the 30% / 40% interface, which contained mainly schizonts, and from the 40% / 50% interface, which contained late trophozoites. Both fractions were combined and washed three times with PBS.

Non-infected RBC were collected from the 50% / 60% interface using blood from a healthy mouse. Also, these RBC were washed three times with PBS.

5.2.1.1. Measurement of RBC concentration and enrichment efficiency

The concentration of isolated red blood cells is determined using a Neubauer chamber to calculate the volume of suspension required to achieve a certain RBC:endothelial cell ratio.

The efficiency of the isolation process was evaluated through a thin smear followed by Giemsa staining. For further experiments, only iRBC from isolates with efficiencies greater than 85% were immediately used (section 5.4.2).

5.2.2. Extracellular vesicles enrichment

The culture medium from RBC cultures was collected by centrifugation as previously described in Section 5.1.3. Supernatants from P. berghei cultures with parasitemias higher than 3%, as well as from control cultures, were collected on days 1 and 2 after culture setup (5 mL per culture per day) and stored at 4 °C for a maximum of two days prior to further use.

Extracellular vesicles produced by RBC and parasites were enriched according to the methodology outlined by Retana Moreira et al. (147) and in accordance with the Minimal Information for the Study of Extracellular Vesicles (MISEV) guidelines (148). Crude supernatants from *P. berghei* and control cultures were subjected to centrifugation at 3000 g for 5 minutes at room temperature and subsequently filtered through 0.45 µm pore membranes to remove remaining cells.

The filtered crude supernatants were subjected to centrifugation at 17,000 g for 60 minutes at 4 °C (large EVs). The supernatant was subsequently filtered through 0.22 µm pore membranes and underwent further ultracentrifugation at 120,000 g for 150 minutes using a Sorvall™ WX80 Ultracentrifuge (Thermo Fisher Scientific, Waltham, MA, USA) to isolate a second fraction (small EVs). Ultracentrifuge tubes were placed on ice between centrifugation cycles and during sample handling to minimize degradation.

The small EV fraction was subjected to two washes in sterile-filtered PBS at the identical gravitational force and duration employed during their isolation and were subsequently resuspended in 500 µL of sterile-filtered PBS. The EV samples and EV-reduced supernatants were used promptly or preserved at 4 °C for a maximum duration of 7 days for functional and characterization assays or at -80 °C for protein analysis (sections 5.6.3 and 5.6.4).

5.2.2.1. Measurement of protein concentration in enriched EV suspension

Immediately after the washing steps, the EV suspension was filtered through 0.22 µm pore membranes to remove aggregates. Protein concentration was then determined using the Micro BCA Protein Assay Kit (Thermo Scientific, catalog number 23235). Following the manufacturer's instructions, a calibration curve was prepared with standards ranging from 2 to 40 µg/mL. A 1:100 dilution of the EV suspension was measured against this curve, and all measurements were performed duplicate.

5.2.3. EV-reduced supernatant obtention

The EV-reduced supernatant was obtained following the second ultracentrifugation step. After isolating small EVs from the cell culture medium, the remaining supernatant was carefully collected and transferred to a new tube. Prior to direct application on endothelial cells, the EV-reduced supernatants were filtered through 0.22 µm pore membranes, their pH was adjusted to 7.40, and they were supplemented with 10 % FCS.

5.2.3.1. Measurement of glucose concentration in EV-reduced supernatant

Immediately following filtration and supplementation, an aliquot of the supernatant was taken to quantify glucose concentration, given its role as a significant mediator of autophagy. Glucose levels in the supernatant were analyzed using an enzymatic reference method with hexokinase (Ref. 04657527190; Roche Diagnostics GmbH, Mannheim, Germany).

5.3. Culture and seeding of tEnd.1 cells

The murine thymic endothelioma 1 cell line or tEnd.1 (RRID: CVCL_6272) transformed with a polyomavirus oncogene was obtained from the Clodomiro Picado Institute. These are immortalized cells and retain key endothelial characteristics, including the expression of adhesion molecules, cytokine responsiveness, and the ability to form capillary-like structures under appropriate conditions.

This cell line was cultivated in RPMI medium. To obtain a complete RPMI medium, it was supplemented with $NaHCO_3$ (24 mmol/L), FCS (10%), penicillin (100

U/mL) and streptomycin (100 µg/mL). Incubation was set at 37 °C in a 5% CO_2 atmosphere.

For cell splitting, the medium was discarded, and cells were washed twice with sterile PBS and treated with 1.0 mL Accutase for 5 minutes at 37 °C. Afterwards, cells were collected with 5 mL of fresh medium to stop the enzymatic reaction and placed into a 15 mL Falcon tube. Then, cells were spun down at 1,000 g for 3 minutes and the pellet was resuspended in 5 mL of medium and split into cell flasks.

5.3.1. Glass coverslip coating

For better adhesion of cells to glass coverslips, they were previously coated with a poly-L-lysine solution (Sigma P4832). The 13 mm glass coverslips were placed in a container with sufficient poly-L-lysine solution to entirely immerse them. The coverslips were incubated in the poly-L-lysine solution for 30 minutes at room temperature while shaken at 100 rpm on an Orbi-Shaker™. Thereafter, the coverslips were rinsed five times with abundant distilled water and dried under ultraviolet light for sterilization.

5.4. Standardization of conditions for autophagy analysis in tEnd.1 cells upon exposure to *Plasmodium berghei*-derived stimuli

For the optimization assays, tEnd.1 cells stably transduced with LC3-GFP were used to generate concentration and incubation time curves with the different experimental treatments. LC3 expression was quantified by direct fluorescence. These assays were performed to determine the most suitable concentrations and incubation periods that promoted autophagic activity. The results from these experiments were used to establish the optimal conditions applied in the subsequent analyses.

5.4.1. Generation of LC3 reporter stables

The tEnd.1 cells were transduced with lentiviral vectors to express constituent LC3 with fluorescent reporters. The lentiviral particles and transduced tEnd.1 cells, a generous gift from Dr. Jorge Arias-Arias, were produced as previously described via triple transfection of HEK293T cells using polyethylenimine and the plasmids psPAX2, pMD2G, and pWPI-LC3-GFP-Puro (149, 150). The final LC3-GFP-Puro lentiviral construct was kindly provided by Dr. Rodrigo Mora-Rodríguez (151). Briefly, tEnd.1 cell monolayers at 80% confluency were stably transduced with lentiviral particles carrying a genetic construct codifying for LC3-GFP. For cell transduction, lentiviral vector particles were added to the cells at a multiplicity of infection (MOI) of 1 and centrifuged for 2 h at 300 g at 25 °C. At 72 h post-transduction, transduced cells were selected with 8 μg/mL of puromycin (Sigma P8833) in RPMI 10% FBS for 2 days, and then survival cell populations were isolated and propagated in RPMI 10% FBS + 0.5 μg/mL of puromycin.

5.4.2. LC3-GFP tEnd.1 cells seeding for stimulation assays

For cell seeding, the medium was discarded, and cells were washed twice with sterile PBS and treated with 1,0 mL Accutase for 5 minutes at 37 °C. Afterwards, cells were collected with 5 mL of fresh medium to stop the enzymatic reaction and placed into a 15 mL Falcon tube. Then, cells were spun down at 1000 g for 3 minutes and the pellet was resuspended in 5 mL of medium.

Dilution of cell suspension with trypan blue was prepared to determine the number of cells. Cells were counted using a Neubauer chamber and dilutions of cells were prepared according to the experiment setting.

Then cells were seeded in poli-L-lysine-treated coverslips in 24-well plate wells. For early time effects (≤ 6 h posttreatment), 3×10^4 cells were seeded; for late time effects (24 h posttreatment), 2×10^4 cells were seeded. Treatments were applied 24 hours after cells were seeded.

5.4.3. Stimulation assays

Twenty-four hours after cell seeding (section 5.4.2), cells were exposed to specific stimuli to assess autophagic pathway activation at different time points and concentrations. Using the LC3-GFP cell line, LC3 expression was monitored by direct fluorescence.

5.4.3.1. Chemical treatments

To characterize tEnd.1 cells as a model for the study of autophagy, different drugs and stimuli well characterized for this purpose were used at 6 hours posttreatment. The drugs used and their corresponding final concentrations used were chloroquine (CQ, 10 µM), 3-methyladenine (3-MA, 5 mM), bafilomycin A1 (BAF, 100 nM) and rapamycin (RAPA, 10 µM). Additionally, starvation-induced autophagy (STV) was achieved by removing cell media, washing 3 times with sterile PBS and incubating the cells with Earle's Balanced Salt Solution (EBSS).

As a negative control, to monitor baseline autophagy levels, cells were incubated with complete RPMI medium for the corresponding time points.

5.4.3.2. Stimulation with infected RBCs

Previously isolated and quantified infected RBCs (iRBCs) were applied to endothelial cells at three different time points (3-, 6-, and 24-hours post-treatment) and using three iRBC:EC ratios (100:1, 500:1, and 1000:1). The iRBCs were suspended to form a uniform layer covering the endothelial cell monolayer. Uninfected RBCs were included as controls at the same time points and ratios, prepared in the same way.

5.4.3.3. Stimulation with EVs

Previously isolated and protein-quantified small EVs from *P. berghei* cultures were applied to endothelial cells at five different time points (10 min, 30 min, 1-, 3-, and 6-hours post-treatment) and at two protein concentrations (10 and 50 µg). Small EVs derived from RBC cultures were included as controls, following the same time points and protein concentrations.

5.4.3.4. Stimulation with EV-reduced supernatants

EV-reduced, supplemented and prewarmed supernatants from *P. berghei* cultures were applied directly to endothelial cells at five different time points (30 min, 1-, 3-, 6-, and 24-hours post-treatment). Supernatant derived from RBC cultures were included as controls, following the same time points and prepared in the same way.

5.4.4. Protocol for slide preparation for direct fluorescence

At the indicated time points after treatment, the culture media was discarded, and cells were washed at least three times with sterile PBS. Cells were fixed in 300 µL of 4%

paraformaldehyde (PFA) in PBS solution, followed by 1 μL of a 1:20 Hoechst 33342 solution for DNA staining. Cells are left in these solutions for 15 minutes at room temperature and protected from light.

Afterwards, cells were washed 3 times with sterile PBS. After washing, the excess liquid was removed, 5 μL of Mowiol fluorescent mounting medium was added onto a slide, and coverslips were placed with cells facing down. Slides were dried at room temperature and protected from light at least 24 hours before imaging.

5.4.5. Protocol for slide preparation and staining for indirect immunofluorescence

For LC3-GFP signal validation, at the indicated time points after treatment, the culture media was discarded, and cells were washed at least three times with sterile PBS. Cells were fixed in 300 μL of 4% paraformaldehyde (PFA) in PBS solution for 15 minutes at room temperature. For cell permeabilization, 300 μL of ice-cold methanol were added for 10 minutes at -20 °C. In cases when cells were going to be stained later, 1 mL of ice-cold methanol was added, and the plate was sealed with Parafilm and stored at -20 °C.

Afterwards, cells were rehydrated with PBS for 10 minutes. Subsequently, 10% FCS in PBS solution was added for 30 minutes at room temperature to block free epitopes. Both primary and secondary antibodies were diluted in 10% FCS in PBS solution.

A humid chamber was prepared for staining by placing parafilm on top of a moist paper towel. Drops (30 μL each) of the primary antibody solution (rabbit anti-LC3B, PA1-46286, Thermo Fisher Scientific; 1:1000) were pipetted onto the parafilm. Fixed coverslips were inverted onto the antibody drops with the cell side facing down and incubated for 2 h at room temperature or overnight at 4 °C. After incubation, coverslips were thoroughly washed with PBS.

The same procedure was performed using the secondary antibody (goat anti-rabbit Alexa Fluor™ 594, A-11012, Thermo Fisher Scientific; 1:5000), together with Hoechst 33342 for DNA staining. Coverslips were incubated for 1 hour at room temperature and protected from light. Then, coverslips were washed with abundant PBS. After washing, the excess liquid was removed, 5 μL of Mowiol fluorescent mounting medium was added onto a slide, and coverslips were placed with cells facing down. Slides were dried at room temperature and protected from light at least 24 hours before imaging.

5.4.6. Image acquisition

Imaging was performed on a Nikon Ti2 inverted microscope equipped with a confocal module (A1R HD25) and controlled using NIS-Elements software. The images were captured at 60× oil immersion lens (NA 1.4), and the correction collar was adjusted for optimal image quality. Laser lines were chosen based on the fluorophores used: 405 nm for Hoescht, 488 nm for GFP, and 561 nm for Alexa Fluor™ 594 and mCherry, with appropriate emission filters applied for each channel.

Images were exported uncompressed as either .nd2 or .jpeg files using the software they had been acquired with. Images were only enhanced as a whole using ImageJ. No information was added or deleted from any image.

5.4.7. LC3 quantification

Quantification of LC3 signal was performed using an image analysis pipeline developed by Dr. Isaac Quirós Fernández in CellProfiler software (version 4.2.8). This pipeline reports the percentage of cellular area occupied by LC3-positive vesicles relative to the total cell area. For each experimental condition, a minimum of 50 cells were analyzed. Based on these results, the optimal time points and concentrations of the different *P. berghei*-derived stimuli were selected for subsequent experiments.

The optimal conditions selected were as follows: for iRBCs, a 500:1 iRBC:EC ratio for 6 hours; for EVs, a protein concentration of 50 µg for 1 hour; and for EV-reduced supernatant for 1 hour.

5.5. Description of autophagy dynamics in tEnd.1 cells upon exposure to *Plasmodium berghei*-derived stimuli

Once the optimal conditions were established, tEnd.1 cells were transfected with a LC3-tandem fluorescence plasmid encoding proteins involved in the canonical autophagy pathway. This approach allowed the assessment of autophagic flux under these conditions.

5.5.1. Transfection method

Wild type tEnd.1 cells (p3 – p6) grown in cell culture flasks were washed twice with sterile PBS and treated with 1,0 mL Accutase for 5 minutes at 37 °C. Afterwards, cells were collected with 5 mL of fresh medium to stop the enzymatic reaction and placed into a 15 mL Falcon tube. Then, cells were spun down at 1000 g for 3 minutes and the pellet was resuspended in 5 mL of medium. A dilution 1:20 with trypan blue was prepared and viable cells were counted using a Neubauer chamber.

For each transfection, a volume equivalent to 1×10^6 cells was pipetted into a 1.5 mL Eppendorf tube and cells were spun down at 800 g for 5 minutes. Then, the supernatant was removed and 100 µL Nucleofactor V solution were added to the cells. The pellet was resuspended, and the resulting suspension was added to an aliquot of 4 µg of the transfection plasmid (tf-LC3, #21074, Addgene, USA).

The Nucleofector-cell-DNA solution was then transferred into an Amaxa cuvette and placed into the electroporation device, and the program T-028 was executed. Immediately following electroporation, 500 µL of pre-warmed RPMI 1640 medium was carefully added. The cell-RPMI mixture was then carefully transferred into an 1.5 mL Eppendorf tube using an Amaxa pipette and incubated at 37 °C and 5% CO_2 for at least 15 minutes. Afterwards, 100 µL of this suspension was seeded into poli-L-lysine-treated coverslips in 24-well plate wells for 24 hours.

5.5.2. Autophagic flux measurement

Autophagic flux was evaluated in tEnd.1 cells under the previously established experimental conditions. Cells were transfected with a GFP-mCherry-LC3 plasmid, which allowed the analysis of LC3 puncta dynamics, including their formation and degradation.

To distinguish between the accumulation of autophagosomes and their degradation, the same chemical treatments and concentrations from section 5.4.3.1 were used as controls at 6 hours. The same protocols for slide preparation (section 5.4.4) and image acquisition (5.4.6) were followed.

Quantification was performed using a distinct CellProfiler pipeline (version 4.2.8) developed by Dr. Isaac Quirós Fernández. This pipeline measures autophagic flux as the ratio between red vesicles (autolysosomes) and yellow vesicles (autophagosomes). In addition, it determines the percentage of the cell area occupied by mCherry-LC3–positive and GFP-mCherry-LC3–positive vesicles relative to the total cell area. For each experimental condition, a minimum of 50 cells were analyzed.

5.6. Characterization of small EVs produced by *Plasmodium berghei in vitro*

The physical characterization of EVs produced *in vitro* by *P. berghei* was first carried out using dynamic light scattering (DLS) and atomic force microscopy (AFM). This was followed by protein characterization to assess differences in banding patterns through SDS-PAGE electrophoresis and protein identification by mass spectrometry.

5.6.1. Physical characterization by DLS

The hydrodynamic size distribution and surface charge of EVs were assessed by DLS and zeta potential measurements to evaluate their integrity and stability. Both analyses were carried out using a Zetasizer Ultra (Malvern Instruments, Ltd.) according to the manufacturer's instructions, as mentioned by (152).

The EV pellet was resuspended in 250 µL of sterile and filtered PBS. Serial dilutions (1:500) were prepared in PBS. The suspension was passed twice through a 0.22 µm filter immediately after preparation and again just before measurement. For particle size and concentration analysis, reduced-volume quartz cuvettes (ZEN2112, Malvern Panalytical) were used, with liposomes as the reference material and water as the dispersant. Measurements were performed at 25 °C with an equilibration time of 120 s and a dispersant scattering mean count rate (kcps) of 422. Each sample was analyzed in triplicate.

Zeta potential measurements were carried out using disposable folded capillary cells (DTS1080, Malvern Panalytical). Measurements were carried out in isotonic PBS, which was selected to preserve EV integrity. A 1:5 dilution of PBS in ultrapure water was additionally tested to reduce ionic strength. All other experimental parameters were kept consistent with the conditions described for the size and particle concentration analyses. Each sample was analyzed in triplicate. Data acquisition and analysis were performed using the ZS XPLORER software (Malvern Panalytical).

5.6.2. Physical characterization by AFM

Atomic force microscopy images and nanomechanical data were collected using a Multimode 8 microscope (Bruker, USA) operating in PeakForce Tapping mode as detailed by (153). Briefly, samples were diluted 1:5000 in sterile-filtered PBS, and 5 µL of the dilution were deposited onto freshly cleaved muscovite mica. After 10 min of adsorption, the substrate was gently rinsed three times with ultrapure water (MilliQ®, Millipore, Burlington, MA, USA) to remove residual salts and subsequently air-dried.

All measurements were performed under ambient conditions using ScanAsyst-Air and MSNL-10 probes (Bruker), with a nominal cantilever length of 175 µm, a tip radius of approximately 2 nm, and a spring constant of 0.07 $N \cdot m^{-1}$. Prior to imaging, probes were calibrated following the manufacturer's protocol using the Bruker calibration kit. Data were collected simultaneously in height sensor, peak force error, Young's modulus (DMT model), and adhesion channels. Raw AFM data were further processed and analyzed using Nanoscope Analysis software v1.7 (Bruker).

Images were typically acquired at a resolution of 256 × 256 pixels and a scan rate of 0.3–0.5 Hz. For each condition, representative images were obtained by scanning at least three different areas from a minimum of three independent samples.

5.6.3. Protein analysis by SDS-PAGE

Ten percent acrylamide gels were prepared, and samples were heated at 98 °C for 10 min prior to loading. A total of 5 µg of protein was loaded per sample. Electrophoresis was carried out at 80 V for 90 min. After separation, gels were stained either with Coomassie Brilliant Blue R-250 or by silver staining according to the established protocol (154).

Briefly, gels were fixed in methanol/acetic acid solution, washed with ultrapure water, and sensitized with periodic acid. After additional washes, gels were incubated in freshly prepared silver nitrate solution, followed by development in sodium carbonate containing formaldehyde until bands appeared. The reaction was stopped by rinsing with ultrapure water, and gels were photographed immediately to avoid degradation.

Gel images were acquired using a ChemiDoc™ Imaging System (Bio-Rad Laboratories).

5.6.4. Proteome profiling of whole EVs by bottom-up shotgun analysis

A preliminary proteome profiling of the whole EV cargo was performed using a bottom-up shotgun strategy as previously described (147, 155). Briefly, samples were processed as outlined in section 5.7.3, and 20 µg of protein per sample were loaded onto 10% acrylamide gels. Electrophoresis was stopped once the migration front had entered approximately 3 mm into the resolving gel. The protein band was visualized by Coomassie staining, excised, destained in 50% acetonitrile, and subsequently subjected to tryptic digestion followed by nano-LC-MS/MS analysis.

Excised SDS-PAGE protein bands were in-gel digested overnight with sequencing-grade trypsin after reduction with 10 mM dithiothreitol and alkylation with 50 mM iodoacetamide, using an automated workstation (Intavis). The resulting peptides were dried, redissolved in water with 0.1% formic acid, and submitted to nano-LCMS/MS. Ten µL of peptide mixture was loaded onto a C_{18} trap column (75 µm × 2 cm, 3 µm particle size; PepMap; Thermo), washed with 0.1% formic acid (solution A), and then separated at a flow rate of 200 nL/min on a C_{18} Easy-spray® column (15 cm × 75 µm, 3 µm particle size).

A gradient to solution B (80% acetonitrile, 0.1% formic acid) was used for elution: 1% B over 3 min, 1–26% B over 62 min, 26–99% B over 30 min, and finally, a 99% B hold for 15 min, for a total run time of 110 min.. MS spectra were acquired on a Q-Exactive™ Plus (Thermo) in positive ion mode at 1.9 kV, with a transfer capillary temperature of 230 °C, using one1 µscan at 400–1600 m/z, maximum injection time of 100 ms, AGC target of 3×10^6 , and orbitrap resolution of 70,000. The top 10 ions with 2–4 positive charges were selected for fragmentation using an isolation window of 1.4 m/z, and MS2 spectra were acquired using an AGC target of 1×10^5, a maximum injection time of 110 ms, resolution of 17,500, and a dynamic exclusion time of 5 s.

Raw MS spectra were processed and analyzed using MaxQuant software for peptide and protein identification by searching against UniProt databases for *Plasmodium berghei* ANKA and *Mus musculus* (December 2025). Both peptide-spectrum match and protein identification were obtained with a 1% FDR. Oxidation of methionine and acetylation of protein N-terminal were specified as variable modifications and cysteine carbamidomethylation was set as a fixed modification. All remaining MaxQuant parameters were kept as default.

The resulting protein groups table was imported into Perseus software for downstream processing. Reverse database hits (decoys), potential contaminants, and proteins identified only by site were removed. Filtered protein intensities were log2-transformed prior to further analysis. Protein-protein interaction networks and functional associations were subsequently explored using the STRING database (https://string-db.org).

5.7. Data analysis

Statistical analyses were performed using GraphPad Prism software (version 8.0.2). The specific statistical tests applied are detailed in the corresponding figure legends. In all cases, differences were considered statistically significant when $P < 0.05$.

Graphical representations were generated using Graphmatik (© 2026 UpSci LLC), an online data visualization platform (https://www.graphmatik.io/), allowing standardized and consistent visualization of the datasets.

6. Results

6.1. Effects of atmospheric conditions, temperature, and medium composition on the short-term growth of *Plasmodium berghei* blood stages

Not all *Plasmodium* species and strains can be grown in laboratory settings. Certain strains are easily established *in vitro*, whilst others are resistant to cultivation or their optimal growth conditions are unknown (145). The effect of the three variables that differ the most in literature for *P. berghei* blood stages culture was evaluated: atmosphere composition, temperature, and medium formulations. In all cases, a closed suspension culture system with mouse (*Mus musculus*) red blood cells as host cells was used.

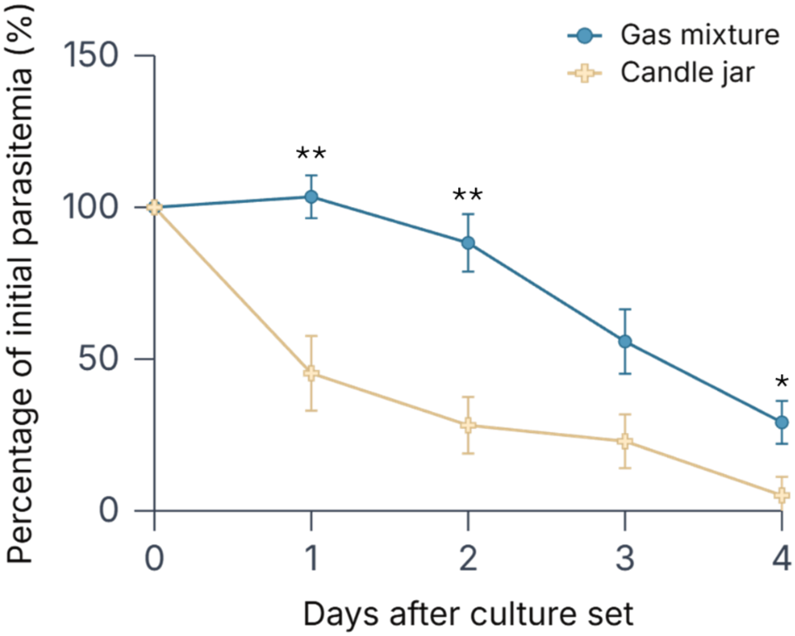

Figure 6.1. Effect of incubation atmosphere in *P. berghei* blood stages culture. Growth curves showing the mean percentage of parasitemia relative to the initial parasitemia on day 0 over a four-day period, using Trager & Jensen medium at 37 °C. Two atmospheric conditions were compared: a candle jar environment and a controlled gas mixture (90% N_2, 5% CO_2, and 5% O_2). Error bars represent the standard deviation of at least three independent experiments. Unpaired t-tests were performed for each day to compare the two conditions. Significant differences were found on day 1 ($P = 0.0083$), on day 2 ($P = 0.0057$), and on day 4 ($P = 0.045$) after culture set.

To assess the influence of atmospheric conditions on *P. berghei* growth, two environments were evaluated: a traditional candle jar system and a controlled gas mixture (90% N_2, 5% O_2, 5% CO_2). As shown in Figure 6.1, cultures in the candle jar system exhibited a drastic decline in parasitemia after the first day, approaching 0% by the end of the experiment.

Morphological analysis of parasites from this condition revealed signs of cell death, including a condensed nucleus and basophilic cytoplasm, in contrast to the healthier appearance of those maintained in the gas mixture. A further indicator of metabolic disparity was the color of the spent medium due to the presence of phenol-red; centrifugation of the gas mixture cultures yielded a yellow-orange supernatant, indicative of anaerobic metabolism and acid production, whereas the medium from the candle jar system remained reddish-pink, suggesting alkalinization (Figure 6.2).

The candle jar system was initially adopted for *Plasmodium* cultures to create a microaerophilic environment by reducing oxygen concentrations (141). However, it was largely replaced by controlled gas mixtures, which provide a more stable, lower oxygen concentration and superior atmospheric regulation (143, 144). For these reasons, the controlled gas mixture was selected for all subsequent experiments.

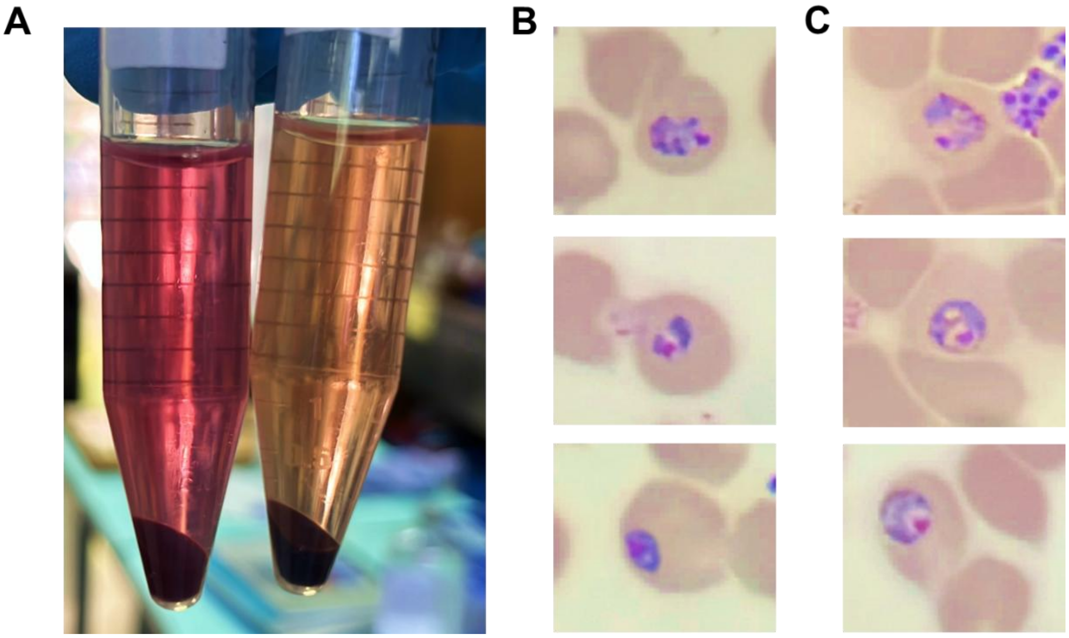

Figure 6.2. Effect of atmospheric conditions on *P. berghei* culture supernatant and parasite morphology. (A) Color difference in culture supernatants after centrifugation, from candle jar (left) and gas mixture (right) systems at 24 hours post-culture initiation. (B, C) Representative microscopy images of trophozoites at 24 hours from the candle jar system (B) and the gas mixture (C). Parasites in (B) exhibit a condensed morphology and basophilic cytoplasm, indicative of low parasite viability, in contrast to the healthier morphology in (C).

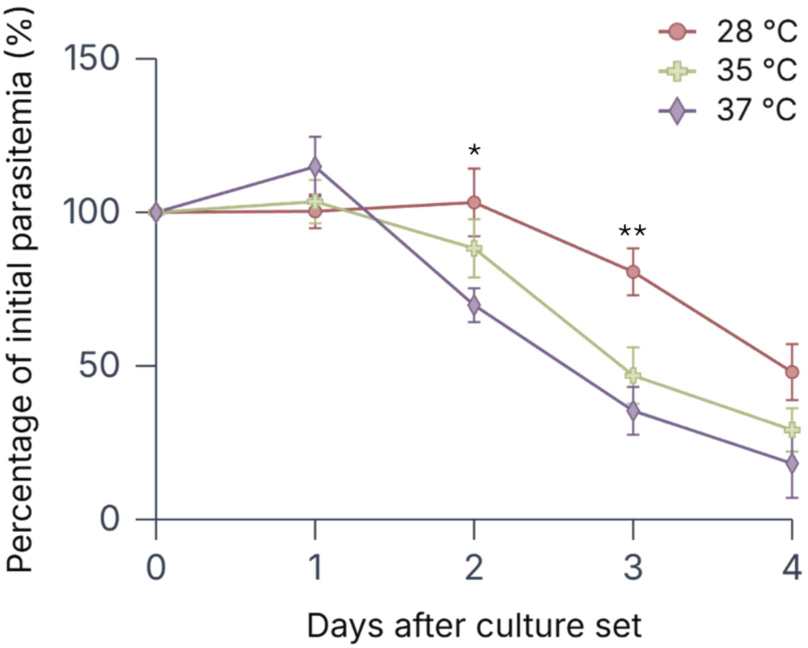

Figure 6.3. Effect of incubation temperature in *P. berghei* blood stages culture. Growth curves showing the mean percentage of parasitemia relative to the initial parasitemia on day 0 over a four-day period, using Trager & Jensen medium under a gas mixture atmosphere. Three different temperatures were compared: 28 °C, 35 °C, and 37 °C. Error bars represent the standard deviation of at least three independent experiments. Statistical analysis was performed using a two-way ANOVA followed by Tukey's post hoc test to assess the effects of temperature and time on parasitemia. Significant differences were observed on day 2 between 28 °C and 37 °C ($P = 0.038$), and on day 3 between 28 °C and both 35 °C ($P = 0.019$) and 37 °C ($P = 0.0044$) after culture set.

For the temperature assessment of *P. berghei* growth, three incubation conditions were tested: 28 °C, 35 °C, and 37 °C. As shown in Figure 6.3, parasitemia remained at higher levels for a longer period at 28 °C, whereas no significant differences were observed between 35 °C and 37 °C.

Morphological analysis of parasite stages (Figure 6.4) revealed that parasite development was strongly influenced by temperature. At 35 °C and 37 °C, schizonts were detectable within the first 24 hours of culture. In contrast, at 28 °C, schizonts did not appear until the third day. Under this lower-temperature condition, parasitemia persisted for a longer duration, but the progression to mature stages was delayed relative to the higher temperatures. The delayed detection of schizonts indicates that the erythrocytic cycle was prolonged at 28 °C.

Temperatures below 37 °C are employed to reduce the parasite's metabolic and growth rate, thereby preventing nutrient depletion and waste accumulation (143). Therefore, the 35 °C condition was selected to slightly slow down parasite metabolism without affecting the life cycle.

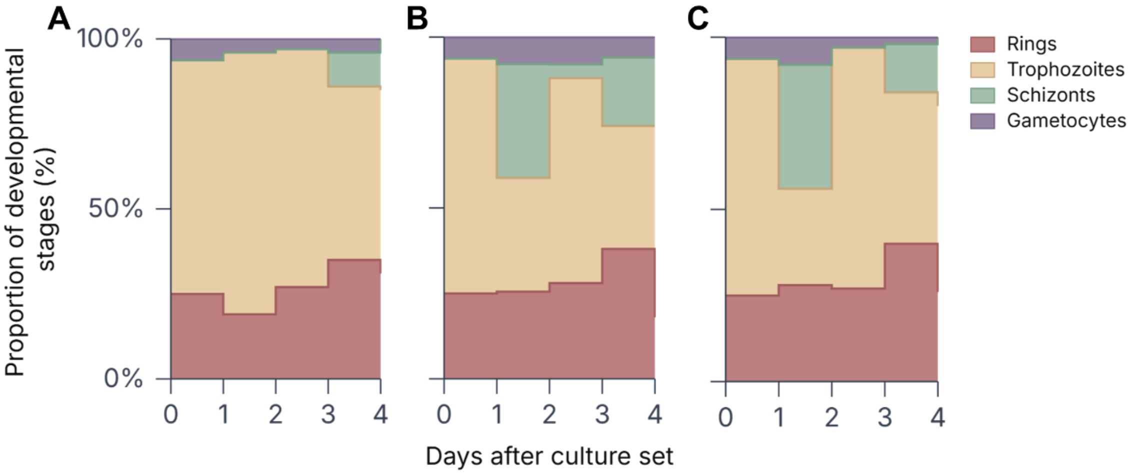

Figure 6.4. Effect of temperature in *P. berghei* developmental stages distribution *in vitro*. Proportion of intraerythrocytic developmental stages of *P. berghei* evaluated over four days of *in vitro* culture at (A) 28 °C, (B) 35 °C, and (C) 37 °C. For each temperature condition, at least 50 infected red blood cells were examined per time point, and the percentages of rings, trophozoites, schizonts, and gametocytes were recorded.

Finally, the effect of medium formulation on *P. berghei* growth was assessed using three literature-based compositions: the modified Trager & Jensen's formulation (1976) for *P. falciparum*, and Janse et al. (1984) and Jambou et al. (2011) formulations for *P. berghei*. As shown in Figure 6.5, Janse's formulation led to a rapid decrease in parasitemia, with few to no parasites remaining by day two. In contrast, no significant differences were observed between the Trager & Jensen's and Jambou's formulations.

A key distinction of Janse's medium is its use of 10% fetal calf serum instead of AlbuMAX™, as well as an alternative antibiotic regimen. Jambou's formulation, based on a mixture of RPMI 1640 and DMEM-F12 and further supplemented with glucose, sodium bicarbonate, choline, and calcium, was considered the most nutrient-rich. To prevent potential nutrient limitations, Jambou's formulation was therefore selected for subsequent experiments.

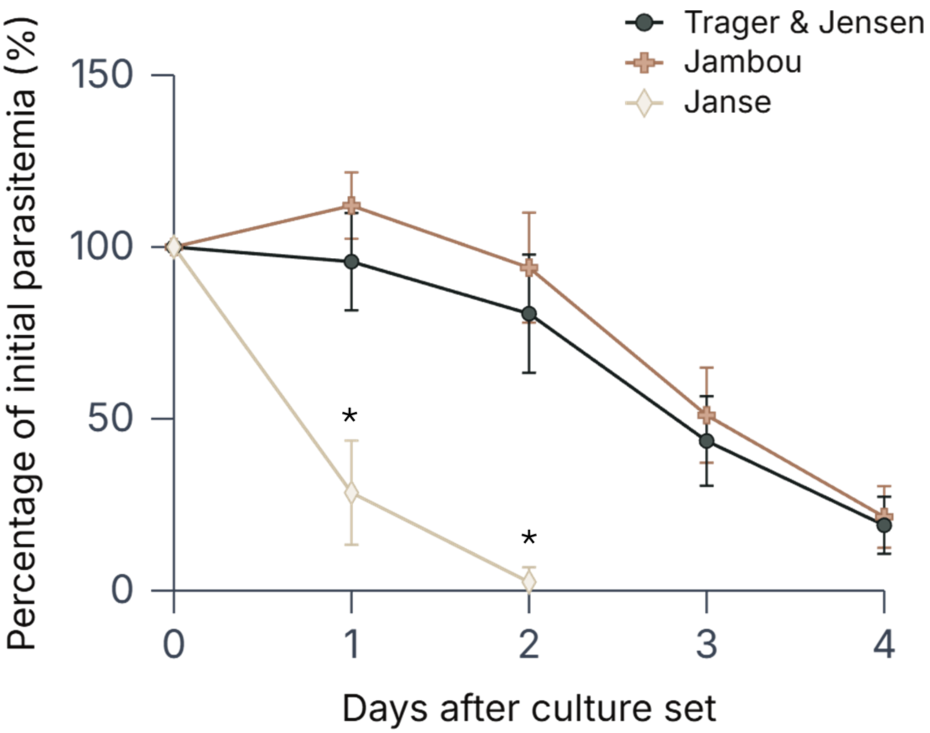

Figure 6.5. Effect of media composition in *P. berghei* blood stages culture. Growth curves showing the mean percentage of parasitemia relative to the initial parasitemia on day 0 over a four-day period, at 35 °C under a gas mixture atmosphere. Three different medium compositions were compared: Trager & Jensen's, Janse's and Jambou's. Error bars represent the standard deviation of at least three independent experiments. Statistical analysis was performed using a two-way ANOVA followed by Tukey's post hoc test to assess the effects of media composition and time on parasitemia. Significant differences were found between Janse's medium and the other two media on day 1, with $P = 0.011$ (vs. Trager & Jensen's) and $P = 0.0053$ (vs. Jambou's), and on day 2, with $P = 0.017$ (vs. Trager & Jensen's) and $P = 0.0083$ (vs. Jambou's).

Based on the results obtained, the most promising conditions for *Plasmodium berghei* blood-stage culture were established as follows: Jambou's medium, due to its higher nutritional complexity; an incubation temperature of 35 °C, to slightly slow down parasite metabolism without disrupting the life cycle; and the gas mixture atmosphere, as it provides greater chemical stability and lower oxygen content.

Although these culture conditions are among the most used in the literature, they remain far from optimal for the long-term maintenance of *Plasmodium berghei in vitro*. Biological and/or methodological limitations still hinder the parasite's ability to be sustained indefinitely under culture conditions. As evidenced in Figure 6.6, the parasite appears capable of completing one or two full intraerythrocytic cycles. However, starting from the third day, an accumulation of free merozoites is observed (merozoites that fail to successfully reinvade RBCs) coinciding with a marked decline in parasitemia. This pattern suggests a progressive loss of culture viability beyond the initial two replication cycles.

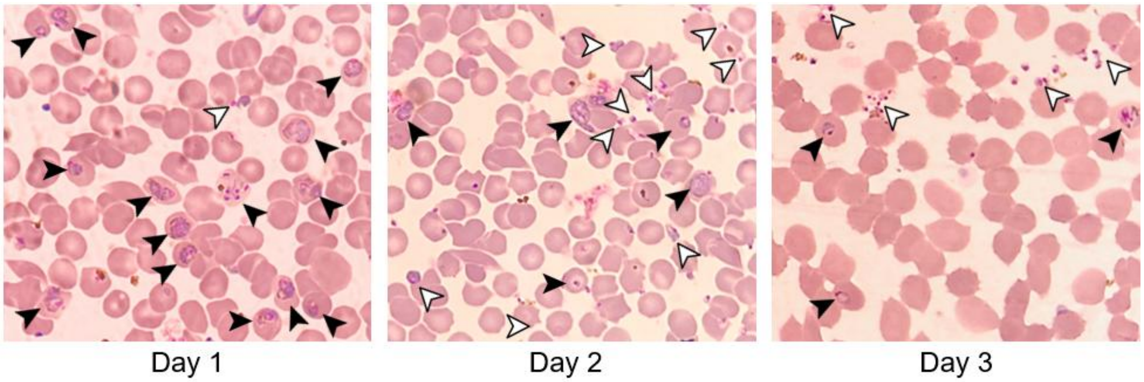

Figure 6.6. Morphological progression of *P. berghei* and red blood cell changes in culture over time. Giemsa-stained blood smears show the progression of *P. berghei* blood-stage parasites *in vitro* at day 1 (left), day 2 (middle), and day 3 (right) post-culture initiation. Cultures were maintained under the selected conditions: Jambou's medium, 35 °C incubation, and a gas mixture atmosphere (90% N_2, 5% CO_2, 5% O_2). Over time, a clear reduction in parasitemia is observed, characterized by a decrease in the number of infected erythrocytes (black arrowheads) and a progressive accumulation of free parasites (white arrowheads). Additionally, a shift in the staining pattern and morphology of uninfected RBC becomes apparent over the culture period, indicating changes in RBC integrity. Together, these observations suggest limited merozoite reinvasion after the second cycle, accompanied by culture-induced alterations in the host RBC population. Images were acquired using bright-field light microscopy at 1000× magnification.

To determine whether the apparent loss of infectivity observed *in vitro* after two days of culture was also reflected *in vivo*, groups of three ICR (CD-1®) mice were intraperitoneally inoculated with 1×10^5 iRBCs collected from day 1 and day 2 cultures. Parasitemia was monitored daily for six days post-inoculation (Figure 6.7). In both groups, blood smears became positive on day 3 post-inoculation, with no significant differences observed between them. These findings suggest that the parasites retain their infectivity for at least two days after culture initiation.

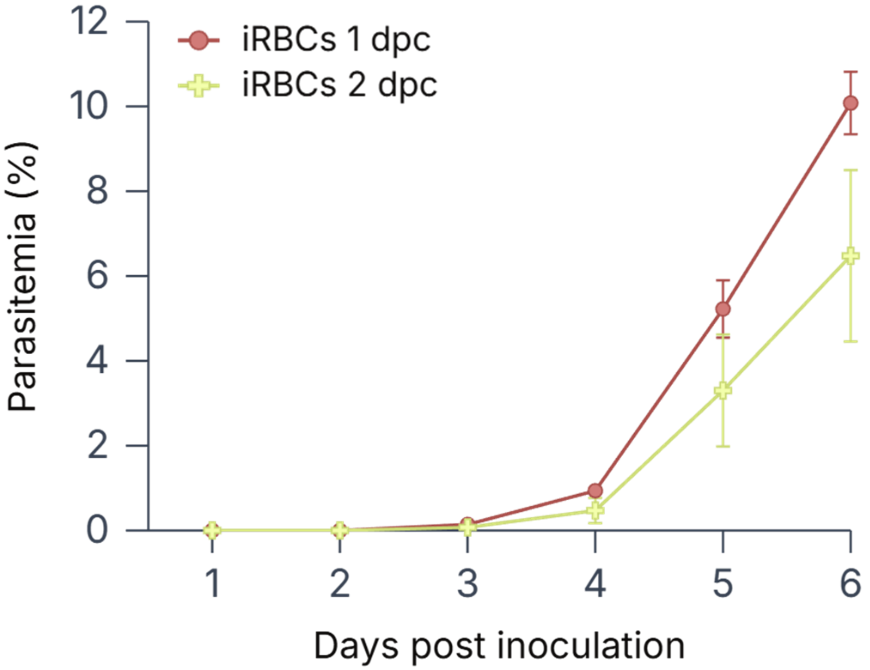

Figure 6.7. Infectivity of cultured infected red blood cells (iRBCs). Average parasitemia curves in ICR (CD-1®) mice over a 6-day period following intraperitoneal inoculation with 1×10^5 iRBCs obtained at 1- and 2-days post-culture (dpc). Error bars indicate standard deviation (n = 3 per group). Comparison of parasitemia levels between the two groups using the Mann–Whitney U test revealed no statistically significant differences ($P = 0.79$).

6.2. Enrichment of *Plasmodium berghei*-derived stimuli

To investigate the endothelial response to *Plasmodium berghei*, three parasite-derived stimuli were isolated for *in vitro* stimulation assays: (1) infected red blood cells (iRBCs), obtained from the peripheral blood of infected mice via density-based separation; (2) culture supernatants, collected from *P. berghei* blood-stage cultures maintained under selected conditions; and (3) extracellular vesicles (EVs), further enriched from these supernatants through differential centrifugation.

Isolation of iRBCs from peripheral blood or *in vitro* cultures using density gradients with Percoll or Nycodenz is one of the most employed approaches (146). However, the optimal gradient composition and centrifugation parameters often vary depending on the *Plasmodium* species (156). In the case of *P. berghei*, relatively few protocols have been described (157, 158), and those available did not yield satisfactory results under our experimental conditions. To overcome this limitation, a custom protocol was developed using a discontinuous Percoll gradient composed of four concentrations

(30%, 40%, 50%, and 60%). This method enabled a more consistent and reproducible separation of different iRBC subpopulations, as shown in Figure 6.8.

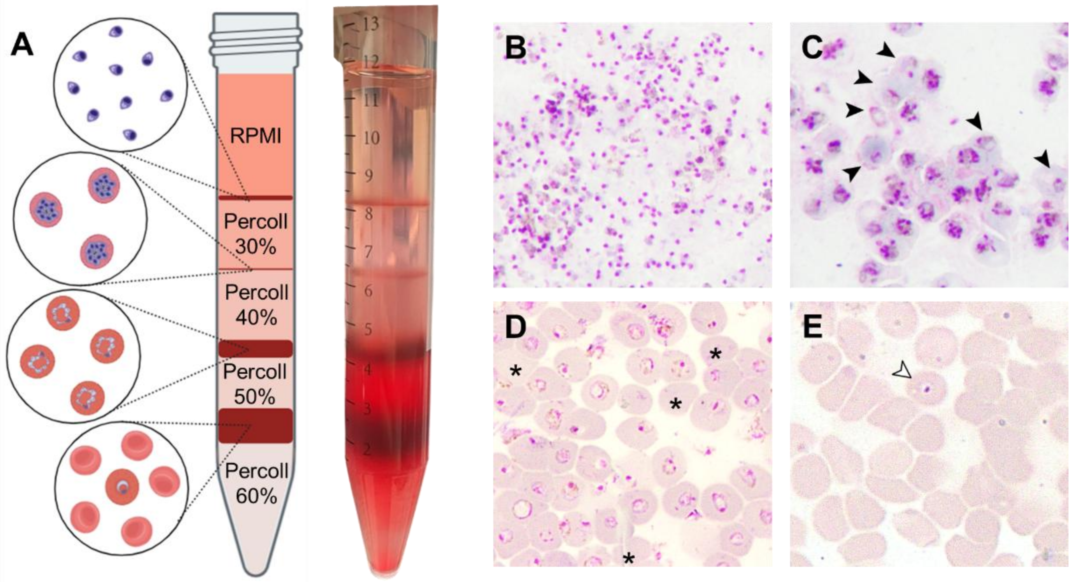

Figure 6.8. Enrichment of different *P. berghei* blood stages using a Percoll gradient. (A) Representation of the discontinuous Percoll gradient used to enrich *P. berghei* blood stages. The diagram on the left shows the distinct parasite stages found at each interphase after centrifugation, and a photograph of the actual gradient is shown on the right. (B–E) Giemsa-stained blood smears corresponding to each interphase: (B) Interphase between RPMI medium (0% Percoll) and 30% Percoll shows free merozoites. (C) Interphase between 30% and 40% Percoll contains mostly schizonts and some trophozoites (black arrowheads). (D) Interphase between 40% and 50% Percoll is enriched in early and late trophozoites, with few uninfected RBCs (marked with *). (E) Interphase between 50% and 60% Percoll contains mostly uninfected RBCs and scarce ring stages (white arrowhead). All micrographs were taken with a bright-field light microscope at 1000× magnification and represent a zoomed-in section of the microscope field for better visualization of the parasite stages. Diagram created with BioRender.

Enrichment of EVs by differential ultracentrifugation remains one of the most widely used and cost-effective methods for concentrating these vesicles into a single pellet (159). This protocol was applied to supernatants from *P. berghei* cultures, which were essential as the sole viable source of parasite-specific EVs, as direct isolation from infected blood is impractical due to low yield and overwhelming host contamination. Following sequential ultracentrifugation and washing steps, a small, reddish pellet with a loose, sticky consistency was obtained for both parasite and control cultures (Figure 6.9). The pellet was resuspended in filtered PBS and stored at 4°C for up to one week for functional or physical characterization assays or at -80°C for protein analysis.

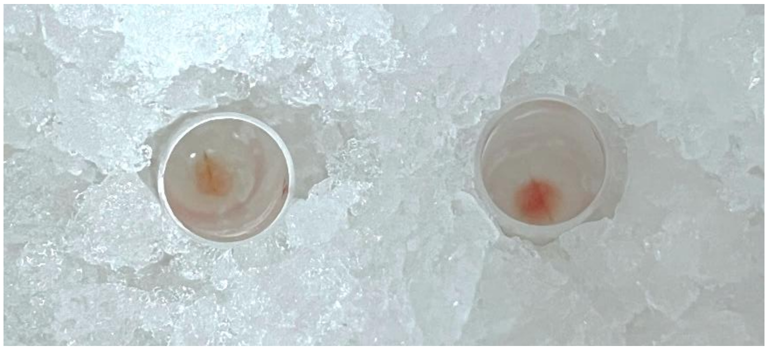

Figure 6.9. Macroscopic appearance of small EVs pellets obtained from *P. berghei* and RBC culture supernatants. *P. berghei* (left) and control culture of RBCs (right) pellets after the washing steps of differential ultracentrifugation. Small, reddish pellets with a loose and tacky consistency can be observed at the bottom of the ultracentrifuge tubes, which were maintained on ice between centrifugation steps.

6.3. Establishment and characterization of LC3-GFP tEnd.1 stable cell lines as autophagy model

To monitor autophagy dynamics, a stable cell line transduced with a lentiviral vector encoding LC3 fused to green fluorescent protein (GFP) was generated by Dr. Jorge Arias-Arias. LC3 was selected as a canonical marker because its lipidated form (LC3-II) is specifically recruited to both the forming phagophore and completed autophagosome double-membrane vesicles of the autophagy pathway (92, 160).

In this system, cytoplasmic LC3-GFP fluorescence allows for the real-time visualization of autophagosome formation and distribution. However, a key limitation of this fluorescent reporter is that the GFP signal is quenched upon autophagosome-lysosome fusion due to the acidic and proteolytic environment of the lysosome (160). Consequently, while an increase in LC3-GFP puncta signal can indicate enhanced autophagosome formation, it can also result from a blockage in the downstream degradation step, leading to the accumulation of undegraded autophagosomes.

To validate the use of the generated LC3 reporter cell lines derived from tEnd.1 cells as a model to study autophagy, cells were exposed to a panel of well-characterized pharmacological treatments known to either induce or inhibit the autophagy pathway. The expression and distribution of LC3 were assessed in the LC3-GFP cell line by fluorescence microscopy, allowing for quantification of autophagic vesicle formation or accumulation under each condition (160, 161).

All treatments with autophagy inducers (rapamycin and starvation), which increase autophagosome formation, as well as inhibitors of autophagosome-lysosome fusion (bafilomycin A1 and chloroquine), which cause autophagosome accumulation, resulted in a significant increase in the LC3-positive area compared to the control. In contrast, cells treated with 3-methyladenine, an inhibitor of autophagosome initiation, showed no significant difference (Figure 6.10). Collectively, these results demonstrate that the LC3-GFP tEnd.1 cell line responds appropriately to autophagy-modulating drugs, supporting its validity as a reliable model for monitoring autophagic activity.

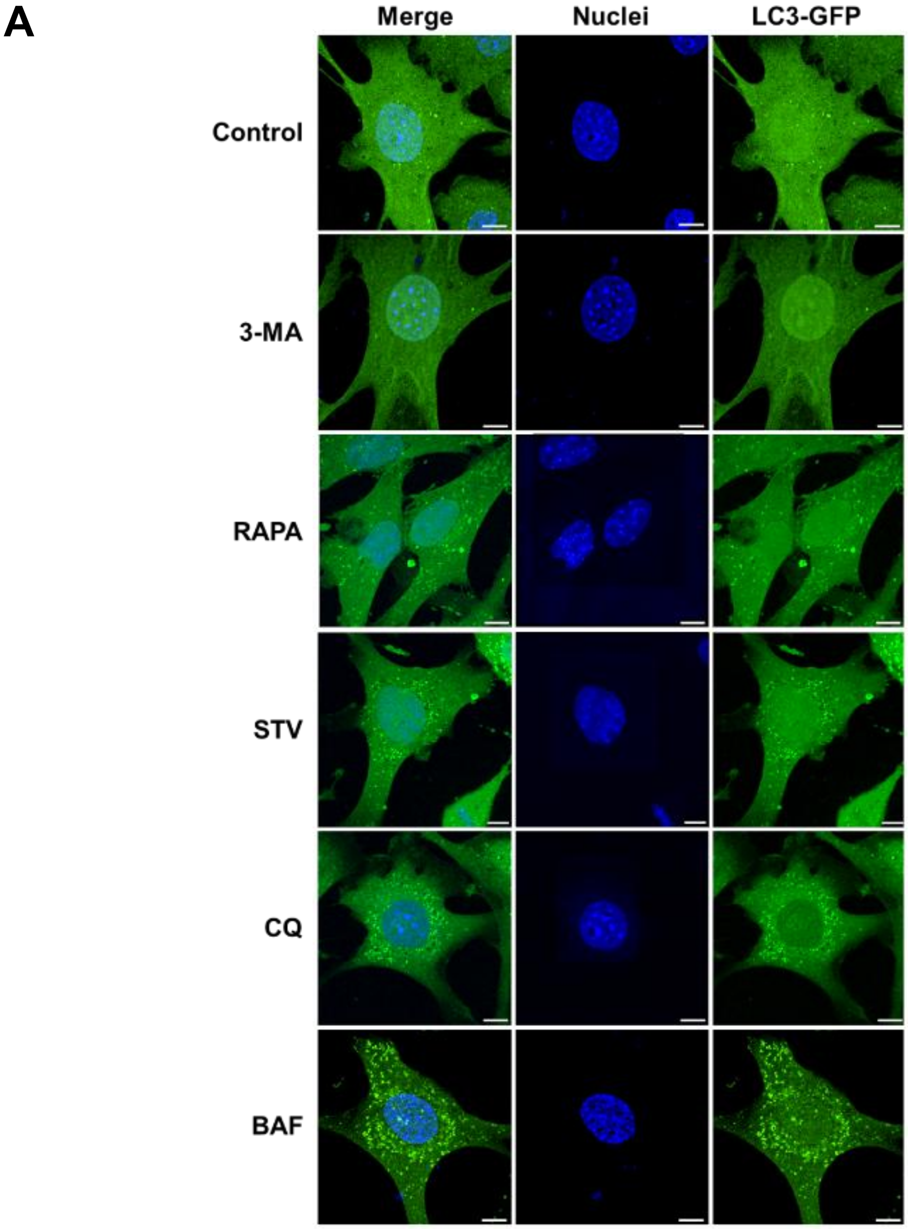

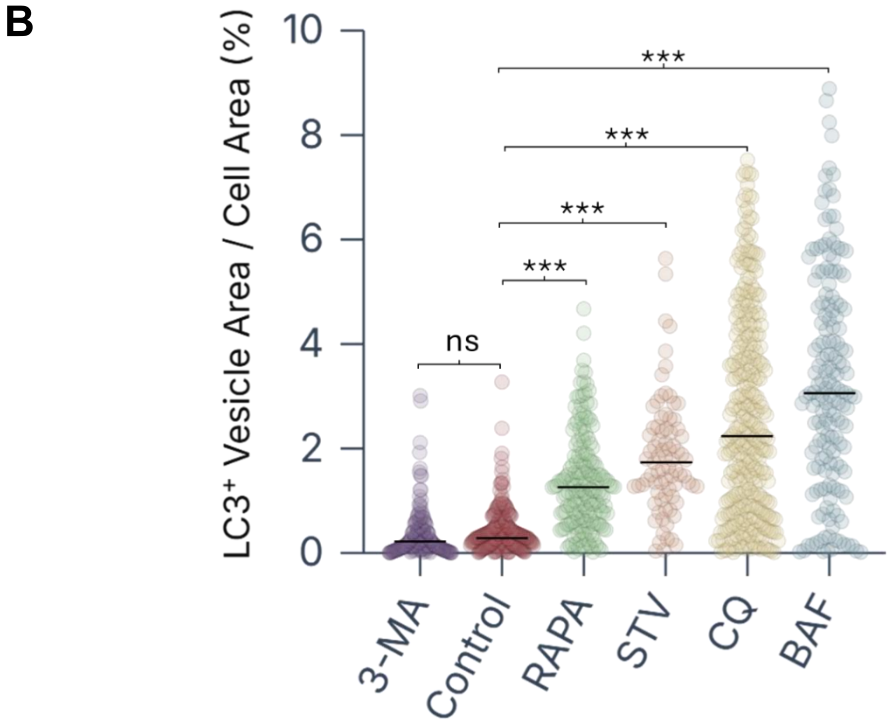

Figure 6.10. Evaluation of the response of LC3-GFP tEnd.1 cells after 6-hour exposure to autophagy-related treatments. (A) Fluorescence imaging of LC3-GFP tEnd.1 cells after different autophagy-related treatments. Nuclei were stained with Hoechst 33342. Scale bars: 10 µm. (B) Spread plots show the percentage of cellular area occupied by LC3-positive vesicles in LC3-GFP tEnd.1 endothelial cells after treatment to different autophagy-modulating treatments, compared to untreated control cells. Each dot represents an individual cell, and horizontal lines indicate median values. Data were obtained from at least n = 50 cells per condition. Statistical analysis was performed using Kruskal–Wallis with Dunn's post hoc test. Significant differences were observed between all treatments and the control ($P < 0.0001$), except for 3-MA ($P = 0.2714$). 3-MA: 3-methyladenine (5 mM); RAPA: rapamycin (10 µM); STV: starvation; CQ: chloroquine (10 µM); BAF: bafilomycin A1 (100 nM).

To validate that the GFP-tagged LC3 accurately reports the distribution of the LC3 positive structures, immunofluorescence was performed with an anti-LC3 antibody. The high degree of colocalization (yellow in merge) between the GFP signal (green) and the antibody staining (red) demonstrated that the reporter correctly localizes to LC3-positive vesicles, confirming the specificity of the model (Figure 6.11). This result supports that the puncta detected in the transduced cells indeed represent LC3 accumulation, validating the use of LC3-GFP tEnd.1 cells as a reliable model for studying autophagy (161).

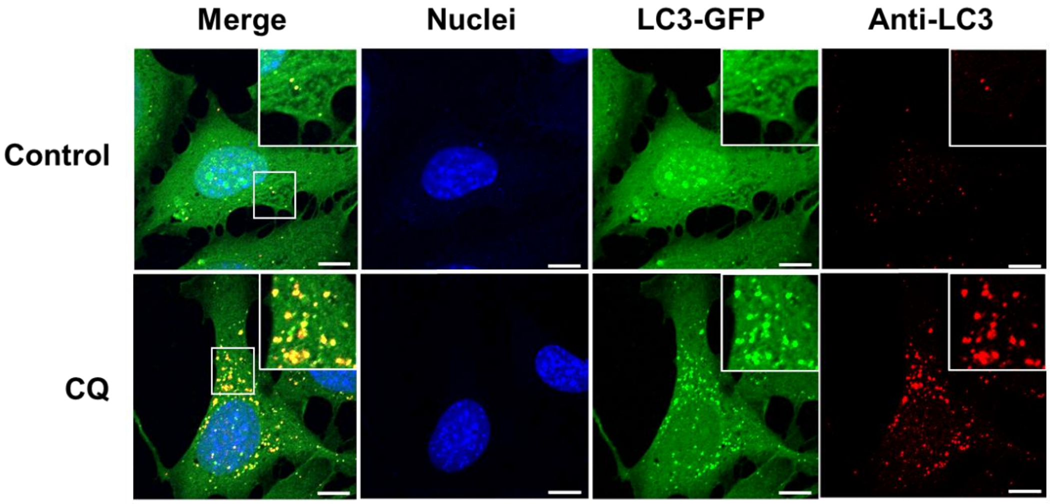

Figure 6.11. Validation of GFP puncta in LC3-GFP tEnd.1 cells. Representative images of LC3-GFP tEnd.1 cells stained with an anti-LC3 antibody to confirm the identity of GFP-labeled vesicles after treatment with CQ for 6 hours and its respective control. The anti-LC3 signal (red) colocalized with most GFP fluorescence (green), indicating its correspondence to LC3-positive vesicles (yellow in merge). Nuclei were stained with Hoechst 33342. Scale bars: 10 µm. CQ: chloroquine (10 µM).

6.4. *Plasmodium berghei* derived stimuli induce time- and dose-dependent LC3 upregulation in LC3-GFP tEnd.1 cells

To evaluate the autophagic response of endothelial cells to *P. berghei*-derived stimuli, dose-response and time-course assays were performed using LC3-GFP tEnd.1 cells. Cells were exposed to increasing concentrations of the stimuli for different incubation periods, and the extent of autophagy was quantified by measuring LC3-positive area relative to total cell area.

These assays allowed to determine both the concentration- and time-dependent effects of *P. berghei* on endothelial autophagic activity, as well as to identify the optimal conditions for LC3 expression to be used in subsequent experiments. The stimuli included iRBCs from blood of infected mice, EVs from *P. berghei* culture, and the corresponding EV-reduced supernatant.

For iRBCs, three RBC to EC ratios (100:1, 500:1, and 1000:1) and three incubation times (3, 6, and 24 hours) were tested using blood from three independent mice. The results showed that, at a given RBC to EC ratio, the LC3-positive area increased over time and in most cases was significantly higher than in the respective controls (Figure 6.12; Figure S.1; and Figure S.2).

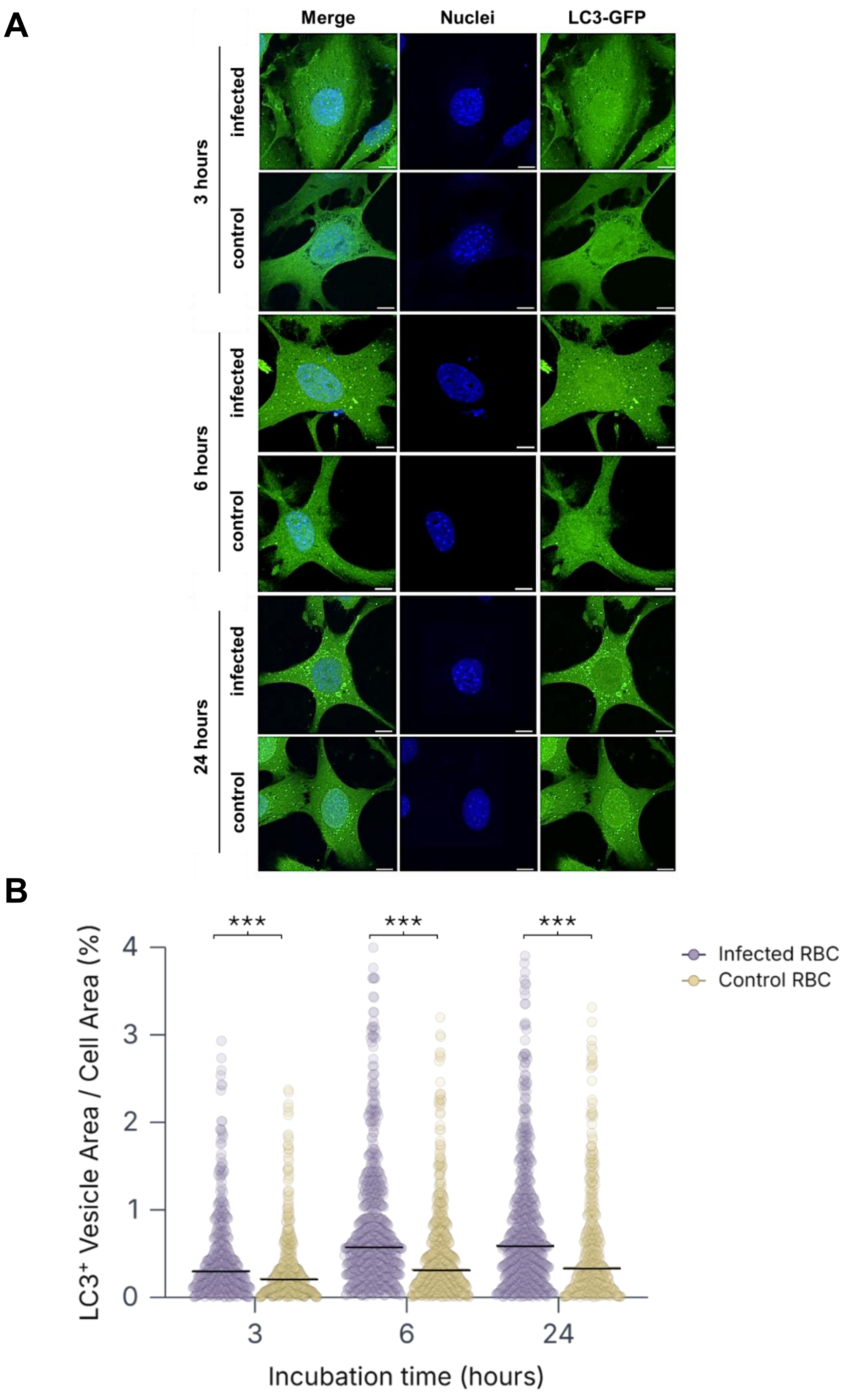
A
Merge
Nuclei
LC3-GFP
3 hours
infected
control
6 hours
infected
control
24 hours
infected
control
B
***
***
***
LC3⁺ Vesicle Area / Cell Area (%)
0
1
2
3
4
3
6
24
Incubation time (hours)
Infected RBC
Control RBC

Figure 6.12. Time-course analysis of LC3 accumulation in LC3-GFP tEnd.1 endothelial cells following incubation with *P. berghei*-iRBCs at a ratio of 500 RBCs per EC. (A) Fluorescence imaging of LC3-GFP tEnd.1 cells after 3, 6, and 24 hours of exposure to *P. berghei* iRBCs (500 iRBCs/EC), compared to controls exposed to non-iRBCs. Nuclei were stained with Hoechst 33342. Scale bars: 10 μm. (B) Spread plots show the percentage of cellular area occupied by LC3-positive vesicles in LC3-GFP tEnd.1 endothelial cells after treatment with different incubation times with iRBCs and control RBCs. Each dot represents an individual cell, and horizontal lines indicate median values. Quantification was performed across three independent experiments, analyzing at least n = 100 cells per condition in total. Statistical significance was assessed using the Mann–Whitney U test. All iRBC-treated groups showed significantly higher LC3-positive area compared to their respective controls at 3 hours ($P < 0.0001$), 6 hours ($P < 0.0001$), and 24 hours ($P < 0.0001$). RBC: red blood cell; iRBCs: infected RBCs; EC: endothelial cell.

Glucose levels were also measured after 6 hours at the 500:1 ratio to exclude nutrient depletion as a confounding factor. Levels were 11.39 ± 0.17 mmol/L (medium only), 11.28 ± 0.11 mmol/L control RBCs), and 9.67 ± 0.44 mmol/L (iRBCs), all within the physiological range for sustained metabolism. This confirms the autophagic response was not driven by glucose exhaustion.

In addition, when comparing different ratios at the same incubation time, a dose-dependent effect was observed, with the 500:1 ratio yielding significantly higher LC3 expression (Figure 6.13). This pattern indicates that the autophagic response reaches a maximum at an intermediate exposure level (500 iRBC), while higher concentrations do not further enhance the response, suggesting the onset of a plateau effect.

These collective results indicate that the most suitable conditions to study autophagy in this model are achieved with a 6-hour incubation at a 500:1 RBC-to-EC ratio, and that the autophagic response is unlikely to be driven by nutrient exhaustion.

The following section addresses the study of stimuli derived from *P. berghei in vitro* cultures. For EVs, five different time points were evaluated (10 min, 30 min, 60 min 180 min, and 360 min). The results showed a rapid accumulation of LC3 as early as 30 minutes after the addition of the EV suspension, both for EVs derived from *P. berghei* and for EVs obtained from cultures of healthy RBCs. A peak in LC3 activation was observed at 1 hour of incubation with parasite-derived EVs. After this peak, LC3 intensity progressively declined in both groups (Figure 6.14).

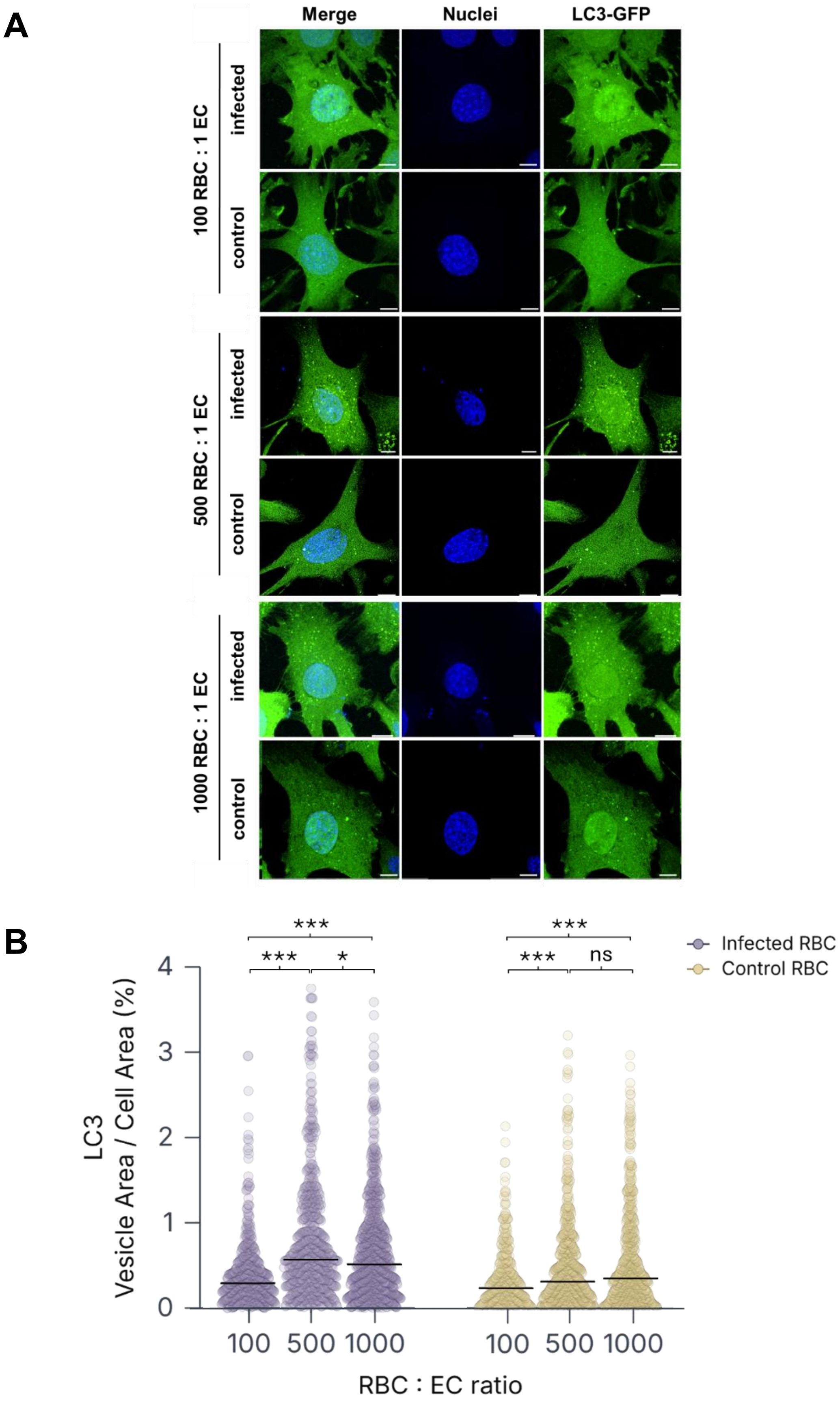
A
Merge
Nuclei
LC3-GFP
100 RBC : 1 EC
infected
control
500 RBC : 1 EC
infected
control
1000 RBC : 1 EC
infected
control
B
LC3
Vesicle Area / Cell Area (%)
0
1
2
3
4
***
***
*
***
***
ns
Infected RBC
Control RBC
100
500
1000
100
500
1000
RBC : EC ratio

Figure 6.13. Evaluation of the effect of the iRBC-to-endothelial cell ratio. (A) Fluorescence imaging of LC3-GFP tEnd.1 cells after 6 hours of exposure to *P. berghei* iRBCs at three different RBC to EC ratio (100:1, 500:1, and 1000:1), compared to controls exposed to non-iRBCs. Nuclei were stained with Hoechst 33342. Scale bars: 10 µm. (B) Spread plots show the percentage of cellular area occupied by LC3-positive vesicles in LC3-GFP tEnd.1 endothelial cells after treatment with different doses of iRBCs and control RBCs. Each dot represents an individual cell, and horizontal lines indicate median values. Quantification was performed across three independent experiments, analyzing at least n = 100 cells per condition in total. Differences among RBC:EC ratios within each group were assessed using the Kruskal-Wallis test followed by multiple comparisons. Among iRBC-treated conditions, significant differences were observed between 100 and 500 ($P < 0.0001$), 100 and 1000 ($P < 0.0001$), and 500 and 1000 ($P = 0.0149$) RBC:EC ratios. In control groups, significant differences were detected between 100 and 500 ($P = 0.0004$) and between 100 and 1000 RBC:EC ratios ($P < 0.0001$), whereas no significant difference was observed between 500 and 1000 RBC:EC ratios ($P > 0.9999$). RBC: red blood cell; iRBCs: infected RBCs; EC: endothelial cell.

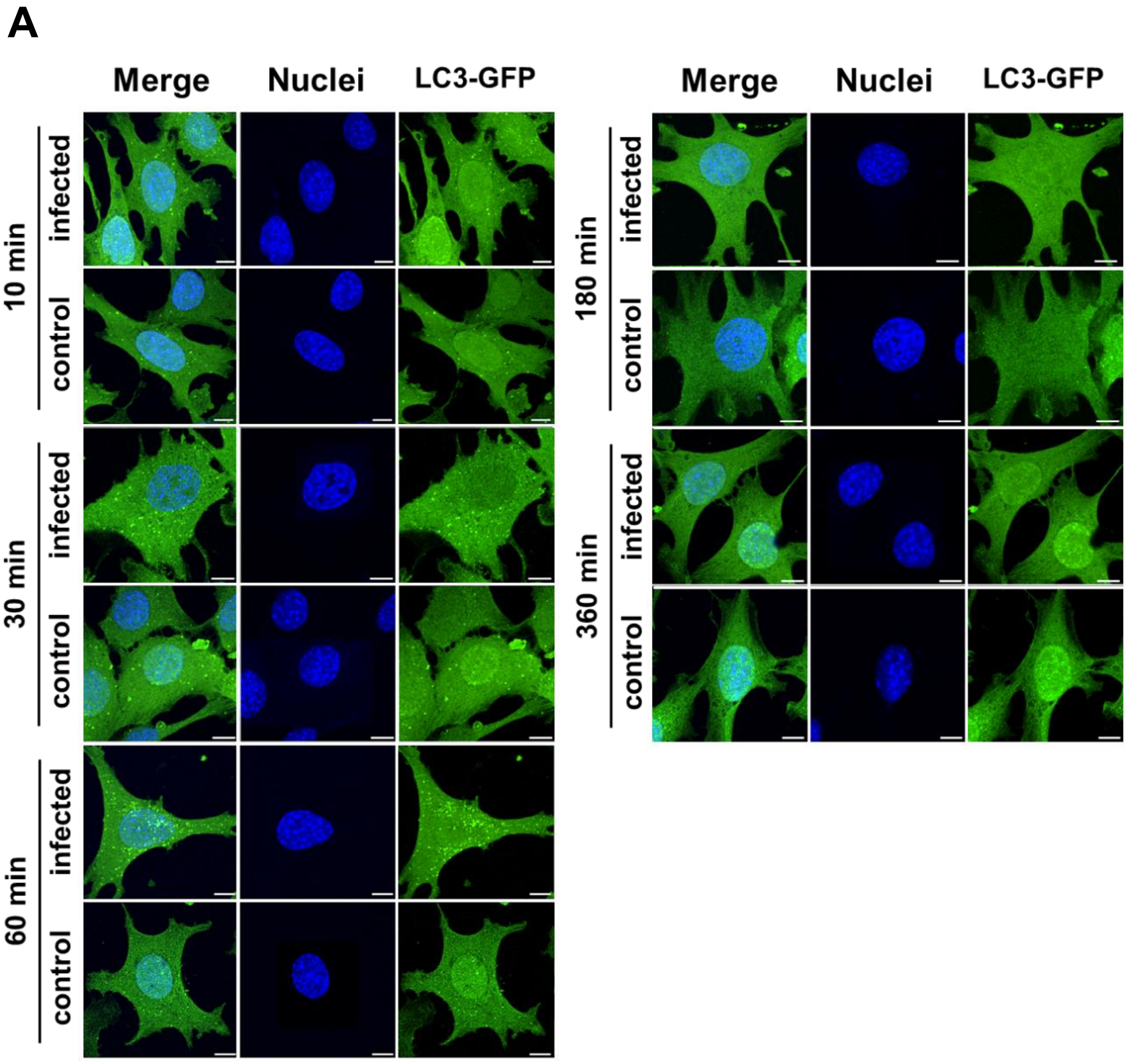

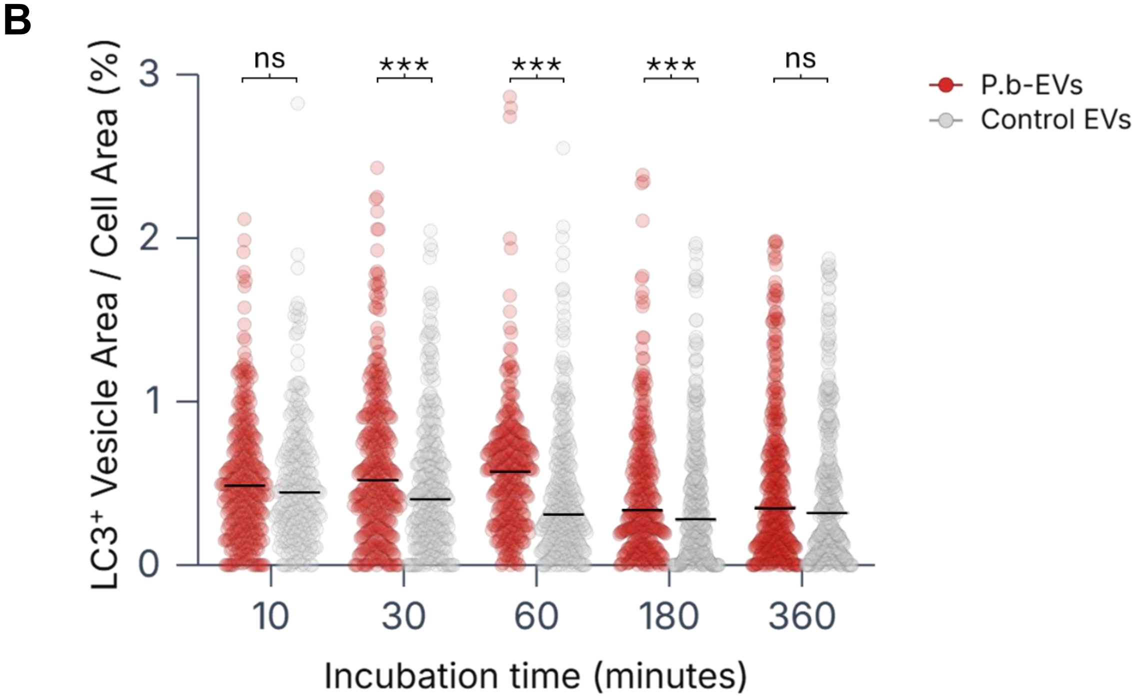

Figure 6.14. Time-course evaluation of LC3 accumulation in LC3-GFP tEnd.1 endothelial cells following incubation with *P. berghei*-derived EVs (*P.b*-EVs). (A) Fluorescence imaging of LC3-GFP tEnd.1 cells after 10, 30, 60, 180, and 360 minutes of exposure to *P.b* derived EVs (50 µg of protein), compared to controls exposed to EVs from control cultures. Nuclei were stained with Hoechst 33342. Scale bars: 10 µm. (B) Spread plots show the percentage of cellular area occupied by LC3-positive vesicles in LC3-GFP tEnd.1 endothelial cells after treatment with different incubation times with *P.b*-EVs and control EVs. Each dot represents an individual cell, and horizontal lines indicate median values. Quantification was performed across three independent experiments, analyzing at least n = 100 cells per condition in total. Statistical analysis was performed using Mann–Whitney U test. Significant differences were observed at 30 minutes ($P = 0.0015$), 60 minutes ($P < 0.0001$) and 180 minutes of incubation ($P = 0.0073$). No statistical differences were found at 10 minutes ($P = 0.4104$) and 360 minutes ($P = 0.1114$). EVs: extracellular vesicles; P.b: *P. berghei*.

Similarly, a dose-dependent effect was assessed by testing two protein concentrations (10 µg and 50 µg) derived from *P. berghei* EVs and their respective controls. The results showed a significant increase in LC3 expression between the two protein concentrations for *P. berghei* EVs, whereas no significant differences were observed among control EVs (Figure 6.15). Taken together, these findings indicate that the condition yielding the strongest LC3 induction in response to EVs was incubation with 50 µg of protein for 60 minutes.

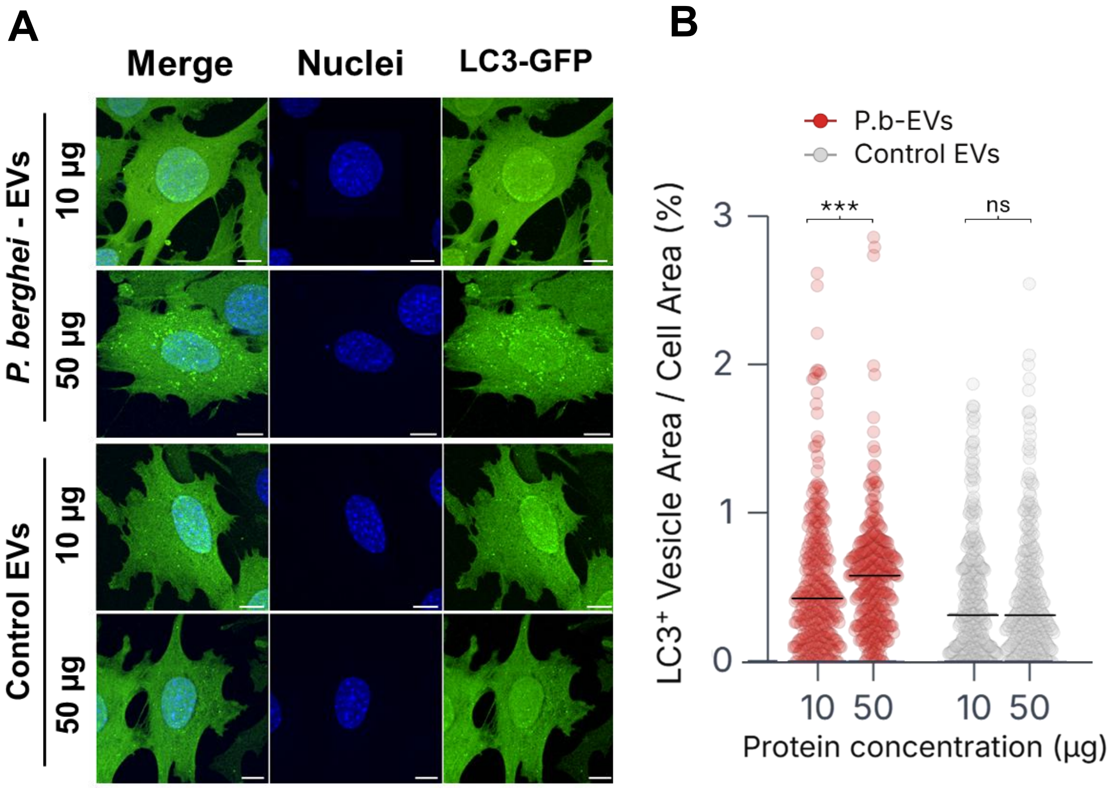

Figure 6.15. Evaluation of the effect of the protein concentration from *P. berghei*-derived EVs (*P.b*-EVs) in LC3-GFP tEnd.1 cells. (A) Fluorescence imaging of LC3-GFP tEnd.1 cells after 60 minutes of exposure to *P. berghei* derived EVs at 10 and 50 µg of protein, compared to controls exposed to EVs from control cultures. Nuclei were stained with Hoechst 33342. Scale bars: 10 µm. (B) Spread plots show the percentage of cellular area occupied by LC3-positiv vesicles in LC3-GFP tEnd.1 endothelial cells after treatment with two protein concentrations o *P.b.*-EVs and control EVs. Each dot represents an individual cell, and horizontal lines indicate median values. Quantification was performed across three independent experiments, analyzing at least n = 100 cells per condition in total. Statistical analysis was performed using Mann–Whitney U test. Significant differences were only observed between both concentrations of protein of *P.b*-EVs ($P = 0.0098$). No statistical differences were found between both concentrations of protein of control EVs ($P = 0.8056$). EVs: extracellular vesicles; P.b: *P. berghei*.

Additionally, the effect of the supernatant obtained after small EV enrichment (EV-reduced supernatant) was evaluated to assess the presence and impact of soluble parasite-derived factors, distinct from EVs, or of smaller vesicles that may not have been removed during ultracentrifugation. Interestingly, a different pattern of LC3 expression was observed, characterized by an oscillatory response in which significant time points alternated with non-significant ones, with the highest LC3 expression after 1 hour of incubation (Figure 6.16).

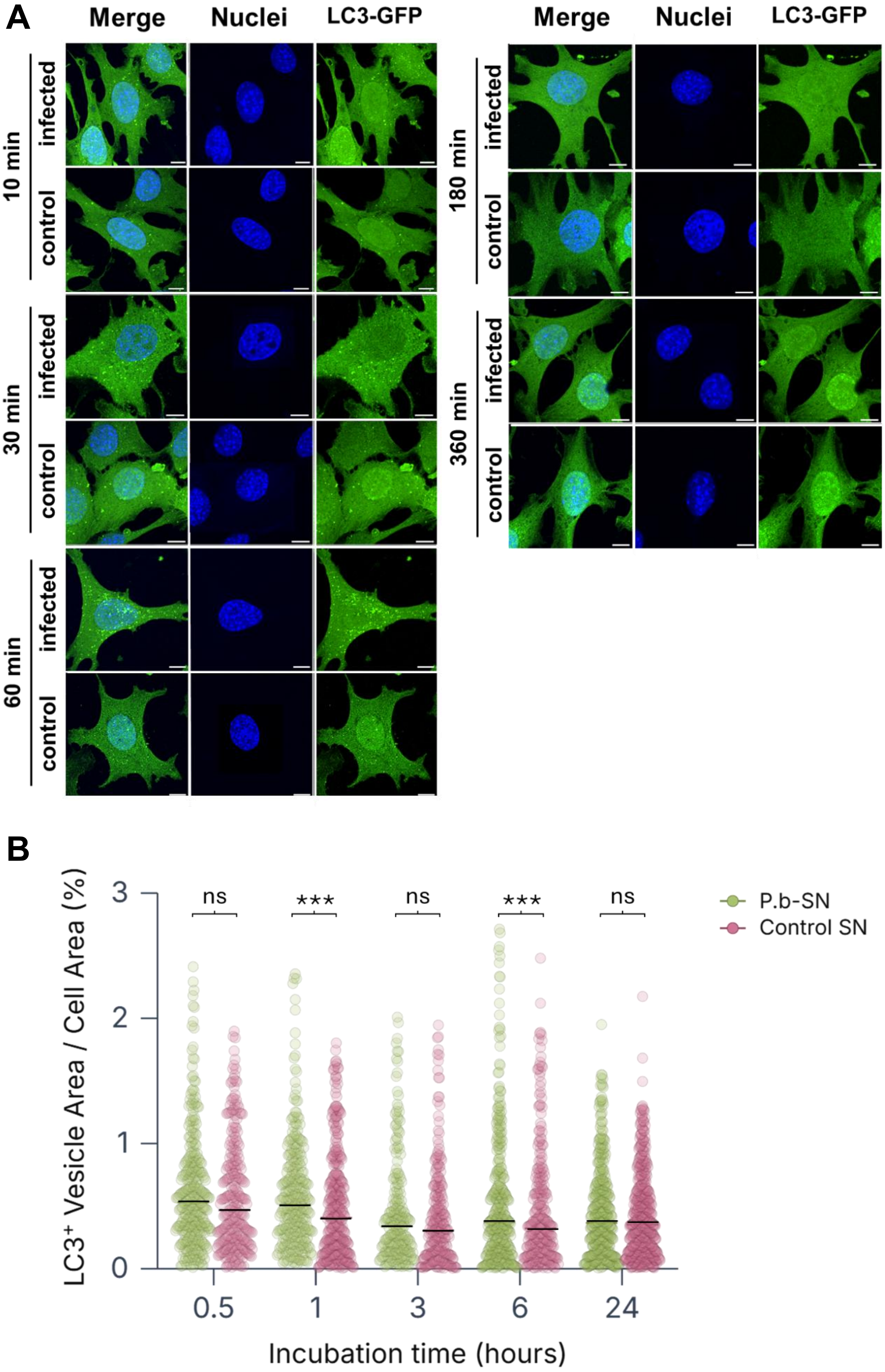
A
Merge
Nuclei
LC3-GFP
10 min
infected
control
30 min
infected
control
60 min
infected
control
180 min
infected
control
360 min
infected
control
B
LC3⁺ Vesicle Area / Cell Area (%)
3
2
1
0
ns
***
ns
***
ns
0.5
1
3
6
24
Incubation time (hours)
P.b-SN
Control SN

Figure 6.16. Time-course evaluation of LC3 accumulation in LC3-GFP tEnd.1 endothelial cells following incubation with *P. berghei*-derived EV-reduced supernatant (*P.b*-SN). (A) Fluorescence imaging of LC3-GFP tEnd.1 cells after 0.5, 1, 3, 6, and 24 hours of exposure to *P. berghei* derived EV-reduced supernatant, compared to EV-reduced supernatant from control cultures. Nuclei were stained with Hoechst 33342. Scale bars: 10 µm. (B) Spread plots show the percentage of cellular area occupied by LC3-positive vesicles in LC3-GFP tEnd.1 endothelial cells after treatment with different incubation times with *P.b*-SN and control SN. Each dot represents an individual cell, and horizontal lines indicate median values. Quantification was performed across three independent experiments, analyzing at least n = 100 cells per condition in total. Statistical analysis was performed using Mann–Whitney U test. Significant differences were observed at 1 hour ($P < 0.0001$), and at 6 hours of incubation ($P = 0.0004$). No statistical differences were found at 0.5 hours ($P = 0.0662$), 3 hours ($P = 0.4993$) or 24 hours ($P = 0.3434$). SN: supernatant; P.b: *P. berghei*.

This oscillatory LC3 expression pattern may be the result of the interaction of multiple factors like parasite derived soluble factors and differences in the glucose composition of the supernatant derived from Jambou medium compared with the medium routinely used for culturing tEnd.1 cells. Because glucose is an important regulator of the autophagy pathway (162), glucose levels were quantified in both media and their respective supernatants using an enzymatic glucose hexokinase assay.

The medium used for tEnd.1 cell culture contained (11.3 ± 0.2) mmol/L glucose, whereas Jambou medium showed a much higher concentration of (31.7 ± 0.7) mmol/L glucose. Although glucose levels decreased in *P. berghei* (24.5 ± 2.2) mmol/L, and control (27.6 ± 1.0) mmol/L supernatants, they remained substantially higher than those in the medium used for the other assays.

Finally, the potential influence of the EV enrichment procedure on the LC3 expression was assessed. For this purpose, two different fractions of the parasite derived culture medium were tested: the crude supernatant, collected prior to ultracentrifugation, and the EV-reduced supernatant, obtained after the EVs enrichment by ultracentrifugation. By comparing these fractions, it was possible to investigate whether the depletion of EVs from the supernatant acted as a determining factor in modulating autophagic activity in tEnd.1 endothelial cells (Figure 6.17).

In both *P. berghei* derived samples and their corresponding controls, no significant differences in LC3 expression were observed between the crude supernatant and the EV-reduced supernatant. These findings indicate that the removal of small EVs during the enrichment procedure did not markedly affect the autophagic response in either condition.

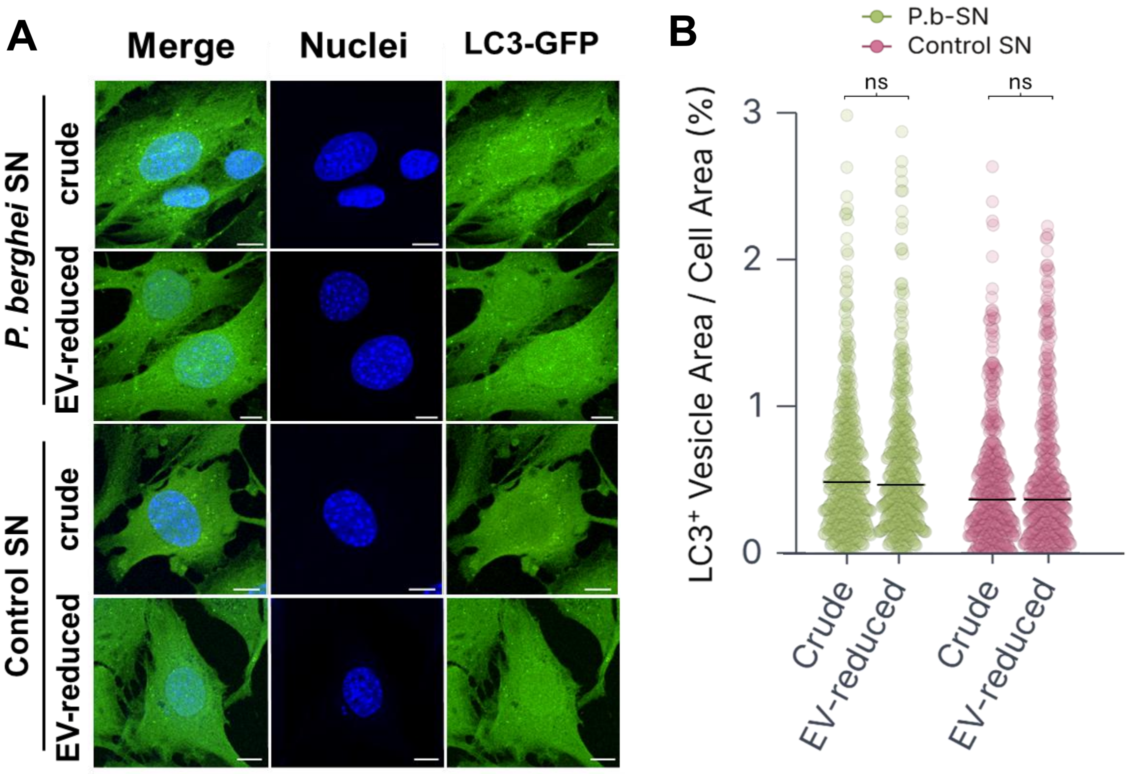

Figure 6.17. Evaluation of the effect in supernatant of the EV enrichment process in LC3-GFP tEnd.1 cells. (A) Fluorescence imaging of LC3-GFP tEnd.1 cells after 60 minutes of exposure to *P. berghei* derived crude and EV-reduced supernatants, compared to controls exposed to those same fractions from control cultures. Nuclei were stained with Hoechst 33342. Scale bars: 10 µm. (B) Spread plots show the percentage of cellular area occupied by LC3-positive vesicles in LC3-GFP tEnd.1 endothelial cells after treatment with two different fractions of *P.b.*-SN and control SN. Quantification was performed across three independent experiments, analyzing at least n = 100 cells per condition in total. Statistical analysis was performed using Mann–Whitney U test. No significant differences were observed between both fractions of control SN (*P* = 0.6488), and *P.b*-SN (*P* = 0.8585). SN: supernatant; EV: extracellular vesicles; P.b: *P. berghei*.

Collectively, the three *P. berghei*-derived stimuli evaluated in this study induced a significant increase in LC3-positive vesicles in endothelial cells in a time- and dose-dependent manner. This effect was consistently observed at defined exposure times and stimulus concentrations, indicating that each stimulus is sufficient to promote an increase of LC3-associated vesicular structures under controlled experimental conditions. However, at this stage it remains unclear whether this increase reflects enhanced autophagosome biogenesis or impaired vesicular degradation due to a defect in autophagic flux.

6.5. tEnd.1 cells display an adequate autophagic flux response when exposed to pharmacological inducers and inhibitors of autophagy

Once the optimal concentrations and incubation times of the different *P. berghei* derived stimuli were established, as those that yielded the highest percentage of cellular area occupied by LC3-positive vesicles, the next step was to characterize the dynamics of the autophagic flux under these conditions.

The aim was to determine if increased LC3 signal resulted from enhanced formation or impaired degradation of autophagosomes. For this, tEnd.1 cells were transfected with a tandem LC3-GFP-mCherry reporter. This tool exploits differential pH sensitivity: GFP is quenched in acidic autolysosomes, while mCherry is stable. Consequently, neutral autophagosomes appear as yellow puncta (GFP+mCherry+), while acidic autolysosomes appear as red-only puncta (mCherry+ only). This distinction allows precise monitoring of autophagic flux (160, 161).

To establish a reliable quantification method, pharmacological treatments (as described in Section 6.4) were applied to design a pipeline for assessing both transfection efficiency and cellular response. Based on this approach, autophagic flux was measured as the ratio of autolysosomes to autophagosomes per cell. Additionally, autophagic flux was quantified as the ratio of autolysosomes to autophagosomes on a per-cell basis. In parallel, the percentage of cellular area occupied by autophagosomes and autolysosomes was also measured, providing complementary spatial information on vesicle distribution and abundance.

Under these conditions, tEnd.1 cells exhibited an appropriate and consistent response to the different treatments used to modulate autophagic flux (Figure 6.18). Autophagy inhibitors, such as chloroquine and bafilomycin, induced a pronounced reduction in autophagic flux, which was reflected by the accumulation of autophagosomes and a relative decrease in autolysosome formation. In contrast, autophagy activators, including rapamycin and nutrient starvation, significantly enhanced autophagic flux, consistent with increased autophagosome formation followed by efficient lysosomal degradation. Meanwhile, treatment with 3-methyladenine did not produce a significant effect in tEnd.1 cells when compared with control conditions.

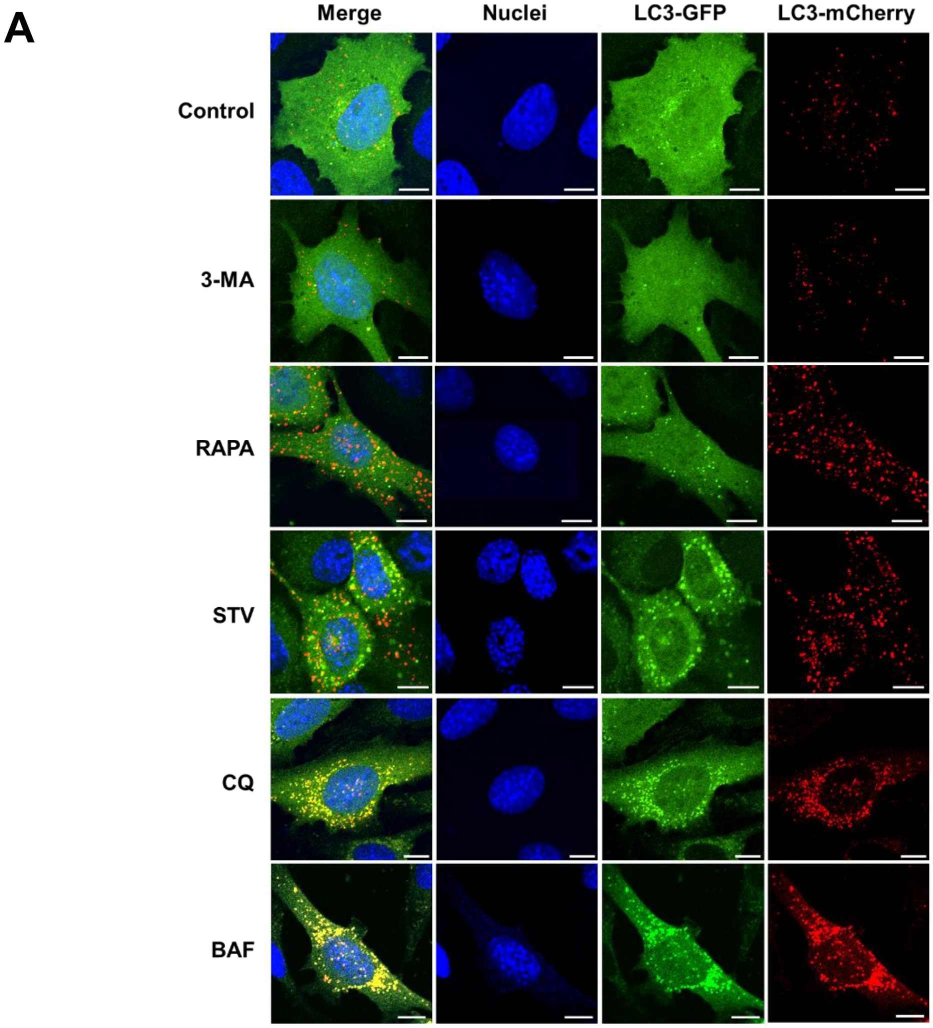
A
Merge
Nuclei
LC3-GFP
LC3-mCherry
Control
3-MA
RAPA
STV
CQ
BAF

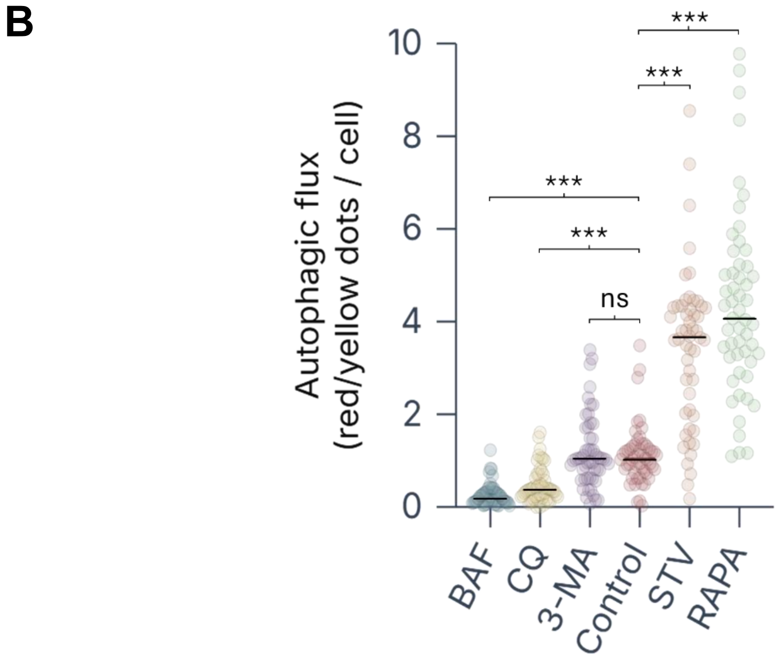
B
Autophagic flux
(red/yellow dots / cell)
0
2
4
6
8
10
BAF
CQ
3-MA
Control
STV
RAPA
***
***
***
***
ns

C

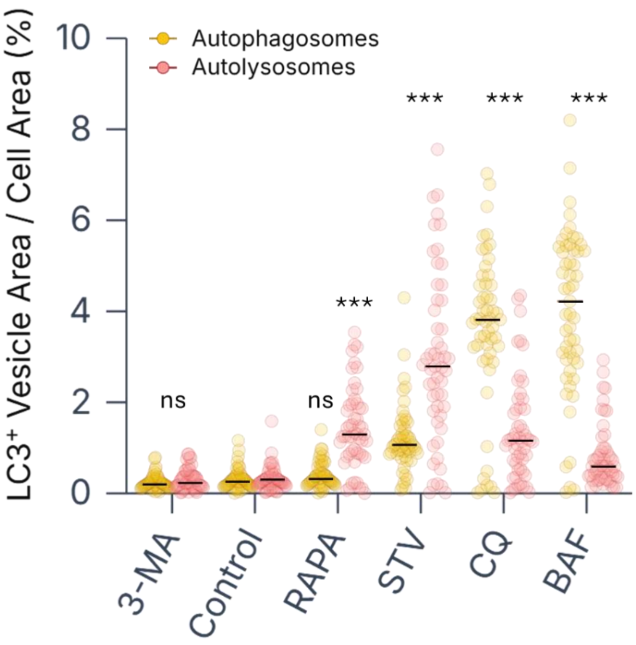

Figure 6.18. Evaluation of the response of LC3-GFP-mCherry transfected tEnd.1 cells after 6-hour exposure to autophagy-related treatments. (A) Fluorescence imaging of LC3-GFP-mCherry transfected tEnd.1 cells after 6 hours of different autophagy-related treatments. Nuclei were stained with Hoechst 33342. Scale bars: 10 µm. (B) Spread plots show the autophagic flux in tEnd.1 cells after 6 hours of different autophagy-modulating treatments, compared to untreated control cells. Each dot represents an individual cell, and horizontal lines indicate median values (n ≥ 50 cells per condition). Statistical analysis was performed using Kruskal–Wallis with Dunn's post hoc test. Significant differences were observed between all treatments and the control ($P < 0.0001$), except for 3-MA ($P > 0.9999$). (C) Spread plots showing the percentage of cellular area occupied by autophagosomes and autolysosomes in tEnd.1 cells after 6 hours of different autophagy-modulating treatments, compared with untreated control cells. Each dot represents an individual cell, and horizontal lines indicate median values (n ≥ 50 cells per condition). Statistical analysis was performed using the Mann–Whitney U test. Significant changes in autophagosome area were observed for all treatments ($P < 0.0001$), except 3-MA and RAPA ($P > 0.9999$). Likewise, autolysosome area differed significantly for all treatments ($P < 0.0001$) except 3-MA ($P > 0.9999$). 3-MA: 3-methyladenine (5 mM); RAPA: rapamycin (10 µM); STV: starvation; CQ: chloroquine (10 µM); BAF: bafilomycin A1 (100 nM).

6.6. *Plasmodium berghei* derived stimuli impair autophagic flux in tEnd.1 endothelial cells

In this section, the stimuli were tested using the concentrations and incubation times previously optimized in Section 6.4. For each stimulus, a single concentration and three time points were evaluated: the time at which the highest LC3 expression had been observed, along with one earlier and one later time point.

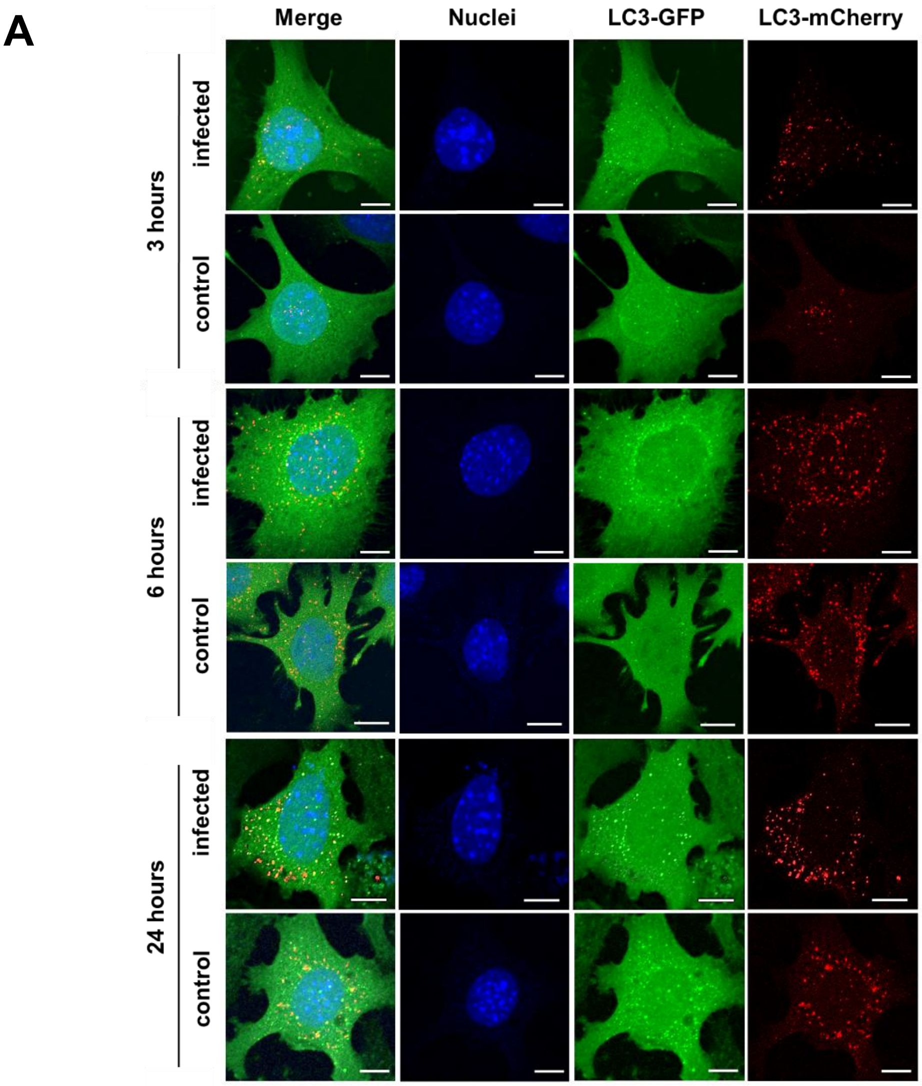
A
Merge
Nuclei
LC3-GFP
LC3-mCherry
3 hours
infected
control
6 hours
infected
control
24 hours
infected
control

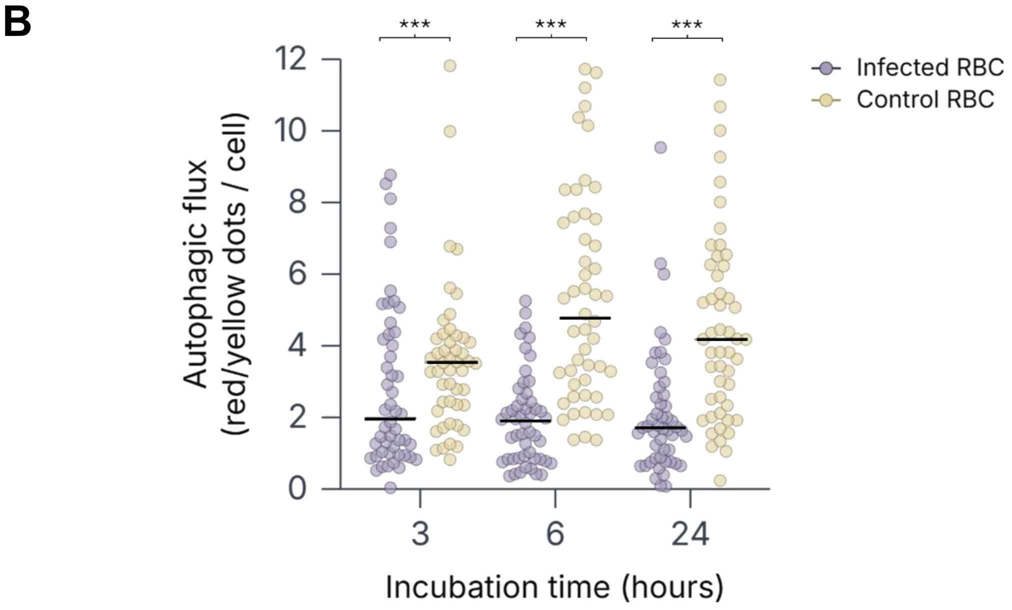
B
***
***
***
Autophagic flux
(red/yellow dots / cell)
0
2
4
6
8
10
12
3
6
24
Incubation time (hours)
Infected RBC
Control RBC

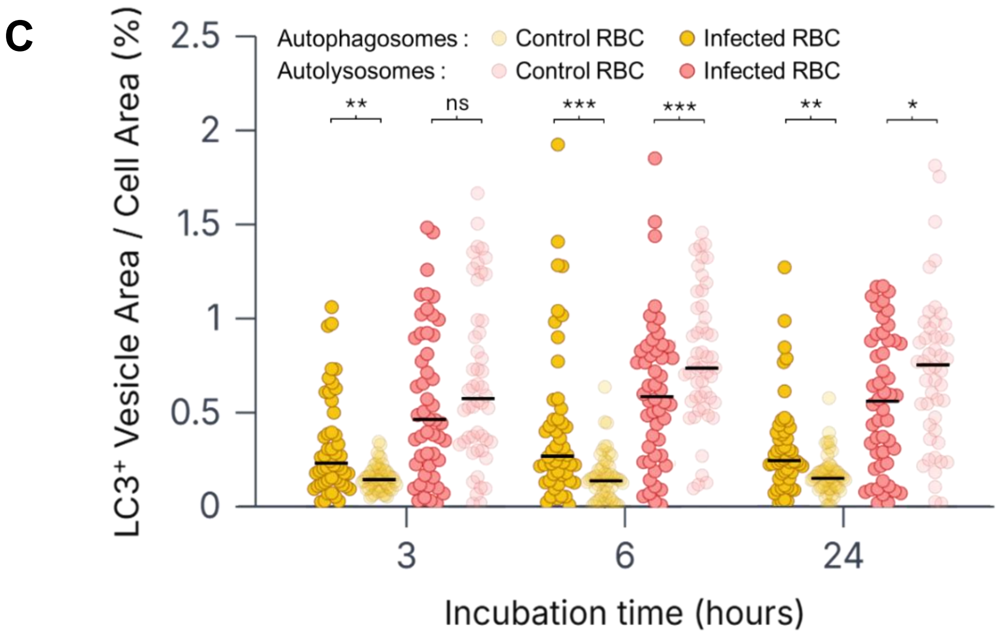

Figure 6.19. Evaluation of the response of LC3-GFP-mCherry transfected tEnd.1 cells following incubation with *P. berghei* infected RBCs. (A) Fluorescence imaging of LC3–GFP–mCherry–expressing tEnd.1 endothelial cells after 3, 6, and 24 hours of exposure to *P. berghei* iRBCs (500 iRBCs/cell) or to non-infected RBC controls. Nuclei were stained with Hoechst 33342. Scale bar: 10 µm. (B) Quantification of autophagic flux in tEnd.1 cells exposed to iRBCs across the three incubation times. Each dot represents an individual cell, and horizontal lines indicate median values (n ≥ 50 cells per condition). Statistical analysis with Mann–Whitney U test showed a significant reduction in autophagic flux at all time points: 3 h (P = 0.0072), 6 h (P < 0.0001), and 24 h (P < 0.0001). (C) Quantification of the percentage of cellular area occupied by autophagosomes and autolysosomes in tEnd.1 cells exposed to iRBCs across the three incubation times. Each dot represents one cell, with median values indicated (n ≥ 50 cells/condition). Autophagosome area significantly increased in iRBC-treated cells at 3 h (P = 0.0007), 6 h (P < 0.0001), and 24 h (P = 0.0005). Autolysosome area differed significantly between iRBC and control treatments at 6 h (P < 0.0001) and 24 h (P = 0.0472), but not at 3 h (P = 0.2523). RBC: red blood cell; iRBC: infected red blood cell.

The effect of a 500 iRBC/EC ratio was evaluated across the three incubation times previously tested (Figure 6.19). At all time points, cells exposed to *P. berghei* iRBCs showed lower autophagic flux than cells treated with control RBCs. The autophagic flux induced by iRBCs remained relatively unchanged at 3, 6, and 24 hours, whereas control RBCs produced a time-dependent increase, with higher values at 6 and 24 hours compared with 3 hours (Figure 6.19B).

Analysis of vesicle composition revealed distinct patterns in autophagy progression. Exposure to iRBCs resulted in an accumulation of LC3-positive autophagosomes and a reduction in autolysosome area at all incubation times. A slight peak in autophagosome accumulation was detected at 6 hours. In contrast, control RBCs maintained a stable autophagosome area over time and promoted an increase in autolysosome area at later time points (Figure 6.19C).

Next, the effect of 50 µg of protein from EVs was assessed (Figure 6.20). EVs from *P. berghei* induced a pronounced reduction in autophagic flux across all incubation times, with the greatest decrease observed after 1 hour. Control EVs from RBC cultures produced a progressive increase in autophagic flux over time (Figure 6.20B).

Vesicle distribution analysis showed increased autophagosome area and reduced autolysosome area at all time points following incubation with *P. berghei* EVs. The highest autophagosome accumulation was observed at 1 hour, while autolysosome area remained similar across time points. In contrast, control EVs produced a peak in autophagosome area at 0.5 hours that subsequently declined, whereas autolysosome area increased over time (Figure 6.20C).

Finally, the effect of *P. berghei* supernatant was evaluated (Figure 6.21). A reduction in autophagic flux was observed at 1 and 3 hours of incubation, although the degree of this decrease was less pronounced than that produced by the other stimuli tested. In contrast, control supernatant induced a slight increase in autophagic flux at 0.5 hours and remained stable at subsequent time points (Figure 6.21B).

Vesicle distribution analysis revealed a different pattern compared with the previous stimuli. No significant differences were found in autophagosome areas at 0.5 h and 3 h between *P. berghei* supernatant and control. A slight peak in autophagosome accumulation was observed at 1 hour of incubation. Autolysosome area increased after 0.5 hour of incubation in both *P. berghei* and control, and there was no difference between both conditions at 0.5 hour incubation (Figure 6.21C).

Taken together, these results are consistent with those reported in Section 6.4, where a time-dependent peak in LC3 expression was observed. The combined analyses showing reduced autophagic flux, increased autophagosome area, and decreased autolysosome area suggest that this pattern reflects impaired autophagic flux with autophagosome accumulation, rather than a stimulation of autophagy.

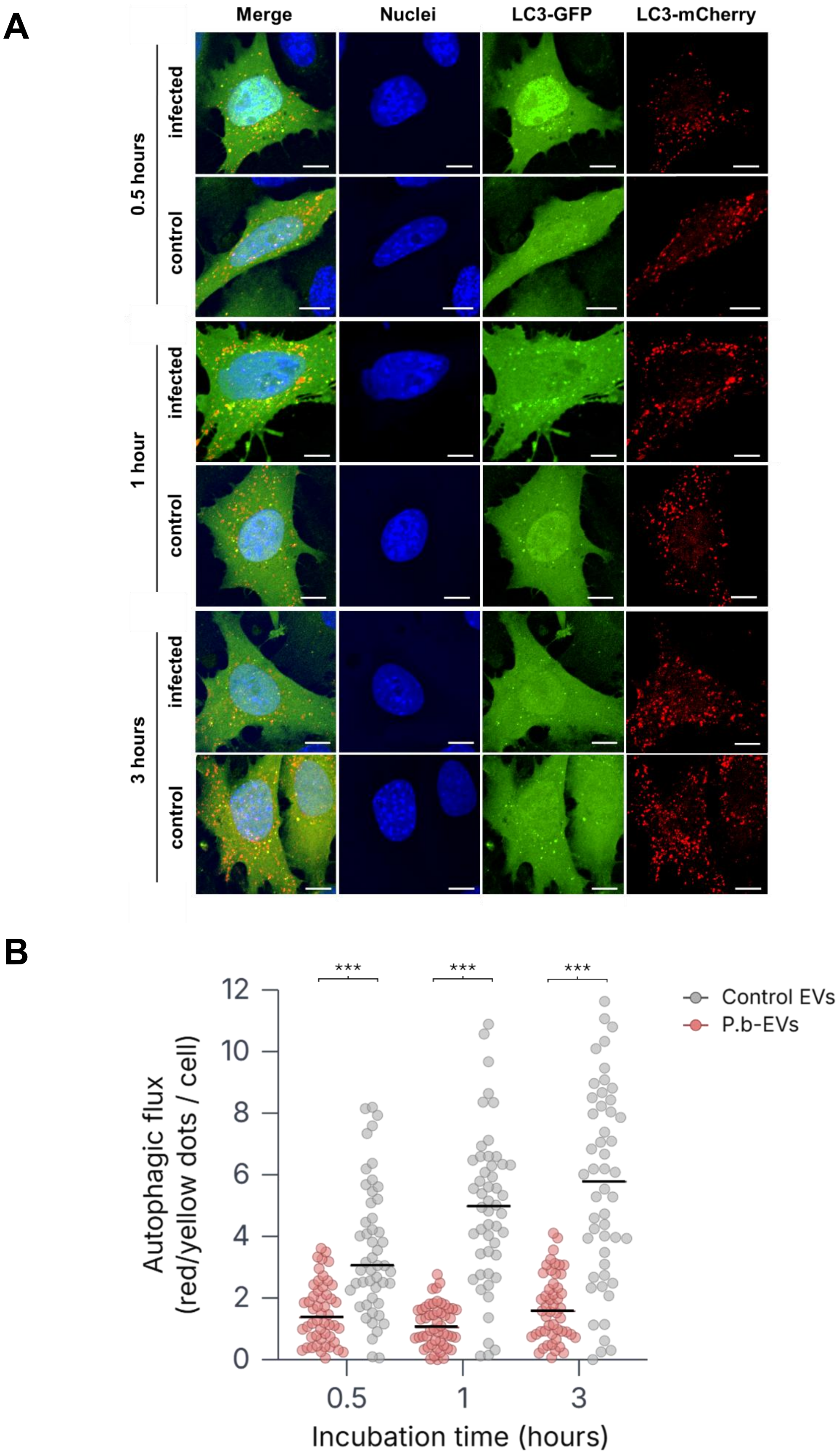
A
Merge
Nuclei
LC3-GFP
LC3-mCherry
0.5 hours
infected
control
1 hour
infected
control
3 hours
infected
control
B
***
***
***
Autophagic flux
(red/yellow dots / cell)
0
2
4
6
8
10
12
0.5
1
3
Incubation time (hours)
Control EVs
P.b-EVs

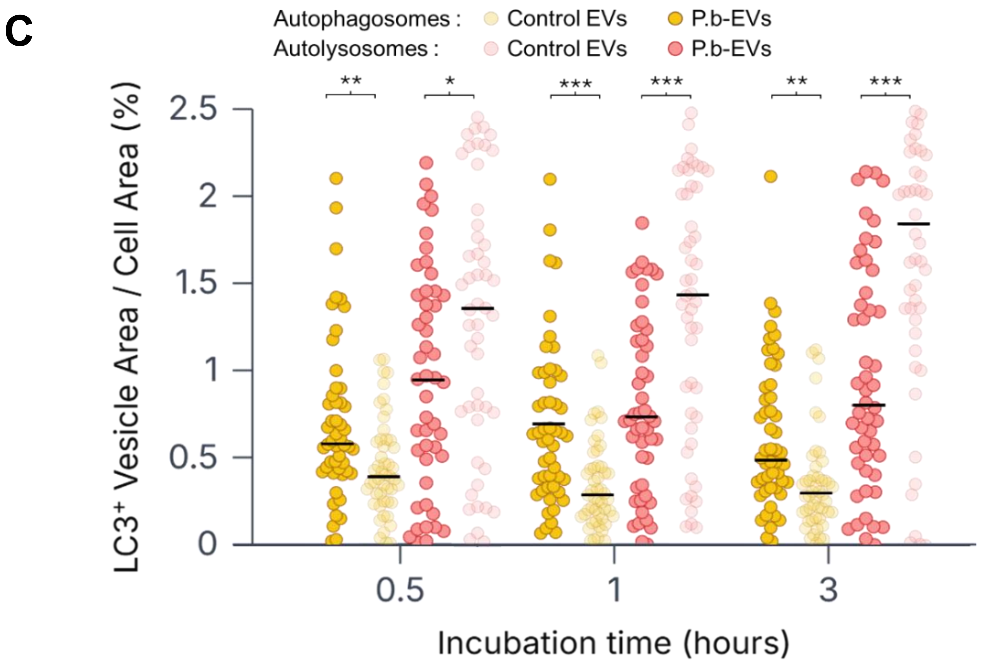

Figure 6.20. Evaluation of the response of LC3-GFP-mCherry transfected tEnd.1 cells following incubation with *P. berghei* EVs (*P.b*-EVs). (A) Fluorescence imaging of LC3–GFP–mCherry–expressing tEnd.1 endothelial cells after 0.5, 1, and 3 hours of exposure to *P. berghei* EVs (50 µg of protein) or to control EVs. Nuclei were stained with Hoechst 33342. Scale bar: 10 µm. (B) Quantification of autophagic flux in tEnd.1 cells exposed to *P.b*-EVs across the three incubation times. Each dot represents an individual cell, and horizontal lines indicate median values (n = 50 cells per condition). Statistical analysis with Mann–Whitney U test showed a significant reduction in autophagic flux at all time points: 0.5 h ($P < 0.0001$), 1 h ($P < 0.0001$), and 3 h ($P < 0.0001$). (C) Quantification of the percentage of cellular area occupied by autophagosomes and autolysosomes in tEnd.1 cells exposed to *P.b*-EVs across the three incubation times. Each dot represents one cell, with median values indicated (n = 50 cells/condition). Autophagosome area significantly increased in *P.b*-EVs treated cells at 0.5 h ($P = 0.0030$), 1 h ($P < 0.0001$), and 3 h ($P = 0.0015$). Likewise, autolysosome area differed significantly between *P.b*-EVs and control treatments at 0.5 h ($P = 0.0354$), 1 h ($P < 0.0001$), and 3 h ($P < 0.0001$). EVs: extracellular vesicles; *P.b*-EVs: *P. berghei*'s EVs.

As observed previously in the LC3-GFP cell line, iRBCs and *P.b*-EVs produced significant differences at the same incubation times evaluated in this section, both in autophagic flux and in LC3-positive area corresponding to autophagosomes (Figures 6.12 and 6.14). For *P.b*-SN, differences in autophagosome area were detected only at the 1-hour time point, consistent with the oscillating pattern shown in Figure 6.16. Together these findings support that the cellular responses to the different pharmacological and biological stimuli are comparable across the two genetically manipulated cell lines.

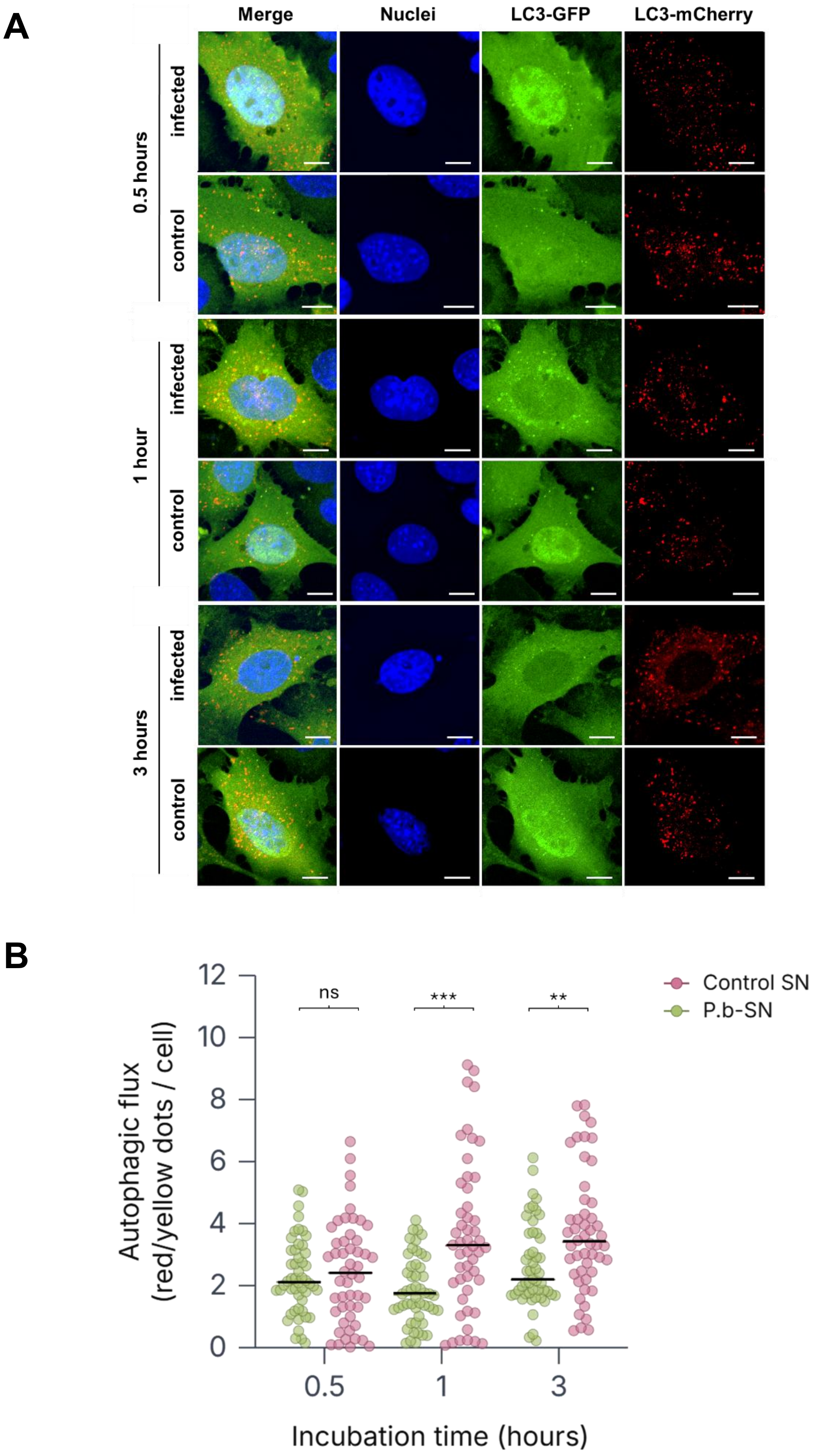
A
Merge
Nuclei
LC3-GFP
LC3-mCherry
0.5 hours
infected
control
1 hour
infected
control
3 hours
infected
control
B
Autophagic flux
(red/yellow dots / cell)
12
10
8
6
4
2
0
ns
***
**
0.5
1
3
Incubation time (hours)
Control SN
P.b-SN

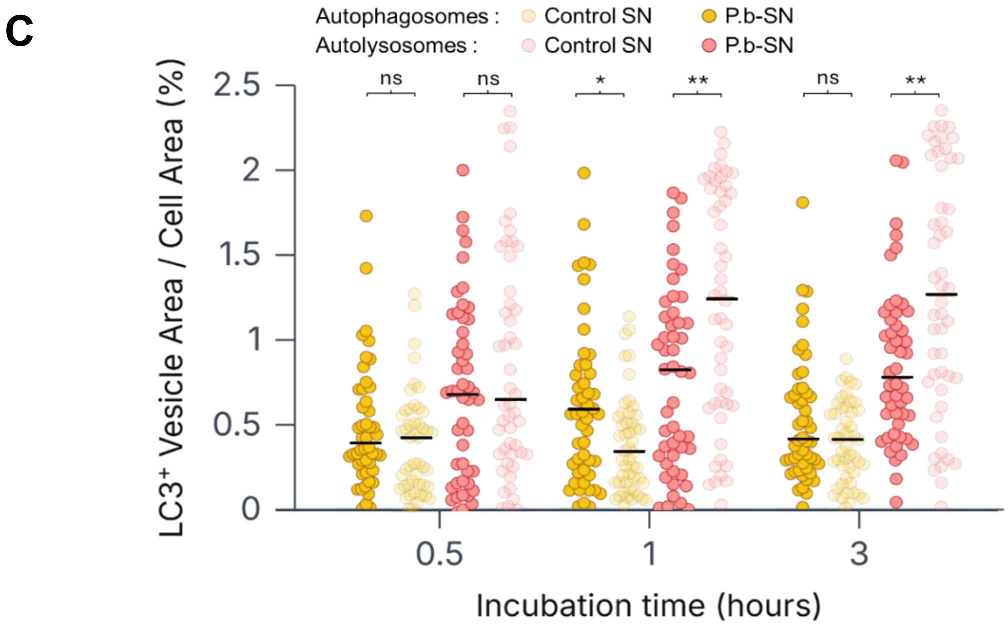

Figure 6.21. Evaluation of the response of LC3-GFP-mCherry transfected tEnd.1 cells following incubation with *P. berghei* supernatant (*P.b*-SN). (A) Fluorescence imaging of LC3–GFP–mCherry–expressing tEnd.1 endothelial cells after 0.5, 1, and 3 hours of exposure to *P. berghei* SN or to control SN. Nuclei were stained with Hoechst 33342. Scale bar: 10 µm. (B) Quantification of autophagic flux in tEnd.1 cells exposed to *P.b*-SN across the three incubation times. Each dot represents an individual cell, and horizontal lines indicate median values (n = 50 cells per condition). Statistical analysis with Mann–Whitney U test showed a significant reduction in autophagic flux at 1 h ($P < 0.0001$), and 3 h ($P = 0.0027$), while no difference was found at 0.5 h ($P = 0.8022$). (C) Quantification of the percentage of cellular area occupied by autophagosomes and autolysosomes in tEnd.1 cells exposed to *P.b*-SN across the three incubation times. Each dot represents one cell, with median values indicated (n = 50 cells/condition). Autophagosome area significantly increased in *P.b*-SN treated cells only at 1 h ($P < 0.0001$), and no differences were found at 0.5 h ($P = 0.3773$) and 3 h ($P = 0.2609$). Autolysosome area differed significantly between *P.b*-SN and control treatments at 1 h ($P = 0.0022$), and 3 h ($P = 0.0039$), but not at 0.5 h ($P = 0.4117$). SN: supernatant; *P.b*-SN: *P. berghei*'s SN.

Overall, the *P. berghei*-derived stimuli showed similar effects on autophagic flux and LC3 vesicle distribution, but with distinct kinetics. iRBC exposure caused a delayed but sustained reduction in autophagic flux. In contrast, *P. berghei*-derived EVs elicited an early and strong response, marked by a rapid decrease in autophagic flux. Treatment with *P. berghei* supernatant also induced an early but more modest response. In parallel, control conditions displayed a linear increase in autophagic flux over time, consistent with basal autophagy progression under the experimental settings.

6.7. Physical characterization of small extracellular vesicles produced by *P. berghei in vitro* show heterogenous size subpopulations

The physical properties of EV-enriched fraction obtained from both parasite-infected cultures and control EVs from non-infected RBCs cultures were evaluated. Parameters such as size, particle concentration, and zeta potential were determined using Dynamic Light Scattering (DLS).

In both experimental groups, three distinct populations of extracellular vesicles were detected, with approximate diameters of 25 nm, 100 nm, and 400 nm. Among these, the vesicles around 100 nm constituted the predominant population in terms of signal intensity, representing approximately 70% of the total (Figure 6.22A). Nevertheless, the 25 nm vesicle population exhibited the highest particle concentration per milliliter (Figure 6.22B). Based on the overall distribution, the mean hydrodynamic size of EVs isolated from *P. berghei* cultures was calculated as 103 ± 12 nm, whereas EVs obtained from the control RBC cultures showed a size of 104 ± 17 nm.

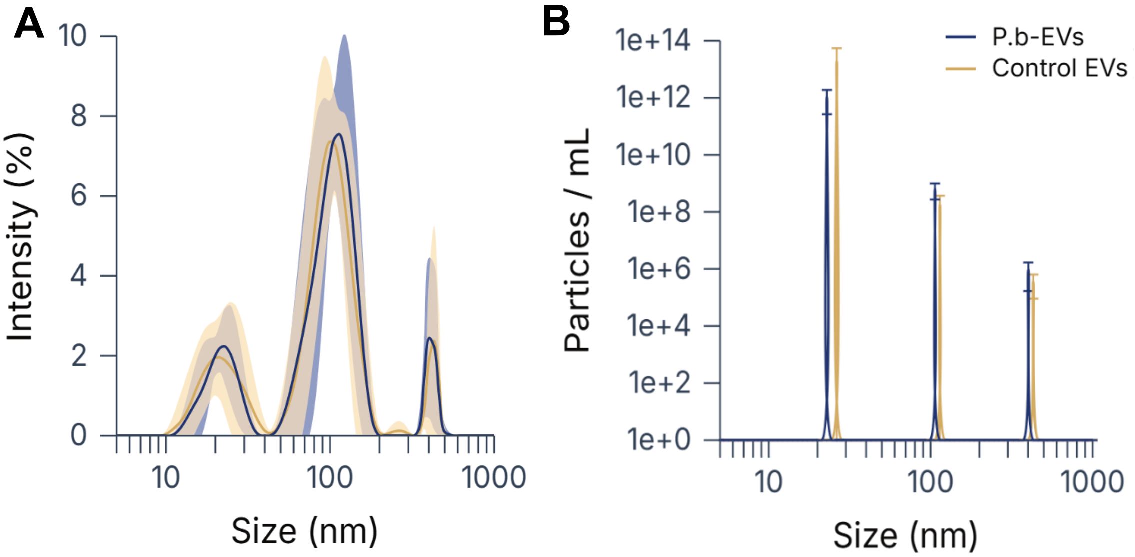

Figure 6.22. Physical characterization of EVs produced by *P. berghei* (*P.b*-EVs) and RBCs cultures (control EVs) using DLS. (A) Distribution of particle populations; the line represents the average signal intensity across different sizes, while the shaded area corresponds to the respective standard deviation. (B) Quantification of particle concentration (particles/mL) for the three identified subpopulations, showing mean values and standard deviations. A total of n = 3 independent EVs preparations obtained from separate cultures were analyzed for each condition, with each sample measured in triplicate.

The polydispersity index (PDI) indicated a heterogeneous EV size distribution. In general, PDI values approaching zero reflect a highly monodisperse population, whereas values closer to unity indicate increasing polydispersity. Both conditions exhibited relatively high PDI values, consistent with substantial heterogeneity in vesicle size distribution (Figure 6.22). In addition, the zeta potential measurements revealed values close to −12 mV for both groups, which points to a low colloidal stability of the vesicle suspensions under the experimental conditions (Table 6.1). No statistically significant differences were observed in these parameters between the two conditions.

Table 6.1. Physical characterization of EVs produced by *P. berghei* (*P.b*-EVs) and RBCs cultures (control EVs) using DLS. Data corresponds to the mean ± standard deviation of n = 3 independent samples, each measured in triplicate. *P*-values were calculated using an unpaired two-tailed Student's t-test to compare parameters between the two experimental groups.

Parameter	***P.b*-EVs**	**Control EVs**	***P*-value**
Size (nm)	103 ± 12	104 ± 17	0.9377
Intensity area (%)	73 ± 7	72 ± 6	0.8601
Polydispersity index	0.56 ± 0.07	0.46 ± 0.06	0.1335
Zeta potential (mV)	−12.2 ± 0.9	−12.55 ± 0.04	0.5379

To provide direct morphological characterization of the isolated vesicles, air-dried samples adsorbed onto freshly cleaved mica were analyzed by Atomic Force Microscopy (AFM) operated in tapping mode under ambient conditions. This high-resolution technique enabled the visualization of individual small EVs at the nanoscale, offering a crucial complement to the ensemble-average size data obtained by DLS.

Representative AFM images are presented in Figure 6.23. The low-magnification topographical map (Figure 6.23A) reveals a heterogeneous population of discrete, spherical nanoparticles deposited across the substrate, alongside occasional aggregates and residual debris. Subsequent higher-magnification analysis, including a three-dimensional topographical rendering (Figure 6.23B) and a corresponding high-resolution height image (Figure 6.23C), confirms the vesicular morphology and allows for the clear resolution of individual particles.

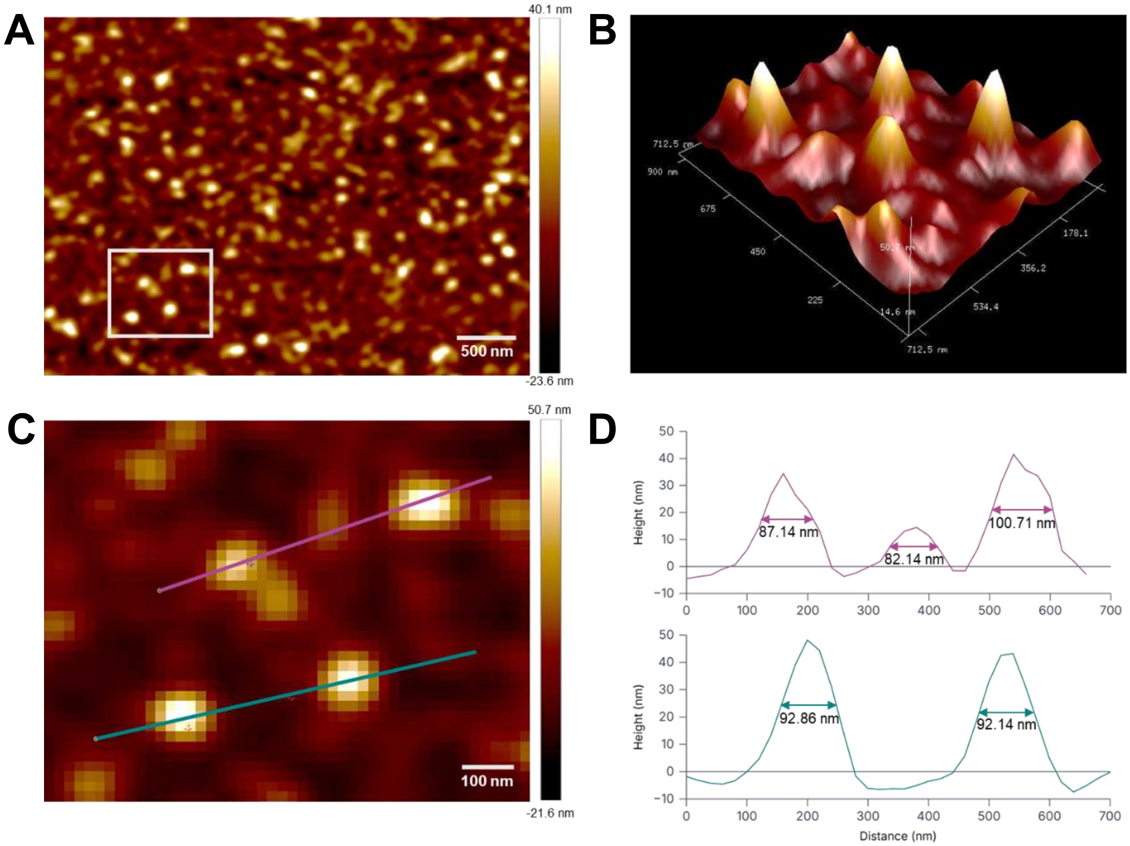

Figure 6.23. Atomic force microscopy (AFM) imaging of small extracellular vesicles derived from a *Plasmodium berghei* culture. (A) Representative low-pass filtered AFM height image depicting a heterogeneous population of spherical nanoparticles isolated from *P. berghei* culture supernatant. (B, C) Higher-magnification views of the region of interest outlined in (A). (B) Three-dimensional topographical rendering of the corresponding AFM height data. (C) High-magnification AFM height image resolving individual extracellular vesicles. (D) Representative cross-sectional height profiles extracted from the line scans marked in (C). Each profile corresponds to an isolated vesicle, with horizontal arrows indicating the full width at half maximum (FWHM) for each peak.

The size of EVs was primarily determined from AFM height measurements of air-dried samples, which are less affected by tip convolution than lateral dimensions. The measured vesicle heights ranged from approximately 14 to 49 nm (Figure 6.23D). In addition, apparent lateral dimensions were estimated from the full width at half maximum (FWHM) of height profiles to provide a comparative measure of vesicle spread and interaction with the substrate (163). These FWHM values for the representative vesicles shown ranged from approximately 82 to 100 nm. The lateral dimensions are consistently larger than the heights, which is expected due to the combined effects of tip-sample convolution and the lateral deformation or flattening of soft vesicles upon adsorption and drying on the solid support (163, 164).

6.8. Proteomic characterization reveals diverse biological functions and subcellular origins of small extracellular vesicles produced by *P. berghei in vitro*

Following physical characterization, protein profiling of the EV-enriched fraction was performed. It should be noted that this approach primarily allows the detection of abundant, soluble proteins and is less suitable for the resolution of low-abundance or transmembrane proteins, which are often underrepresented. SDS-PAGE was carried out on 10% acrylamide gels, and the proteins were visualized using different staining methods, including Coomassie Blue R-250 (Figure 6.24A) and silver staining (Figure 6.24B). Each lane was loaded with 5 µg of protein from either the EV preparations or the corresponding EV-reduced culture supernatants (SN) from which the EVs had been enriched, in order to compare banding patterns between sample types (EVs vs SN) and between experimental conditions (*P. berghei* vs control).

The gel images revealed clear differences in the banding patterns between the two sample types. In Figure 6.24A, bands around ~95 kDa were observed exclusively in the EV lanes and were absent in the corresponding SN lanes. In addition, a higher band density was detected in the EV lanes in the upper region of the gel (>170 kDa). A faint band between 26 and 34 kDa was also visible in the EV lanes but not in the SN.

Similarly, in Figure 6.24B, the ~95 kDa band was again detected exclusively in the EV samples. Marked differences were also observed in the lower molecular weight region (17-34 kDa). Three bands were present in the control EV lane but were absent in the corresponding supernatant lane. In contrast, the *P. berghei* EV lane displayed a single prominent band at approximately 34 kDa, while the bands at 17 and 25 kDa were faint or not clearly detectable.

Collectively, the distinct protein profiles observed between EV fractions and their paired supernatant samples support the effective enrichment of vesicle-associated proteins. However, no clear qualitative differences were detected between control and *P. berghei*-derived EVs, suggesting the need for more sensitive analytical techniques to accurately identify potential differences in their protein composition.

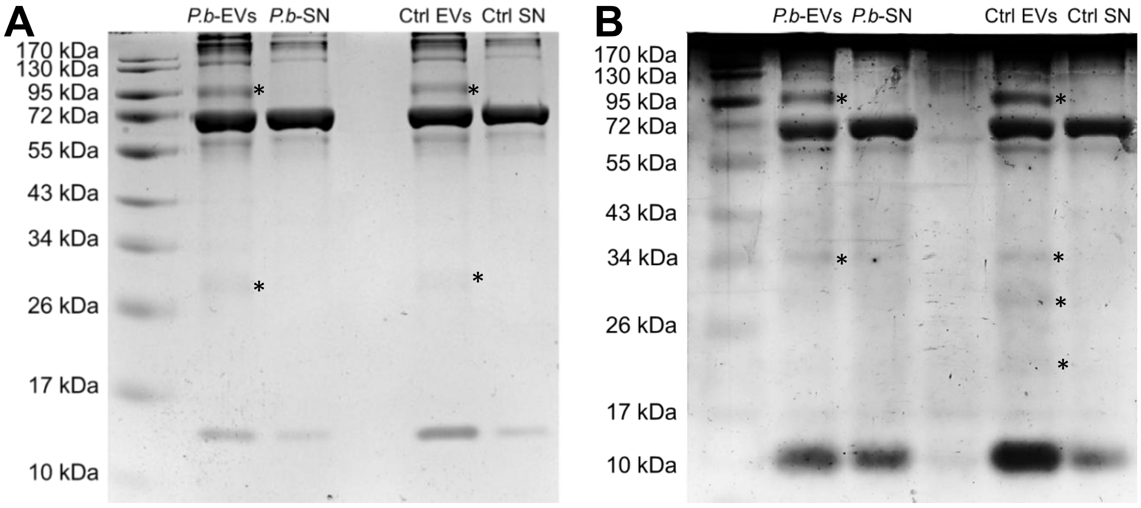

Figure 6.24. Electrophoretic SDS-PAGE protein profile of EVs and EV-reduced supernatants (SN) from *P. berghei* (*P.b*) and RBCs cultures (Ctrl). (A) Coomassie blue and (B) silver stains showing distinct banding patterns between sample types. Asterisks (*) indicate protein bands detected in the EV lanes but absent in their corresponding SN lanes. For both staining methods, 5 µg of protein per sample were loaded onto the gels.

Furthermore, proteomic profiling of the enriched small EV fraction was undertaken to identify their protein cargo and infer their subcellular origins in the parasite. This analysis identified 60 proteins from *P. berghei* in the small EV fraction. In contrast, only 14 proteins were detected in the EV-depleted supernatant. Notably, the majority of supernatant proteins (12 out of 14) overlapped with those identified in the small EVs (Figure 6.25A). The complete list of identified *P. berghei* proteins found in small EVs and in its corresponding EV-reduced supernatant is provided in Table 6.2 and Table 6.3, respectively.

Conversely, the proteomic cargo was prominently composed of RBC-derived proteins. A total of 99 *Mus musculus* proteins were identified in the EV fraction, compared to 32 in the corresponding EV-reduced supernatant, with 26 proteins shared between both fractions. Key identifications comprised major cytosolic components (e.g., hemoglobin, carbonic anhydrase, heat shock proteins), integral membrane proteins (e.g., Band 3), and cytoskeletal elements (e.g., spectrin, ankyrin, actin) consistent with previous reports (165–167) (Table S.1).

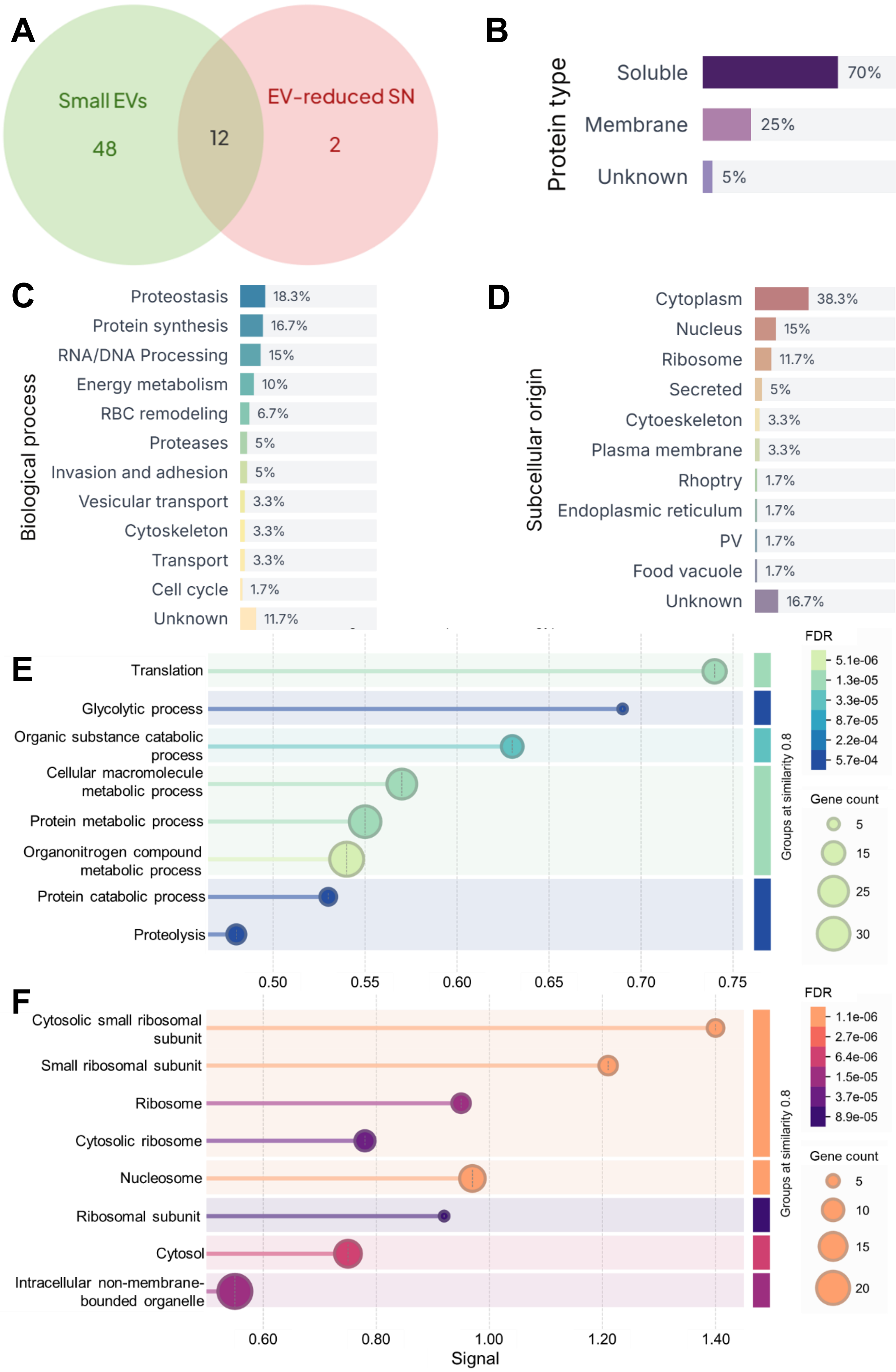
A
Small EVs
48
12
EV-reduced SN
2
B
Protein type
Soluble 70%
Membrane 25%
Unknown 5%
C
Biological process
Proteostasis 18.3%
Protein synthesis 16.7%
RNA/DNA Processing 15%
Energy metabolism 10%
RBC remodeling 6.7%
Proteases 5%
Invasion and adhesion 5%
Vesicular transport 3.3%
Cytoskeleton 3.3%
Transport 3.3%
Cell cycle 1.7%
Unknown 11.7%
D
Subcellular origin
Cytoplasm 38.3%
Nucleus 15%
Ribosome 11.7%
Secreted 5%
Cytoskeleton 3.3%
Plasma membrane 3.3%
Rhoptry 1.7%
Endoplasmic reticulum 1.7%
PV 1.7%
Food vacuole 1.7%
Unknown 16.7%
E
Translation
Glycolytic process
Organic substance catabolic process
Cellular macromolecule metabolic process
Protein metabolic process
Organonitrogen compound metabolic process
Protein catabolic process
Proteolysis
0.50
0.55
0.60
0.65
0.70
0.75
Groups at similarity 0.8
FDR
5.1e-06
1.3e-05
3.3e-05
8.7e-05
2.2e-04
5.7e-04
Gene count
5
15
25
30
F
Cytosolic small ribosomal subunit
Small ribosomal subunit
Ribosome
Cytosolic ribosome
Nucleosome
Ribosomal subunit
Cytosol
Intracellular non-membrane-bounded organelle
0.60
0.80
1.00
1.20
1.40
Signal
Groups at similarity 0.8
FDR
1.1e-06
2.7e-06
6.4e-06
1.5e-05
3.7e-05
8.9e-05
Gene count
5
10
15
20

Figure 6.25. Proteomic profiling of small extracellular vesicles produced by *P. berghei in vitro*. (A) Venn diagram showing the distribution of *P. berghei* proteins identified in the enriched small EV fraction and their respective EV-reduced supernatant (SN). A total of 60 parasite proteins were identified in the EV fraction, of which 48 were unique to this fraction. (B-D) Classification of the 60 *P. berghei* proteins identified in the small EV fraction based on UniProt annotations. Proteins are categorized by (B) their association with membranes, (C) their primary biological process, and (D) their predicted subcellular origin within the parasite. (E, F) Gene Ontology (GO) enrichment analysis for (E) Biological Process and (F) Cellular Component categories. Enrichment analysis was performed using the STRING database (version 12.0), and the eight GO terms with the highest signal values meeting the significance threshold (FDR < 0.01) are shown. PV: parasitophorous vacuole.

The 60 *P. berghei* proteins identified in the small EVs were classified by their physicochemical properties and biological functions to delineate the nature of the vesicular cargo. Based on their association with cellular membranes, the majority of proteins (70%) were soluble, with membrane-associated proteins constituting 25% and 5% remaining unclassified (Figure 6.25B).

Functional categorization, based on UniProt annotations, revealed a diverse proteome with representants of core cellular processes. The largest functional groups were involved in proteostasis (e.g., chaperones, proteasome subunits), protein synthesis (e.g., ribosomal proteins, elongation factors), and nucleic acid processing (e.g., histones, RNA-binding proteins). Central energy metabolism (e.g., glycolytic enzymes) was also present. Importantly, proteins with direct roles in pathogenesis were identified, including those involved in host cell invasion and adhesion and RBC remodeling. A substantial proportion (11.7%) of proteins had no annotated function (Figure 6.25C).

Supporting this functional profile, Gene Ontology (GO) enrichment analysis of the EV-associated proteins confirmed a significant overrepresentation of specific biological processes (Figure 6.25E). The most enriched processes included metabolic pathways such as glycolysis, as well as protein-related processes including translation, protein catabolism, and proteolysis.

Notably, the analysis confirmed the presence of several protein classes previously established as components of *Plasmodium* EVs. These included ribosomal proteins, glycolytic enzymes, heat shock proteins, proteins associated with host cell invasion (e.g., MSP1 and MSP9), and factors implicated in RBC remodeling (e.g., Kelch and RESA domain containing proteins) as shown in Table 6.2 (166, 167).

To gain insight into the potential subcellular origins of the EVs within the parasite, the identified proteins were mapped to their primary compartmental localization based on UniProt annotations (Figure 6.25D). The analysis revealed that the cytoplasm was the predominant source, followed by ribosomal and nuclear compartments. This finding was corroborated and supported by GO Cellular Component enrichment analysis, which confirmed a significant overrepresentation of cytosolic components, ribosomal components, and nucleosome (Figure 6.25F). Additionally, proteins typically destined for secretory pathways or localized to parasite-specific organelles, such as the rhoptry and food vacuole, were present, though in lower proportions.

The combined profile of membrane-associated proteins and soluble cargo from multiple subcellular compartments indicates a heterogeneous population of EVs. This heterogeneity likely reflects vesicles originating from distinct cellular sources or pathways within the parasite. Supporting this notion, it was demonstrated that EVs derived from *in vitro* cultured *P. falciparum* are released throughout all asexual blood stages and originate from specific subcellular microdomains (167).

Collectively, these results establish the first comprehensive proteomic profile of small extracellular vesicles from *P. berghei*. The identified cargo, enriched in core cellular components and specific virulence factors, suggests that extracellular vesicles might have alternative biogenesis pathways in Apicomplexa due to genomic evidence indicating a simplified ESCRT machinery in *Plasmodium* (168).

Table 6.2. Parasite-derived proteins identified in small extracellular vesicles (EVs) enriched from *Plasmodium berghei* culture.

UniProt ID	Description/Name	Biological function
A0A077XDU3	Elongation factor 1-alpha	protein biosynthesis
A0A509AF83	Tubulin alpha chain	cytoskeleton
A0A509AFB5	Proteasome subunit alpha type	proteolysis
A0A509AGL9	40S ribosomal protein S19, putative	translation
A0A509AGS1	mRNA-decapping enzyme subunit 1, putative	mRNA processing
A0A509AGU3	DNA recombination and repair protein Rad51-like C-terminal domain-containing protein	double-strand break repair via synthesis-dependent strand annealing
A0A509AHK5	Serine repeat antigen 2 (PbSERA2)	proteolysis

A0A509AI32	T-complex protein 1 subunit alpha	stress response
A0A509AI36	40S ribosomal protein S11, putative	translation
A0A509AI62	Tryptophan-rich protein	unknown
A0A509AID9	Probable ATP-dependent 6-phosphofructokinase	glycolysis
A0A509AIJ0	GTP-binding nuclear protein	protein transport
A0A509AIM6	Phosphoglycerate kinase	glycolysis
A0A509AJ75	Tryptophan-rich protein	unknown
A0A509AJG0	Endoplasmic reticulum chaperone BIP	stress response
A0A509AJW1	Vacuolar protein sorting-associated protein 9, putative	vesicle-mediated transport
A0A509AJX6	Plasmepsin IV	proteolysis
A0A509AK18	26S protease regulatory subunit 6A, putative	proteolysis
A0A509AK78	Heat shock 70 kDa protein	stress response
A0A509AKH1	Uncharacterized protein	unknown
A0A509AKL5	Cell division cycle protein 48 homologue, putative	cell division
A0A509AL04	40S ribosomal protein S25	translation
A0A509ALB0	40S ribosomal protein S15, putative	translation
A0A509ALB2	Merozoite surface protein 1	attachment; invasion
A0A509ALB6	Membrane associated histidine-rich protein 1a	host erythrocyte remodeling & Maurer's cleft biogenesis
A0A509ALD2	Uncharacterized protein	unknown
A0A509ALK9	Rhoptry-associated protein 1	invasion
A0A509ALN8	rRNA 2'-O-methyltransferase fibrillarin	nucleic acid processing
A0A509ALS9	Kelch domain-containing protein, putative	host cell remodeling
A0A509AMA0	Histone H4	DNA packaging
A0A509AMG6	*Plasmodium* RESA N-terminal domain-containing protein	host cell remodeling
A0A509AMU2	ABC transporter E family member 1, putative	transport
A0A509AMZ0	Small ribosomal subunit protein uS10	translation
A0A509ANB9	Heat shock protein 90, putative	stress response
A0A509ANN1	T-complex protein 1 subunit epsilon	stress response
A0A509APS4	26S proteasome regulatory subunit RPN11, putative	proteolysis
A0A509APY8	60S ribosomal protein L27, putative	translation
A0A509APZ5	Spatacsin C-terminal domain-containing protein	proteolysis
A0A509AQ04	Glyceraldehyde-3-phosphate dehydrogenase	glycolysis
A0A509AQ68	Enolase	glycolysis

A0A509AQB1	Elongation factor 2, putative	protein synthesis
A0A509AQF4	Histone H2B	DNA packaging
A0A509AQH1	40S ribosomal protein S4	translation
A0A509AQP3	Small ribosomal subunit protein eS1	translation
A0A509AQR5	Histone H2A	DNA packaging
A0A509AQX1	DNA/RNA-binding protein Alba 4, putative	nucleic acid processing
A0A509AR35	Uncharacterized protein	unknown
A0A509AR45	Proteasome subunit beta	proteolysis
A0A509AR46	Vacuolar import/degradation Vid27 C-terminal domain-containing protein	unknown
A0A509AR47	Uncharacterized protein	unknown
A0A509ASB5	Vacuolar protein sorting-associated protein 4, putative	vesicle-mediated transport
A0A509ASE6	Histone H3	DNA packaging
A0A509AT96	Exported protein IBIS1	host cell remodeling
A0A509ATH3	26S protease regulatory subunit 10B, putative	proteolysis
A0A509AU86	DNA/RNA-binding protein Alba 1, putative	nucleic acid processing
A0A509AVK2	Proteasome subunit alpha type-1, putative	proteolysis
A0A509B0Y3	Merozoite surface protein 9, putative	attachment; invasion
P49577	Fructose-bisphosphate aldolase 2	glycolysis
Q4Z1L3	Actin-1	cytoskeleton
Q7SI97	L-lactate dehydrogenase	glycolysis

Table 6.3. Parasite-derived proteins identified in EV-reduced supernatant (SN) from *Plasmodium berghei* culture. Proteins marked with an asterisk (*) were detected exclusively in the EV-reduced supernatant fraction.

UniProt ID	Description/Name	Biological function
A0A077XDU3	Elongation factor 1-alpha	protein biosynthesis
A0A509AGL4	Niemann-Pick type C1-related protein *	transport; membrane biogenesis
A0A509AGU3	DNA recombination and repair protein Rad51-like C-terminal domain-containing protein	double-strand break repair via synthesis-dependent strand annealing
A0A509ALB2	Merozoite surface protein 1	attachment; invasion
A0A509AMG6	*Plasmodium* RESA N-terminal domain-containing protein	host cell remodeling
A0A509AQ04	Glyceraldehyde-3-phosphate dehydrogenase	glycolysis
A0A509AQ68	Enolase	glycolysis
A0A509AQR5	Histone H2A	DNA packaging

A0A509AR35	Uncharacterized protein	unknown
A0A509AR46	Vacuolar import/degradation Vid27 C-terminal domain-containing protein	unknown
A0A509ASB5	Vacuolar protein sorting-associated protein 4, putative	vesicle-mediated transport
A0A509AYN3	Uncharacterized protein *	unknown
P49577	Fructose-bisphosphate aldolase 2	glycolysis
Q7SI97	L-lactate dehydrogenase	glycolysis

7. Discussion

This study aimed to optimize *Plasmodium berghei* culture conditions to validate it as a robust *in vitro* model for murine malaria. Then, the effect of blood-stage *P. berghei* stimuli on the autophagy pathway in endothelial cells was evaluated to determine its possible involvement in malaria physiopathology. Therefore, a physicochemical characterization of *P. berghei*-derived extracellular vesicles was conducted to analyze parasite behavior *in vitro* and to further validate the convenience of the culture for future research.

7.1. Limited *in vitro* maintenance of *Plasmodium berghei* requires defined and short-term culture conditions.

In vitro pathogen culture has enabled the study of numerous infectious diseases in an isolated setting, reducing or eliminating the need for host organisms. However, establishing long-term cultures of fastidious microorganisms, including many protozoa, remains a significant challenge (169).

Among *Plasmodium* blood stages, just a few species have been successfully cultured *in vitro* to date. For human parasites, only *P. falciparum* and *P. knowlesi* can be maintained in long-term cultures (145, 170). *P. falciparum* was the first to be cultivated in 1976 and has been central in advancing the understanding of parasite biology and enabling genetic manipulation (141, 145). Among murine parasites, progress has been more limited. Species such as *P. chabaudi* and *P. yoelii* have shown varying degrees of success in short-term *in vitro* maintenance, but none has achieved a reliable continuous culture system like *P. falciparum* (145, 170, 171).

For other human and murine species, including *P. vivax* and *P. berghei* respectively, cultivation has been restricted to short-term or *ex vivo* systems sustaining only a few replication cycles (172, 173). However, there are claims in the literature of long-term *P. berghei* culture systems being maintained for up to 90 days, and in one instance, for 45 weeks (140, 143).

Under the tested laboratory conditions, *P. berghei* exhibited short-term growth, sustaining viability for approximately four days post-culture initiation across all variables. These conditions, selected to optimize parasite's viability and growth rate, were based on established literature and included variations in temperature, gas atmosphere composition, and media formulation.

The gas atmosphere composition was found to be critical for parasite viability. Optimal results were achieved using a controlled gas mixture (90% N_2, 5% O_2, 5% CO_2).

In contrast, cultures maintained in a candle jar system showed a drastic reduction in parasitemia from the first day post-initiation (Figure 6.1). By day two, most parasites under this condition exhibited degraded morphology, including condensed nucleus and basophilic cytoplasm. Furthermore, a visible difference in the color of the culture supernatant, due to its pH indicator, confirmed a sharp distinction in metabolic activity and supernatant pH between the two conditions (Figure 6.2), providing an additional explanation for the observed loss of viability and cellular degradation in the candle jar system.

The literature on *P. berghei* culture presents conflicting reports regarding the candle jar method, with some authors considering insufficient (174) and others claiming successful long-term cultures (140).

Similar results were reported by (175), who compared the growth rate and hemozoin production of *P. falciparum* in low oxygen (93% N_2, 3% O_2, 4% CO_2) versus high oxygen (candle jar) environments. They used blood from donors with normal hemoglobin (AA), sickle cell trait (AS), and sickle cell disease (SS). Parasites in AA and AS RBCs showed higher growth rates in low oxygen, especially in AA cells. However, the opposite effect was observed in SS RBCs. This demonstrates the parasite's adaptability to various biological conditions and supports established malaria theory.

This dependency on a specific microaerophilic environment is consistent with *Plasmodium*'s biology. Gas composition is critical for parasite growth and development. CO_2 plays an essential role in maintaining the CO_2/HCO_3^- buffering system, which helps stabilize the culture pH, as well as for pyrimidine biosynthesis (176). O_2 is equally important, as blood-stage *Plasmodium* parasites rely predominantly on anaerobic glycolysis for energy production and possess limited antioxidant defenses. Moreover, the digestion of hemoglobin generates free heme, which can produce reactive oxygen species (ROS) in the presence of oxygen, making the parasite particularly vulnerable to oxidative stress (177, 178). As an intracellular protozoan, it is adapted to low oxygen concentrations (approximately 3-5%) for optimal growth (178). While the candle jar method is a common and inexpensive technique used for cultivating microorganisms like *P. falciparum*, it only reduces oxygen to approximately 16-18% (175, 179). Furthermore, it offers less precise control over the gas composition compared to a regulated gas mixture.

Today, sophisticated incubation systems are available that provide stable, long-term control of the atmospheric environment, which is essential for achieving robust and reproducible culture results (179).

Next, the assessment of incubation temperature revealed that lower temperatures (28 °C) sustained significantly higher parasitemia for extended periods. In contrast, cultures maintained at physiological temperatures (35 °C and 37 °C) showed no significant changes in parasite growth (Figure 6.3). Most of existing literature reports incubation temperatures ranging from 22 °C to 37 °C, with results showing similar tendencies to those observed in this study.

The study by Ramaiya et al., evaluated the multiplication rate of *P. berghei* over four days at three temperatures (22 °C, 27 °C, and 37 °C) with a 1.0% initial parasitemia. Until day three, parasites incubated at 22 °C showed the highest parasitemia (34.50%), while those at 37 °C showed the lowest (12.40%). On the following day, the 27 °C condition resulted in the highest parasitemia (53.47%) (140). The most frequently used temperature for *P. berghei* culture is 37 °C (143, 144, 174), although some studies recommend lower temperatures (32 °C to 34 °C) (144, 180), as they maintain the parasite's life cycle duration without apparent changes.

Temperature is a critical variable for cell growth, regulating the rate of biochemical and enzymatic reactions necessary for metabolism and biomass increase. *P. berghei* presents a particular challenge due to its high replication rate and short erythrocytic cycle (22-24 hours), which is faster than that of human parasites (ranging from 24-48 hours in *P. falciparum* to up to 72 hours in *P. malariae*) (27). In a closed *in vitro* system, this rapid growth can quickly deplete nutrients and available host cells, and lead to the accumulation of toxic waste products.

Lower temperatures (20°C to 30°C) are also used to reduce the parasite's multiplication rate, allowing for longer observation of specific stages and reducing the need for medium changes and new RBCs addition (143). However, this may induce important biological changes in parasite growth and metabolism.

To highlight temperature relevance on parasite development, one study on *P. falciparum* showed that a mild drop to 34 °C had no significant impact compared to the standard 37 °C. Nevertheless, more extreme temperatures were clearly harmful. Incubation at 4 °C completely arrested development at the ring stage, and although exposure to 40 °C briefly sped up the parasite cycle, sustained high temperatures ultimately became lethal (181).

This temperature-dependent effect on parasite development has also been documented in the present experiments. At 28 °C, parasitemia could be maintained for longer periods, but the progression through the erythrocytic cycle was noticeably slower. This was reflected in the delayed appearance of schizonts, which are typically scarce in the peripheral blood of infected mice (182–184). At 35 °C and 37 °C, schizonts were detectable within the first 24 hours of culture, whereas at 28 °C they appeared only around the third day (Figure 6.4). Such a delay suggests an extension of the asexual cycle from the usual 22–24 hours to approximately 60–72 hours. This is consistent with previous reports describing temperature-induced alterations in parasite replication, in which schizonts are rarely observed during the first 24 hours of culture at lower temperatures (185, 186).

Therefore, 35 °C was selected as the optimal incubation temperature. This condition maintained the parasite's normal developmental life cycle, as indicated by shifts in the predominant life stages observed on different days. Furthermore, it slightly reduced the metabolic rate, thereby preventing nutrient depletion and toxic waste accumulation between medium changes.

Finally, the impact of media formulation was assessed by comparing three variations derived from the original *P. falciparum* culture medium proposed by Trager and Jensen (1976). All three formulations were based on RPMI 1640 but differed in their supplements: the Trager and Jensen modified medium (1976), the formulation by Janse et al. (1984), and the formulation by Jambou et al. (2011).

The results revealed distinct effects on parasite viability. Parasites cultured in the modified Trager & Jensen's medium and in Jambou's medium exhibited very similar growth dynamics. In contrast, Janse's medium led to a rapid decline in parasitemia and viability, with few to no parasites remaining by day two (Figure 6.5). However, a direct comparison of these studies is challenging due to significant variability in their specific culture conditions and media formulations.

While Trager & Jensen's medium was formulated for *P. falciparum* and the Janse’s and Jambou’s media for *P. berghei*, all three have supported long-term cultures in their original studies: up to 53 days, 90 days, and 12 days, respectively (141, 143, 144). However, some authors have noted that stable parasitemias are typically maintained for only 7 days or less, and that most *in vitro* cultures are used primarily to generate schizonts for transfection (180, 187). In these protocols, cultures intended for schizont production are generally maintained only overnight. Following transfection, parasites are generally returned to a living host, underscoring the limited ability to sustain continuous culture *in vitro* (180, 187). The durations reported in most studies are considerably longer than the 4-day viability observed here, likely reflecting the inability to reproduce the same physical, chemical, or biological conditions.

A key difference between formulations is the use of serum. The original Trager & Jensen formulation used 10% human serum, while modern modified versions, including those of modified Trager & Jensen and Jambou, replace it with AlbuMAX™ (a lipid-rich bovine serum albumin) and supplement hypoxanthine as a purine source (141, 142). This substitution enhances reproducibility, reduces biological risks, and minimizes batch-to-batch variability.

In contrast, Janse’s medium retains 10% fetal calf serum (FCS) instead of AlbuMAX™ and does not include exogenous hypoxanthine (143). *Plasmodium* lacks *de novo* purine synthesis metabolism, so it depends entirely on salvage pathways for hypoxanthine or related nucleosides to sustain replication (188, 189). While FCS naturally contains variable amounts of salvageable purines, AlbuMAX™-based media require explicit hypoxanthine supplementation. This reliance on the inconsistent purine content of FCS likely explains the poor performance of Janse’s formulation under these conditions.

Although FCS is a common supplement in other cell culture systems, these results demonstrate that it is detrimental to *P. berghei* growth under these conditions. No definitive explanation was found for this anomalous result. One possibility is that there is an insufficient supply of purines to sustain parasite replication. The hypoxanthine concentration in FCS has been reported to be approximately 74.7 ± 31.9 µmol/L (190). This is far lower than the 200 µmol/L explicitly supplemented in the other two formulations, and, as Janse's medium uses only 10% FCS, the final available concentration in the culture would be diluted to roughly 7.5 µmol/L.

This hypothesis, however, presents a paradox: in mice sera, hypoxanthine levels are reported to be much lower (1.1 ± 0.8 µmol/L) and could explain Janse's prolonged culture (143, 190). Also, this discrepancy may suggest that the parasite's *in vitro* purine requirement may not be directly comparable to its *in vivo* environment, possibly due to the presence of alternative nucleoside sources *in vivo*.

Moreover, these considerations become even more relevant for *P. berghei*, whose erythrocytic cycle (22–24 h) and rapid metabolic turnover impose substantially higher purine requirements than those of *P. falciparum*. A faster DNA replication rate and accelerated biomass accumulation likely make *P. berghei* more sensitive to fluctuations in purine availability, particularly *in vitro* where continuous supply mechanisms are absent.

Such differences between *in vivo* and *in vitro* purine availability were illustrated by Tewari et al. in *P. falciparum*, who demonstrated that low hypoxanthine concentrations (0.5 µmol/L) are insufficient to sustain long-term parasite viability. After 72 h of deprivation, growth could not be restored even when cultures were subsequently supplemented with high hypoxanthine levels (90 µmol/L). The loss of viability was associated with broad metabolic dysfunction, including alterations in fatty acid synthesis, the pentose phosphate pathway, methionine metabolism, and coenzyme A biosynthesis (188).

Additionally, Jambou's medium consisted of a 3:1 mixture of RPMI 1640 and DMEM-F12, supplemented with higher concentrations of glucose and $NaHCO_3$, as well as calcium, choline, and gelatin. The DMEM-F12 component contributed key nutritive elements not present in standard RPMI 1640, including a broader spectrum of amino acids (e.g., alanine, cysteine), higher levels of vitamins (such as lipoic acid and thiamin), and additional trace elements like iron, copper, and zinc, which can be crucial for parasite metabolism and growth.

According to the authors, this nutrient-rich formulation and set up were designed to address specific challenges in *P. berghei* long-term culture. Specifically, gelatin was included to prevent hemolysis due to mouse RBC instability. For this reason, Jambou's formulation was selected for this study, as it represented the most nutrient-rich option, designed to fulfill the parasite's established nutritional requirements (144). For this reason, Jambou's formulation was selected for this study, as it represented the most nutrient-rich option, designed to fulfill the parasite's established nutritional requirements.

Beyond the nutritional formulation, the physical conditions of culture are critical for parasite yield and RBC integrity. While other protocols, such as the one described by Janse *et al.*, employ constant agitation using a magnetic stirrer, Jambou *et al.,* demonstrated that orbital shaking significantly reduces hemolysis compared to magnetic stirring (143, 144). This method facilitates the gentle release of merozoites trapped within the RBC membrane while preserving host cell stability. Therefore, an orbital shaker was selected as the agitation method for this study to optimize both parasite propagation and the maintenance of RBC viability.

One significant difference between the experimental conditions in this study and those in the literature was the source of RBCs. This study utilized RBCs from ICR (CD-1®) mice, whereas Jambou *et al.* used CBA/Ca and C57BL/6 mice, and Janse *et al.* used Wistar rat RBCs (143, 144). This is a major variable, as the strain and species of the host can significantly influence parasite infectivity due to differences in cell surface receptors and RBC stability. Consequently, the use of ICR mouse RBCs remained a key variable that could directly affect the outcome and comparability of the culture experiments in this study.

The impact of this biological variable is best demonstrated by Janse's experiments, where the shift from mouse to rat RBCs extended the viability of *P. berghei* cultures from only 9 days to a remarkable 90 days (143). This underscores that the host RBC source can be an even more critical factor for long-term culture than the nutrient composition of the medium itself.

This differential infectivity has been documented in *P. berghei*, affecting exo-erythrocytic stages as well as overall infection progression and mortality across different host strains (191, 192). For example, whereas only 50 sporozoites were required to infect all C57BL/6 mice, up to 20,000 were needed to achieve the same effect in ICR (CD-1®) mice (191). A similar trend was observed with *P. yoelii*, the infective dose 50 (ID_{50}) for strains like BALB/c, C57BL/6, A/J, and B10BR ranged from 4.9 to 10.6 sporozoites, but was 147 sporozoites for ICR (CD-1®) mice (193). This inherent resistance to *Plasmodium* infection of the ICR (CD-1®) mice, the RBC source in this study, likely constitutes a major factor behind the limited culture viability observed.

Several other limitations for long-term *P. berghei* cultivation, both reported in the literature and observed in this study, include low RBC stability, the parasite's specific tropism for reticulocytes, and the failure of merozoites to reinvade new host cells (143, 144).

Low RBC stability is closely related to media formulation. It has been demonstrated that serum-free formulations lacking essential components like cholesterol induce significant changes in RBC membrane integrity (194). For this reason, serum protein substitutes such as AlbuMAX™ are a standard supplement in *Plasmodium* culture media to provide protein and lipid stability to the RBC membrane (142). This was observed in Giemsa-stained smears after three days in culture, where RBCs appeared flattened, more fragile, and exhibited an altered staining pattern (Figure 6.6). The absence of serum also impairs critical biological processes, such as the export of parasite proteins to the RBC membrane (e.g., PfEMP1 in *P. falciparum*) and the commitment and maturation of gametocytes in both *P. falciparum* and *P. berghei* (195, 196).

Additionally, the choice of serum source (FCS, mouse serum, or rat serum) in serum-containing media, introduces another layer of variability. These sources differ not only in their lipid profiles and nutrient composition but also in the presence of species-specific antibodies, hormones, and other bioactive molecules like EVs. Consequently, the serum component can directly affect parasite invasion, growth rate, and the osmotic stability and longevity of the host RBCs in culture.

To address the issue of hemolysis due to poor RBC membrane stability, gelatin was included in Jambou's formulation. Low concentrations of gelatin (0.1%) reduce *in vitro* hemolysis by acting as a protective colloid, increasing medium viscosity, forming a hydrated macromolecular layer on the erythrocyte surface, and dampening local mechanical and osmotic stresses (144, 197). However, no appreciable differences in RBC stability were observed when compared to gelatin-free media. Therefore, for subsequent stimulation assays, iRBCs were isolated directly from mice blood to ensure biological relevance. This approach avoided potential alterations to the RBC membrane and surface antigen exposure that may arise from *in vitro* culture conditions.

A further complication is the distinct tropism of *P. berghei* for reticulocytes, which express the CD71+ receptor, a key ligand for parasite invasion. The proportion of reticulocytes in murine peripheral blood is naturally low (approximately 1-5% of total RBCs), creating a limited pool of target cells and necessitating the constant addition of reticulocyte-rich blood (198, 199). The constant addition of reticulocyte-rich blood, in turn requires the use of a larger number of animal donors to sustain the culture. This marked tropism was also observed, with newly infected cells being notably larger and showing the diffuse basophilia typical of these young RBCs.

To overcome this, some protocols recommend pre-treating mice with hemolytic agents like phenylhydrazine to increase reticulocyte counts, while others consider this step unnecessary (140, 143, 144, 200).

In this study, supplementing cultures every 2 days with fresh blood from phenylhydrazine-treated mice did not significantly improve viability, contrary to some literature reports (140, 143). This discrepancy could be attributed to the short lifespan of mouse reticulocytes (20-40 hours), as they continue to mature *in vitro*, or to the method of supplementation itself, which added the entire RBC population rather than an enriched reticulocyte fraction, being insufficient to support parasite growth (201).

The high demand for fresh reticulocytes is likely directly linked to the failure of merozoites to reinvade new RBCs after a few replication cycles (202, 203). This explains why supplementation with whole mouse blood in this study did not yield a measurable improvement in culture longevity. Furthermore, the ICR (CD-1®) mouse model used here may have a lower baseline reticulocyte count or different maturation kinetics compared to the strains (e.g., CBA/Ca, C57BL/6) or species (rat) used in more successful protocols.

Additionally, this loss of infectivity *in vitro* has been attributed to the absence of serum factors in the culture medium, which might be essential for the invasion process (204, 205). These factors potentially include lipids, hormones, and specific proteins that stabilize the RBC membrane or directly interact with merozoite ligands. However, serum was deliberately excluded from the defined culture medium used in this study to maintain a controlled environment. The addition of exogenous serum would introduce a confounding variable by providing a complex and undefined mixture of proteins, exogenous EVs, species-specific antibodies, and metabolites.

Regardless of the underlying cause, a consistent loss of invasion capacity after two days in culture was observed. This phenomenon, which is well-documented in *P. berghei* blood-stage cultures, was evidenced here by the microscopic accumulation of free merozoites attached to RBC membranes and the consequent stagnation or decline in parasitemia (Figure 6.6) (144). This marked the point at which the *in vitro* system failed to sustain the parasite's life cycle, primarily due to the inability of merozoites to successfully reinvade new, susceptible host cells.

To determine whether the loss of infectivity observed *in vitro* also occurs *in vivo*, ICR (CD-1®) mice were inoculated intraperitoneally with 10^5 iRBCs collected after 1 to 2 days in culture. The inoculated mice developed parasitemia by day 3 post-inoculation and exhibited a clinical course identical to that of animals infected directly with blood stabilates (Figure 6.7).

These findings are consistent with those of Jambou et al., who reported that CBA/J mice inoculated with 10^6 iRBCs from 12-day cultures developed parasitemia after 7 days and coursed with cerebral malaria (144). Collectively, these results demonstrate that *P. berghei* does not lose its infectivity *in vivo* after a limited number of *in vitro* replication cycles.

However, it remains to be investigated whether the duration of *in vitro* maintenance correlates with a loss of infectivity *in vivo*. This is suggested by the findings of Jambou et al., where a longer culture time may be associated with a delayed onset of parasitemia, despite the use of a more susceptible mouse strain and a higher infectious dose.

Collectively, these results demonstrate that short-term *in vitro* cultivation of *P. berghei* is achievable under the selected conditions of Jambou's formulation, at 35 °C and within a controlled gas atmosphere. The culture system supported adequate life cycle progression and maintained normal parasite morphology throughout the experiment, thereby validating its use for further assays. This approach is highly useful for studying parasite biology in a controlled setting, avoiding the complexities of *in vivo* environments such as the host immune response and stage sequestration.

While the method has limitations, its utility depends on the specific research question. For instance, the use of serum-free medium, while a limitation for RBC-based stimulation assays due to potential membrane alterations, was essential for the clean enrichment of parasite-derived EVs, as serum is a significant source of contaminating host EVs.

Finally, the *in vivo* infectivity assay confirmed that cultured parasites retain their ability to invade RBCs. The challenge of sustaining long-term cultures likely stems from the high demand for fresh reticulocytes, culture-induced changes in RBC membrane integrity, and the absence of serum-derived factors critical for efficient invasion. To overcome these hurdles and extend cultivation times, future efforts could focus on using more susceptible mouse strains, employing selective reticulocyte enrichment from healthy donors, and testing various concentrations of mouse or rat serum instead of fetal calf serum.

7.2. Established cost-effective protocols for the enrichment of biologically active *P. berghei* derived stimuli. The successful enrichment of *P. berghei*-derived stimuli was a prerequisite for investigating the parasite's interaction with tEnd.1 endothelial cells. For iRBC isolation, density-based gradients using polymers such as silica-based Percoll or iohexol-based Nycodenz remain among the most straightforward and cost-effective approaches (146).

To address the limitations of existing protocols, a customized discontinuous Percoll gradient with an increased number of concentration steps was established (157, 158). This modification enabled the reproducible enrichment of iRBC subpopulations according to their developmental stage (Figure 6.8). Despite this improvement, a slight degree of cross-contamination between fractions was observed, highlighting a persistent challenge in achieving absolute purity.

Several measures can be implemented to minimize this cross-contamination. These include increasing the volume of Percoll layers to enhance physical separation and further diluting the mouse blood to prevent system overloading, as an excessive number of RBCs can impede effective separation. Alternative approaches, such as magnetic-activated cell sorting (MACS) based on the paramagnetic properties of hemozoin in the parasite's digestive vacuole, offer significant advantages. These include high parasitemia yields (>90%), reduced toxicity compared to polymer gradients, and improved recovery of mature stages, which contain greater amounts of hemozoin (206, 207).

For the enrichment of EVs, differential ultracentrifugation was employed, as it remains the most widely used and accessible method for this purpose, providing a fundamental baseline for EV concentration (159). A key modification to the standard protocol was implemented: the supernatant was filtered through a 0.45 and 0.22 µm membrane prior to the ultracentrifugation steps. This critical step removed residual cellular debris and large aggregates, thereby reducing a major source of co-isolation contamination and improving the specificity of the EV pellet. The physical appearance of the obtained pellets: a cloudy, floating layer over a compact, gelatinous pellet, which was consistent with typical reports for heterogeneous EV populations (208). The slight reddish hue observed in the present EV preparation was likely due to residual hemoglobin contamination (Figure 6.9).

While the inclusion of a filtration step probably refined the protocol, several additional refinements could further enhance purity and yield in future studies. These include: introducing a gentle washing step (resuspension and re-ultracentrifugation in filtered PBS) to reduce soluble protein contamination; implementing density gradient centrifugation (e.g., iodixanol gradient) as a subsequent step to separate EVs more precisely from remaining contaminants based on buoyant density; and optimizing the handling and storage conditions of the conditioned medium before ultracentrifugation and EV pellet after enrichment (148, 209). Specifically, ensuring immediate processing or cryopreservation at -80°C after the medium change is critical to prevent residual cells or parasites, not fully removed during prior centrifugation, from remaining metabolically active and contributing a confounding source of EVs during storage (148).

However, the definitive characterization of these vesicles as actual *P. berghei*-derived EVs and the exclusion of host-derived contaminants remain essential. This is particularly important because ultracentrifugation is susceptible to co-isolating high levels of non-vesicular extracellular particles (NVEPs) such as protein aggregates, lipoproteins, and cellular debris, which can constitute the majority of the isolated material and confound downstream analyses (159).

Furthermore, it is critical to consider that *P. berghei*-derived EVs likely constitute a minority within the total EV pellet, as they are likely outnumbered by the abundance of RBC-derived EVs, which are known to be remarkably abundant in circulation, with concentrations up to approximately 170 EVs/µL of plasma (210). For this reason, the implementation of more selective methods is necessary for the specific enrichment of *P. berghei*-derived EVs. This could be achieved through techniques such as affinity columns targeting antigens uniquely present on the parasite-derived vesicles (211, 212).

Storage conditions can represent another critical variable for EV analysis. EVs are dynamic, membrane-bound structures susceptible to degradation, aggregation, and changes in surface epitope availability over time. For physicochemical analysis such as Dynamic Light Scattering (DLS) and Atomic Force Microscopy (AFM), improper storage (e.g., at 4 °C for long periods or following repeated freeze-thaw cycles) can lead to the formation of large aggregates, artificially skewing the particle size distribution and masking the true population of individual vesicles, leading to inaccurate morphological assessments.

Most critically, for functional biological assays, the loss of membrane integrity or the inactivation of labile surface proteins during storage can directly diminish or completely abrogate biological activity (213, 214). The EV suspensions in this study were maintained in particle-free PBS at 4 °C and analyzed or used within a strict 3-day window post-isolation for physical characterization or functional assays or stored at -80 °C for proteomic analysis.

Together, these protocols provide an accessible and practical initial approximation for stimulation assays. While not ideal, they permit the first functional analyses of the roles of iRBCs and parasitic EVs in endothelial autophagy and murine malaria pathogenesis.

7.3. Implementation and validation of genetically modified tEnd.1 models for endothelial autophagy. There are various approaches to study autophagy in cell models, including fluorescence microscopy, immunohistochemistry, and protein or transcript analysis. Among these, fluorescence microscopy is one of the most accessible and direct methods, particularly when using genetically modified cells to express a fluorescent autophagy marker (215, 216). This strategy enables real-time, live-cell or fixed-cell imaging while bypassing the need for additional techniques like immunostaining, and provides specific visualization of autophagic structures with high sensitivity and spatial resolution, allowing a more accurate assessment of autophagic flux (160, 217).

To establish a robust model for studying endothelial autophagy in response to *P. berghei*, this section aimed to establish and validate two genetically modified tEnd.1 cell lines: one expressing a single LC3-GFP reporter and another expressing a tandem LC3-GFP-mCherry construct. Both cell lines were first validated using a panel of pharmacological agents which served a dual purpose: first, to confirm the responsiveness of the reporter systems, and second, to define the image acquisition and analytical parameters necessary for accurate quantification. Subsequently, these validated models were employed to assess the autophagic response triggered by biologically relevant *P. berghei*-derived stimuli, including iRBCs, culture supernatants and EVs.

The tEnd.1 cell line used in this study is an immortalized murine endothelial cell population originally derived from a thymic hemangioma induced by the polyomavirus middle T (mT) oncogene. Although transformed, these cells preserve several fundamental endothelial characteristics, including expression of von Willebrand factor and PECAM-1/CD31, as well as functional responsiveness to cytokines such as IL-1 and TNF. They also display contact inhibition, uptake acetylated LDL, and secrete cytokines like IL-6 upon inflammatory stimulation, consistent with primary endothelial cell behavior (218, 219).

Notably, the oncogenic transformation has conferred tEnd.1 cells with distinct functional alterations, including elevated proteolytic activity via increased urokinase-type plasminogen activator (uPA) production and a dysregulated nitric oxide synthase (NOS) profile, featuring high constitutive and inducible NOS levels. These modifications reflect significant remodeling of extracellular matrix interactions and signaling pathways (220, 221). Nevertheless, the retention of a differentiated endothelial phenotype makes tEnd.1 cells a valuable and practical model system for mechanistic studies of endothelial function and response.

One of the most common markers for monitoring autophagy is LC3, a member of the LC3/GABARAP protein family. Its lipidated form, LC3-II, specifically associates with isolation membranes and autophagosomes, making it the standard marker for these structures. The cellular level of LC3-II generally correlates with autophagosome abundance. However, an increase in LC3-positive structures does not always correspond to a high autophagic activity, as it can also result from a blockage in autophagosome degradation (92, 99, 222).

In fluorescence-based autophagy analysis, two reporter strategies can be employed: single-tag constructs (e.g., LC3-GFP) and tandem-tag constructs (e.g., LC3-GFP-mCherry). The use of a single reporter, such as LC3-GFP, allows for the simple visualization of LC3 recruitment in the cytoplasm under a given condition. However, this approach has inherent interpretative limitations (215).

Three primary limitations constrain the interpretation of LC3-GFP reporter assays. First, the GFP fluorescent signal is rapidly quenched in the acidic lysosomal environment, hiding the actual turnover of autophagosomes. Second, an observed increase in LC3-GFP puncta does not definitively indicate enhanced autophagic flux, as it could result from either increased autophagosome formation or impaired lysosomal degradation. This ambiguity necessitates complementary experimental approaches. Third, the potential ectopic recruitment of LC3 to non-autophagosomal membranes, which are not subject to lysosomal turnover, adds another layer of interpretive complexity (215, 217, 222, 223).

Consistent with established principles, treatment of the LC3-GFP cell line with various autophagy modulators successfully induced the expected phenotype: a significant increase in the LC3-positive vesicle area (Figure 6.10). This result validated the cellular model and the imaging assay for detecting perturbations in autophagy. The assay robustly captured the common phenotypic endpoint of such perturbations, vesicle accumulation, regardless of the specific mechanism of action. For instance, rapamycin (an mTORC1 inhibitor) and nutrient starvation (an AMPK activator) both induce autophagy upstream, while bafilomycin A1 and chloroquine inhibit autophagosome degradation by disrupting lysosomal acidification downstream (224). Therefore, while this assay is a powerful tool for confirming autophagy modulation, it functions as a downstream readout of net autophagic flux. To dissect the precise mechanism, whether an increase in vesicle area stems from enhanced initiation or impaired degradation, complementary assays that measure flux, such as the tandem LC3-GFP-mCherry reporter or Western blot analysis of LC3-II turnover, are required.

An additional critical consideration is the fidelity of the reporter system. This requires validating that the GFP puncta correspond to authentic LC3-positive structures and assessing the relative expression of the exogenous GFP-tagged LC3 versus the endogenous protein (217, 225). To address this, immunofluorescence with an anti-LC3 antibody was performed. The results showed a strong colocalization (yellow signal in merge) between the GFP fluorescence (green) and the anti-LC3 immunostaining (red), confirming that the GFP-positive structures are indeed LC3-positive autophagic vesicles (Figure 6.11). Notably, most puncta were observed co-stained with both fluorescent markers for LC3, indicating that the exogenous LC3-GFP was the predominant source of LC3 signal in these cells.

To further characterize autophagic flux in tEnd.1 cells and overcome the limitations of the single-tag LC3-GFP reporter, cells were transfected with a tandem-tag construct (LC3-GFP-mCherry). This system leverages a second, pH-stable reporter (mCherry) to bypass two key constraints of the single reporter: the quenching of GFP in lysosomes and the inability to directly measure LC3 turnover. Consequently, autophagosomes (neutral pH) appear as yellow puncta (GFP+/mCherry+), while autolysosomes (acidic pH) appear as red puncta (mCherry+ only) due to GFP quenching (160, 215, 217).

By quantifying the transition from yellow (mCherry+GFP+) to red (mCherry+ only) puncta, this assay provides a direct, ratiometric measure of autophagic flux. This critical feature allows it to mechanistically distinguish between a genuine upregulation of autophagosome formation, reflecting a net activation of the autophagic pathway, and an impairment in the downstream lysosomal degradation step, which signifies a disruption of autophagic turnover.

To discriminate between both autophagic states, the tandem-reporter system was employed. Treatment with autophagy inducers (rapamycin and starvation) resulted in a high autolysosome-to-autophagosome ratio, indicative of increased autophagic flux. Conversely, treatment with lysosomal inhibitors (chloroquine and bafilomycin A1) led to an accumulation of undegraded autophagosomes and a relatively low autolysosome area, confirming impaired flux due to blocked degradation (Figure 6.18).

An interesting observation was the lack of significant differences between control and 3-methyladenine (3-MA)-treated cells in both reporter systems (Figures 6.10 and 6.18). While 3-MA is a class III PI3-kinase inhibitor expected to reduce autophagosome formation, evidence suggests it has a dual role due to its differential temporal effects on PI3K isoforms. 3-MA persistently inhibits class I PI3K (an autophagy inhibitor) while its suppression of class III PI3K (an autophagy initiator) is transient. Consequently, under prolonged treatment in nutrient-rich conditions, as used here, 3-MA can paradoxically promote autophagic flux, explaining why it did not reduce LC3-positive vesicles in our assays, despite its ability to inhibit starvation-induced autophagy (224, 226).

Additionally, a high cell-to-cell variability was observed during quantification and statistical analysis. Autophagy is inherently dynamic and heterogeneous, with LC3 puncta number, size, and turnover differing even among genetically identical cells under identical conditions due to fluctuations in metabolic state, cell cycle stage, and vesicle trafficking kinetics. This variability was further amplified by the methodological approach used for cell line generation. The stable LC3-GFP cell line was established by pooling puromycin-resistant cells rather than by isolating single-cell clones via flow cytometry. Consequently, the resulting population comprised a mixture of cells with variable transgene copy numbers and expression levels. Also, in the transiently transfected tandem LC3-GFP-mCherry experiments, variability was also inherent due to differences in plasmid uptake and expression efficiency between cells. This heterogeneity has been extensively reported in the literature and is considered part of the biological and technical limitations of the differential expression patterns in these cells (161, 216).

tEnd.1 cells present distinct advantages as a model for autophagy research. Their robust growth, stable phenotype, and high transfection efficiency render them particularly amenable to microscopy-based assays, including the use of LC3 reporters and tandem-tag constructs. Furthermore, their retention of critical endothelial receptors and inflammatory signaling pathways allows for the investigation of autophagy in a biologically relevant context, where it intersects with endothelial activation, pathogen sensing, and vascular pathophysiology (218, 219).

Conversely, this transformed nature also introduces important limitations. The expression of the mT antigen profoundly rewires central signaling pathways, including PI3K, Src-family kinases, MAPK, and PP2A-dependent cascades, all of which intersect with canonical autophagy regulation. Consequently, basal autophagic activity, responsiveness to metabolic stimuli, and vesicle trafficking dynamics in tEnd.1 cells may differ from those in primary endothelium. Moreover, their elevated proteolytic and NOS activity could directly or indirectly influence lysosomal function and redox balance, introducing variables not typically present in non-transformed vascular cells (220, 221, 227).

The tEnd.1 cell line offers a high-throughput and reliable model for mechanistic exploration. To build upon these findings, future confirmation in primary endothelial cultures will reinforce the biological validity and translatability of these observations within a more native physiological context.

7.4. Impaired autophagic flux in endothelial tEnd.1 cells exposed to *Plasmodium berghei* blood stages derived stimuli. Dysregulated autophagy in vascular endothelial cells has been implicated in the pathogenesis of severe malaria, contributing to inflammation, barrier dysfunction, and organ injury (41). While autophagy can serve as a protective response during infection, sustained or altered flux may drive endothelial maladaptation under pathological stress (116, 117). Building on the validated LC3-GFP and tandem LC3-GFP-mCherry reporter systems established in the previous section, this study examined the autophagic response of tEnd.1 endothelial cells to biologically relevant *P. berghei* stimuli, including iRBCs from peripheral blood of infected mice, and EVs, and EV-reduced supernatants from *P. berghei* cultures.

The role of host cell autophagy during the hepatic stages of *Plasmodium* infection has been well established, acting both as a defense mechanism for parasite clearance and as a pathway exploited by the parasite to access host resources (126, 133). Since the symptomatic blood stage enables systemic dissemination and exposes the parasite to diverse tissues, its potential effects on the autophagy pathways of other cell types, such as endothelial cells, require investigation. While the primary host cells of this stage, unnucleated RBCs, lack an autophagic machinery and serve as inert vehicles for immune evasion and circulation, parasites are not entirely silent. They actively remodel the RBC membrane and secrete a variety of soluble effectors, potentially influencing systemic host responses, including endothelial cells (42, 131).

The vascular endothelium constitutes the primary tissue interface exposed to *Plasmodium*-derived effectors during the blood stage infection, and vascular dysfunction is a hallmark of severe malaria pathology. This dysfunction manifests as endothelial activation, impaired perfusion and tissue oxygenation, and ultimately contributes to organ failure (41). While numerous studies have documented the impact of *Plasmodium* stimuli on endothelial activation, inflammatory signaling, cellular adhesion, sequestration, microvascular dysfunction, and alterations in the nitric oxide (NO) pathway, the specific activation and role of autophagy pathways in endothelial cells during malaria infection remain unexplored (182, 228, 229).

The three stimuli analyzed in this study produced a consistent pattern: all induced an increase in LC3-positive vesicles accumulation due to a measurable reduction in autophagic flux at specific doses and time points. However, interesting differences were observed in their temporal kinetics. While the effect of iRBCs was delayed, with the maximum response occurring at 6 hours post-stimulation, EVs and EV-reduced supernatants triggered a much more rapid response, significantly altering flux within 1 hour.

The sustained temporal profile of the endothelial response to iRBCs suggests a prolonged engagement, where continuous exposure to parasite-derived components leads to a progressive impairment of autophagic flux. Quantitatively, LC3 expression increased and autophagic flux decreased in iRBC-exposed cells over time, peaking at 6 hours and remaining similar through 24 hours of exposure (Figures 6.12, 6.19, S.1, and S.2). This kinetic pattern indicates that extended contact is required to elicit a full autophagic response, which could be due to either a contact-dependent mechanism or the time needed for the parasite to synthesize and release sufficient soluble factors into the medium.

Comparable time-dependent alterations in autophagy have been reported in other host-pathogen systems, including protozoan parasites such as *Toxoplasma gondii* and *Leishmania* spp., where sustained exposure or intracellular persistence leads to progressive modulation or blockade of autophagic flux rather than an acute response (230, 231).

Interestingly, control RBCs elicited a gradual increase in LC3 expression and autophagic flux over time, which may reflect a mild homeostatic response to prolonged static contact. However, it is important to note that this *in vitro* condition differs fundamentally from the physiological state, where continuous blood flow prevents sustained RBC-endothelial adhesion. The static culture system may introduce confounding factors such as localized nutrient diffusion limitations or unphysiological mechanical stress, which could contribute to the observed autophagic response and represent a limitation of the experimental model.

A dose-dependent response in LC3 expression was observed, exhibiting a characteristic plateau-shaped profile (Figure 6.13). At low doses (100 iRBC:1 EC), the limited amount of parasite-derived stimuli elicited a modest autophagic response. An intermediate dose (500 iRBC:1 EC) provided an optimal level of parasite signaling, effectively inducing autophagosome formation while simultaneously saturating or partially impairing lysosomal clearance, resulting in maximal LC3 accumulation.

At higher doses (1000 iRBC:1 EC), the apparent response slightly declined, likely due to the interplay of counteracting processes such as lysosomal overload, increased cellular stress, inhibitory inflammatory feedback, and physical constraints on cellular uptake or contact area. This plateau or attenuation may suggest saturation of contact-dependent receptors or adhesion interfaces mediating iRBC-endothelial cell interactions, or alternatively the activation of compensatory regulatory mechanisms aimed at limiting excessive autophagy and preserving cellular homeostasis. Such non-linear responses have been described in contexts of autophagic overload, inflammatory signaling, and impaired phagocytosis due to limited physical contact. Importantly, autophagy must be tightly regulated, as excessive or dysregulated activation can ultimately promote cell death (232–235).

Notably, the magnitude of the difference between 100 and 500 iRBC:1 EC was greater than that observed between 500 and 1000 iRBC:1 EC. This reflects the larger relative change in parasite load between the former conditions, where the dose increases fivefold, compared with only a twofold increase between the latter. A similar pattern was observed in control RBC-treated cells, where significant differences were detected only between conditions involving large dose changes (100 vs 500 RBC:1 EC or 100 vs 1000 RBC:1 EC), but not between the two highest ratios (500 vs 1000 RBC:1 EC).

Parasites may activate autophagy in endothelial cells through contact-dependent mechanisms during iRBC interactions. A primary route involves cytoadhesion, in which parasite proteins displayed on the RBC surface bind to host endothelial receptors, analogous to the vascular sequestration observed in *P. falciparum*. *P. berghei* iRBCs also exhibited strong adhesive properties, as evidenced by their resistance to detachment during washing steps compared to uninfected RBCs (182, 236).

This firm adhesion can exert physical or mechanical stress on endothelial cells, potentially inducing cytoskeletal reorganization. Given that microtubule and actin dynamics are essential for autophagosome transport and fusion, such cytoskeletal disruption may directly impair autophagic flux (237, 238). At the molecular level, adhesive interactions can initiate signaling cascades. For example, in *P. falciparum*, the binding of PfEMP1 to CD36 triggers phosphorylation of Src family kinases and recruitment of actin-regulating proteins (236).

Notably, Src kinase pathways are reported to be altered in the mT-transformed tEnd.1 endothelial cell line used in this study, which may bias adhesion-dependent signaling toward sustained Src activation. Prolonged Src signaling has been predominantly associated with negative regulation of autophagic flux, mainly through activation of the PI3K-Akt-mTOR axis and interference with cytoskeletal and vesicular trafficking processes required for autophagosome maturation. In this context, adhesion-mediated Src activation induced by iRBCs may contribute to the accumulation of LC3-positive structures (227, 239, 240).

Alternatively, autophagy may be triggered and/or impaired by the release and secretion of parasite-derived stimuli, which are sensed by endothelial cells and elicit diverse cellular responses. As indicated by the lower glucose concentration in the supernatant after 6 hours of incubation, parasites within iRBCs remain metabolically active during co-culture. This viability suggests they can continue their intraerythrocytic cycle, potentially leading to the release of soluble effectors, such as pathogen-associated molecular patterns (PAMPs) or extracellular vesicles. These factors are known to induce inflammatory signaling.

Vascular inflammation is a defining feature of severe malaria and is tightly associated with endothelial dysfunction, as blood-stage parasites activate endothelial inflammatory pathways such as MAPK and NF-κB signaling in both human and murine models (241, 242). Parasite-derived factors released from lysed iRBCs, including hemozoin (HZ), free heme, nucleic acids, and oxidized lipids, promote inflammasome activation and pro-inflammatory cytokine production, while the poor degradability of hemozoin contributes to sustained inflammatory responses (243, 244). In this setting, inflammation and autophagy are bidirectionally regulated: autophagy normally limits excessive inflammation by degrading inflammasome components and inflammatory mediators, whereas persistent activation of inflammatory signaling pathways can disrupt autophagic flux, shifting autophagy from a protective mechanism to a dysfunctional process (233, 245, 246).

Another related mechanism may involve NO dysregulation. During *Plasmodium* infection, endothelial and immune cells produce elevated levels of NO via inducible nitric oxide synthase (iNOS) in response to parasite products and cytokines. While moderate NO production exerts anti-parasitic effects and helps maintain vascular homeostasis, excessive or sustained NO and its reactive nitrogen species (RNS) can induce oxidative and nitrosative stress (247, 248). Pathologically, S-nitrosylation of autophagy proteins and regulators such as mTORC1 and cathepsin B has been shown to impair autolysosome function, a mechanism implicated in neurodegenerative diseases (249, 250). Given that the tEnd.1 cell line constitutively overexpresses NOS isoforms, elevated NO production may represent an underlying contributor to the observed impairment of autophagic flux (221).

An important methodological consideration, beyond the static nature of the co-culture, is that the incubation conditions for iRBCs during stimulation assays differed from the optimized culture parameters established earlier for *P. berghei*. The iRBCs were exposed to tEnd.1 cell medium, at 37 °C, and a 5% CO_2 atmosphere, rather than the selected conditions for *P. berghei in vitro* growth (Jambou's medium, 35 °C, and microaerophilic gas mixture). This disparity represents an inherent limitation of co-culture systems involving adherent host cells and intraerythrocytic parasites, as simultaneous maintenance of optimal conditions for both cell types is not technically feasible, where incubation parameters are adjusted to prioritize host cell viability and functional readouts rather than parasite replication.

In contrast, the other two stimuli (EVs and EV-reduced supernatant) elicited a much more rapid response, with peak LC3 accumulation and minimal autophagic flux occurring within approximately one hour of incubation. This early and pronounced effect suggests these preparations are enriched in pre-formed, bioactive effectors capable of directly impairing autophagy in tEnd.1 cells. Unlike iRBCs, which may require time for adhesion, cellular engagement, and *de novo* synthesis of signaling molecules, EVs and their associated soluble factors appear to deliver an immediate signal that disrupts autophagic flux.

Time-course analyses revealed that *P. berghei*–derived EVs induced a rapid and sustained increase in LC3-positive vesicles compared to control RBC-EVs, with significant divergence emerging after 30 minutes and peaking at 60 minutes (Figure 6.14). While early LC3 recruitment was detectable in both groups, the progressive separation between parasite- and control-derived EVs suggests a cargo-dependent effect. Concomitant autophagic flux measurements showed marked impairment with *P. berghei*-EVs, exhibiting kinetics similar to that of iRBCs: elevated autophagosome area alongside low autolysosome area (Figure 6.20).

A dose-dependent effect was also evident, as *P. berghei*-derived EVs at 50 µg protein induced significantly greater LC3 recruitment than at 10 µg, whereas control RBC-EVs showed no dose-related differences (Figure 6.15). Although these studies do not specifically address autophagy, the observed response pattern is consistent with general dose-dependent cellular effects of EVs reported across multiple *in vitro* systems, where the magnitude and nature of cellular responses scale with EV concentration and are strongly influenced by vesicle origin (251–253).

The early increase in LC3 observed at 10 minutes for both *P. berghei*-EVs and control EVs suggests that EVs, irrespective of their source, are potent bioactive complexes rapidly recognized by endothelial cells. This rapid engagement is consistent with their role as key intercellular messengers; for instance, uptake of both RBC and *P. falciparum*-derived EVs by other RBCs has been demonstrated within 15 minutes (254). Therefore, the early LC3 response likely reflects a generalized endothelial reaction to vesicular uptake, while the subsequent, specific impairment of flux may be driven by the unique pathogenic cargo of *P. berghei*-EVs.

This interpretation fits within the wider understanding of RBC-derived EVs, the most abundant vesicle population in circulation. Under physiological conditions, they are key modulators of endothelial homeostasis and barrier integrity (165, 255). However, in pathological contexts such as diabetes, cardiovascular disease, or, as suggested here, malaria, their cargo can become dysregulated and promote endothelial dysfunction (256, 257). The *in vivo* importance of this vesicular crosstalk is underscored by studies like that of Verweij et al. in zebrafish, where disrupting exosome release impaired vascular development, highlighting their essential role in intercellular communication (258).

The mechanisms underlying autophagic flux impairment by *P. berghei*-EVs may overlap with those of iRBCs, but a key difference is the rapidity of the EV-induced response, facilitated by efficient endothelial uptake. One plausible pathway is LC3-associated phagocytosis (LAP) or its related process, LC3-associated endocytosis (LANDO). Unlike canonical autophagy, both involve the direct conjugation of LC3 to the single membrane phagosome or endosome, a mechanism that accelerates cargo degradation by promoting acidification and fusion with lysosomes. This pathway is engaged during the internalization of various cargos, including pathogens, apoptotic bodies, and protein aggregates (259, 260). Therefore, the quick LC3 recruitment observed with EVs could reflect the initial engagement of this rapid-clearance machinery.

This mechanism has already been documented in *Plasmodium* infections. For instance, during the hepatic stage of *P. vivax*, a subset of sporozoites is targeted by a LAP-like response in hepatocytes, requiring Beclin-1, PI3K, and Atg5 (130). More directly relevant to endothelial responses, *P. berghei*-derived EVs have been shown to be internalized by astrocytes via LAP. In this model, inhibition of LAP with 3-methyladenine blocks EV uptake, while impairment of lysosomal acidification with bafilomycin leads to intracellular accumulation of EVs and prevents cerebral malaria pathology in mice (133, 134).

This evidence suggests that the pathogenic effect of *P. berghei*-EVs depends on their efficient internalization, potentially via lipid raft-dependent or LAP-like pathways, and the subsequent lysosomal processing of their cargo (261). These findings align with this study model: the rapid LC3 response likely reflects immediate vesicle uptake, while the sustained impairment of autophagic flux indicates a failure in the complete degradation of internalized contents. This lysosomal impairment could lead to endothelial dysfunction through two non-exclusive mechanisms: the intracellular accumulation of undegraded material, as seen in some lysosomal storage disorders, or the pathological release of pro-inflammatory mediators during incomplete degradation, which can further disrupt autophagic flux (262–264).

Parasite-derived EVs carry a diverse repertoire of bioactive molecules that have been implicated in malaria pathogenesis. In *P. berghei*, EV-associated miRNAs promote the release of pro-inflammatory cytokines such as TNF upon uptake by macrophages, contributing to inflammatory amplification. Similarly, in *P. falciparum*, elevated levels of circulating parasite-derived EVs correlate with severe disease and vascular dysfunction, largely attributed to the presence of miRNA-Ago2 complexes capable of modulating host gene expression and altering endothelial barrier function, cytokine production, and vascular integrity (167).

In addition, *P. berghei*-derived EVs have been shown to exacerbate liver pathology during blood-stage infection by driving excessive inflammatory responses and promoting macrophage polarization toward a pro-inflammatory M1 phenotype through miRNA delivery (265). In contrast, non-canonical autophagy pathways such as LC3-associated phagocytosis (LAP) have been described as protective and anti-inflammatory in other infectious contexts, including fungal infections (266). This contrast raises the possibility that EV-induced engagement of autophagy-related pathways during malaria may initially serve a homeostatic function but become subverted by pathogenic cargo, or alternatively, directly contribute to inflammatory pathology. However, the precise role of LAP and related pathways in *Plasmodium* infection remains unresolved.

However, it is critical to acknowledge that the properties of EVs secreted by parasites or host cells are highly dependent on their metabolic state and the specific culture conditions. Consequently, EV preparations are inherently heterogeneous, comprising subpopulations that vary in size, molecular composition, and biophysical properties. For instance, studies in *P. falciparum* have identified at least two distinct EV subpopulations with different sizes, protein profiles, membrane rigidity, and fusion capacities, indicating they may have specific cellular targets and functions (83, 267). This intrinsic heterogeneity poses a significant challenge for ensuring strict reproducibility between experiments and complicates the attribution of biological effects to a single, defined vesicular entity.

Therefore, two important considerations should be noted regarding these EV preparations. First, the *P. berghei*-EV fraction represents a mixture of vesicles derived from both the parasite and the host RBC, as well as NVEPs, as no specific purification step was used to isolate exclusively parasite-derived EVs. Consequently, the observed effects may result from a combined or dominant influence of RBC-EVs or NVEPs, and the relative contribution of genuine parasite EVs remains unclear. Second, the method of dosage itself presents a challenge. Dosing by total protein concentration, while common, may not accurately reflect bioactive cargo, as it can underestimate non-protein components (e.g., lipids, nucleic acids) and be contaminated by residual medium proteins or batch variability. The use of particle concentration is increasingly recommended to standardize EV dosing and improve reproducibility in future studies (148, 253, 268).

Finally, the culture supernatant derived from *P. berghei*-iRBCs represents one of the most complex and heterogenous fractions examined in this study. In contrast to intact iRBCs or enriched EVs, it contains only soluble molecules, ranging from small metabolites and inflammatory mediators to lipid byproducts and low-molecular-weight proteins released during parasite growth and RBC lysis, as well as smaller EVs. Its inherent heterogeneity results in a dynamic and multifaceted cellular response, thereby enabling the exploration of a distinct dimension of host-parasite communication.

Similar to the other two tested stimuli, the *P. berghei*-derived supernatant increased LC3-positive vesicles and reduced autophagic flux. This response occurred rapidly, like the effect of EVs. However, the supernatant elicited a distinct and irregular kinetic profile. Unlike the more consistent responses to iRBCs or EVs, the difference between the parasite-derived and control supernatants showed an oscillatory pattern over time, with periods of statistical significance alternating with periods of no significant difference. Importantly, this oscillatory behavior was reproducible across both tEnd.1 reporter cell lines (LC3-GFP and the tandem LC3-GFP-mCherry) as shown in Figures 6.16 and 6.21, respectively.

A primary explanation for the distinct kinetic response may lie in the compositional difference between the culture media. tEnd.1 cells were maintained in standard RPMI, while the applied supernatant was derived from *P. berghei* cultures grown in the nutrient-rich Jambou's formulation (a mixture of RPMI and DMEM-F12 supplemented with glucose, sodium bicarbonate, calcium, choline, gelatin, and hypoxanthine) (144). Beyond adjustments for pH and serum, the glucose concentration is substantially higher in Jambou's medium.

Glucose is a critical regulatory metabolite in autophagy, as high concentrations can suppress the pathway by inhibiting AMPK and by inducing osmotic and oxidative stress, potentially triggering an adaptive response in endothelial cells (162). In the context of the *P. berghei* supernatant, the autophagic outcome likely represents the net effect of competing signals. Pro-inflammatory factors released from lysed iRBCs, such as hemozoin and oxidized lipids, may stimulate the pathway, while the high glucose content of Jambou's medium may simultaneously exert an inhibitory force (241, 244, 245).

This dynamic interplay between inducer and suppressor molecules within the complex supernatant could explain the oscillatory and less predictable autophagic response observed. This presents an intriguing question: does this fluctuation represent an adaptive cellular response to multiple soluble signals, or does it reflect inherent instability in the autophagic signaling pathway under these "different" conditions?

Several studies investigating the effects of *Plasmodium*'s secretome in clinical samples, particularly from patients with complicated and uncomplicated malaria, have demonstrated that direct contact with iRBCs is not required to elicit a proinflammatory response in endothelial cells. For instance, serum from *P. falciparum*-infected patients has been shown to upregulate inflammatory cytokines and significantly affect key endothelial processes such as cell migration, proliferation, and tube formation. This inflammatory phenotype is often accompanied by cytoskeletal reorganization, leading to increased vascular permeability (269–271).

Notably, this effect on endothelial integrity has been partly attributed to kinins secreted into *P. falciparum*-conditioned medium, which act via bradykinin B2 and/or B1 receptors. These mediators not only enhance iRBC adhesion to the endothelial monolayer but also impair endothelial junctional proteins such as zonulin and β-catenin, thereby compromising blood-brain barrier (BBB) integrity (271, 272). These findings highlight the potent role of soluble parasitic factors in driving endothelial dysfunction and vascular pathology during malaria infection.

On the other hand, an interesting comparison was made between the crude supernatant (collected before EV enrichment) and the EV-reduced supernatant (obtained after ultracentrifugation). The expectation was that the crude supernatant would induce a stronger LC3 recruitment, given that it contains the full spectrum of EVs, which alone have been shown to significantly increase LC3-positive vesicles. However, no significant differences in LC3 expression were observed between these two fractions, neither in the *P. berghei*-derived samples nor in their corresponding controls (Figure 6.17).

This result suggests that soluble factors present in the supernatant, rather than EVs, may be the primary mediators of the autophagic modulation observed under these conditions. One possible explanation is that the concentration of EVs in the crude supernatant was insufficient to elicit a detectable response beyond that induced by soluble components, especially when compared to the highly enriched EV preparations used in earlier experiments. Alternatively, the complex composition of the supernatant, particularly the marked difference in medium formulation and the potential balance between autophagy activators and inhibitors, could have masked or modulated EV-specific effects. Such a dynamic equilibrium of stimulatory and suppressive signals might explain why EV partial removal did not significantly alter the overall autophagic response.

The impact of EV-reduced culture media has been investigated in various cellular systems, particularly concerning FCS, which in standard conditions constitutes a significant exogenous source of EVs. In EV research, it is recommended to use EV-depleted FCS to avoid confounding effects, a limitation in the present study, as non-depleted FCS was employed throughout all stimulation assays. Importantly, while serum-derived EVs have been reported to modulate general cellular signaling, there is no consistent evidence that FCS-derived EVs alone induce sustained autophagic flux activation or impairment (148, 273).

Importantly, the use of EV-reduced media has been shown to alter endothelial cell physiology: it increases apoptosis rates, elevates IL-8 secretion, reduces IL-6 production, and modifies the protein profile of endothelium-derived EVs toward pathways related to cell adhesion and platelet activation (274). These findings underline that EV content in culture media can actively shape cellular responses, and thus, the presence of serum-derived EVs in these supernatant preparations may have influenced the autophagic and inflammatory outcomes observed.

However, the specific impact of EV enrichment on the biological activity of the original matrix, especially in the context of parasitic infections, has not been explored. To better distinguish between the roles of soluble factors and EVs in our model, future experiments should use EV-depleted culture media. This would help clarify whether the effects we observed come from *P. berghei*-derived soluble molecules, host or serum-derived EVs, or a combination of both.

Altogether, the present results indicate that *P. berghei*-derived stimuli do not enhance autophagic activity, but rather trigger a state of impaired autophagic flux, characterized by autophagosome accumulation without progression to lysosomal degradation. This impairment manifested distinctly depending on the stimulus: iRBCs induced a sustained, moderate, and likely adhesion-dependent response; EVs triggered a rapid and potent inhibition of autophagic flux, possibly due to their efficient uptake and specific targeting of LC3-related pathways; while the supernatant elicited an inconsistent and temporally variable effect, likely influenced by differences in medium composition and the presence of soluble regulators. The main upstream triggers associated with these effects are summarized in Figure 7.1A, while the downstream cellular mechanisms proposed to interfere with autophagic flux are depicted in Figure 7.1B.

Although this experimental approach allowed the individual contributions of each stimulus to be dissected, under physiological conditions endothelial cells are simultaneously exposed to a combination of all these factors which may amplify or modulate the observed autophagic response observed in this study.

These findings suggest that endothelial autophagic pathways may represent an underappreciated mechanism in the vascular complications associated with malaria. However, whether autophagy serves a protective or pathological role in endothelial cells during the blood stage of the disease remains to be elucidated, as does the nature of the crosstalk between autophagic and inflammatory signaling pathways in the context of malaria, as conceptually framed by the trigger-mechanism model presented in Figure 7.1.

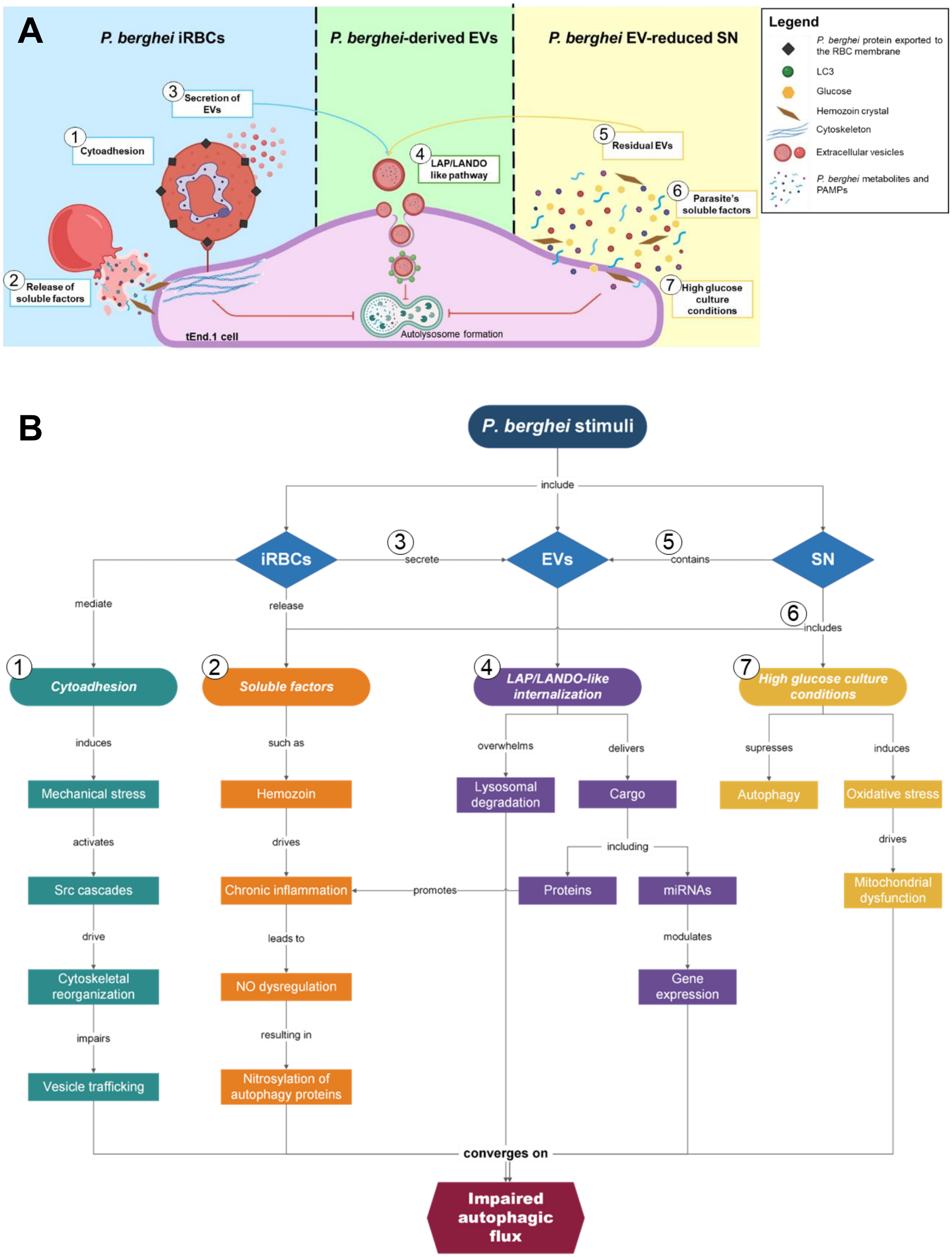

Figure 7.1. Proposed triggers and mechanisms underlying autophagic flux impairment in tEnd.1 endothelial cells exposed to *Plasmodium berghei*-derived stimuli. (A) Schematic representation of the putative triggers derived from *P. berghei*'s iRBCs, EVs, and SN that may interfere with endothelial autophagic flux. (B) Mechanistic framework connecting *P. berghei*-derived stimuli to impaired autophagic flux. iRBCs display parasite-exported proteins on the RBC membrane that enable adhesion to endothelial cells ①, generating mechanical stress that activates Src signaling cascades. This leads to cytoskeletal remodeling and ultimately impairs vesicular trafficking. In parallel, parasite egress from iRBCs results in the release of soluble and virulence factors, such as hemozoin ②, which drive chronic inflammation, NO dysregulation, and nitrosylation of key autophagy regulators, including mTOR and cathepsins. In addition, parasites secrete EVs ③, which are rapidly internalized through LAP/LANDO-like pathways ④. Once internalized, EVs become LC3-coated and are targeted for lysosomal degradation, potentially overwhelming lysosomal capacity and enabling cargo release. EV cargo includes proteins that promote inflammation, similar to soluble factors, and miRNAs that modulate host gene expression. The parasite-derived SN may also contain residual EVs ⑤ and soluble factors ⑥ acting through comparable mechanisms. Importantly, high-glucose culture conditions ⑦, independent of parasite-derived stimuli, suppress autophagy via AMPK inhibition and induce oxidative stress, leading to mitochondrial dysfunction. Collectively, these mechanisms converge on impaired autophagic flux. RBC: red blood cell; iRBC: infected RBC; EV: extracellular vesicle; SN: supernatant; NO: nitric oxide.

7.5. Decoding *P. berghei* EVs: first evidence of protein cargo enriched in virulence factors and cellular machinery. Extracellular vesicles (EVs) have emerged as crucial mediators of intercellular communication in malaria, as well as for other infectious and chronic diseases, potentially influencing parasite biology, host cell remodeling, and disease pathogenesis (79, 84, 166, 208). While EVs from the human malaria parasite *P. falciparum* have been relatively well-studied, the physical and molecular characteristics of EVs from rodent malaria models, such as *P. berghei*, remain less defined. This study provides the first integrated analysis of small EVs produced by *P. berghei* from *in vitro* cultures, combining physical characterization with proteomic profiling.

According to the MISEV guidelines, the rigorous physical and molecular characterization of enriched vesicle preparations is essential to define the studied population, ensure reproducibility, and allow for meaningful cross-study comparisons (148, 209). A cornerstone of this characterization is the assessment of vesicle size distribution and concentration, parameters that define the "extracellular vesicle" umbrella term which distinctions exosomes and ectosomes, from other extracellular particles.

In this study, Dynamic Light Scattering (DLS) was employed as a primary technique to determine the hydrodynamic size distribution and particle concentration of vesicles isolated from *P. berghei*-infected and control RBCs cultures. DLS provides a robust, ensemble-averaged measurement of particles in suspension, which is recommended for initial population profiling (148, 275). The results revealed a heterogeneous population with three modal sizes with approximate diameters of 25 nm, 100 nm, and 400 nm (Figure 6.22), a finding that underscores the complexity of EV preparations even from defined *in vitro* systems.

It is important to note that DLS provides reliable size measurements primarily for monodispersed suspensions. In highly polydisperse samples, the accuracy is reduced because larger particles disproportionately scatter light, skewing the intensity-weighted distribution (275). To mitigate this inherent limitation and obtain more representative data, the EV suspension was prepared in filtered PBS and passed through a 0.22 µm filter immediately prior to analysis.

However, polydispersity index (PDI) values exceeding 0.4 in both conditions indicate a high degree of polydispersity. In DLS analyses, PDI values ≤0.1 are considered highly monodisperse, values between 0.1 and 0.4 indicate moderate polydispersity, and values >0.4 reflect highly polydisperse samples (276, 277). This degree of heterogeneity suggests substantial size variability and is consistent with the potential co-isolation of vesicle aggregates or non-vesicular material, a common limitation in EV preparations derived from complex biological sources.

Furthermore, the difference between the intensity-weighted size distribution and the particle concentration profile (Figure 6.22) is a well-documented phenomenon in DLS analysis of polydisperse samples. Because the intensity of scattered light is proportional to the particle diameter, larger vesicles (100 nm and 400 nm) dominate the intensity signal even if they are less abundant numerically (278, 279). Conversely, the concentration plot reveals the true numerical predominance of smaller nanoparticles (25 nm), which scatter light weakly. This pattern has been consistently observed in EV studies, using different techniques, where intensity-based measurements often highlight a population of exosome-sized vesicles, while concentration-based techniques uncover a greater abundance of smaller particles, co-isolates, and/or aggregates (152, 280). Therefore, both parameters provide a more comprehensive representation of the heterogeneous EV preparation.

Based on this information and previous reports, the size distribution of EVs isolated from *P. berghei* cultures aligns with the heterogeneous populations documented in studies of both *Plasmodium* and RBCs. The predominant population, centered around 100 nm, corresponds to small exosome-like vesicles commonly described in *P. falciparum* cultures and released from human RBCs using various techniques (83, 281, 282). In contrast, the larger population (400 nm) likely represents *in situ* vesicle aggregates, as individual vesicles of this size should have been removed during the 0.22 μm filtration step. This finding is consistent with the high PDI and the low magnitude of the zeta potential, which indicates limited electrostatic repulsion between particles. The minor peak at 25 nm may correspond to very small EVs, co-isolated lipoproteins and other NVEPs, or debris, a known consideration in EV studies from blood-derived samples (211, 283).

Another DLS study of murine malaria analyzed EVs isolated from the plasma of *P. yoelii*-infected mice. The study measured the size of EVs from infected and control mice on days 7, 8, and 9 post-inoculation, reporting mean sizes of 145.1 nm, 162.2 nm, and 138.7 nm for the infected group, and 141.3 nm, 136.7 nm, and 129.4 nm for the control group, respectively. The study also reported high PDI values, ranging from 0.309 to 0.685 for infected mice and from 0.706 to 0.709 for the controls (284). It is important to note that, unlike EVs from culture systems, which originate almost exclusively from RBCs and parasites, plasma-derived EVs constitute a heterogeneous population originating from many cell types throughout the organism.

Nanoparticle Tracking Analysis (NTA) studies of *P. falciparum* cultures have consistently identified heterogeneous EV subpopulations. For example, Vimonpatranon et al. reported two distinct vesicle populations with mean sizes of (97.9 ± 8.1) nm for exosomes and (159.7 ± 27.2) nm for microvesicles (285). Furthermore, Opadokun et al. demonstrated that EV size distributions vary with the parasite's developmental stage, reporting mean diameters of 159.7 nm for rings, 116.9 nm for trophozoites, 148.6 nm for schizonts, and 134.6 nm for control RBCs (281). Complementary data from Tunable Resistive Pulse Sensing (TRPS) of RBC cultures also reveal a bimodal distribution, with populations centered around 80-100 nm and 160-200 nm (282). Collectively, these reports corroborate the DLS findings of multiple EV populations and underscore the inherent size heterogeneity of vesicles released from both infected and non-infected RBCs.

Additionally, the measured zeta potential of approximately -12 mV for both *P. berghei*-derived and control EVs indicates low to moderate colloidal stability in PBS, suggesting a propensity for vesicle aggregation over time. This negative surface charge, typical of biological nanoparticles, originates from ionizable groups on membrane lipids and adsorbed proteins. It is important to note that buffer composition significantly influences zeta potential; higher ionic strengths are known to compress the electrical double layer, shifting values toward less negative potentials (286). In the present study, zeta potential was therefore measured in isotonic PBS to preserve EV integrity. Although a 1:5 dilution of PBS in deionized water was initially tested in an attempt to reduce ionic strength, this condition led to osmotic lysis of the EVs.

Reported values for EVs from human RBCs vary, with some studies indicating potentials around (-36 ± 8) mV and others around -19 mV (287, 288). In case of *Plasmodium*, there is no data available on zeta potential measurements in EVs produced by the parasite, since literature reports that include zeta potential values of EVs of parasitic origin are very scarce, particularly for obligate intracellular protozoa. The limited available data for other parasites include values such as (-12.2 ± 4.8) mV for *Naegleria fowleri;* (-16 ± 4) mV and (-18 ± 8) mV for trypomastigote and epimastigote forms of *Trypanosoma cruzi*, respectively; and a range of -0.86 to -6.38 mV for EVs isolated from the plasma of *P. yoelii*-infected mice (147, 284, 289).

However, it is known that *P. falciparum* infection alters the RBC membrane potential; for example, Tokumasu et al. reported a shift from -15.7 mV in healthy RBCs to -14.6 mV in iRBCs (290). Because *Plasmodium*-derived EVs are enveloped by the host RBC membrane, such infection-induced changes could moderately influence their zeta potential and potentially affect EV-cell interactions and uptake, although the functional consequences of these alterations remain largely unexplored.

EVs isolated from *P. berghei*-infected cultures exhibited mean hydrodynamic size and zeta potential values comparable to those of control RBC-derived EVs (Table 6.1), in agreement with previous DLS- and NTA-based studies. Similar overlap in size and surface charge has been reported for *P. yoelii*-derived EVs, with minimal differences between control and infected samples at early stages of infection, although more pronounced changes emerge at later time points (284). Likewise, EVs from *P. falciparum*-iRBCs display broad, stage-dependent size distributions that substantially overlap with control EV populations, highlighting the limited discriminatory power of bulk physical parameters alone (281).

The similar mean hydrodynamic sizes and zeta potentials measured for both *P. berghei*-derived and control EVs by DLS likely result from a combination of methodological and biological factors. Discrepancies with sizes reported in other studies can be attributed to differences in isolation and measuring techniques (e.g., sucrose cushion vs. ultracentrifugation or NTA vs DLS), the measurement principle of DLS, which is biased toward larger particles in polydisperse suspensions, and inherent biological variations between parasite species (*P. berghei, P. yoelii* or *P. falciparum*).

Furthermore, several specific scenarios may explain the observed similarity in physical parameters such as size and zeta potential. First, given that the cultures had a parasitemia of approximately 3-5%, EVs originating from the vastly more numerous uninfected RBCs could have dominated the suspension. In such a polydisperse mixture, DLS lacks the sensitivity to resolve and quantify distinct subpopulations, potentially masking a less abundant, specific population of parasite-induced vesicles (278, 279). Second, since *P. berghei*-derived EVs are enveloped in the host RBC membrane, their fundamental physical properties, such as size and surface charge, may not differ notably from those of EVs budded directly from healthy RBCs. This shared membrane architecture could result in overlapping hydrodynamic and electrokinetic profiles, making the two populations indistinguishable by bulk measurement techniques like DLS.

Dynamic Light Scattering is a widely accessible technique recommended by MISEV guidelines for initial particle size profiling, providing a rapid assessment of the mean hydrodynamic diameter and polydispersity of EV suspensions in their native state (68, 148). However, its significant limitation is an intensity-based bias that overrepresents larger particles due to the light-scattering dependence, making it less suitable for determining absolute concentration or resolving complex subpopulations in polydisperse samples (278). For this reason, the MISEV guidelines recommend complementing DLS with single-particle analysis techniques. NTA would enable a direct visual count and concentration measurement of individual vesicles, while TRPS could offer higher-resolution size data and concurrent zeta potential analysis on a particle-by-particle basis (280). Employing an integrated approach would be essential to accurately quantify subpopulations, ascertain the true concentration of parasite-specific EVs, and achieve a better understanding of the physical heterogeneity in *Plasmodium* EV preparations.

Simultaneously, Atomic Force Microscopy (AFM) was employed to provide direct and high-resolution topographical imaging of individual vesicles (291, 292). Unlike ensemble or diffusion-based methods, AFM enables the physical visualization and morphological validation of EVs adsorbed onto a substrate, offering information like their spherical morphology, structural integrity, and the presence of possible aggregates or non-vesicular contaminants that may remain undetected by light-scattering techniques (292). This approach allows for the corroboration of the size profiles obtained by DLS with direct imaging at the single-particle level, thereby addressing two key limitations of DLS in polydisperse EV samples: first, the intensity-based bias that overrepresents larger particles due to their stronger light-scattering signal; and second, size overestimation due to the fact that DLS measures the hydrodynamic diameter (278, 279, 292).

The low-magnification topographical map (Figure 6.23A) provided the first direct visual evidence of a heterogeneous population of isolated nanoparticles deposited across the mica substrate. This image confirmed the successful isolation of a particulate fraction and supports the high PDI observed in DLS. Beyond confirming vesicular morphology and structural heterogeneity, the AFM topographs may reflect underlying biological diversity in vesicle biogenesis and cargo loading as previously reported in *P. falciparum* (83). The presence of vesicles with varying degrees of lateral spreading and cap geometry suggests differences in membrane composition, rigidity, or surface protein density, which could influence their interaction with the substrate and, by extension, with target cells *in vivo* (293). Subsequently, the three-dimensional rendering (Figure 6.23B) offered unambiguous confirmation of the spherical, cap-shaped morphology typical of EVs adsorbed onto a solid support, allowing a single-particle, morphological verification (294).

The direct height measurements obtained by AFM of individual EVs revealed that the adsorbed vesicles ranged from approximately 14 to 49 nm (Figure 6.23D).

Importantly, these height values are notably lower than the mean hydrodynamic diameter of approximately 100 nm determined by DLS (Figure 6.22, Table 6.1). This discrepancy is expected and well-documented when comparing dry-state AFM measurements with solution-based light scattering techniques (295). The DLS intensity-based bias causes the signal from larger vesicles to disproportionately influence the size distribution, in polydisperse samples (278). Furthermore, the hydrodynamic diameter encompasses contributions from the particle core as well as its hydration shell, thereby overestimating the particle size by up to 20 nm compared with the physical dimensions (296).

In contrast, AFM performed on air-dried samples captures the physical height of the vesicle core after dehydration and adsorption onto a solid substrate. This process leads to vesicle collapse, flattening, and the loss of the solvation layer, resulting in smaller measured dimensions. The electrostatic forces that immobilize EVs on the mica surface also distort their shape from globular geometry to a cup-shape geometry, which is recognized as a sample preparation artifact (297).

Hence, the measured height of the EVs represents a conservative, but underestimate of their native vertical dimension due to deformations induced during sample preparation and imaging (297). Furthermore, even when operating in tapping mode to minimize vertical force, the finite tip-sample interaction can induce additional nanoscale compression of the EVs' upper membrane, particularly for highly deformable structures (298, 299).

In contrast, the width of the EVs were approximated from the full width at half maximum (FWHM) of the cross-sectional height profiles, yielding values between 82 and 100 nm (Figure 6.23D). These values are larger than the height measurements and are close to the dimensions obtained by DLS analysis. However, these lateral dimensions are predominantly enlarged by the tip convolution effect, a well-characterized artifact in AFM. The imaging tip, with a finite radius of curvature, interacts with the sides of the nanoparticle before reaching its apex, resulting in a broadened topographic profile that overestimates the true particle width (163). The degree of broadening depends on tip geometry and particle height. Additionally, the soft, adhesive nature of EV membranes promotes lateral spreading on the hydrophilic mica surface, further contributing to an increased footprint (293, 300).

Thus, while height is preferable for reporting vesicle size in the dry state, neither metric alone accurately captures the native hydrodynamic diameter; instead, they should be interpreted together as indicators of vesicle morphology, deformability, and adsorption behavior, ideally complemented by solution-based techniques such as DLS or NTA (148, 297).

For instance, AFM analysis of two subpopulations (F3 and F4) of *P. falciparum*-derived EVs isolated from culture was reported by Abou Karam et al. AFM measurements performed in liquid (PBS) revealed average diameters of (26 ± 14) nm for F3-EVs and (69 ± 46) nm for F4-EVs. In comparison, cryo-TEM yielded slightly larger average diameters of (55 ± 11) nm for F3-EVs and (108 ± 53) nm for F4-EVs (83). Collectively, these findings demonstrate that methodological variations in sample preparation, imaging conditions, and inherent resolution among microscopy platforms can introduce systematic discrepancies in the reported dimensions of EVs (292). This underscores the necessity for a multimodal analytical framework to accurately resolve vesicle size and ultrastructure.

Consequently, the application of DLS and AFM has provided a complementary and multi-faceted first physical characterization of *P. berghei*-derived small EVs. DLS established the bulk hydrodynamic profile of the EV suspension, revealing a polydisperse population with a mean hydrodynamic diameter of approximately 100 nm and a low surface charge consistent with colloidal vesicles in a biological buffer. Conversely, AFM provided the essential nanoscale morphological validation, confirming the isolation of discrete, spherical nanoparticles and providing direct, single-particle measurements that avoid the intensity-based bias inherent to light-scattering techniques. Notably, the dimensions obtained by AFM (heights of 14-49 nm; width of 82-100 nm) were consistently smaller than those reported by DLS, a direct consequence of fundamental methodological differences. This orthogonal strategy aligns with MISEV guidelines for initial EV characterization (68, 148) and establishes that the isolated material comprises a heterogeneous population of nano-sized, membranous structures morphologically consistent with small EVs.

Once the physical and morphological identity of the isolated nanoparticles was established as being consistent with small EVs, confirming their enrichment from the *P. berghei* culture supernatant, their protein composition and biological cargo were subsequently characterized to gain insight into their potential functional roles. Accordingly, biochemical and proteomic profiling was performed, beginning with comparative SDS-PAGE analysis of EV fractions relative to their corresponding supernatants, followed by liquid chromatography-tandem mass spectrometry (LC-MS/MS) to comprehensively identify *P. berghei*-derived proteins within the EVs enrichment fraction.

The initial biochemical characterization was performed using SDS-PAGE, which provided a first-level assessment of their protein content and purity relative to the source supernatant. The electrophoretic profiles (Figure 6.24) revealed distinct banding patterns between the EV-enriched fractions and their corresponding EV-reduced supernatants, further confirming the successful enrichment of a protein-rich vesicular fraction. Notably, a prominent band at approximately 95 kDa was consistently observed exclusively in the EV lanes from both *P. berghei* and control RBC preparations (Figures 6.24A and 6.24B). In addition, a differential banding pattern was evident in the lower molecular weight region (17-34 kDa), where several distinct bands were present in the control RBC-EV lane but appeared reduced or absent in the *P. berghei* EV lane. The absence of these bands in the corresponding supernatant lanes strongly suggests preferential association with EVs rather than co-isolation of soluble proteins, supporting the vesicular nature of the preparation.

Some potential protein candidates corresponding to these EV-exclusive bands can be proposed based on their apparent molecular weight and reported association with EVs. In the ~95 kDa region, possible candidates include conserved vesicle-associated proteins such as heat shock proteins (e.g., HSP90), which are frequently enriched in EVs across diverse biological systems; the ESCRT-associated protein Alix, a well-established exosome marker; or the RBC membrane structural protein Band 3, which has previously been identified in RBC-derived EVs (68, 148). For the 17-34 kDa molecular weight range, potential candidates include canonical exosome-associated proteins such as tetraspanins (e.g., CD63, CD81), as well as other RBC-related proteins, including annexins or glycophorins, which are commonly reported in RBC-derived EVs (68, 148, 301, 302).

However, the presence of classical exosome markers as defined by the MISEV guidelines is unlikely in EVs derived from mature RBCs, as these enucleated cells lack the endosomal trafficking machinery required for canonical exosome biogenesis (301). Furthermore, comprehensive genomic and proteomic analyses have thus far failed to identify homologs of key ESCRT-related proteins, including tetraspanins and Alix, in *Plasmodium* genome (303). This observation reinforces the growing evidence suggesting that EV biogenesis pathways in protozoan parasites diverge significantly from the canonical models established in most eukaryotic cells, especially those of mammalian origin (80, 168).

While the SDS-PAGE analysis revealed differential banding patterns from EV fraction and their corresponding supernatants, this technique possesses inherent limitations that constrain a deeper biological interpretation. Primarily, SDS-PAGE provides solely a separation based on molecular weight, offering no information on protein identity, post-translational modifications, or relative abundance beyond visual band intensity (304). Consequently, any proposed protein assignments remain speculative and rely exclusively on apparent molecular weight, a parameter that can be influenced by factors such as protein complex formation or detergent binding (305). Furthermore, the limited sensitivity of gel-based protein detection methods, on the order of 10-100 ng for Coomassie staining and 1-10 ng for silver staining, particularly for low-abundance proteins, suggests that the observed gel profiles likely reflect only the most abundant EV-associated proteins, potentially overlooking critical low-abundance regulators or parasite-derived effectors. Finally, the presence of background bands, particularly in silver-stained gels, can complicate the distinction between genuine EV cargo and co-isolated contaminants (306).

To overcome these limitations and advance to definitive molecular identification and quantification, LC-MS/MS, an unbiased and high-sensitivity proteomic approach, was employed. This analysis was designed to comprehensively catalogue the protein cargo of *P. berghei*-derived EVs, validate the presence of hypothesized protein candidates, identify parasite-specific components, and functionally classify the vesicular proteome in order to infer its biological origin and potential roles.

The LC-MS/MS analysis provided evidence of successful enrichment of an EV-associated proteome. A marked disparity in protein identifications was observed between the small EV fraction and the corresponding EV-reduced supernatant. Specifically, 60 *P.*

berghei proteins were identified in the small EV fraction, compared to 14 in the matched supernatant (Figure 6.25A). Notably, 48 of the EV-associated proteins (80%) were detected exclusively in the EV fraction, corroborating the electrophoretic observations of EV-specific protein bands. Importantly, only two proteins were exclusively detected in the EV-reduced supernatant, including a Niemann-Pick type C1-related protein involved in lipid transport and membrane biogenesis and one uncharacterized protein.

A similar pattern was observed for host (*M. musculus*) proteins, with a total of 105 proteins identified, of which the majority (70%) were exclusive to the EV fraction (Figure S.3A). The limited overlap of shared proteins likely reflects a subset of highly abundant host proteins present in both fractions and/or, a minor contribution from residual small EVs remaining in the supernatant.

Briefly, characterization of the host-derived protein component in *P. berghei* EV preparations revealed multiple *M. musculus* proteins previously reported as markers or common constituents of RBC-derived EVs (Tables S1 and S2). These include canonical RBC membrane and cytoskeletal proteins such as band 3, ankyrin-1, protein 4.1, α- and β-spectrin, and dematin, which play crucial roles in maintaining membrane integrity and mechanical properties. Additionally, cytoplasmic proteins highly abundant in RBCs, like hemoglobin subunits, carbonic anhydrase 1, heat shock proteins, and peroxiredoxin-2, were also identified, aligning with their frequent presence in RBC-derived EV cargo due to their high intracellular concentration (165–167). While mature RBCs and *Plasmodium* parasites lack the canonical endosomal machinery for classical exosome biogenesis, previous studies have reported the presence of tetraspanins in EVs derived from *P. falciparum* cultures (281).

Gene Ontology (GO) enrichment analysis of the *M. musculus* proteins identified in the EV fraction provided functional and origin-related insights. The most significantly enriched biological processes were associated with hemostasis and responses to vascular damage, including "regulation of blood coagulation," "regulation of wound healing," "platelet aggregation," and "platelet activation" (Figure S.3B). In addition, the enrichment of processes such as "proteasome core complex" (Figure S.3C) suggests the presence of protein degradation machinery within or associated with the vesicles. These findings are consistent with previous reports describing RBC-derived EVs as functionally linked to hemostasis, coagulation, and proteasome-related activity (255, 307, 308).

On the other hand, the proteomic profile of *P. berghei*-derived EVs remains largely uncharacterized, with no published data available from either *in vivo* or *in vitro* studies during blood stage. In contrast, most of the existing knowledge is derived from research on *P. falciparum*, though the reported EV proteomes vary considerably across studies, both in terms of the number and identity of proteins identified. For instance, the reported number of *P. falciparum* proteins in EVs ranges from as few as 20 to as many as 387, while host (human) proteins identified in the same preparations vary from approximately 80 to over 300 (83, 166, 285, 301, 307, 309, 310). These studies analyzed EVs isolated from culture supernatants via ultracentrifugation and employed different parasite strains (e.g., 3D7, NF54, CS2), further complicating cross-study comparisons due to potential strain-specific variations in EV cargo. Notably, these published works restricted their analysis to the EV fraction itself, without examining the corresponding EV-depleted supernatants, limiting the ability to distinguish between genuine vesicular cargo and co-isolated soluble proteins or NVEPs.

In murine malaria models, only one proteomic study of EVs has been reported to date: De Sousa et al. characterized EVs isolated from plasma of mice infected with *P. yoelii* 17XNL, identifying 40 parasite proteins, 23 of which were uncharacterized, and 360 host proteins (284). However, plasma represents a highly complex biological matrix containing EVs derived from diverse host cell types, which complicates the enrichment and characterization of EVs originating exclusively from iRBCs. This highlights a major gap in the field, namely the lack of systematic proteomic studies of EVs from rodent malaria species, especially using *in vitro* systems. Such controlled settings allow parasite-derived EVs to be examined against a defined supernatant background, making it easier to confidently attribute vesicular cargo to the parasite during the blood stage of infection.

Protein classification based on UniProt annotations show that most proteins (70%) were classified as soluble while membrane-associated proteins constitute a smaller, yet significant, proportion (25%); and the remaining 5% were unclassified (Figure 6.25B). Although protein solubility is not a common classification criterion in other studies, the high percentage of soluble proteins aligns with several proteomic analyses of *Plasmodium*

EVs. For instance, studies of EVs from iRBCs frequently report a substantial proportion of cytosolic proteins, such as metabolic enzymes, chaperones, ribosomal proteins, and translation factors (83, 166, 284, 301, 310). In contrast, other authors report a higher proportion of membrane-associated proteins. These include GPI-anchored proteins like MSP-1, proteins associated with apical organelles (rhoptries, micronemes, dense granules), and proteins involved in RBC remodeling localized to structures such as Maurer's clefts (307, 309).

While the classification in Figure 6.25B indicates that soluble proteins constitute the majority of the identified *P. berghei* EV proteome, it is crucial to consider the methodological biases inherent to the proteomic workflow. The standard sample preparation for LC-MS/MS typically involves protein solubilization and digestion in aqueous buffers, a process that is notoriously inefficient for integral membrane proteins, particularly those with multiple transmembrane domains. These hydrophobic proteins are often under-represented or entirely missed due to poor extraction, solubility, and digestion efficiency (311, 312). Consequently, the relatively low percentage of membrane-associated proteins reported here may not fully reflect their true abundance in the EV membrane.

Then proteins were classified based on the biological process they participated in using UniProt annotations (Figure 6.25C) and GO enrichment analysis (Figure 6.25E). The classification in Figure 6.25C reveals a diverse functional repertoire dominated by proteins involved in proteostasis, protein synthesis, metabolism, and nucleic acid processing. Additionally, proteins involved in pathogenesis, including host cell invasion/adhesion and RBC remodeling were also found in less amounts. The GO enrichment analysis (Figure 6.25E) statistically validates and refines these functional insights. The most significantly enriched processes include glycolysis and protein-related processes such as translation, protein catabolism, and proteolysis.

Glycolytic enzymes have been consistently reported in multiple *P. falciparum* proteomic studies of extracellular vesicles. The most frequently identified enzymes include enolase, aldolase, and GAPDH, with LDH and pyruvate kinase reported less frequently (83, 166, 285, 307, 309). In the present study, all of these enzymes except pyruvate kinase were detected (Table 6.2). Consistently, the glycolytic process itself has also been reported as significantly enriched in GO analyses of *Plasmodium*-derived EV proteomes (83, 285).

The strong enrichment of glycolytic enzymes is particularly noteworthy. Glycolysis constitutes the primary energy pathway for intra-erythrocytic *Plasmodium* parasites, making these enzymes highly abundant cytosolic components (313). However, this selective enrichment in EVs could be explained by the phenomenon of moonlighting, wherein a single protein performs multiple, often mechanistically distinct functions. Many glycolytic enzymes are paradigmatic moonlighting proteins across pathogens, with documented roles in adhesion, immune modulation, and transcriptional regulation (314, 315).

Several glycolytic enzymes identified in *Plasmodium*-derived EVs are well-established moonlighting proteins that perform essential non-metabolic functions during parasite invasion and host interaction (315). For example, aldolase plays a central structural role in the invasion machinery by providing an unconventional binding interface between the actin cytoskeleton and TRAP, thereby mechanically coupling parasite adhesins to actin-driven motility independently of its catalytic activity (316, 317). Enolase, on the other hand, is expressed on the parasite surface despite lacking a signal peptide and functions as a plasminogen-binding protein through conserved lysine motifs. This interaction promotes localized generation of plasmin, facilitating extracellular matrix degradation and enhancing host cell invasion (313, 314). GAPDH has also been identified on the surface of *Plasmodium* sporozoites, where it has been proposed to contribute to liver-stage invasion through interactions with host cell components (317, 318).

Alongside glycolysis, GO enrichment analysis revealed a significant overrepresentation of processes related to protein dynamics: translation, protein catabolism, and proteolysis (Figure 6.25E). The presence of these cytosolic abundant ribosomal proteins, elongation factors, proteasome subunits, and chaperones in the EV cargo corroborates this functional signature (Figure 6.25C and Table 6.2). Consistent with this study, ribosomal proteins (RPs) from both the 40S (S19, S4, S11, S15) and 60S (L27) subunits, as well as elongation factors (EF-1α and EF-2), proteasome subunits (α and β), and heat shock proteins (HSP70 and HSP90), have previously been reported in *P. falciparum*-derived EVs (83, 166, 285, 307, 309, 310). Moreover, several of these processes have also been identified as significantly enriched in GO analyses of *Plasmodium*-derived EV proteomes in independent studies (83, 285, 307).

The incorporation of core components of the translational machinery, including ribosomal proteins and elongation factors, into EVs has been reported in a variety of pathogens as well as in cancer cells. Although these proteins have traditionally been considered strictly intracellular, accumulating evidence from other biological systems suggests that translation-related factors can be exported within EVs and may exert regulatory functions in recipient cells (319). In *P. falciparum*, the selective packaging of evolutionarily conserved RPs, such as RPS3, into host-derived EVs has been proposed to contribute to immune evasion and host cell modulation, potentially through molecular mimicry. By exploiting structural and functional similarities between parasite and host RPs, such vesicular cargo may interfere with host cellular pathways, including translational control, NF-κB signaling, and apoptotic responses (320). Similarly, in *P. berghei*, EVs have been shown to contain EF-1α, which has been implicated in immunomodulatory activity, including the inhibition of antigen-specific T-cell activation, thereby contributing to immune evasion and the establishment of persistent infection (321).

Likewise, Dekel et al. demonstrated that *P. falciparum* exports functional 20S proteasome complexes within EVs as part of a pre-invasion virulence strategy. These EVs deliver active proteolytic machinery and parasite kinases to uninfected RBCs, resulting in the phosphorylation and subsequent degradation of key cytoskeletal linker proteins, including β-adducin, ankyrin-1, dematin, and Epb4.1. This targeted remodeling disrupts the connection between the plasma membrane and the spectrin network, increasing membrane deformability and reducing cellular stiffness. As a result, uninfected RBCs are mechanically predisposed to facilitate subsequent merozoite invasion (310). Finally, HSPs have been consistently reported in *Plasmodium*-derived EVs and part of the parasite's exportome (83, 166, 285, 307, 309). In *P. falciparum*, HSPs are involved in the formation of knobs, which facilitate cell adhesion and immune evasion (322).

Therefore, the selective incorporation of moonlighting proteins and core cellular machinery into EVs supports a model in which the parasite functionally extends its biological interface with the host, enabling long-range interactions that modulate host cell signaling, metabolism, and immune responses beyond the constraints of direct cell-cell contact. Other biological processes of interest identified in this study include nucleic acid processing and packaging, reflected by the presence of histones (H2A, H2B, H3, H4) and the DNA/RNA-binding protein Alba-1/-4; parasite adhesion and invasion, represented by MSP-1, MSP-9, and rhoptry-associated protein 1; and host red blood cell remodeling, as suggested by the enrichment of Kelch- and RESA-domain–containing proteins (Table 6.2).

Notably, some GO enrichment analyses have revealed a significant presence of nucleic acid-binding proteins within *Plasmodium* EV proteomes, including parasite histones, which have been detected within EV preparations from *P. falciparum*-iRBCs (83, 307, 309). In these vesicles, histones co-localize with EV-associated genomic DNA, suggesting that nucleosomal structural units are selectively packaged rather than arising from nonspecific cellular disruption. Such nucleosomal cargo has been implicated in parasite-parasite genetic exchange and in host-pathogen interactions, where parasite-derived DNA can act as a virulence-associated signal sensed by host cytosolic immune receptors (167, 323). In addition, members of the *Plasmodium* Alba protein family are evolutionarily conserved DNA/RNA-binding proteins that directly interact with both genomic DNA and RNA and have been shown to modulate the expression of virulence- and stage-specific transcripts (324, 325). Although members of this protein family have been reported in *P. falciparum*-derived EVs, the functional relevance of their potential EV-associated localization remains to be fully elucidated (309).

Additionally, parasite proteins classically associated with RBC adhesion, invasion, and remodeling, including merozoite surface proteins (e.g., MSP-1, MSP-3, MSP-7, MSP-9), apical membrane antigen 1 (AMA1), and other apical complex ligands such as EBA-175 and rhoptry-associated proteins (e.g., RAP1, RAP2), as well as RBC remodeling proteins involved in knob formation and Maurer’s clefts organization (e.g., RESA, KAHRP, MAHRP) are consistently identified within EVs subpopulations (166, 285, 307, 309). Their presence has potential biological significance; functional studies indicate that EVs can modulate invasion dynamics and parasite density-dependent behavior (326, 327). Moreover, the encapsulation of invasion and remodeling ligands within EVs supports a role for parasite EVs in inter-parasite communication and in the modulation of host cell susceptibility and immune recognition. Through interactions with host receptors or presentation to immune effectors, EV-delivered ligands may contribute to parasite survival, sequestration, cytoadherence, and evasion of splenic clearance, thereby reinforcing the multifaceted role of EVs in malaria pathogenesis (167, 328, 329).

While the functional analysis of the *P. berghei* EV proteome reveals a cargo enriched in virulence-associated and core cellular proteins, it also provides indirect insights into the otherwise elusive biogenesis pathways of EVs in *Plasmodium*. Understanding the subcellular origins of EV cargo is particularly significant given the parasite's unique cellular biology and the genomic evidence suggesting a simplified ESCRT machinery (168, 303). The subcellular localization analysis (Figure 6.25D), supported by GO Cellular Component enrichment (Figure 6.25F), indicates that most of the identified parasite proteins originate from cytoplasmic, nuclear, and ribosomal compartments. This distribution is consistent with complementary findings showing that most proteins are soluble and with the enrichment of biological processes related to glycolysis, protein synthesis, and protein degradation, which are predominantly cytoplasmic and ribosomal pathways. In addition, the detection of nucleosome-associated components further supports a contribution from nuclear compartments, collectively reinforcing the intracellular origin of the EV protein cargo.

These findings are also consistent with previously reported GO Cellular Component enrichment analyses, in which cytoplasmic, nuclear, and ribosomal compartments are the predominant contributors to the EV proteome. Additional enriched cellular component categories include extracellular or host cell-exported proteins, as well as proteins associated with rhoptries, highlighting the potential heterogeneous subcellular origins of parasite-derived EV cargo (166, 285, 309).

Moreover, canonical exosome markers recommended by the MISEV guidelines were not detected in this study and therefore do not provide direct evidence for a classical endosome-derived exosome biogenesis pathway. As discussed above, this likely reflects methodological constraints associated with bulk protein profiling approaches, and biological particularities of the parasite, including EV biogenesis pathways that remain incompletely characterized and likely differ from those of other eukaryotic systems. Consequently, the absence of these markers should not be interpreted as evidence against the presence of exosome-like vesicles, but rather as a limitation in conclusively assigning their biogenetic origin.

Notably, despite these limitations, a protein related to vacuolar protein sorting-associated protein 4 (VPS4; A0A509ASB5) was detected for the first time in a *Plasmodium* EV proteome. VPS4 homologs in *P. falciparum* and *Toxoplasma gondii* have been shown to participate in multivesicular body formation, a key step in exosome biogenesis in eukaryotic cells. In *Plasmodium*, several VPS components are part of a reduced ESCRT-III associated machinery that has been implicated in EV formation and parasite protein export, suggesting that endosome-related pathways may contribute to EV biogenesis in this system, even if classical exosome markers are not readily detectable. (303, 326, 330).

Although the presence of this protein alone cannot be considered definitive proof of canonical exosome enrichment, its detection provides biologically relevant support for the involvement of ESCRT-related mechanisms in EV biogenesis within the unique cellular context of *Plasmodium*, offering a more realistic framework for interpreting exosome-like vesicle formation in this parasite.

In summary, this research provides the first comprehensive proteomic characterization of *P. berghei*-derived EVs released by blood-stage parasites using an *in vitro* system. The strong overlap between the proteins identified here and those previously reported for *P. falciparum* supports the successful enrichment of an EV fraction. Although canonical markers of classical exosome biogenesis were not detected, the presence of an ESCRT-related protein, namely a VPS4 homolog, provides a plausible mechanistic link to EV formation in *Plasmodium*. Collectively, these findings advance our understanding of EV biology in rodent malaria models and highlight the potential role of EVs as mediators of host-parasite interactions, immune modulation, and malaria pathogenesis.

8. Conclusions

The present research established and validated an *in vitro* system for the study of *Plasmodium berghei* and its interaction with endothelial cells, with a specific focus on the characterization of parasite-derived stimuli and their impact on vascular autophagy. Based on the obtained results, it is concluded that short-term maintenance of *P. berghei* under defined culture conditions is feasible, providing a controlled model that preserves parasite viability and infectivity. This model enabled the implementation of accessible protocols for enriching biologically active stimuli, like extracellular vesicles (EVs), which were subsequently used in functional assays.

The establishment of genetically modified tEnd.1 endothelial cell lines expressing LC3 fluorescent reporters provided a robust and validated tool for dynamically monitoring autophagic activity. Using these models, it was demonstrated that *P. berghei*-derived stimuli (iRBCs, EVs, and EV-reduced supernatants) consistently induce a state of increased LC3 positive structures with impaired autophagic flux in endothelial cells. This impairment is characterized by the accumulation of autophagosomes without effective progression to lysosomal degradation, a dysregulation that manifests with distinct temporal kinetics depending on the stimulus. These findings position the dysregulation of endothelial autophagy as a novel and plausible cellular mechanism contributing to the vascular dysfunction characteristic of severe malaria.

Furthermore, this work provides the first integrated biophysical and proteomic characterization of small EVs released by blood-stage *P. berghei* in an *in vitro* system. The isolated vesicular population was confirmed to be heterogeneous and with an average size of approximately 100 nm. Its proteomic cargo was dominated by soluble, cytosolic proteins associated with core metabolic pathways such as glycolysis, protein synthesis, and turnover. The significant presence of established moonlighting proteins and virulence factors within the EVs supports a model in which the parasite strategically packages its biomolecules to extend its biological interface with the host. Concurrently, the host-derived protein component within the EV preparations, enriched for markers of RBC cytoskeleton and hemostasis pathways, underscores the complex dual origin of these vesicles and suggests their potential involvement in coagulopathic responses during infection.

Although canonical exosome biogenesis markers were not detected, this is consistent with the predominantly membrane-associated or transmembrane nature of many of these proteins, which are unlikely to be efficiently captured or resolved by the bulk proteomic strategy employed in this study. In this context, the proteomic detection of an ESCRT-related protein, specifically a VPS homolog-related protein, offers initial mechanistic support for the involvement of conserved vesicle formation pathways in Plasmodium, even within its unique cellular context. Collectively, the findings of this study not only fill a critical gap in the understanding of EV biology in rodent malaria models but also delineate a novel axis of host-pathogen interaction centered on endothelial autophagic flux. This work provides a foundational framework and valuable tools for future investigations into the role of vesicular communication and cellular homeostasis pathways in the pathogenesis of malaria.

9. References

1. Cox F. 2010. History of the discovery of the malaria parasites and their vectors. Parasit Vectors 3.
2. WHO. 2024. World Malaria Report 2024. World Health Organization.
3. Talapko J, Škrlec I, Alebić T, Jukić M, Včev A. 2019. Malaria: The past and the present. Microorganisms 7.
4. Dagen M. 2020. History of malaria and its treatment, p. 1–48. In Patrick, G (ed.), Antimalarial Agents: Design and Mechanism of Action. Elsevier Ltd.
5. Su X, Zhang C, Joy D. 2020. Host-Malaria Parasite Interactions and Impacts on Mutual Evolution. Front Cell Infect Microbiol 10.
6. Carter R, Mendis KN. 2002. Evolutionary and historical aspects of the burden of malaria. Clin Microbiol Rev 15:564–594.
7. Nosten F, Richard-Lenoble D, Danis M. 2022. A brief history of malaria. Presse Medicale 51.
8. Ministerio de Salud. 2025. Boletín Epidemiológico N°42 de 2025.
9. Escalante A, Ayala F. 1995. Evolutionary origin of *Plasmodium* and other Apicomplexa based on rRNA genes. Proceedings of the National Academy of Sciences 92:5793–5797.
10. Sato S. 2021. *Plasmodium*—a brief introduction to the parasites causing human malaria and their basic biology. J Physiol Anthropol 40.
11. Cowman AF, Healer J, Marapana D, Marsh K. 2016. Malaria: Biology and Disease. Cell 167:610–624.
12. Ejigiri I, Sinnis P. 2009. *Plasmodium* sporozoite-host interactions from the dermis to the hepatocyte. Curr Opin Microbiol 12:401–407.
13. Sinnis P, Zavala F. 2012. The skin: Where malaria infection and the host immune response begin. Semin Immunopathol 34:787–792.
14. Vaughan A, Stefan H. 2017. Malaria Parasite Liver Infection and Exoerythrocytic Biology. Cold Spring Harbor Laboratory Press 2017:1–22.
15. Goswami D, Minkah NK, Kappe SHI. 2022. Malaria parasite liver stages. J Hepatol 76:735–737.
16. Risco-Castillo V, Topçu S, Marinach C, Manzoni G, Bigorgne AE, Briquet S, Baudin X, Lebrun M, Dubremetz JF, Silvie O. 2015. Malaria sporozoites traverse host cells within transient vacuoles. Cell Host Microbe 18:593–603.
17. Stanway RR, Mueller N, Zobiak B, Graewe S, Froehlke U, Zessin PJM, Aepfelbacher M, Heussler VT. 2011. Organelle segregation into *Plasmodium* liver stage merozoites. Cell Microbiol 13:1768–1782.
18. Graewe S, Rankin KE, Lehmann C, Deschermeier C, Hecht L, Froehlke U, Stanway RR, Heussler V. 2011. Hostile takeover by *Plasmodium*: Reorganization of parasite and host cell membranes during liver stage egress. PLoS Pathog 7.

19. Beeson JG, Drew DR, Boyle MJ, Feng G, Fowkes FJI, Richards JS. 2016. Merozoite surface proteins in red blood cell invasion, immunity and vaccines against malaria. FEMS Microbiol Rev 40:343–372.

20. Weiss GE, Gilson PR, Taechalertpaisarn T, Tham WH, de Jong NWM, Harvey KL, Fowkes FJI, Barlow PN, Rayner JC, Wright GJ, Cowman AF, Crabb BS. 2015. Revealing the sequence and resulting cellular morphology of receptor-ligand interactions during *Plasmodium falciparum* invasion of erythrocytes. PLoS Pathog 11:1–25.

21. Voß Y, Klaus S, Guizetti J, Ganter M. 2023. *Plasmodium* schizogony, a chronology of the parasite's cell cycle in the blood stage. PLoS Pathog 19:1–21.

22. Pollitt LC, Colegrave N, Khan SM, Sajid M, Reece SE. 2010. Investigating the evolution of apoptosis in malaria parasites: The importance of ecology. Parasit Vectors 3:105.

23. Bennink S, Kiesow MJ, Pradel G. 2016. The development of malaria parasites in the mosquito midgut. Cell Microbiol 18:905–918.

24. Nureye D, Solomon A. 2020. Old and recent advances in life cycle, pathogenesis, diagnosis, prevention, and treatment of malaria including perspectives in Ethiopia. The Scientific World Journal 2020.

25. Matthews H, Duffy CW, Merrick CJ. 2018. Checks and balances? DNA replication and the cell cycle in *Plasmodium*. Parasit Vectors 11:1–13.

26. Lee AH, Symington LS, Fidock DA. 2014. DNA repair mechanisms and their biological roles in the malaria parasite *Plasmodium falciparum*. Microbiology and Molecular Biology Reviews 78:469–486.

27. Simwela N, Waters A. 2022. Current status of experimental models for the study of malaria. Parasitology 149:729–750.

28. Zuzarte-Luis V, Mota MM, Vigário AM. 2014. Malaria infections: What and how can mice teach us. J Immunol Methods 410:113–122.

29. Yoshikawa Y, Kimura S, Soga A, Sugiyama M, Ueno A, Kondo H, Zhu Z, Ochiai K, Nakayama K, Hakozaki J, Kusakisako K, Haraguchi A, Kitano T, Orino K, Fukumoto S, Ikadai H. 2022. *Plasmodium berghei* Brca2 is required for normal development and differentiation in mice and mosquitoes. Parasit Vectors 15.

30. Craig AG, Grau GE, Janse C, Kazura JW, Milner D, Barnwell JW, Turner G, Langhorne J. 2012. The role of animal models for research on severe malaria. PLoS Pathog 8.

31. Langhorne J, Buffet P, Galinski M, Good M, Harty J, Leroy D, Mota MM, Pasini E, Renia L, Riley E, Stins M, Duffy P. 2011. The relevance of non-human primate and rodent malaria models for humans. Malar J 10:10–13.

32. Thurston JP. 1953. *Plasmodium berghei*. Parasitological Reviews 2:311–332.

33. Vincke IH, Lips M. 1948. Un nouveau plasmodium d'un rongeur sauvage du Congo: *Plasmodium berghei* n.sp. Ann Soc Belg Med Trop 28:97–104.

34. Basir R, Fazalul Rahiman S, Hasballah K, Chong W, Talib H, Yam M, Jabbarzare M, Tie T, Othman F, Moklas M, Abdullah W, Ahmad Z. 2012. *Plasmodium berghei* ANKA Infection in ICR Mice as a Model of Cerebral Malaria. Iranian J Parasitol 7:62–74.

35. Bartoloni A, Zammarchi L. 2012. Clinical aspects of uncomplicated and severe malaria. Mediterr J Hematol Infect Dis https://doi.org/10.4084/MJHID.2012.026.

36. White NJ. 2022. Severe malaria. Malar J. BioMed Central Ltd https://doi.org/10.1186/s12936-022-04301-8.

37. Laishram DD, Sutton PL, Nanda N, Sharma VL, Sobti RC, Carlton JM, Joshi H. 2012. The complexities of malaria disease manifestations with a focus on asymptomatic malaria.

38. Liehl P, Zuzarte-Luís V, Chan J, Zillinger T, Baptista F, Carapau D, Konert M, Hanson KK, Carret C, Lassnig C, Müller M, Kalinke U, Saeed M, Chora AF, Golenbock DT, Strobl B, Prudêncio M, Coelho LP, Kappe SH, Superti-Furga G, Pichlmair A, Vigário AM, Rice CM, Fitzgerald KA, Barchet W, Mota MM. 2014. Host-cell sensors for *Plasmodium* activate innate immunity against liver-stage infection. Nat Med 20:47–53.

39. Lourembam SD, Sawian CE, Baruah S. 2013. Dysregulation of cytokines expression in complicated *P. falciparum* malaria with increased TGF-β and IFN-γ and decreased IL-2 and IL-12. Cytokine 64:503–508.

40. Popa GL, Popa MI. 2021. Recent advances in understanding the inflammatory response in malaria: a review of the dual role of cytokines. J Immunol Res. Hindawi Limited https://doi.org/10.1155/2021/7785180.

41. Bush MA, Anstey NM, Yeo TW, Florence SM, Granger DL, Mwaikambo ED, Weinberg JB. 2021. Vascular dysfunction in malaria: understanding the role of the endothelial glycocalyx. Front Cell Dev Biol. Frontiers Media S.A. https://doi.org/10.3389/fcell.2021.751251.

42. Miller LH, Ackerman HC, Su XZ, Wellems TE. 2013. Malaria biology and disease pathogenesis: Insights for new treatments. Nat Med 19:156–167.

43. Mbanefo A, Kumar N. 2020. Evaluation of malaria diagnostic methods as a key for successful control and elimination programs. Trop Med Infect Dis. MDPI AG https://doi.org/10.3390/tropicalmed5020102.

44. Fitri LE, Widaningrum T, Endharti AT, Prabowo MH, Winaris N, Nugraha RYB. 2022. Malaria diagnostic update: From conventional to advanced method. J Clin Lab Anal 36:1–14.

45. Tangpukdee N, Duangdee C, Wilairatana P, Krudsood S. 2009. Malaria diagnosis: A brief review. Korean Journal of Parasitology 47:93–102.

46. Gimenez AM, Marques RF, Regiart M, Bargieri DY. 2021. Diagnostic methods for non-falciparum malaria. Front Cell Infect Microbiol 11:1–24.

47. Costa GL, Alvarenga DAM, Aguiar ACC, Louzada J, Pereira DB, de Oliveira TF, Fonseca Júnior AA, Carvalho LH, Ferreira Alves de Brito C, Nóbrega de Sousa T. 2022. Improving the molecular diagnosis of malaria: droplet digital PCR-based method using saliva as a DNA source. Front Microbiol 13:1–12.

48. Belete TM. 2020. Recent progress in the development of new antimalarial drugs with novel targets. Drug Des Devel Ther 14:3875–3889.

49. Haldar K, Bhattacharjee S, Safeukui I. 2018. Drug resistance in *Plasmodium*. Nat Rev Microbiol 16:156–170.

50. Wangdi K, Furuya-Kanamori L, Clark J, Barendregt J, Gatton ML, Banwell C, Kelly G, Doi S, Clements A. 2018. Comparative effectiveness of malaria prevention measures: A systematic review and network meta-analysis. Parasit Vectors 11.

51. El-Moamly AA, El-Sweify MA. 2023. Malaria vaccines: the 60-year journey of hope and final success—lessons learned and future prospects. Trop Med Health 51.

52. Genton B. 2023. R21/Matrix-MTM malaria vaccine: a new tool to achieve WHO's goal to eliminate malaria in 30 countries by 2030? J Travel Med 1–3.

53. Chen Y, Yu L. 2022. Extracellular vesicles: from bench to bedside. Current Medicine 1.

54. Doyle LM, Wang MZ. 2019. Overview of extracellular vesicles, their origin, composition, purpose, and methods for exosome isolation and analysis. Cells. MDPI https://doi.org/10.3390/cells8070727.

55. Couch Y, Buzàs EI, Vizio D Di, Gho YS, Harrison P, Hill AF, Lötvall J, Raposo G, Stahl PD, Théry C, Witwer KW, Carter DRF. 2021. A brief history of nearly EV-erything – The rise and rise of extracellular vesicles. J Extracell Vesicles. John Wiley and Sons Inc https://doi.org/10.1002/jev2.12144.

56. Chargaff E, West R. 1946. The biological significance of the thromboplastic protein of blood. Journal of Biological Chemistry 166:189–197.

57. Bazzan E, Tinè M, Casara A, Biondini D, Semenzato U, Cocconcelli E, Balestro E, Damin M, Radu CM, Turato G, Baraldo S, Simioni P, Spagnolo P, Saetta M, Cosio MG. 2021. Critical review of the evolution of extracellular vesicles' knowledge: From 1946 to today. Int J Mol Sci. MDPI https://doi.org/10.3390/ijms22126417.

58. Aaronson S, Behrens U, Orner R, Haines TH. 1971. Ultrastructure of intracellular and extracellular vesicles, membranes, and myelin figures produced by *Ochromonas danica*. J Ultrastruct Res 35:418–430.

59. Sheta M, Taha EA, Lu Y, Eguchi T. 2023. Extracellular Vesicles: New Classification and Tumor Immunosuppression. Biology (Basel) 12.

60. Buzas E. 2023. The roles of extracellular vesicles in the immune system. Nat Rev Immunol 23:236–250.

61. Yáñez-Mó M, Siljander PRM, Andreu Z, Zavec AB, Borràs FE, Buzas EI, Buzas K, Casal E, Cappello F, Carvalho J, Colás E, Cordeiro-Da Silva A, Fais S, Falcon-Perez JM, Ghobrial IM, Giebel B, Gimona M, Graner M, Gursel I, Gursel M, Heegaard NHH, Hendrix A, Kierulf P, Kokubun K, Kosanovic M, Kralj-Iglic V, Krämer-Albers EM, Laitinen S, Lässer C, Lener T, Ligeti E, Line A, Lipps G, Llorente A, Lötvall J, Manček-Keber M, Marcilla A, Mittelbrunn M, Nazarenko I, Nolte-'t Hoen ENM, Nyman TA, O'Driscoll L, Olivan M, Oliveira C, Pállinger É, Del Portillo HA, Reventós J, Rigau M, Rohde E, Sammar M, Sánchez-Madrid F, Santarém N, Schallmoser K, Ostenfeld MS, Stoorvogel W, Stukelj R, Van Der Grein SG, Helena Vasconcelos M, Wauben MHM, De Wever O. 2015. Biological properties of extracellular vesicles and their physiological functions. J Extracell Vesicles 4:1–60.

62. Krylova S V., Feng D. 2023. The Machinery of Exosomes: Biogenesis, Release, and Uptake. Int J Mol Sci 24.

63. Han QF, Li WJ, Hu KS, Gao J, Zhai WL, Yang JH, Zhang SJ. 2022. Exosome biogenesis: machinery, regulation, and therapeutic implications in cancer. Mol Cancer 21.

64. Clancy JW, Schmidtmann M, D'Souza-Schorey C. 2021. The ins and outs of microvesicles. FASEB Bioadv 3:399–406.

65. Teng F, Fussenegger M. 2021. Shedding Light on Extracellular Vesicle Biogenesis and Bioengineering. Advanced Science 8.

66. Tricarico C, Clancy J, D'Souza-Schorey C. 2017. Biology and biogenesis of shed microvesicles. Small GTPases 8:220–232.

67. De Sousa KP, Rossi I, Abdullahi M, Ramirez MI, Stratton D, Inal JM. 2023. Isolation and characterization of extracellular vesicles and future directions in diagnosis and therapy. Wiley Interdiscip Rev Nanomed Nanobiotechnol 15.

68. Théry C, Witwer KW, Aikawa E, Alcaraz MJ, Anderson JD, Andriantsitohaina R, Antoniou A, Arab T, Archer F, Atkin-Smith GK, Ayre DC, Bach JM, Bachurski D, Baharvand H, Balaj L, Baldacchino S, Bauer NN, Baxter AA, Bebawy M, Beckham C, Bedina Zavec A, Benmoussa A, Berardi AC, Bergese P, Bielska E, Blenkiron C, Bobis-Wozowicz S, Boilard E, Boireau W, Bongiovanni A, Borràs FE, Bosch S, Boulanger CM, Breakefield X, Breglio AM, Brennan M, Brigstock DR, Brisson A, Broekman MLD, Bromberg JF, Bryl-Górecka P, Buch S, Buck AH, Burger D, Busatto S, Buschmann D, Bussolati B, Buzás EI, Byrd JB, Camussi G, Carter DRF, Caruso S, Chamley LW, Chang YT, Chaudhuri AD, Chen C, Chen S, Cheng L, Chin AR, Clayton A, Clerici SP, Cocks A, Cocucci E, Coffey RJ, Cordeiro-da-Silva A, Couch Y, Coumans FAW, Coyle B, Crescitelli R, Criado MF, D'Souza-Schorey C, Das S, de Candia P, De Santana EF, De Wever O, del Portillo HA, Demaret T, Deville S, Devitt A, Dhondt B, Di Vizio D, Dieterich LC, Dolo V, Dominguez Rubio AP, Dominici M, Dourado MR, Driedonks TAP, Duarte F V., Duncan HM, Eichenberger RM, Ekström K, EL Andaloussi S, Elie-Caille C, Erdbrügger U, Falcón-Pérez JM, Fatima F, Fish JE, Flores-Bellver M, Försönits A, Frelet-Barrand A, Fricke F, Fuhrmann G, Gabrielsson S, Gámez-Valero A, Gardiner C, Gärtner K, Gaudin R, Gho YS, Giebel B, Gilbert C, Gimona M, Giusti I, Goberdhan DCI, Görgens A, Gorski SM, Greening DW, Gross JC, Gualerzi A, Gupta GN, Gustafson D, Handberg A, Haraszti RA, Harrison P, Hegyesi H, Hendrix A, Hill AF, Hochberg FH, Hoffmann KF, Holder B, Holthofer H, Hosseinkhani B, Hu G, Huang Y, Huber V, Hunt S, Ibrahim AGE, Ikezu T, Inal JM, Isin M, Ivanova A, Jackson HK, Jacobsen S, Jay SM, Jayachandran M, Jenster G, Jiang L, Johnson SM, Jones JC, Jong A, Jovanovic-Talisman T, Jung S, Kalluri R, Kano S ichi, Kaur S, Kawamura Y, Keller ET, Khamari D, Khomyakova E, Khvorova A, Kierulf P, Kim KP, Kislinger T, Klingeborn M, Klinke DJ, Kornek M, Kosanović MM, Kovács ÁF, Krämer-Albers EM, Krasemann S, Krause M, Kurochkin I V., Kusuma GD, Kuypers S, Laitinen S, Langevin SM, Languino LR, Lannigan J, Lässer C, Laurent LC, Lavieu G, Lázaro-Ibáñez E, Le Lay S, Lee MS, Lee YXF, Lemos DS, Lenassi M, Leszczynska A, Li ITS, Liao K, Libregts SF, Ligeti E, Lim R, Lim SK, Linē A, Linnemannstöns K, Llorente A, Lombard CA, Lorenowicz MJ, Lörincz ÁM, Lötvall J, Lovett J, Lowry MC, Loyer X, Lu Q, Lukomska B, Lunavat TR, Maas SLN, Malhi H, Marcilla A, Mariani J, Mariscal J, Martens-Uzunova ES, Martin-Jaular L, Martinez MC, Martins VR, Mathieu M, Mathivanan S, Maugeri M, McGinnis LK, McVey MJ, Meckes DG, Meehan KL, Mertens I, Minciacchi VR, Möller A, Møller Jørgensen M, Morales-Kastresana A, Morhayim J, Mullier F, Muraca M, Musante L, Mussack V, Muth DC, Myburgh KH, Najrana T, Nawaz M, Nazarenko I, Nejsum P, Neri C, Neri T, Nieuwland R, Nimrichter L, Nolan JP, Nolte-'t Hoen ENM, Noren Hooten N, O'Driscoll L, O'Grady T, O'Loghlen A, Ochiya T, Olivier M, Ortiz A, Ortiz LA, Osteikoetxea X, Ostegaard O, Ostrowski M, Park J, Pegtel DM, Peinado H, Perut F, Pfaffl MW, Phinney DG, Pieters BCH, Pink RC, Pisetsky DS, Pogge von Strandmann E,

Polakovicova I, Poon IKH, Powell BH, Prada I, Pulliam L, Quesenberry P, Radeghieri A, Raffai RL, Raimondo S, Rak J, Ramirez MI, Raposo G, Rayyan MS, Regev-Rudzki N, Ricklefs FL, Robbins PD, Roberts DD, Rodrigues SC, Rohde E, Rome S, Rouschop KMA, Rughetti A, Russell AE, Saá P, Sahoo S, Salas-Huenuleo E, Sánchez C, Saugstad JA, Saul MJ, Schiffelers RM, Schneider R, Schøyen TH, Scott A, Shahaj E, Sharma S, Shatnyeva O, Shekari F, Shelke GV, Shetty AK, Shiba K, Siljander PRM, Silva AM, Skowronek A, Snyder OL, Soares RP, Sódar BW, Soekmadji C, Sotillo J, Stahl PD, Stoorvogel W, Stott SL, Strasser EF, Swift S, Tahara H, Tewari M, Timms K, Tiwari S, Tixeira R, Tkach M, Toh WS, Tomasini R, Torrecilhas AC, Tosar JP, Toxavidis V, Urbanelli L, Vader P, van Balkom BWM, van der Grein SG, Van Deun J, van Herwijnen MJC, Van Keuren-Jensen K, van Niel G, van Royen ME, van Wijnen AJ, Vasconcelos MH, Vechetti IJ, Veit TD, Vella LJ, Velot É, Verweij FJ, Vestad B, Viñas JL, Visnovitz T, Vukman K V., Wahlgren J, Watson DC, Wauben MHM, Weaver A, Webber JP, Weber V, Wehman AM, Weiss DJ, Welsh JA, Wendt S, Wheelock AM, Wiener Z, Witte L, Wolfram J, Xagorari A, Xander P, Xu J, Yan X, Yáñez-Mó M, Yin H, Yuana Y, Zappulli V, Zarubova J, Žėkas V, Zhang J ye, Zhao Z, Zheng L, Zheutlin AR, Zickler AM, Zimmermann P, Zivkovic AM, Zocco D, Zuba-Surma EK. 2018. Minimal information for studies of extracellular vesicles 2018 (MISEV2018): a position statement of the International Society for Extracellular Vesicles and update of the MISEV2014 guidelines. J Extracell Vesicles 7.

69. Akbar A, Malekian F, Baghban N, Kodam SP, Ullah M. 2022. Methodologies to isolate and purify clinical grade extracellular vesicles for medical applications. Cells 11.

70. Meggiolaro A, Moccia V, Brun P, Pierno M, Mistura G, Zappulli V, Ferraro D. 2023. Microfluidic Strategies for Extracellular Vesicle Isolation: Towards Clinical Applications. Biosensors (Basel) 13.

71. Hartjes TA, Mytnyk S, Jenster GW, van Steijn V, van Royen ME. 2019. Extracellular vesicle quantification and characterization: Common methods and emerging approaches. Bioengineering. MDPI AG https://doi.org/10.3390/bioengineering6010007.

72. Mohammadipoor A, Hershfield MR, Linsenbardt HR, Smith J, Mack J, Natesan S, Averitt DL, Stark TR, Sosanya NM. 2023. Biological function of Extracellular Vesicles (EVs): a review of the field. Mol Biol Rep 50:8639–8651.

73. Yates AG, Pink RC, Erdbrügger U, Siljander PRM, Dellar ER, Pantazi P, Akbar N, Cooke WR, Vatish M, Dias-Neto E, Anthony DC, Couch Y. 2022. In sickness and in health: The functional role of extracellular vesicles in physiology and pathology in vivo: Part I: Health and Normal Physiology. J Extracell Vesicles 11.

74. Fang Y, Wang Z, Liu X, Tyler BM. 2022. Biogenesis and Biological Functions of Extracellular Vesicles in Cellular and Organismal Communication With Microbes. Front Microbiol 13.

75. György B, Hung ME, Breakefield XO, Leonard JN. 2015. Therapeutic applications of extracellular vesicles: Clinical promise and open questions. Annu Rev Pharmacol Toxicol 55:439–464.

76. Jnana A, Sadiya S, Satyamoorthy K, Murali T. 2023. Extracellular vesicles in bacterial and fungal diseases–Pathogenesis to diagnostic biomarkers. Virulence 14.

77. Sharma M, Lozano-Amado D, Chowdhury D, Singh U. 2023. Extracellular Vesicles and their impact on the biology of protozoan parasites. Trop Med Infect Dis 8.

78. Khosravi M, Mirsamadi ES, Mirjalali H, Zali MR. 2020. Isolation and functions of extracellular vesicles derived from parasites: The promise of a new era in immunotherapy, vaccination, and diagnosis. Int J Nanomedicine 15:2957–2969.

79. Xander P, Cronemberger-Andrade A, Torrecilhas AC. 2019. Extracellular vesicles in parasitic disease, p. 179–198. In Exosomes: A Clinical Compendium. Elsevier.

80. Wang X, Chen J, Zheng J. 2022. The state of the art of extracellular vesicle research in protozoan infection. Front Genet 13.

81. Drurey C, Coakley G, Maizels RM. 2020. Extracellular vesicles: new targets for vaccines against helminth parasites. Int J Parasitol 50:623–633.

82. Cheng IS, Sealy BC, Tiberti N, Combes V. 2020. Extracellular vesicles, from pathogenesis to biomarkers: The case for cerebral malaria. Vessel Plus 4.

83. Abou Karam P, Rosenhek-Goldian I, Ziv T, Ben Ami Pilo H, Azuri I, Rivkin A, Kiper E, Rotkopf R, Cohen SR, Torrecilhas AC, Avinoam O, Rojas A, Morandi MI, Regev-Rudzki N. 2022. Malaria parasites release vesicle subpopulations with signatures of different destinations. EMBO Rep 23.

84. Shetty AK, Upadhya R. 2021. Extracellular vesicles in health and disease. Aging Dis 12:1358–1362.

85. Zhang X, Liu D, Gao Y, Lin C, An Q, Feng Y, Liu Y, Liu D, Luo H, Wang D. 2021. The biology and function of extracellular vesicles in cancer development. Front Cell Dev Biol 9.

86. Qian K, Fu W, Li T, Zhao J, Lei C, Hu S. 2022. The roles of small extracellular vesicles in cancer and immune regulation and translational potential in cancer therapy. Journal of Experimental and Clinical Cancer Research 41.

87. Aman Y, Schmauck-Medina T, Hansen M, Morimoto RI, Simon AK, Bjedov I, Palikaras K, Simonsen A, Johansen T, Tavernarakis N, Rubinsztein DC, Partridge L, Kroemer G, Labbadia J, Fang EF. 2021. Autophagy in healthy aging and disease. Nat Aging 1:634–650.

88. Tsukada M, Ohsumi Y. 1993. Isolation and characterization of autophagy-defective mutants of Saccharomyces cerevisiae. FEBS Lett 333:169–174.

89. Dikic I, Elazar Z. 2018. Mechanism and medical implications of mammalian autophagy. Nat Rev Mol Cell Biol 19:349–364.

90. Ichimiya T, Yamakawa T, Hirano T, Yokoyama Y, Hayashi Y, Hirayama D, Wagatsuma K, Itoi T, Nakase H. 2020. Autophagy and autophagy-related diseases: A review. Int J Mol Sci https://doi.org/10.3390/ijms21238974.

91. Vargas JNS, Hamasaki M, Kawabata T, Youle RJ, Yoshimori T. 2023. The mechanisms and roles of selective autophagy in mammals. Nat Rev Mol Cell Biol 24:167–185.

92. Parzych KR, Klionsky DJ. 2014. An overview of autophagy: Morphology, mechanism, and regulation. Antioxid Redox Signal 20:460–473.

93. Feng Y, He D, Yao Z, Klionsky DJ. 2014. The machinery of macroautophagy. Cell Res 24:24–41.

94. Fleming A, Bourdenx M, Fujimaki M, Karabiyik C, Krause GJ, Lopez A, Martín-Segura A, Puri C, Scrivo A, Skidmore J, Son SM, Stamatakou E, Wrobel L, Zhu Y, Cuervo AM, Rubinsztein DC. 2022. The different autophagy degradation pathways and neurodegeneration. Neuron 110:935–966.

95. Codogno P, Mehrpour M, Proikas-Cezanne T. 2012. Canonical and non-canonical autophagy: variations on a common theme of self-eating? Nat Rev Mol Cell Biol 13.

96. Feng H, Wang N, Zhang N, Liao H. 2022. Alternative autophagy: mechanisms and roles in different diseases. Cell Communication and Signaling. BioMed Central Ltd https://doi.org/10.1186/s12964-022-00851-1.

97. Hurley JH, Young LN. 2017. Mechanisms of Autophagy Initiation. Annu Rev Biochem 86:225–244.

98. Burman C, Ktistakis NT. 2010. Regulation of autophagy by phosphatidylinositol 3-phosphate. FEBS Lett https://doi.org/10.1016/j.febslet.2010.01.011.

99. Melia TJ, Lystad AH, Simonsen A. 2020. Autophagosome biogenesis: From membrane growth to closure. Journal of Cell Biology. Rockefeller University Press https://doi.org/10.1083/JCB.202002085.

100. Shpilka T, Weidberg H, Pietrokovski S, Elazar Z. 2011. Atg8: an autophagy-related ubiquitin-like protein family. Genome Biol 12.

101. Kumar S, Wan W, Almannai M. 2022. WIPI proteins: Biological functions and related syndromes. Front Mol Neurosci 15.

102. Shimizu T, Tamura N, Nishimura T, Saito C, Yamamoto H, Mizushima N. 2023. Comprehensive analysis of autophagic functions of WIPI family proteins and their implications for the pathogenesis of β-propeller associated neurodegeneration. Hum Mol Genet 32:2623–2637.

103. Jiang W, Chen X, Ji C, Zhang W, Song J, Li J, Wang J. 2021. Key regulators of autophagosome closure. Cells. MDPI https://doi.org/10.3390/cells10112814.

104. Kraft C, Reggiori F. 2023. Phagophore closure, autophagosome maturation and autophagosome fusion during macroautophagy in the yeast Saccharomyces cerevisiae. FEBS Lett. John Wiley and Sons Inc https://doi.org/10.1002/1873-3468.14720.

105. Jiang P, Nishimura T, Sakamaki Y, Itakura E, Hatta T, Natsume T, Mizushima N. 2014. The HOPS complex mediates autophagosome-lysosome fusion through interaction with syntaxin 17. Mol Biol Cell 25:1327–1337.

106. Lőrincz P, Juhász G. 2020. Autophagosome-Lysosome Fusion. J Mol Biol. Academic Press https://doi.org/10.1016/j.jmb.2019.10.028.

107. Yim WWY, Mizushima N. 2020. Lysosome biology in autophagy. Cell Discov 6.

108. Kobayashi S. 2015. Choose Delicately and Reuse Adequately: The Newly Revealed Process of Autophagy. Biol Pharm Bull 38:1098–1103.

109. Hansen M, Rubinsztein DC, Walker DW. 2018. Autophagy as a promoter of longevity: insights from model organisms. Nat Rev Mol Cell Biol. Nature Publishing Group https://doi.org/10.1038/s41580-018-0033-y.

110. Dupont N, Roccio F, Codogno P. 2021. Overview of noncanonical autophagy, p. 41–67. In Petroni, G, Galluzi, L (eds.), Non-Canonical Autophagy: Mechanisms and Pathophysiological Implications, 1st ed. Elsevier, London.

111. Li WW, Li J, Bao JK. 2012. Microautophagy: Lesser-known self-eating. Cellular and Molecular Life Sciences 69:1125–1136.

112. Wang L, Klionsky DJ, Shen HM. 2023. The emerging mechanisms and functions of microautophagy. Nat Rev Mol Cell Biol 24:186–203.

113. Mijaljica D, Prescott M, Devenish RJ. 2011. Microautophagy in mammalian cells: Revisiting a 40-year-old conundrum. Autophagy 7:673–682.

114. Cuervo AM. 2010. Chaperone-mediated autophagy: Selectivity pays off. Trends in Endocrinology and Metabolism 21:142–150.

115. Kaushik S, Cuervo AM. 2018. The coming of age of chaperone-mediated autophagy. Nat Rev Mol Cell Biol 19:365–381.

116. Verhoeven J, Baelen J, Agrawal M, Agostinis P. 2021. Endothelial cell autophagy in homeostasis and cancer. FEBS Lett 595:1497–1511.

117. Mameli E, Martello A, Caporali A. 2022. Autophagy at the interface of endothelial cell homeostasis and vascular disease. FEBS Journal 289:2976–2991.

118. McHugh D, Gil J. 2018. Senescence and aging: Causes, consequences, and therapeutic avenues. Journal of Cell Biology 217:65–77.

119. Vion AC, Kheloufi M, Hammoutene A, Poisson J, Lasselin J, Devue C, Pic I, Dupont N, Busse J, Stark K, Lafaurie-Janvore J, Barakat AI, Loyer X, Souyri M, Viollet B, Julia P, Tedgui A, Codogno P, Boulanger CM, Rautou PE. 2017. Autophagy is required for endothelial cell alignment and atheroprotection under physiological blood flow. Proc Natl Acad Sci U S A 114:E8675–E8684.

120. Weikel KA, Cacicedo JM, Ruderman NB, Ido Y. 2015. Glucose and palmitate uncouple AMPK from autophagy in human aortic endothelial cells. Am J Physiol Cell Physiol 308:249–263.

121. Kim KA, Kim D, Kim JH, Shin YJ, Kim ES, Akram M, Kim EH, Majid A, Baek SH, Bae ON. 2020. Autophagy-mediated occludin degradation contributes to blood-brain barrier disruption during ischemia in bEnd.3 brain endothelial cells and rat ischemic stroke models. Fluids Barriers CNS 17.

122. Jeong IH, Bae WY, Choi JS, Jeong JW. 2020. Ischemia induces autophagy of endothelial cells and stimulates angiogenic effects in a hindlimb ischemia mouse model. Cell Death Dis 11.

123. Evans RJ, Sundaramurthy V, Frickel EM. 2018. The interplay of host autophagy and eukaryotic pathogens. Front Cell Dev Biol 6.

124. Ghartey-Kwansah G, Adu-Nti F, Aboagye B, Ankobil A, Essuman EE, Opoku YK, Abokyi S, Abu EK, Boampong JN. 2020. Autophagy in the control and pathogenesis of parasitic infections. Cell Biosci 10.

125. Romano PS, Akematsu T, Besteiro S, Bindschedler A, Carruthers VB, Chahine Z, Coppens I, Descoteaux A, Lopes Alberto Duque T, He CY, Heussler V, Le Roch KG, Li

F-J, Perrone Bezerra de Menezes J, Menna-Barreto RFS, Mottram JC, Schmuckli-Maurer J, Turk B, Tavares Veras PS, Salassa BN, Vanrell MC. 2023. Autophagy in protists and their hosts: When, how and why? Autophagy Reports 2.

126. Prado M, Eickel N, De Niz M, Heitmann A, Agop-Nersesian C, Wacker R, Schmuckli-Maurer J, Caldelari R, Janse CJ, Khan SM, May J, Meyer CG, Heussler VT. 2015. Long-term live imaging reveals cytosolic immune responses of host hepatocytes against *Plasmodium* infection and parasite escape mechanisms. Autophagy 11:1561–1579.

127. Agop-Nersesian C, Niklaus L, Wacker R, Heussler VT. 2018. Host cell cytosolic immune response during *Plasmodium* liver stage development. FEMS Microbiol Rev 42:324–334.

128. Bindschedler A, Wacker R, Egli J, Eickel N, Schmuckli-Maurer J, Franke-Fayard BM, Janse CJ, Heussler VT. 2020. *Plasmodium berghei* sporozoites in nonreplicative vacuole are eliminated by a PI3P-mediated autophagy-independent pathway. Cell Microbiol 23.

129. Setua S, Enguita FJ, Chora ÂF, Ranga-prasad H, Lahree A, Marques S, Sundaramurthy V, Mota MM. 2020. Disrupting *Plasmodium* UIS3–host LC3 interaction with a small molecule causes parasite elimination from host cells. Commun Biol 3.

130. Boonhok R, Rachaphaew N, Duangmanee A, Chobson P, Pattaradilokrat S, Utaisincharoen P, Sattabongkot J, Ponpuak M. 2016. LAP-like process as an immune mechanism downstream of IFN-γ in control of the human malaria *Plasmodium vivax* liver stage. Proc Natl Acad Sci U S A 113:E3519–E3528.

131. Zhang J, Wu K, Xiao X, Liao J, Hu Q, Chen H, Liu J, An X. 2015. Autophagy as a regulatory component of erythropoiesis. Int J Mol Sci 16:4083–4094.

132. Malleret B, Li A, Zhang R, Tan K, Suwanarusk R, Claser C, Sun Cho J, Geok Liang Koh E, Chu C, Pukrittayakamee S, W Tan KS, Chu CS, Lee Ng M, Ginhoux F, Guan Ng L, Teck Lim C, Nosten F, Snounou G, Russell B. 2015. *Plasmodium vivax*: restricted tropism and rapid remodeling of CD71-positive reticulocytes. Blood 125:1314–1324.

133. Leleu I, Alloo J, Cazenave PA, Roland J, Pied S. 2022. Autophagy Pathways in the Genesis of *Plasmodium*-Derived Microvesicles: A Double-Edged Sword? 12.

134. Leleu I, Genete D, Desnoulez SS, Saidi N, Brodin P, Lafont F, Tomavo S, Pied S. 2022. A noncanonical autophagy is involved in the transfer of *Plasmodium*-microvesicles to astrocytes. Autophagy 18:1583–1598.

135. Barateiro A, Junior ARC, Epiphanio S, Marinho CRF. 2022. Homeostasis Maintenance in *Plasmodium*-Infected Placentas: Is There a Role for Placental Autophagy During Malaria in Pregnancy? Front Immunol 13.

136. De Niz M, Heussler V. 2018. Rodent malaria models: insights into human disease and parasite biology. Curr Opin Microbiol 46:93–101.

137. Sena-Dos-Santos C, Braga-Da-Silva C, Marques D, Dos Santos Pinheiro JA, Ribeiro-Dos-santos Â, Cavalcante GC. 2021. Unraveling cell death pathways during malaria infection: What do we know so far? Cells 10:1–29.

138. Graewe S, Retzlaff S, Struck N, Janse CJ, Heussler VT. 2009. Going live: A comparative analysis of the suitability of the RFP derivatives RedStar, mCherry and tdTomato for intravital and in vitro live imaging of *Plasmodium* parasites. Biotechnol J 4:895–902.

139. Franke-Fayard B, Trueman H, Ramesar J, Mendoza J, Van Der Keur M, Van Der Linden R, Sinden RE, Waters AP, Janse CJ. 2004. A *Plasmodium berghei* reference line that constitutively expresses GFP at a high level throughout the complete life cycle. Mol Biochem Parasitol 137:23–33.

140. Ramaiya ML, Kamath VR, Renapurkar DM. 1987. Long-term in vitro cultivation of *Plasmodium berghei*. Int J Parasitol 17:1329–1330.

141. Trager W, Jensen J. 1976. Human Malaria Parasites in Continuous Culture. New York.

142. Cranmer S, Magowan C, Liang J, Coopel R, Cooke B. 1997. An alternative to serum for cultivation of *Plasmodium falciparum in vitro*. Victoria.

143. Janse CJ, Croon JJAB, Van Der Kaay HJ. 1984. Long-term in vitro cultures of *Plasmodium berghei* and preliminary observations on gametocytogenesis. International Journey for Parasitology 14:3–17.

144. Jambou R, El-Assaad F, Combes V, Grau GE. 2011. *In vitro* culture of *Plasmodium berghei*-ANKA maintains infectivity of mouse erythrocytes inducing cerebral malaria. Malar J 10.

145. Schuster FL. 2002. Cultivation of *Plasmodium* spp. Clin Microbiol Rev 15:355–364.

146. Miao J, Cui L. 2011. Rapid isolation of single malaria parasite-infected red blood cells by cell sorting. Nat Protoc 6:140–146.

147. Retana Moreira L, Steller Espinoza MF, Chacón Camacho N, Cornet-Gomez A, Sáenz-Arce G, Osuna A, Lomonte B, Abrahams Sandí E. 2022. Characterization of extracellular vesicles secreted by a clinical isolate of *Naegleria fowleri* and identification of immunogenic components within their protein cargo. Biology (Basel) 11.

148. Welsh JA, Goberdhan DCI, O'Driscoll L, Buzas EI, Blenkiron C, Bussolati B, Cai H, Di Vizio D, Driedonks TAP, Erdbrügger U, Falcon-Perez JM, Fu QL, Hill AF, Lenassi M, Lim SK, Mahoney Mỹ. G, Mohanty S, Möller A, Nieuwland R, Ochiya T, Sahoo S, Torrecilhas AC, Zheng L, Zijlstra A, Abuelreich S, Bagabas R, Bergese P, Bridges EM, Brucale M, Burger D, Carney RP, Cocucci E, Crescitelli R, Hanser E, Harris AL, Haughey NJ, Hendrix A, Ivanov AR, Jovanovic-Talisman T, Kruh-Garcia NA, Faustino VKL, Kyburz D, Lässer C, Lennon KM, Lötvall J, Maddox AL, Martens-Uzunova ES, Mizenko RR, Newman LA, Ridolfi A, Rohde E, Rojalin T, Rowland A, Saftics A, Sandau US, Saugstad JA, Shekari F, Swift S, Ter-Ovanesyan D, Tosar JP, Useckaite Z, Valle F, Varga Z, van der Pol E, van Herwijnen MJC, Wauben MHM, Wehman AM, Williams S, Zendrini A, Zimmerman AJ, Théry C, Witwer KW, Ahmad S, Ahmed DAK, Ahmed SH, Aikawa E, Akbar N, Akiyoshi K, Al-Adra DP, Al-Masawa ME, Albanese M, Alberro A, Alcaraz MJ, Alexander-Brett J, Alexander KL, Ali N, Alibhai FJ, Allelein S, Allenby MC, Almeida F, de Almeida LP, Almousa SW, Altan-Bonnet N, Altei WF, Alvarez-Llamas G, Alvarez CL, An HJ, Anand K, Andaloussi SEL, Anderson JD, Andriantsitohaina R, Ansari KI, Anselmo A, Antoniou A, Aqil F, Arab T, Archer F, Arif S, Armstrong DA, Arntz OJ, Arsène P, Arteaga-Blanco L, Asokan N, Aspelin T, Atkin-Smith GK, Aubert D, Ayyar KK, Azlan M, Azoidis I, Bécot A, Bach JM, Bachurski D, Bae S, Bagge RO, Baj-Krzyworzeka M, Balaj L, Balbi C, van Balkom BWM, Ballal AR, Bano A, Banzet S, Bare Y, Barile L, Barman B, Barranco I, Barreca V, Bart G, Barteneva NS, Basso M, Batish M, Bauer NR, Baxter AA, Bazié WW, Bazzan E, Beaumont JEJ, Bebawy M, Bebelman MP, Bedina-Zavec A, Beetler DJ, Beke-Somfai T, Belleannée C, Benedikter BJ, Benediktsdóttir BE, Berardi AC, Bergamelli M, Bertolini I, Bhattacharyya

A, Bhattacharyya SN, Biller SJ, Billottet C, Bissler JJ, Blanc-Brude O, Blijdorp CJ, Bobis-Wozowicz S, Bodart-Santos V, Bodnár BR, Boilard E, Boireau W, Bokun V, Bollard SM, Bollini S, Bongiovanni A, Bongiovanni L, Bonifay A, Boppart MD, Borràs FE, Bosch S, Boselli D, Bottini M, Bouffard J, Boulanger CM, Boutros PC, Boyadjian O, Boysen AT, Bozkurt BT, Bramich KP, Braun F, Del Carmen Bravo-Miana R, Breakefield XO, Brenna S, Brennan K, Brennan M, Breyne K, Brigstock DR, Brisson AR, Brodie C, Bruno KA, Bucci C, Buch S, Buck A, Bukva M, Bulte JWM, Buratta S, Burgy O, Burnier J V., Burrows K, Busatto S, Buzas K, Byrd JB, Cáceres-Verschae A, Caires HR, Campos-Silva C, Camussi G, de Candia P, Carceller C, Fernandez-Becerra C, Carrasco AGM, Carter DRF, Cavallaro S, Cavallero S, Cavallero S, Cerda-Troncoso C, Chahwan R, Chalupská R, Chamley LW, Chandra PK, Chang WW, Charest A, Chen C, Chen H, Chen Q, Chen S, Chen S, Chen Y, Cheng L, Chernyshev VS, Chetty VK, Chitti S V., Cho SG, Cho YK, Choi BH, Chutipongtanate S, Cicardi ME, Cifuentes-Rius A, Ciullo A, Clayton A, Cleary JA, Cocozza F, Coffey RJ, Collino F, Colombo F, Colosetti P, Compañ-Bertomeu A, Constanzo J, Corbeil D, Cordeiro-da-Silva A, Costa J, Couch Y, Courageux Y, Coutant K, Coyle B, Cretich M, Cronemberger-Andrade A, Crossland RE, Cucher MA, Czystowska-Kuzmicz M, D'Acunzo P, D'Agnano I, D'Agostino VG, D'Arrigo D, D'Souza-Schorey C, Dagur RS, Danielson KM, Das S, Dauphin T, Davidson SM, Davies OG, Davies RL, Davis CN, Deep G, Degosserie J, Van Delen M, Deliwala V, Dellar ER, Van Deun J, Dev A, Deville S, Devitt A, Dhondt B, Dieterich LC, Dittmer DP, Dobosh B, Dobra G, Dogra N, Dohi E, Dolo V, Domashevich T V., Dominici M, Dong L, Doré E, Dragovic RA, Drittanti L, Droste M, Duan W, Durmaz E, Dutta S, Eguchi T, Eichenberger RM, Eitan E, Ekström K, Eldh M, Elie-Caille C, Enciso-Martinez A, Esmaeili R, Ettelaie C, Försönits AI, Fabbri M, Falasca M, Fan H, Fatima F, Fazeli A, Fernández-Rhodes M, Fernandez-Prada C, Ferraro MJ, Ferreira J, Ferreira RF, Figueroa-Hall LK, Figueroa-Valdés AI, Fioretti P V., Flenady S, Flores-Bellver M, Fok EK, Fonseka P, Forbes K, Ford VJ, Fornaguera C, Forte D, Forte S, Fortunato O, Franklin JL, Freitas D, Frelet-Barrand A, Fujita Y, Gärtner K, Görgens A, Gabriel ÁM, Gabrielli M, Gabrielsson S, Galinsoga A, Galisova A, Gamage TKJB, Gao Y, Garcia-Contreras M, Garcia Garcia MM, Garcia MN, Gargiulo E, Garibotti HGK, Mc Gee MM, Genard GC, Geraci F, Ghanam J, Ghatak S, Ghavami M, Ghebosu RE, Gho YS, Ghosal S, Giamas G, Giebel B, Gilbert C, Gimona M, Girão H, Giusti I, Gizzie EA, Glamočlija S, Glass SE, Gobbo J, Godbole N, Goetz JG, Gololobova O, Gomez-Florit M, Goncalves JP, Gorgun C, Gori A, Gorska S, Graner MW, Grau GE, Grech L, Greening DW, Groß RM, Gross JC, Gruber J, Gualerzi A, Guanzon D, Gudbergsson JM, Guerin CL, Guerra F, Guillén MI, Gujar V, Guo W, Gupta VB, Gupta VK, Gustafson D, Gyukity-Sebestyén E, Hölker P, Hade MD, Hagey DW, Han C, Han P, Hanayama R, Handberg A, Harada M, Harmati M, Harrison P, Harrison RA, Haynes PA, He M, Hegyesi H, van Herwijnen MJC, Hisey CL, Hochberg FH, Nolte-'tHoen ENMN, Holcar M, Holder B, Holnthoner W, Holthofer H, Hooper DC, Hosseini-Beheshti E, Hosseinkhani B, Howard J, Howe KL, Hoyle NR, Hrdy J, Hu G, Huang Y, Huber V, Hudoklin S, Hufnagel A, Hulett MD, Hunt S, Hyenne V, Di Ianni E, Iannotta D, Ibrahim AGE, Ibrahim SA, Ikezu S, Ikezu T, Im H, Inal JM, Inic-Kanada A, Inngjerdingen M, Inoshima Y, Ivanova A, Izquierdo E, Jørgensen MM, Jackson HK, Jacobsen S, Jadue F, Javeed N, Jay SM, Jayachandran M, Jayasinghe MK, Jenster G, Jeppesen DK, Jerónimo C, Jiang L, Jin J, Jingushi K, Jo DG, Joerger-Messerli MS, Jones JC, Jones MK, de Jong OG, Ferrante AW, Coleman LG, Juncker D, Jung S, Jurek B, Jurga M, Justilien V, Kabani M, Kalluri R, Kamali-Moghaddam M, Kanada M, Kang T, Kano SI, Kaparakis-Liaskos M, Karnas E, Karoichan A, Kashanchi F, Kashani SA, Kashyap NN, Katsur M, Kau-Strebinger S, Kauffman AC, Kaur S, Kehoe O, Kelwick RJR, Kenari AN, Kestecher BM, Keulers TG, Van Keuren-Jensen KR, Khalaj K, Khamari D, Khanabdali R, Khomyakova E, Khoo A, Kim DH, Kim D, Kim HS, Kim IS, Kim S, Kim Y, Kima PE, Kislinger T, Klingeborn M, Knight R, Komuro H, Koncz A, Konstantinou T, van der Koog L, Kooijmans SAA, Kornek MT, Kosanović M, Kostallari E, Koukoulis TF, Kourembanas S, Krämeralbers EM, Kralj-Iglic V, Krasemann S, Krasnodembskaya AD, Krawczynska NJ, Kreft ME, Kuehn MJ, Kuipers ME, Kulaj K, Kuligowski J, Kumagai Y, Kumar A, Kumar S, Kumar S, Kumari M, Kundrotas G, Kurochkin I V., Kuroda M, Kurzawa-Akanbi M, Kweskin SJ, Lázaro-Ibáñez E, Lőrincz Á, Lai A, Lai CP, Laitinen S, Landreville S, Lange S, Langevin SM, Langlois MA, Languino LR, Lannigan J, Lark DS, Larregina AT, Laurent LC, Laurin D, Lavieu G, Lawson C, Le Lay S, Leandro K, Ledreux A, Lee C, Lee DS, Lee H, Lee H, Lee SY, Lee TR, Lee WL, Lefterov I, Lei X, Leivo J, Lemaire Q, Leme AFP, Lemon SM, Lenzini S, Leor J, Levy E, Li B, Li G, Li JJ, Li Q, Li X, Liang X, Lim R, Limongi T, Linē A, Lins PP, Lippens L, Liu G, Llorente A, Longjohn MN, van de Loo FAJ, Lorenowicz MJ, Lorico A, Loudig O, Loyer X, Lozano-Andrés E, Lu B, Lu Q, Lubart Q, Lucien F, Lunavat TR, Lundberg LE, Lundy DJ, Luoto JC, Lyden DC, Müller JA, Macphee DJ, Madec E, Magaña SM, Mahairaki V, Mahoney Mỹ. G, Malhi H, Malnou CE, Mamand DR, Man K, Manno M, Mantel PY, Marangon T, Marbán E, Marcilla A, Maremanda KP, Margolis L, Mariñas-Pardo L, Marić I, Martín SS, Martínez-Martínez E, Martel C, Martin-Duque P, Martin-Jaular L, Martinez-Murillo PA, Martinez-Pacheco S, Martins-Marques T, Mary B, Marzan AL, Matamoros-Angles A, Mathivanan S, Matsuzaki J, Mayan MD, Mazzeo C, Mbengue M, McCann MJ, McIlvenna LC, McVey MJ, Meisner-Kober N, Mellergaard M, Melli G, Menck K, Menjivar NG, Menon R, Mentkowski KI, Miklavcic JJ, Miklosi AG, Milutinovic B, Minciacchi VR, Mirzaei M, Mishra S, Mitchell MI, Mladenović D, Mohamadi E, Momen-Heravi F, Mondal SK, Monguió-Tortajada M, Moon J, Morandi MI, Moreau V, Moreira LR, Morelli AE, Mori MA, Morimoto M, Mosser M, Motaung TE, Moussay E, Mugoni V, Mullier F, Muraca M, Murugesan S, Musante L, Musicò A, Németh A, Németh K, Nadeau A, Nam GH, Naora H, Natoli R, Nawaz M, Nazarenko I, Ndukaife JC, Nedeva C, Nejsum P, Nelissen I, Neri C, Neri T, Neviani P, Ng CY, van Niel G, Nikiforova N, Nimrichter L, Nitin C, Njock MS, Noël D, Noghero A, Nolan JP, Noppen S, Noren Hooten N, da Silva Novaes A, O'loghlen A, Oesterreicher J, Oh SW, Oláh A, Olivier M, Ong SL, Ortiz A, Ortiz LA, Østergaard O, Osorio OA, Osteikoetxea X, Ostrowski M, Otaegui D, Otahal A, Ozawa PMM, Ozkocak DC, Pálóczi K, Pérez-González R, Pachane BC, Padinharayil H, Paget D, Paggetti J, Palacio PCL, Pallasch CP, Palmulli R, Pang B, Paniushkina L, Pantazi P, Paolini L, Papademetrio DL, Parisse P, Park DJ, Park J, Park YG, Patton JG, Peake NJ, Pegtel DM, Peinado H, Perut F, Pfaffl MW, Pfeiffer A, Phan TK, Phinney DG, Phylactou LA, Picciolini S, Pietrowska M, Piffoux M, Pinheiro C, Pink RC, Pleet ML, Pocsfalvi G, Poh QH, Poojary G, Poon IKH, Poppa G, Del Portillo HA, Pospichalova V, Potter S, Powell BH, Powis SJ, Prada I, Prasadam I, Preußer C, Pua HH, Pucci F, Puhm F, Puig B, Pulliam L, Purnianto A, Puutio JMM, Quilang RC, Rabbani PS, Rackov G, Radeghieri A, Radu CM, Raffai RL, Raghav A, Rahbari M, Rahman MDM, Rahman MM, Rai AJ, Raimondo S, Raju S, Rak J, Ramaswamy L, Ramirezricardo J, Ramirez MI, Rani S, Raposo G, Rather HA, Razim A, Reale A, Reategui E, Reddel CJ, Reddy SK, Redenti S, Reed SL, Regevrudzki N, Reiners KS, Resnik N, Rice GE, Ricklefs FL, Rilla K, Rimmer MP, Roballo KCS, Robbins PD, Roberts DD, Roca J, Rodal AA, Rodrigues-Junior DM, Rodrigues ML, Roefs MT, Rogers RG, Romani R, Romano M, Rome S, Romih R, Romolo A, De Rossi T, Rouschop KM, Routenberg DA, Roux Q, van Royen ME, Rozo AJ, Rufino-Ramos D, Rughetti A, Russell AE, Rutter SF, Rysmakhanov MS, Sánchez CA, Sadovsky Y, Safavi-Sohi R, Sagar R, Saidu NEB, Saint-Pol J, Salas-Huenuleo E, Salazar-Puerta AI, Saleem A, Salekdeh GH, Salomon C, Salviano-Silva A, Salybekov AA, Samuels M, Santavanond JP, Santoro J, Santos M, Sanwlani R, Saul MJ, Schøyen TH, Schabussova I, Scharrig E, Schekman R, Schiavi-Tritz J, Schiffelers RM, Schmid

AM, Schneider R, Schneider S, Schoeberlein A, Schorey JS, Seo N, Seras-Franzoso J, Shahi S, Shatnyeva O, Shea DF, Shelke G V., Shetty AK, Shiba K, Shiju TM, Shrivastava S, Shukla S, Siljander PRM, Silva AM, Singh AP, Singh S, Skliar M, Skog J, Sluijter JPG, Snyder OL, Soekmadji C, Somaida A, Somiya M, Soroczyńska K, Sotillo J, Souza-Fonseca-guimaraes F, Spada S, Spiers HVM, Spitzberg JD, Srivastava A, Srivastava AK, Stępień E, St-Denis-bissonnette F, Stahl PD, Stam J, Stambouli O, Stanton BA, Stassen FRM, Staufer O, Steiner L, Stepanova G, Stoka V, Stoorvogel W, von Strandmann EP, Strunk D, Stylli SS, Su H, Subramanian S, Sui B, Sukreet S, Sulaiman E, Sung BH, Sunkara V, Suo Z, Svenningsen P, Swatler J, Symonds EKC, Szeifert V, Szigyártó IC, Tóth E, Taşli NP, Tahara H, Takahashi RU, Takakura Y, Takikawa O, Takov K, Tang VA, Taverna S, Tawil N, Teeuwen L, Tejedor S, Tertel T, Thakur A, Thompson-Felix T, Tian C, Tikhonov A, Tiwari S, Toh WS, Tomes JJ, Tonoli E, Trinidad C V., Tritten L, Trivedi R, Troyer Z, Tsamchoe M, Tscherrig V, Tsering T, Turkova K, Tutanov OS, Ueda K, Upadhya D, Urabe F, Urbanelli L, Urzì O, Vacchi E, Vader P, Vago R, Valadi H, Valkonen S, Varas-Godoy M, Varga Z, Vasconcelos MH, Vechetti IJ, Veiga SI, Vella LJ, Velot É, Verweij FJ, Vestad B, Vinay L, Viola M, Visnovitz T, Vreeland WN, Vukman K V., Wade PK, van de Wakker SI, Walther L, Wang T, Wang X, Watson DC, Weaver AM, Webber JP, Weber V, Weiss L, Weiss ML, Weiss R, Weissleder R, Wen Y, de Wever O, Wheelock AM, White KE, Whitehead B, Whiteside TL, Whitley J, Wiener Z, Van Wijnen AJ, Wiklander OPB, Winston CN, Wolf M, Wolfram J, Wu L, Wu Y, Wysmołek ME, Xander P, Xavier CPR, Xiao Y, Xu R, Yáñez-Mó M, Yamamoto T, Yamamoto Y, Yamamoto Y, Yan X, Yang L, Yang Y, Yarani R, Yea K, Yedigaryan L, Yenuganti VR, Yerneni SS, Yeung V, Yildizhan Y, Yin H, Yokoi A, Yoshioka Y, You Y, Yuan LQ, Yunga ST, Zakeri A, Zani A, Zanoni M, Zappulli V, Zarovni N, Zarubova J, Zempleni J, Žėkas V, Zhang H, Zhang Q, Zhao Z, Zhou Y, Zickler AM, Zimmermann P, Zivkovic AM, Zocco D, Zuba-Surma EK, Zubair H. 2024. Minimal information for studies of extracellular vesicles (MISEV2023): From basic to advanced approaches. J Extracell Vesicles 13.

149. Arias-Arias JL, MacPherson DJ, Hill ME, Hardy JA, Mora-Rodríguez R. 2020. A fluorescence-activatable reporter of flavivirus NS2B–NS3 protease activity enables live imaging of infection in single cells and viral plaques. Journal of Biological Chemistry 295:2212–2226.

150. Quiros-Fernandez I, Figueroa-Protti L, Arias-Arias JL, Brenes-Cordero N, Siles F, Mora J, Mora-Rodríguez RA. 2021. Perturbation-based modeling unveils the autophagic modulation of chemosensitivity and immunogenicity in breast cancer cells. Metabolites 11.

151. Kovaleva V, Mora R, Park YJ, Plass C, Chiramel AI, Bartenschlager R, Doḧner H, Stilgenbauer S, Pscherer A, Lichter P, Seiffert M. 2012. miRNA-130a targets ATG2B and DICER1 to inhibit autophagy and trigger killing of chronic lymphocytic leukemia cells. Cancer Res 72:1763–1772.

152. Abello J, Nguyen TDT, Marasini R, Aryal S, Weiss ML. 2019. Biodistribution of gadolinium- and near infrared-labeled human umbilical cord mesenchymal stromal cell-derived exosomes in tumor bearing mice. Theranostics 9:2325–2345.

153. Mora-Castro R, Hernández-Jiménez M, Sáenz-Arce G, Porras-Peñaranda J, Hanson-Snortum P, Avendaño-Soto E. 2020. Connecting biology, optics and nanomechanical properties in micro-wasps. Sci Rep 10.

154. Chevallet M, Luche S, Rabilloud T. 2006. Silver staining of proteins in polyacrylamide gels. Nat Protoc 1:1852–1858.

155. Lomonte B, Fernández J. 2022. Solving the microheterogeneity of *Bothrops asper* myotoxin-II by high-resolution mass spectrometry: Insights into C-terminal region variability in Lys49-phospholipase A2 homologs. Toxicon 210:123–131.

156. Sy Thau N, Nguyen TK, Truong N Van, Chu TTH, Na SH, Moon RW, Lau YL, Nyunt MH, Park WS, Chun WJ, Lu F, Lee SK, Han JH, Han ET. 2024. Characterization of merozoite-specific thrombospondin-related anonymous protein (MTRAP) in *Plasmodium vivax* and *P. knowlesi* parasites. Front Cell Infect Microbiol 14.

157. Promeneur D, Liu Y, Maciel J, Agre P, King LS, Kumar N. 2007. Aquaglyceroporin PbAQP during intraerythrocytic development of the malaria parasite *Plasmodium berghei*. Proceedings of the National Academy of Sciences 104.

158. Tosta CE, Sedegah M, Henderson DC, Wedderburn N. 1980. *Plasmodium yoelii* and *Plasmodium berghei*: Isolation of Infected Erythrocytes from Blood by Colloidal Silica Gradient Centrifugation. Exp Parasitol 50:7–15.

159. Livshts MA, Khomyakova E, Evtushenko EG, Lazarev VN, Kulemin NA, Semina SE, Generozov E V., Govorun VM. 2015. Isolation of exosomes by differential centrifugation: Theoretical analysis of a commonly used protocol. Sci Rep 5.

160. Yoshii SR, Mizushima N. 2017. Monitoring and measuring autophagy. Int J Mol Sci 18.

161. Klionsky DJ, Kamal Abdel-Aziz A, Abdelfatah S, Abdellatif M, Abdoli A, Abel S, Abeliovich H, Abildgaard MH, Princely Abudu Y, Acevedo-Arozena A, Adamopoulos IE, Adeli K, Adolph TE, Adornetto A, Aflaki E, Agam G, Agarwal A, Aggarwal BB, Agnello M, Agostinis P, Agrewala JN, Agrotis A, Aguilar P V, Tariq Ahmad S, Ahmed ZM, Ahumada-Castro U, Aits S, Aizawa S, Akkoc Y, Akoumianaki T, Aysin Akpinar H, Al-Abd AM, Al-Akra L, Al-Gharaibeh A, Alaoui-Jamali MA, Alberti S, Alcocer-Gómez E, Alessandri C, Ali M, Abdul Alim Al-Bari M, Aliwaini S, Alizadeh J, Almacellas E, Almasan A, Alonso A, Alonso GD, Altan-Bonnet N, Altieri DC, C Álvarez ÉM, Alves S, Alves da Costa C, Alzaharna MM, Amadio M, Amantini C, Amaral C, Ambrosio S, Amer AO, Ammanathan V, An Z, Andersen SU, Andrabi SA, Andrade-Silva M, Andres AM, Angelini S, Ann D, Anozie UC, Ansari MY, Antas P, Antebi A, Antón Z, Anwar T, Apetoh L, Apostolova N, Araki T, Araki Y, Arasaki K, Araújo WL, Araya J, Arden C, Arévalo M-A, Arguelles S, Arias E, Arikkath J, Arimoto H, Ariosa AR, Armstrong-James D, Arnauné-Pelloquin L, Aroca A, Arroyo DS, Arsov I, Artero R, Maria Lucia Asaro D, Aschner M, Ashrafizadeh M, Ashur-Fabian O, Atanasov AG, Au AK, Auberger P, Auner HW, Aurelian L, Autelli R, Avagliano L, Ávalos Y, Aveic S, Alexandra Aveleira C, Avin-Wittenberg T, Aydin Y, Ayton S, Ayyadevara S, Azzopardi M, Baba M, Backer JM, Backues SK, Bae D-H, Bae O-N, Han Bae S, Baehrecke EH, Baek A, Baek S-H, Hee Baek S, Bagetta G, Bagniewska-Zadworna A, Bai H, Bai J, Bai X, Bai Y, Bairagi N, Baksi S, Balbi T, Baldari CT, Balduini W, Ballabio A, Ballester M, Balazadeh S, Balzan R, Bandopadhyay R, Banerjee S, Banerjee S, Bánréti Á, Bao Y, Baptista MS, Baracca A, Barbati C, Bargiela A, Barilà D, Barlow PG, Barmada SJ, Barreiro E, Barreto GE, Bartek J, Bartel B, Bartolome A, Barve GR, Basagoudanavar SH, Bassham DC, Bast Jr RC, Basu A, Batoko H, Batten I, Baulieu EE, Baumgarner BL, Bayry J, Beale R. 2021. Guidelines for the use and interpretation of assays for monitoring autophagy (4th edition). Autophagy.

162. Wang B, Shi Y, Chen J, Shao Z, Ni L, Lin Y, Wu Y, Tian N, Zhou Y, Sun L, Wu A, Hong Z, Wang X, Zhang X. 2021. High glucose suppresses autophagy through the AMPK pathway while it induces autophagy via oxidative stress in chondrocytes. Cell Death Dis 12.

163. Giblin-Burnham J, Javanmardi Y, Moeendarbary E, Hoogenboom BW. 2024. Finite element modelling of atomic force microscopy imaging on deformable surfaces. Soft Matter 20:9483–9492.

164. Imanbekova M, Suarasan S, Lu Y, Jurchuk S, Wachsmann-Hogiu S. 2022. Recent advances in optical label-free characterization of extracellular vesicles. Nanophotonics 11:2827–2863.

165. Joshi U, George LB, Highland H. 2025. Red blood cell extracellular vesicles: new frontiers in hematological biomarker discovery. Front Med (Lausanne) 12.

166. Mantel PY, Hoang AN, Goldowitz I, Potashnikova D, Hamza B, Vorobjev I, Ghiran I, Toner M, Irimia D, Ivanov AR, Barteneva N, Marti M. 2013. Malaria-infected erythrocyte-derived microvesicles mediate cellular communication within the parasite population and with the host immune system. Cell Host Microbe 13:521–534.

167. Sima N, Ayllon-Hermida A, Fernández-Becerra C, del Portillo HA. 2025. Extracellular vesicles in malaria: proteomics insights, in vitro and in vivo studies indicate the need for transitioning to natural human infections. mBio 16.

168. Camacho AC, Alfandari D, Kozela E, Regev-Rudzki N. 2023. Biogenesis of extracellular vesicles in protozoan parasites: The ESCRT complex in the trafficking fast lane? PLoS Pathog 19.

169. Sutrave S, Richter MH. 2021. Truman show for protozoan parasites: A review of *in vitro* cultivation platforms. PLoS Negl Trop Dis 15.

170. Moon RW, Hall J, Rangkuti F, Ho YS, Almond N, Mitchell GH, Pain A, Holder AA, Blackman MJ. 2013. Adaptation of the genetically tractable malaria pathogen *Plasmodium knowlesi* to continuous culture in human erythrocytes. Proc Natl Acad Sci U S A 110:531–536.

171. Lewis-Hughes P, Howell M. 1984. *In vitro* culture of *Plasmodium yoelii* blood stages. Int J Parasitol 14:447–492.

172. Udomsangpetch R, Somsri S, Panichakul T, Chotivanich K, Sirichaisinthop J, Yang Z, Cui L, Sattabongkot J. 2007. Short-term in vitro culture of field isolates of *Plasmodium vivax* using umbilical cord blood. Parasitol Int 56:65–69.

173. Kumari S, Sinha A. 2023. Culture and transfection: Two major bottlenecks in understanding *Plasmodium vivax* biology. Front Microbiol 14.

174. Mons B, Janse CJ, Croon JJ, Van Der Kmy HJ. 1983. In vitro culture of *Plasmodium berghei* using a new suspension system. Int J Parasitol 13:213–211.

175. Orjih AU. 2005. Comparison of *Plasmodium falciparum* growth in sickle cells in low oxygen environment and candle-jar. Acta Trop 94:25–34.

176. Olszewski KL, Llinás M. 2011. Central carbon metabolism of *Plasmodium* parasites. Mol Biochem Parasitol 175:95–103.

177. Torrentino-Madamet M, Alméras L, Desplans J, Priol Y Le, Belghazi M, Pophillat M, Fourquet P, Jammes Y, Parzy D. 2011. Global response of *Plasmodium falciparum* to hyperoxia: A combined transcriptomic and proteomic approach. Malar J 10.

178. Torrentino-Madamet M, Desplans J, Travaillé C, Jammes Y, Parzy D. 2010. Microaerophilic Respiratory Metabolism of *Plasmodium falciparum* Mitochondrion as a Drug Target. Curr Mol Med 10:29–46.

179. Bei AK, Patel SD, Volkman SK, Ahouidi AD, Ndiaye D, Mboup S, Wirth DF. 2014. An adjustable gas-mixing device to increase feasibility of *in vitro* culture of *Plasmodium falciparum* parasites in the field. PLoS One 9.

180. Hanifian H, Nateghpour M, Motevalli Haghi A, Teimouri A, Razavi S, Fariver L. 2022. Development and optimizing a simple and cost-effective medium for *in vitro* culture of *Plasmodium berghei*-ANKA strain with conserving its infectivity in BALB/c mice. BMC Res Notes 15:1–6.

181. Arunrerkdeewong K, Pattaradilokrat S, Siripoon N, Harnyuttanakorn P. 2017. Effect of temperatures on the parasitaemia of *Plasmodium falciparum in vitro*. J Health Res 31.

182. El-Assaad F, Wheway J, Mitchell AJ, Lou J, Hunt NH, Combes V, Grau GER. 2013. Cytoadherence of *Plasmodium berghei*-infected red blood cells to murine brain and lung microvascular endothelial cells in vitro. Infect Immun 81:3984–3991.

183. Franke-Fayard B, Janse CJ, Cunha-Rodrigues M, Ramesar J, Bü Scher P, Que I, Lö Wik C, Voshol PJ, Den Boer MAM, Van Duinen SG, Febbraio M, Mota MM, Waters AP. 2005. Murine malaria parasite sequestration: CD36 is the major receptor, but cerebral pathology is unlinked to sequestration. Proceedings of the National Academy of Sciences 102.

184. Franke-Fayard B, Fonager J, Braks A, Khan SM, Janse CJ. 2010. Sequestration and tissue accumulation of human malaria parasites: Can we learn anything from rodent models of malaria? PLoS Pathog https://doi.org/10.1371/journal.ppat.1001032.

185. Janse CJ, Boorsma EG, Ramesar J, Grobbee MJ, Mons B. 1989. Host cell specificity and schizogony of *Plasmodium berghei* under different *in vitro* conditions. Int J Parasitol 19.

186. Smalley ME, Butcher GA. 1975. The *in vitro* culture of the blood stages of *Plasmodium berghei*. Int J Parasitol 5:131–132.

187. Soga A, Bando H, Ko-Ketsu M, Masuda-Suganuma H, Kawazu SI, Fukumoto S. 2017. High efficacy in vitro selection procedure for generating transgenic parasites of Plasmodium berghei using an antibiotic toxic to rodent hosts. Sci Rep 7.

188. Tewari SG, Rajaram K, Schyman P, Swift R, Reifman J, Prigge ST, Wallqvist A. 2019. Short-term metabolic adjustments in *Plasmodium falciparum* counter hypoxanthine deprivation at the expense of long-term viability. Malar J 18.

189. Asahi H, Kanazawa T, Kajihara Y, Takahashi K, Takahashi WT. 1996. Hypoxanthine: a low molecular weight factor essential for growth of erythrocytic *Plasmodium falciparum* in a serum-free medium. Parasitology 113:19–23.

190. Harkness RA, Simmonds RJ, Gough P, Priscott PK, Squire JA. 1980. Purine base and nucleoside, cytidine and uridine concentrations in foetal calf and other sera. J Clin Chem Biochem 8:429–430.

191. Scheller LF, Wirtz RA, Azad" AF. 1994. Susceptibility of different strains of mice to hepatic infection with *Plasmodium berghei*. Infect Immun 62:4844–4847.

192. Eling W, Van Zon A, Jerusalem C. 1977. The course of a *Plasmodium berghei* Infection in six different mouse strains. Z Parasitenk 54:29–45.

193. Belmonte M, Jones TR, Lu M, Arcilla R, Smalls T, Belmonte A, Rosenbloom J, Carucci DJ, Sedegah M. 2003. The infectivity of *Plasmodium yoelii* in different strains of mice. Journal of Parasitology 89:602–603.

194. Claessen MJAG, Yagci N, Fu K, Brandsma E, Kersten MJ, von Lindern M, van den Akker E. 2024. Production and stability of cultured red blood cells depends on the concentration of cholesterol in culture medium. Sci Rep 14.

195. Frankland S, Elliott SR, Yosaatmadja F, Beeson JG, Rogerson SJ, Adisa A, Tilley L. 2007. Serum lipoproteins promote efficient presentation of the malaria virulence protein PfEMP1 at the erythrocyte surface. Eukaryot Cell 6:1584–1594.

196. Hentzschel F, Gibbins MP, Attipa C, Beraldi D, Moxon CA, Otto TD, Marti M. 2022. Host cell maturation modulates parasite invasion and sexual differentiation in *Plasmodium berghei*. Sci Adv 8:7348.

197. CHIEN S. 1975. Biophysical Behavior of Red Cells in Suspensions, p. 1031–1133. In The Red Blood Cell. Elsevier.

198. Mathers A, Evans GO, Bleby J. 2012. Reticulocyte measurements in rat, dog and mouse whole blood samples using the Sysmex XT-2000iV. Comp Clin Path 21:631–637.

199. Srivastava A, Creek DJ, Evans KJ, De Souza D, Schofield L, Müller S, Barrett MP, McConville MJ, Waters AP. 2015. Host reticulocytes provide metabolic reservoirs that can be exploited by malaria parasites. PLoS Pathog 11.

200. Zhu X, Liu J, Feng Y, Pang W, Qi Z, Jiang Y, Shang H, Cao Y. 2015. Phenylhydrazine administration accelerates the development of experimental cerebral malaria. Exp Parasitol 156:1–11.

201. Singh I, Nagiec EE, Thompson JM, Krzyzanski W, Singh P. 2015. A systems pharmacology model of erythropoiesis in mice induced by small molecule inhibitor of prolyl hydroxylase enzymes. CPT Pharmacometrics Syst Pharmacol 4:106–115.

202. McNally J, O'donovan SM, Dalton JP. 1992. *Plasmodium berghei* and *Plasmodium chabaudi chabaudi*: Development of simple *in vitro* erythrocyte invasion assays. Parasitology 105:355–362.

203. Dalton JP, McNally J, O'Donovan SM. 1993. *In vitro* assays for the study of erythrocyte invasion by malarial parasites. Parasitology Today 9.

204. Asahi H, Kanazawa T, Hirayama N, Kajihara Y. 2005. Investigating serum factors promoting erythrocytic growth of Plasmodium falciparum. Exp Parasitol 109:7–15.

205. Holmberg S, Schulman S, Vanderberg JP. 1981. Role of a serum factor in enhancement of in vitro interactions between *Plasmodium berghei* sporozoites and hamster peritoneal macrophages. J Parasitol 67:893–897.

206. Bhakdi SC, Ottinger A, Somsri S, Sratongno P, Pannadaporn P, Chimma P, Malasit P, Pattanapanyasat K, Neumann HP. 2010. Optimized high gradient magnetic separation for isolation of *Plasmodium*-infected red blood cells. Malar J 9.

207. Mata-Cantero L, Lafuente MJ, Sanz L, Rodriguez MS. 2014. Magnetic isolation of *Plasmodium falciparum* schizonts iRBCs to generate a high parasitaemia and synchronized in vitro culture. Malar J 13.

208. Lawson C, Kovacs D, Finding E, Ulfelder E, Luis-Fuentes V. 2017. Extracellular Vesicles: Evolutionarily Conserved Mediators of Intercellular Communication. Yale Journal of Biology and Medicine 90:481–491.

209. Witwer KW, Goberdhan DC, O'driscoll L, Théry C, Welsh JA, Blenkiron C, Buzás EI, Vizio D Di, Erdbrügger U, Falcón-Pérez JM. 2021. Updating MISEV: Evolving the minimal requirements for studies of extracellular vesicles. J Extracell Vesicles 10.

210. Willekens FLA, Werre JM, Groenen-Döpp YAM, Roerdinkholder-Stoelwinder B, De Pauw B, Bosman GJCGM. 2008. Erythrocyte vesiculation: A self-protective mechanism? Br J Haematol 141:549–556.

211. Fernandez-Becerra C, Xander P, Alfandari D, Dong G, Aparici-Herraiz I, Rosenhek-Goldian I, Shokouhy M, Gualdron-Lopez M, Lozano N, Cortes-Serra N, Karam PA, Meneghetti P, Madeira RP, Porat Z, Soares RP, Costa AO, Rafati S, da Silva AC, Santarém N, Fernandez-Prada C, Ramirez MI, Bernal D, Marcilla A, Pereira-Chioccola VL, Alves LR, Portillo H Del, Regev-Rudzki N, de Almeida IC, Schenkman S, Olivier M, Torrecilhas AC. 2023. Guidelines for the purification and characterization of extracellular vesicles of parasites. Journal of Extracellular Biology 2.

212. Aparici-Herraiz I, Gualdrón-López M, Castro-Cavadía CJ, Carmona-Fonseca J, Yasnot MF, Fernandez-Becerra C, del Portillo HA. 2022. Antigen discovery in circulating extracellular vesicles from *Plasmodium vivax* patients. Front Cell Infect Microbiol 11.

213. Gelibter S, Marostica G, Mandelli A, Siciliani S, Podini P, Finardi A, Furlan R. 2022. The impact of storage on extracellular vesicles: A systematic study. J Extracell Vesicles 11.

214. Ahmadian S, Jafari N, Tamadon A, Ghaffarzadeh A, Rahbarghazi R, Mahdipour M. 2024. Different storage and freezing protocols for extracellular vesicles: a systematic review. Stem Cell Research and Therapy 15.

215. Kim H, Seong J. 2021. Fluorescent protein-based autophagy biosensors. Materials 14.

216. Mizushima N, Yoshimori T, Levine B. 2010. Methods in Mammalian Autophagy Research. Cell 140:313–326.

217. Lopez A, Fleming A, Rubinsztein DC. 2018. Seeing is believing: Methods to monitor vertebrate autophagy in vivo. Open Biol 8.

218. Williams L, Courtneidge SA, Wagner EF. 1988. Embryonic lethalities and endothelial tumors in chimeric mice expressing polyoma virus middle T oncogene. Cell 52:121–131.

219. Boraschi D, Rambaldi A, Sica A, Ghiara P, Colotta F, Wang JM, De Rossi M, Zoia C, Remuzzi G, Bussolino F, Scapigliati G, Stoppacciaro A, Ruco L, Tagliabue A, Mantovani A. 1991. Endothelial cells express the interleukin-1 receptor type I. Blood 78:1262–1267.

220. Montesano R, Pepper MS, Möhle-Steinlein : U, Risau W, Wagner EF, Orci L. 1990. Increased proteolytic activity is responsible for the aberrant morphogenetic behavior of endothelial cells expressing the middle T oncogene. Cell 62:435–445.

221. Ghigo D, Arese M, Todde R, Vecchi A, Silvagno F, Costamagna C, Dong QG, Alessio M, Heller R, Soldi R, Trucco F, Garbarino G, Pescarmona G, Mantovani A, Bussolino F, Bosia A. 1995. Middle T antigen-tranfformed endothelial cells exhibit an increased activity of nitric oxide synthase. J Exp Med 181:9–19.

222. Hansen TE, Johansen T. 2011. Following autophagy step by step. BMC Biol 9.

223. Kuma A, Komatsu M, Mizushima N. 2017. Autophagy-monitoring and autophagy-deficient mice. Autophagy 13:1619–1628.

224. Yang YP, Hu LF, Zheng HF, Mao CJ, Hu WD, Xiong KP, Wang F, Liu CF. 2013. Application and interpretation of current autophagy inhibitors and activators. Acta Pharmacol Sin 34:625–635.

225. Mizushima N. 2025. Autophagic flux measurement: Cargo degradation versus generation of degradation products. Curr Opin Cell Biol 93.

226. Wu YT, Tan HL, Shui G, Bauvy C, Huang Q, Wenk MR, Ong CN, Codogno P, Shen HM. 2010. Dual role of 3-methyladenine in modulation of autophagy via different temporal patterns of inhibition on class I and III phosphoinositide 3-kinase. Journal of Biological Chemistry 285:10850–10861.

227. Kiefer F, Anhausert I, Soriano P, Aguzzi A, Courtneidge SA, Wagner EF. 1994. Endothelial cell transformation by polyomavirus middle T antigen in mice lacking Src-related kinases. Current Biology 4:100–109.

228. Liu M, Dickinson-Copeland C, Hassana S, Stiles JK. 2016. *Plasmodium*-infected erythrocytes (pRBC) induce endothelial cell apoptosis via a heme-mediated signaling pathway. Drug Des Devel Ther 10:1009–1018.

229. Gillrie MR, Ho M. 2017. Dynamic interactions of *Plasmodium* spp. with vascular endothelium. Tissue Barriers 5.

230. Sardiello M, Palmieri M, di Ronza A, Medina D, Valenza M, Gennarino A, Di Malta C, Donaudy F, Embrione V, Polishchuk R, Banfi S, Parenti G, Cattaneo E, Ballabio A. 2009. A gene network regulating lysosomal biogenesis and function. Science (1979) 325:473–476.

231. Pang Y, Wu L, Tang C, Wang H, Wei Y. 2022. Autophagy-inflammation interplay during infection: Balancing pathogen clearance and host inflammation. Front Pharmacol 13.

232. Champion JA, Mitragotri S. 2006. Role of target geometry in phagocytosis. PNAS 103:4930–4934.

233. Calabrese EJ, Mattson MP. 2017. How does hormesis impact biology, toxicology, and medicine? Aging and Mechanisms of Disease 3.

234. Davis SP, Amrein M, Gillrie MR, Lee K, Muruve DA, Ho M. 2012. *Plasmodium falciparum* -induced CD36 clustering rapidly strengthens cytoadherence via p130CAS-mediated actin cytoskeletal rearrangement. The FASEB Journal 26:1119–1130.

235. Kast DJ, Dominguez R. 2017. The cytoskeleton–autophagy connection. Current Biology 27:R318–R326.

236. Aguilera MO, Berón W, Colombo MI. 2012. The actin cytoskeleton participates in the early events of autophagosome formation upon starvation induced autophagy. Autophagy 8:1590–1603.

237. Tripathi AK, Sha W, Shulaev V, Stins MF, Sullivan DJ. 2009. *Plasmodium falciparum*-infected erythrocytes induce NF-κB regulated inflammatory pathways in human cerebral endothelium. Blood 114.

238. Xu W, Liu S, Li W, Xu B, Shan T, Lin R, Du YT, Chen G. 2025. *Plasmodium* infection modulates host inflammatory response through circRNAs during the intracellular stage in red blood cells. ACS Infect Dis 11:1018–1029.

239. Shio MT, Kassa FA, Bellemare MJ, Olivier M. 2010. Innate inflammatory response to the malarial pigment hemozoin. Microbes Infect 12:889–899.

240. Olivier M, Van Den Ham K, Shio MT, Kassa FA, Fougeray S. 2014. Malarial pigment hemozoin and the innate inflammatory response. Front Immunol 5.

241. Qian M, Fang X, Wang X. 2017. Autophagy and inflammation. Clin Transl Med 6.

242. Levine B, Mizushima N, Virgin HW. 2011. Autophagy in immunity and inflammation. Nature 469:323–335.

243. Kotepui KU, Mahittikorn A, Wilairatana P, Masangkay FR, Kotepui M. 2023. Association between *Plasmodium* infection and nitric oxide levels: A systematic review and meta-analysis. Antioxidants 12.

244. Vasquez M, Zuniga M, Rodriguez A. 2021. Oxidative stress and pathogenesis in malaria. Front Cell Infect Microbiol 11.

245. Montagna C, Rizza S, Maiani E, Piredda L, Filomeni G, Cecconi F. 2016. To eat, or NOt to eat: S-nitrosylation signaling in autophagy. FEBS Journal 283:3857–3869.

246. Kim KR, Cho EJ, Eom JW, Oh SS, Nakamura T, Oh C ki, Lipton SA, Kim YH. 2022. S-Nitrosylation of cathepsin B affects autophagic flux and accumulation of protein aggregates in neurodegenerative disorders. Cell Death Differ 29:2137–2150.

247. Tabak S, Schreiber-Avissar S, Beit-Yannai E. 2018. Extracellular vesicles have variable dose-dependent effects on cultured draining cells in the eye. J Cell Mol Med 22:1992–2000.

248. Hagey DW, Ojansivu M, Bostancioglu BR, Saher O, Bost JP, Gustafsson MO, Gramignoli R, Svahn M, Gupta D, Stevens MM, Görgens A, Andaloussi S EL. 2023. The cellular response to extracellular vesicles is dependent on their cell source and dose. Sci Adv 9.

249. Gupta D, Zickler AM, El Andaloussi S. 2021. Dosing extracellular vesicles. Adv Drug Deliv Rev 178.

250. Borgheti-Cardoso LN, Kooijmans SAA, Chamorro LG, Biosca A, Lantero E, Ramírez M, Avalos-Padilla Y, Crespo I, Fernández I, Fernandez-Becerra C, del Portillo HA, Fernàndez-Busquets X. 2020. Extracellular vesicles derived from *Plasmodium*-infected and non-infected red blood cells as targeted drug delivery vehicles. Int J Pharm 587.

251. Thangaraju K, Neerukonda SN, Katneni U, Buehler PW. 2021. Extracellular vesicles from red blood cells and their evolving roles in health, coagulopathy and therapy. Int J Mol Sci 22:1–25.

252. Solga I, Yogathasan V, Wischmann P, Pang TY, Götzmann L, Kleimann P, Temme S, Hofer L, Stefanski A, Lang A, Nickenig G, Jung C, Gerdes N, Hosen MR, Kelm M, Chennupati R. 2025. Large extracellular vesicles derived from red blood cells in coronary artery disease patients with anemia promote endothelial dysfunction.

253. Collado A, Humoud R, Kontidou E, Eldh M, Swaich J, Zhao A, Yang J, Jiao T, Domingo E, Carlestål E, Mahdi A, Tengbom J, Végvári Á, Deng Q, Alvarsson M, Gabrielsson S, Eriksson P, Zhou Z, Pernow J. 2025. Erythrocyte-derived extracellular vesicles induce endothelial dysfunction through arginase-1 and oxidative stress in type 2 diabetes. Journal of Clinical Investigation 135.

254. Verweij FJ, Revenu C, Arras G, Dingli F, Loew D, Pegtel DM, Follain G, Allio G, Goetz JG, Zimmermann P, Herbomel P, Del Bene F, Raposo G, van Niel G. 2019. Live Tracking of Inter-organ Communication by Endogenous Exosomes In Vivo. Dev Cell 48:573-589.e4.

255. Heckmann BL, Green DR. 2019. LC3-associated phagocytosis at a glance. J Cell Sci 132.

256. Peña-Martinez C, Rickman AD, Heckmann BL. 2022. Beyond autophagy: LC3-associated phagocytosis and endocytosis. Sci Adv 8:1702.

257. Longo A, Manganelli V, Misasi R, Riitano G, Caglar TR, Fasciolo E, Recalchi S, Sorice M, Garofalo T. 2025. Extracellular vesicles in the crosstalk of autophagy and apoptosis: A role for lipid rafts. Cells 14.

258. Pedrioli G, Paganetti P. 2021. Hijacking Endocytosis and Autophagy in Extracellular Vesicle Communication: Where the inside meets the outside. Front Cell Dev Biol 8.

259. Romenskaja D, Jonavičė U, Pivoriūnas A. 2024. Extracellular vesicles promote autophagy in human microglia through lipid raft-dependent mechanisms. FEBS Journal 291:3706–3722.

260. Wei W, Pan Y, Yang X, Chen Z, Heng Y, Yang B, Pu M, Zuo J, Lai Z, Tang Y, Xin W. 2022. The emerging role of the interaction of extracellular vesicle and autophagy—novel insights into neurological disorders. J Inflamm Res 15:3395–3407.

261. Zhang X, Zhang M, Wang QR, Hou X, Zhou T, Liu J, Wang Q, Liu W, Liu X, Jin X, Liu Z, Huang B. 2023. Malaria-derived exosomes exacerbate liver injury during blood stage of *Plasmodium berghei* infection. Acta Trop 239.

262. Oikonomou V, Moretti S, Renga G, Galosi C, Borghi M, Pariano M, Puccetti M, Palmerini CA, Amico L, Carotti A, Prezioso L, Spolzino A, Finocchi A, Rossi P, Velardi A, Aversa F, Napolioni V, Romani L. 2016. Noncanonical fungal autophagy inhibits inflammation in response to IFN-γ via DAPK1. Cell Host Microbe 20:744–757.

263. Blow F, Buck AH. 2022. Extracellular vesicles from malaria-infected red blood cells: not all are secreted equal. EMBO Rep 23.

264. Whittaker TE, Nagelkerke A, Nele V, Kauscher U, Stevens MM. 2020. Experimental artefacts can lead to misattribution of bioactivity from soluble mesenchymal stem cell paracrine factors to extracellular vesicles. J Extracell Vesicles 9.

265. Oggungwan K, Glaharn S, Ampawong S, Krudsood S, Viriyavejakul P. 2018. FTY720 restores endothelial cell permeability induced by malaria sera. Sci Rep 8.

266. Wongsawat M, Glaharn S, Srisook C, Dechkhajorn W, Chaisri U, Punsawad C, Techarang T, Chotivanich K, Krudsood S, Viriyavejakul P. 2024. Immunofluorescence study of cytoskeleton in endothelial cells induced with malaria sera. Malar J 23.

267. Raacke M, Kerr A, Dörpinghaus M, Brehmer J, Wu Y, Lorenzen S, Fink C, Jacobs T, Roeder T, Sellau J, Bachmann A, Metwally NG, Bruchhaus I. 2021. Altered cytokine response of human brain endothelial cells after stimulation with malaria patient plasma. Cells 10.

268. Silva LS, Pinheiro AS, Teixeira DE, Silva-Aguiar RP, Peruchetti DB, Scharfstein J, Caruso-Neves C, Pinheiro AAS. 2019. kinins released by erythrocytic stages of *Plasmodium falciparum* enhance adhesion of infected erythrocytes to endothelial cells and increase blood brain barrier permeability via activation of bradykinin receptors. Front Med (Lausanne) 6.

269. Liao Z, Muth DC, Eitan E, Travers M, Learman LN, Lehrmann E, Witwer KW. 2017. Serum extracellular vesicle depletion processes affect release and infectivity of HIV-1 in culture. Sci Rep 7.

270. Garcia LFC, Wowk PF, Albrecht L. 2024. Unraveling the impact of extracellular vesicle-depleted serum on endothelial cell characteristics over time. Int J Mol Sci 25.

271. Szatanek R, Baj-Krzyworzeka M, Zimoch J, Lekka M, Siedlar M, Baran J. 2017. The methods of choice for extracellular vesicles (EVs) characterization. Int J Mol Sci 18.

272. Danaei M, Dehghankhold M, Ataei S, Hasanzadeh Davarani F, Javanmard R, Dokhani A, Khorasani S, Mozafari MR. 2018. Impact of particle size and polydispersity index on the clinical applications of lipidic nanocarrier systems. Pharmaceutics 10.

273. Stetefeld J, McKenna SA, Patel TR. 2016. Dynamic light scattering: a practical guide and applications in biomedical sciences. Biophys Rev 8:409–427.

274. Jia Z, Li J, Gao L, Yang D, Kanaev A. 2023. Dynamic light scattering: a powerful tool for *in situ* nanoparticle sizing. Colloids and Interfaces 7.

275. van der Pol E, Coumans FAW, Grootemaat AE, Gardiner C, Sargent IL, Harrison P, Sturk A, van Leeuwen TG, Nieuwland R. 2014. Particle size distribution of exosomes and microvesicles determined by transmission electron microscopy, flow cytometry, nanoparticle tracking analysis, and resistive pulse sensing. Journal of Thrombosis and Haemostasis 12:1182–1192.

276. Opadokun T, Agyapong J, Rohrbach P. 2022. Protein profiling of malaria-derived extracellular vesicles reveals distinct subtypes. Membranes (Basel) 12:397.

277. de Oliveira GP, Welsh JA, Pinckney B, Palu CC, Lu S, Zimmerman A, Barbosa RH, Sahu P, Noshin M, Gummuluru S, Tigges J, Jones JC, Ivanov AR, Ghiran IC. 2023. Human red blood cells release microvesicles with distinct sizes and protein composition that alter neutrophil phagocytosis. Journal of Extracellular Biology 2.

278. Lucien F, Gustafson D, Lenassi M, Li B, Teske JJ, Boilard E, von Hohenberg KC, Falcón-Perez JM, Gualerzi A, Reale A, Jones JC, Lässer C, Lawson C, Nazarenko I, O'Driscoll L, Pink R, Siljander PRM, Soekmadji C, Hendrix A, Welsh JA, Witwer KW, Nieuwland

R. 2023. MIBlood-EV: Minimal information to enhance the quality and reproducibility of blood extracellular vesicle research. J Extracell Vesicles 12.

279. De Sousa KP, Potriquet J, Mulvenna J, Sotillo J, Groves PL, Loukas A, Apte SH, Doolan DL. 2022. Proteomic identification of the contents of small extracellular vesicles from *in vivo Plasmodium yoelii* infection. Int J Parasitol 52:35–45.

280. Vimonpatranon S, Roytrakul S, Phaonakrop N, Lekmanee K, Atipimonpat A, Srimark N, Sukapirom K, Chotivanich K, Khowawisetsut L, Pattanapanyasat K. 2022. Extracellular vesicles derived from early and late stage *Plasmodium falciparum*-infected red blood cells contain invasion-associated proteins. J Clin Med 11.

281. Midekessa G, Godakumara K, Ord J, Viil J, Lättekivi F, Dissanayake K, Kopanchuk S, Rinken A, Andronowska A, Bhattacharjee S, Rinken T, Fazeli A. 2020. Zeta potential of extracellular vesicles: Toward understanding the attributes that determine colloidal stability. ACS Omega 5:16701–16710.

282. Nguyen DB, Tran HT, Kaestner L, Bernhardt I. 2022. The relation between extracellular vesicles released from red blood cells, their cargo, and the clearance by macrophages. Front Physiol 13.

283. Biagiotti S, Canonico B, Tiboni M, Abbas F, Perla E, Montanari M, Battistelli M, Papa S, Casettari L, Rossi L, Guescini M, Magnani M. 2024. Efficient and highly reproducible production of red blood cell-derived extracellular vesicle mimetics for the loading and delivery of RNA molecules. Sci Rep 14.

284. Moreira LR, Prescilla-Ledezma A, Cornet-Gomez A, Linares F, Jódar-Reyes AB, Fernandez J, Vannucci AKI, De Pablos LM, Osuna A. 2021. Biophysical and biochemical comparison of extracellular vesicles produced by infective and non-infective stages of *Trypanosoma cruzi*. Int J Mol Sci 22.

285. Tokumasu F, Ostera GR, Amaratunga C, Fairhurst RM. 2012. Modifications in erythrocyte membrane zeta potential by *Plasmodium falciparum* infection. Exp Parasitol 131:245–251.

286. Sharma S, Rasool HI, Palanisamy V, Mathisen C, Schmidt M, Wong DT, Gimzewski JK. 2010. Structural-mechanical characterization of nanoparticle exosomes in human saliva, using correlative AFM, FESEM, and force spectroscopy. ACS Nano 4:1921–1926.

287. Wang Z, Zhou X, Kong Q, He H, Sun J, Qiu W, Zhang L, Yang M. 2024. Extracellular vesicle preparation and analysis: A state-of-the-art review. Advanced Science 11.

288. Feng Y, Liu M, Li X, Li M, Xing X, Liu L. 2023. Nanomechanical signatures of extracellular vesicles from hematologic cancer patients unraveled by atomic force microscopy for liquid biopsy. Nano Lett 23:1591–1599.

289. Ridolfi A, Conti L, Brucale M, Frigerio R, Cardellini J, Musicò A, Romano M, Zendrini A, Polito L, Bergamaschi G, Gori A, Montis C, Panella S, Barile L, Berti D, Radeghieri A, Bergese P, Cretich M, Valle F. 2023. Particle profiling of EV-lipoprotein mixtures by AFM nanomechanical imaging. J Extracell Vesicles 12.

290. Hoo CM, Starostin N, West P, Mecartney ML. 2008. A comparison of atomic force microscopy (AFM) and dynamic light scattering (DLS) methods to characterize nanoparticle size distributions. Journal of Nanoparticle Research 10:89–96.

291. Varga Z, Fehér B, Kitka D, Wacha A, Bóta A, Berényi S, Pipich V, Fraikin JL. 2020. Size measurement of extracellular vesicles and synthetic liposomes: the impact of the hydration shell and the protein corona. Colloids Surf B Biointerfaces 192.

292. Skliar M, Chernyshev VS. 2019. Imaging of extracellular vesicles by atomic force microscopy. Journal of Visualized Experiments 2019.

293. Ukraintsev E, Kromka A, Kozak H, Remeš Z, Rezek B. 2012. Artifacts in Atomic Force Microscopy of Biological Samples, p. . In Bellitto, V (ed.), Atomic force microscopy – imaging, measuring and manipulating surfaces at the atomic scale, 1st ed. InTech.

294. Shih HJ, Shih PJ. 2015. Tip effect of the tapping mode of atomic force microscope in viscous fluid environments. Sensors (Switzerland) 15:18381–18401.

295. Sebaihi N, De Boeck B, Yuana Y, Nieuwland R, Pétry J. 2017. Dimensional characterization of extracellular vesicles using atomic force microscopy. Meas Sci Technol 28.

296. Joshi U, Shah S, Gupta S, George LB, Highland H. 2025. Evaluation of Exosomal Proteins as Potential Biomarkers from RBC Stages of Plasmodium falciparum 3D7. ACS Infect Dis 11:164–180.

297. Ma SR, Xia HF, Gong P, Yu ZL. 2023. Red blood cell-derived extracellular vesicles: an overview of current research progress, challenges, and opportunities. Biomedicines 11.

298. Avalos-Padilla Y, Georgiev VN, Lantero E, Pujals S, Verhoef R, Borgheti-Cardoso LN, Albertazzi L, Dimova R, Fernàndez-Busquets X. 2021. The ESCRT-III machinery participates in the production of extracellular vesicles and protein export during *Plasmodium falciparum* infection. PLoS Pathog 17.

299. Kilic P, Karabudak S, Cosar B, Savran BN, Yalcin M. 2024. Residual protein analysis by SDS–PAGE in clinically manufactured BM-MSC products. Electrophoresis 45:1606–1617.

300. Rath A, Glibowicka M, Nadeau VG, Chen G, Deber CM. 2009. Detergent binding explains anomalous SDS-PAGE migration of membrane proteins. PNAS 106.

301. Miller I, Crawford J, Gianazza E. 2006. Protein stains for proteomic applications: Which, when, why? Proteomics 6:5385–5408.

302. Sampaio NG, Emery SJ, Garnham AL, Tan QY, Sisquella X, Pimentel MA, Jex AR, Regev-Rudzki N, Schofield L, Eriksson EM. 2018. Extracellular vesicles from early stage *Plasmodium falciparum*-infected red blood cells contain PfEMP1 and induce transcriptional changes in human monocytes. Cell Microbiol 20.

303. Ben-Nissan G, Katzir N, Füzesi-Levi MG, Sharon M. 2022. Biology of the extracellular proteasome. Biomolecules 12.

304. Abdi A, Yu L, Goulding D, Rono MK, Bejon P, Choudhary J, Rayner J. 2017. Proteomic analysis of extracellular vesicles from a *Plasmodium falciparum* Kenyan clinical isolate defines a core parasite secretome. Wellcome Open Res 2.

305. Dekel E, Yaffe D, Rosenhek-Goldian I, Ben-Nissan G, Ofir-Birin Y, Morandi MI, Ziv T, Sisquella X, Pimentel MA, Nebl T, Kapp E, Ohana Daniel Y, Karam PA, Alfandari D, Rotkopf R, Malihi S, Temin TB, Mullick D, Revach OY, Rudik A, Gov NS, Azuri I, Porat Z, Bergamaschi G, Sorkin R, Wuite GJL, Avinoam O, Carvalho TG, Cohen SR, Sharon

M, Regev-Rudzki N. 2021. 20S proteasomes secreted by the malaria parasite promote its growth. Nat Commun 12.

306. Helbig AO, Heck AJR, Slijper M. 2010. Exploring the membrane proteome-Challenges and analytical strategies. J Proteomics 73:868–878.

307. Whitelegge JP. 2013. Integral membrane proteins and bilayer proteomics. Anal Chem 85:2558–2568.

308. Ghosh K, Jacobs-Lorena M. 2011. Surface-expressed enolases of *Plasmodium* and other pathogens. Mem Inst Oswaldo Cruz.

309. Werelusz P, Galiniak S, Mołoń M. 2024. Molecular functions of moonlighting proteins in cell metabolic processes. Biochim Biophys Acta Mol Cell Res 1871.

310. Ginger ML. 2014. Protein moonlighting in parasitic protists. Biochem Soc Trans 42:1734–1739.

311. Bosch J, Buscaglia CA, Krumm B, Ingason BP, Lucas R, Roach C, Cardozo T, Nussenzweig V, Hol WGJ. 2007. Aldolase provides an unusual binding site for thrombospondin-related anonymous protein in the invasion machinery of the malaria parasite. PNAS 104.

312. Alam A, Neyaz MK, Hasan SI. 2014. Exploiting unique structural and functional properties of malarial glycolytic enzymes for antimalarial drug development. Malar Res Treat 2014.

313. Cha SJ, Kim MS, Pandey A, Jacobs-Lorena M. 2016. Identification of GAPDH on the surface of *Plasmodium* sporozoites as a new candidate for targeting malaria liver invasion. Journal of Experimental Medicine 213:2099–2112.

314. Ochkasova A, Arbuzov G, Malygin A, Graifer D. 2023. Two “edges” in our knowledge on the functions of ribosomal proteins: The revealed contributions of their regions to translation mechanisms and the issues of their extracellular transport by exosomes. Int J Mol Sci 24.

315. Armijos-Jaramillo V, Mosquera A, Rojas B, Tejera E. 2021. The search for molecular mimicry in proteins carried by extracellular vesicles secreted by cells infected with *Plasmodium falciparum*. Commun Integr Biol 14:212–220.

316. Demarta-Gatsi C, Rivkin A, Di Bartolo V, Peronet R, Ding S, Commere PH, Guillonneau F, Bellalou J, Brûlé S, Abou Karam P, Cohen SR, Lagache T, Janse CJ, Regev-Rudzki N, Mécheri S. 2019. Histamine releasing factor and elongation factor 1 alpha secreted via malaria parasites extracellular vesicles promote immune evasion by inhibiting specific T cell responses. Cell Microbiol 21.

317. Daniyan MO, Przyborski JM, Shonhai A. 2019. Partners in mischief: Functional networks of heat shock proteins of *Plasmodium falciparum* and their influence on parasite virulence. Biomolecules 9.

318. Sisquella X, Ofir-Birin Y, Pimentel MA, Cheng L, Abou Karam P, Sampaio NG, Penington JS, Connolly D, Giladi T, Scicluna BJ, Sharples RA, Waltmann A, Avni D, Schwartz E, Schofield L, Porat Z, Hansen DS, Papenfuss AT, Eriksson EM, Gerlic M, Hill AF, Bowie AG, Regev-Rudzki N. 2017. Malaria parasite DNA-harbouring vesicles activate cytosolic immune sensors. Nat Commun 8.

319. Acharya D, Bavikatte AN, Ashok VV, Hegde SR, Macpherson CR, Scherf A, Vembar SS. 2025. Ectopic overexpression of *Plasmodium falciparum* DNA-/RNA-binding Alba proteins misregulates virulence gene homeostasis during asexual blood development. Microbiol Spectr 13.

320. Muñoz EE, Hart KJ, Walker MP, Kennedy MF, Shipley MM, Lindner SE. 2017. ALBA4 modulates its stage-specific interactions and specific mRNA fates during *Plasmodium yoelii* growth and transmission. Mol Microbiol 106:266–284.

321. Mantel PY, Marti M. 2014. The role of extracellular vesicles in *Plasmodium* and other protozoan parasites. Cell Microbiol 16:344–354.

322. Babatunde KA, Yesodha Subramanian B, Ahouidi AD, Martinez Murillo P, Walch M, Mantel PY. 2020. Role of extracellular vesicles in cellular cross talk in malaria. Front Immunol 11.

323. Paing M, Salinas N, Adams Y, Oksman A, Jensen A, Goldberg D, Tolia N. 2018. Shed EBA-175 mediates red blood cell clustering that enhances malaria parasite growth and enables immune evasion. Elife 7.

324. Mills JP, Diez-Silva M, Quinn DJ, Dao M, Lang MJ, W Tan KS, Lim CT, Milon G, David PH, Mercereau-Puijalon O, Bonnefoy S, Suresh S. 2007. Effect of plasmodial RESA protein on deformability of human red blood cells harboring *Plasmodium falciparum*. PNAS 104:9213–9217.

325. Yang M, Coppens I, Wormsley S, Baevova P, Hoppe HC, Joiner KA. 2004. The *Plasmodium falciparum* Vps4 homolog mediates multivesicular body formation. J Cell Sci 117:3831–3838.

10. Supplementary material

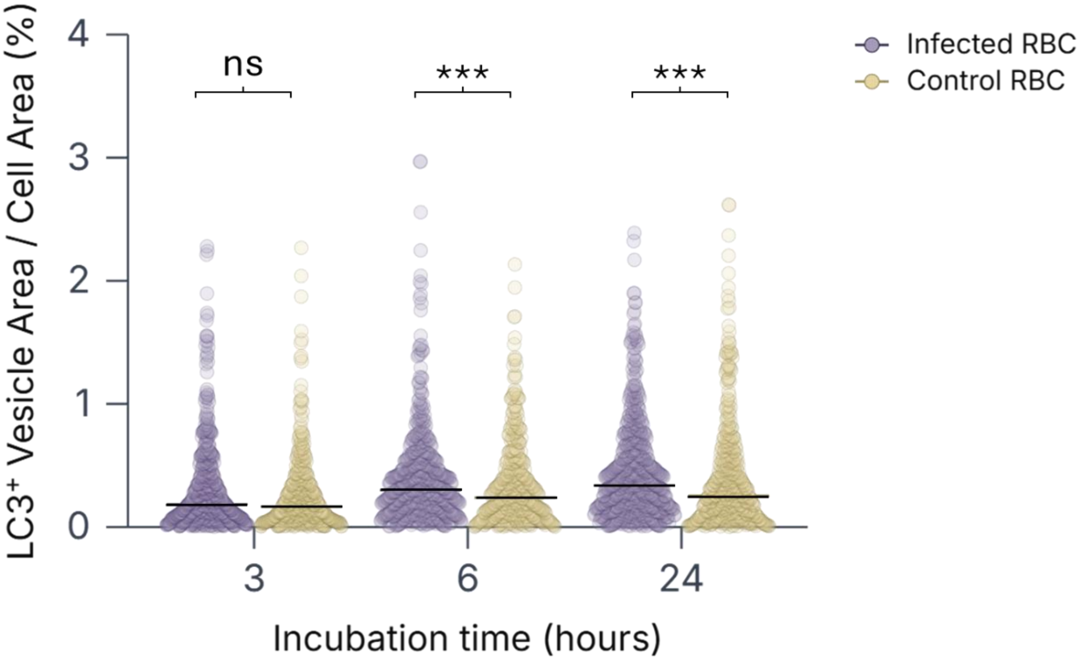

Figure S.1. Time-course analysis of LC3 accumulation in LC3-GFP tEnd.1 endothelial cells following incubation with *P. berghei*-iRBCs at a ratio of 100 RBCs per EC. Spread plots show the percentage of cellular area occupied by LC3-positive vesicles in LC3-GFP tEnd.1 endothelial cells after treatment for 3, 6 and 24 hours with 100 iRBCs and control RBCs per endothelial cell. Each dot represents an individual cell, and horizontal lines indicate median values. Quantification was performed across three independent experiments, analyzing at least n = 100 cells per condition in total. Statistical significance was assessed using the Mann–Whitney U test. All iRBC-treated groups showed a higher LC3-positive area compared to their respective controls; however, statistically significant differences were only observed at 6 hours ($P = 0.0021$) and 24 hours ($P < 0.0001$), whereas no significant difference was detected at 3 hours ($P = 0.0683$). RBC: red blood cell; iRBCs: infected RBCs; EC: endothelial cell.

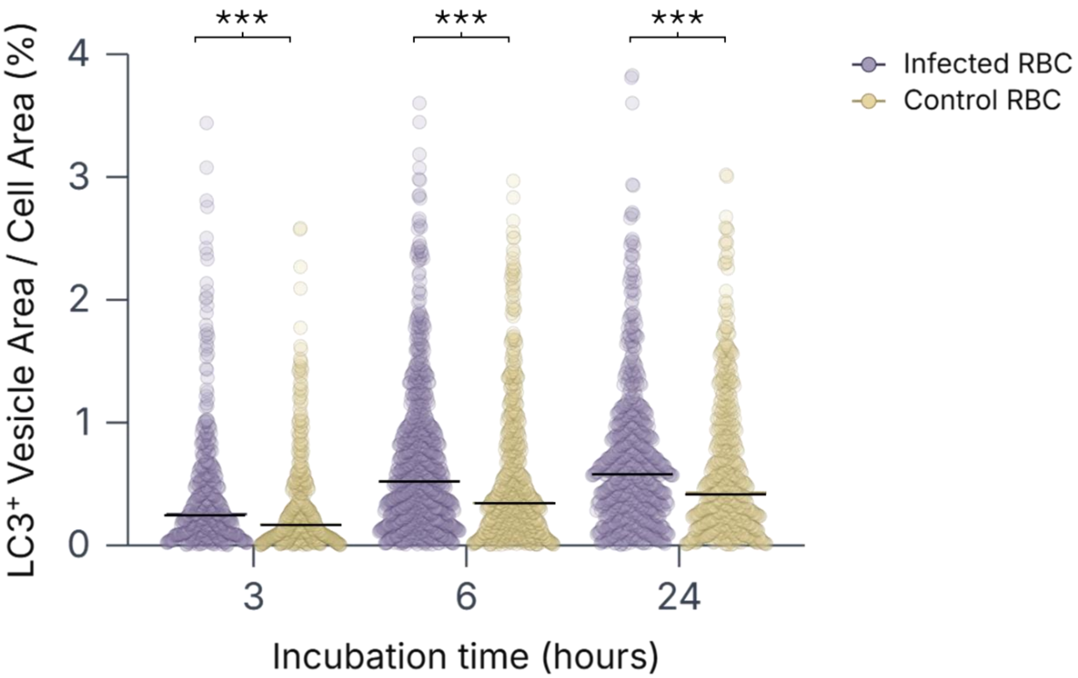

Figure S.2. Time-course analysis of LC3 accumulation in LC3-GFP tEnd.1 endothelial cells following incubation with *P. berghei*-iRBCs at a ratio of 1000 RBCs per EC. Spread plots show the percentage of cellular area occupied by LC3-positive vesicles in LC3-GFP tEnd.1 endothelial cells after treatment for 3, 6 and 24 hours with 1000 iRBCs and control RBCs per endothelial cell. Each dot represents an individual cell, and horizontal lines indicate median values. Quantification was performed across three independent experiments, analyzing at least n = 100 cells per condition in total. Statistical significance was assessed using the Mann–Whitney U test. All iRBC-treated groups showed a higher LC3-positive area compared to their respective controls, statistically significant differences were observed at 3 hours ($P < 0.0001$), 6 hours ($P < 0.0001$) and 24 hours ($P = 0.0002$). RBC: red blood cell; iRBCs: infected RBCs; EC: endothelial cell.

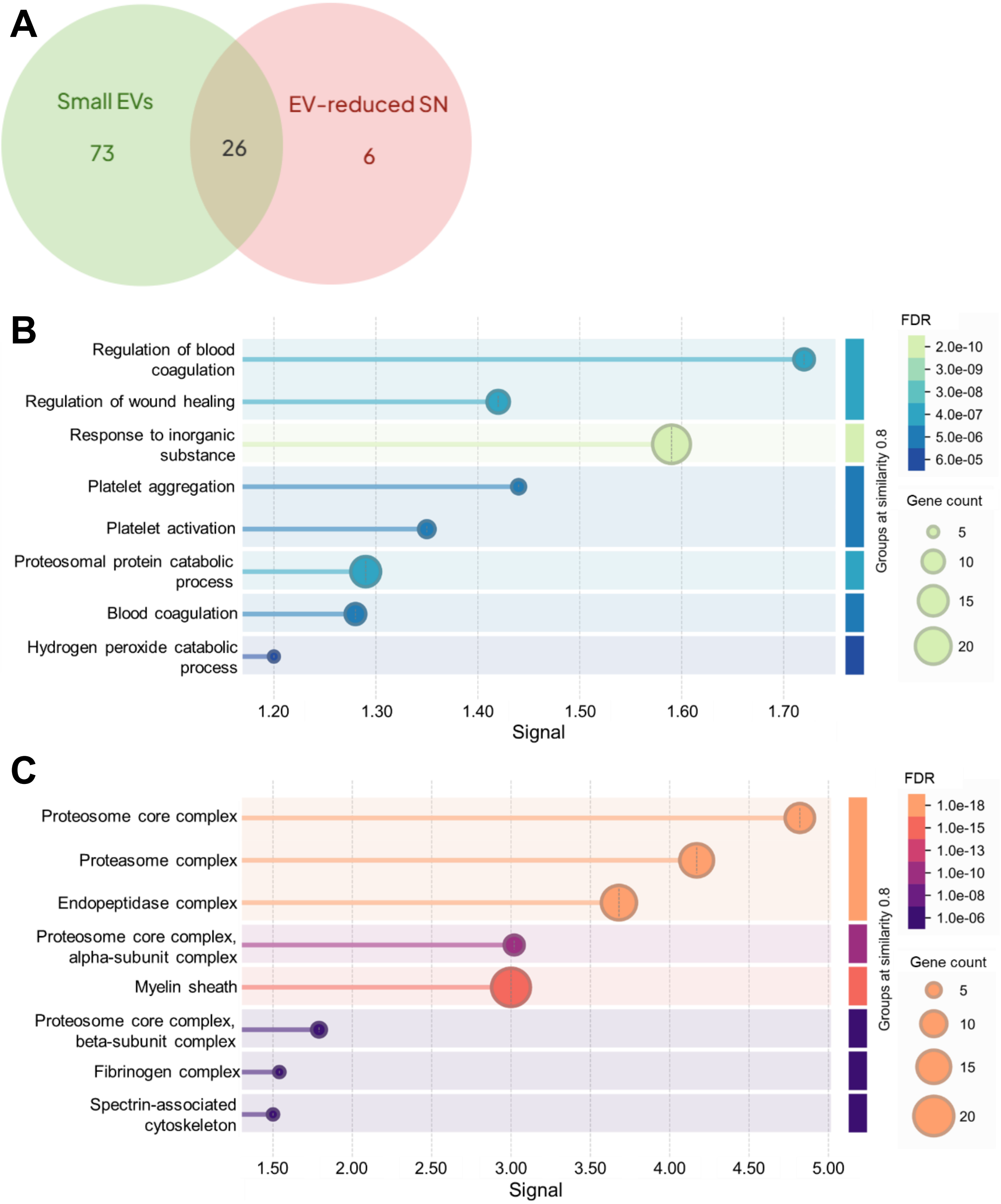

Figure S.3. Proteomic profiling of small extracellular vesicles produced by RBCs in a *P. berghei* culture. (A) Venn diagram showing the distribution of *Mus musculus* proteins identified in the enriched small EV fraction and their respective EV-reduced supernatant (SN). A total of 99 host proteins were identified in the EV fraction, of which 73 were unique to this fraction. (B, C) Gene Ontology (GO) enrichment analysis for (B) Biological Process and (C) Cellular Component categories. Enrichment analysis was performed using the STRING database (version 12.0), and the eight GO terms with the highest signal values meeting the significance threshold (FDR < 0.01) are shown.

Table S.1. Host-derived proteins identified in small extracellular vesicles (EVs) enriched from *Plasmodium berghei* culture.

UniProt ID	Description/Name
C0HKE5	Histone H2A type 1-G
E9PV24	Fibrinogen alpha chain
O08529	Calpain-2 catalytic subunit
O54890	Integrin beta-3
O55222	Integrin-linked protein kinase
O55234	Proteasome subunit beta type-5
Q812C9	Amine oxidase [copper-containing] 2
O70435	Proteasome subunit alpha type-3
O88685	26S proteasome regulatory subunit 6A
P00920	Carbonic anhydrase 2
P01649	Ig kappa chain V-V regions
P01837	Immunoglobulin kappa constant
P01872	Immunoglobulin heavy constant mu
P01942	Hemoglobin subunit alpha
P02088	Hemoglobin subunit beta-1
P02089	Hemoglobin subunit beta-2
P84244	Histone H3.3
P04919	Band 3 anion transport protein
P05064	Fructose-bisphosphate aldolase A
P05213	Tubulin alpha-1B chain
P06151	L-lactate dehydrogenase A chain
P07724	Albumin
P08032	Spectrin alpha chain
P08226	Apolipoprotein E
P09528	Ferritin heavy chain
P10126	Elongation factor 1-alpha 1
P10518	Delta-aminolevulinic acid dehydratase
Q8CGP2	Histone H2B type 1-P
P11087	Collagen alpha-1(I) chain
P11276	Fibronectin
P11352	Glutathione peroxidase 1
P15105	Glutamine synthetase
P15327	Bisphosphoglycerate mutase
P15508	Spectrin beta chain
Q01768	Nucleoside diphosphate kinase B
P15864	Histone H1.2
P16858	Glyceraldehyde-3-phosphate dehydrogenase
P20152	Vimentin
P24270	Catalase

P24549	Aldehyde dehydrogenase 1A1
P26039	Talin-1
P28654	Decorin
P29391	Ferritin light chain 1
P29788	Vitronectin
P32261	Antithrombin-III
P34884	Macrophage migration inhibitory factor
P48193	Protein 4.1
P49722	Proteasome subunit alpha type-2
P52480	Pyruvate kinase PKM
P53657	Pyruvate kinase PKLR
P63260	Actin
P62806	Histone H4
P63017	Heat shock cognate 71 kDa protein
P68368	Tubulin alpha-4A chain
P68372	Tubulin beta-4B chain
P70195	Proteasome subunit beta type-7
P80314	T-complex protein 1 subunit beta
P80316	T-complex protein 1 subunit epsilon
P99026	Proteasome subunit beta type-4
Q00623	Apolipoprotein A-I
Q01149	Collagen alpha-2(I) chain
Q01853	Transitional endoplasmic reticulum ATPase
Q02053	Ubiquitin-like modifier-activating enzyme 1
Q02357	Ankyrin-1
Q3UDE2	Tubulin--tyrosine ligase-like protein 12
Q9D3R6	Katanin p60 ATPase-containing subunit A-like 2
Q3UVK0	Endoplasmic reticulum metallopeptidase 1
Q571I9	Aldehyde dehydrogenase family 16 member A1
Q60605	Myosin light polypeptide 6
Q60692	Proteasome subunit beta type-6
Q61171	Peroxiredoxin-2
Q61646	Haptoglobin
Q61838	Alpha-2-macroglobulin 165 kDa subunit
Q62351	Transferrin receptor protein 1
Q64523	Histone H2A type 2-C
Q7TMM9	Tubulin beta-2A chain
Q8K0E8	Fibrinogen beta chain
Q8K1B8	Fermitin family homolog 3
Q8K274	Ketosamine-3-kinase
Q8R016	Bleomycin hydrolase
Q8R146	Acylamino-acid-releasing enzyme
Q8VCM7	Fibrinogen gamma chain

Q8VDD5	Myosin-9
Q8VDM4	26S proteasome non-ATPase regulatory subunit 2
Q8VE10	N-alpha-acetyltransferase 40
Q921I1	Serotransferrin
Q922D8	C-1-tetrahydrofolate synthase
Q99J99	3-mercaptopyruvate sulfurtransferase
Q99JI6	Ras-related protein Rap-1b
Q9CWJ9	Bifunctional purine biosynthesis protein ATIC
Q9ESB3	Histidine-rich glycoprotein
Q9QUM9	Proteasome subunit alpha type-6
Q9R1P0	Proteasome subunit alpha type-4
Q9R1P3	Proteasome subunit beta type-2
Q9R1P4	Proteasome subunit alpha type-1
Q9WV69	Dematin
Q9Z2U0	Proteasome subunit alpha type-7
Q9Z2U1	Proteasome subunit alpha type-5
Q9Z2W0	Aspartyl aminopeptidase

Table S.2. Host-derived proteins identified in EV-reduced supernatant (SN) from *Plasmodium berghei* culture. Proteins marked with an asterisk (*) were detected exclusively in the EV-reduced supernatant fraction.

UniProt ID	Description/Name
C0HKE5	Histone H2A type 1-G
E9PV24	Fibrinogen alpha chain
P00920	Carbonic anhydrase 2
P01942	Hemoglobin subunit alpha
P02088	Hemoglobin subunit beta-1
P02089	Hemoglobin subunit beta-2
P84244	Histone H3.3
P04919	Band 3 anion transport protein
P05064	Fructose-bisphosphate aldolase A
P06151	L-lactate dehydrogenase A chain
P07724	Albumin
P10126	Elongation factor 1-alpha 1
P11087	Collagen alpha-1(I) chain
P13634	Carbonic anhydrase 1*
P15327	Bisphosphoglycerate mutase
Q01768	Nucleoside diphosphate kinase B
P16858	Glyceraldehyde-3-phosphate dehydrogenase
P17751	Triosephosphate isomerase *
P24270	Catalase

P32261	Antithrombin-III
P63260	Actin
P68510	14-3-3 protein eta *
Q00623	Apolipoprotein A-I
Q01149	Collagen alpha-2(I) chain
Q03265	ATP synthase subunit alpha *
Q3UVK0	Endoplasmic reticulum metallopeptidase 1
Q61171	Peroxiredoxin-2
Q61838	Alpha-2-macroglobulin 165 kDa subunit
Q8VCM7	Fibrinogen gamma chain
Q921I1	Serotransferrin
Q923D2	Flavin reductase (NADPH) *
Q99KK7	Dipeptidyl peptidase 3 *